

The Pennsylvania State University
The Graduate School
Eberly College of Science

4 DEVELOPMENT OF SCALABLE APPROACHES TO NEUTRINO MASS 5 MEASUREMENT WITH THE PROJECT 8 EXPERIMENT

A Thesis in
The Physics Department
by
Andrew Douglas Ziegler

10 © 2023 Andrew Douglas Ziegler

Submitted in Partial Fulfillment
of the Requirements
for the Degree of

14 Doctor of Philosophy

15 December 2023

¹⁶ The thesis of Andrew Douglas Ziegler was reviewed and approved* by the following:

Luiz de Viveiros Souza
Assistant Professor of Physics
Thesis Advisor
Chair of Committee

Carmen Carmona
Assistant Professor of Physics

¹⁷ Doug Cowan
Professor of Physics and Astrophysics

Xingjie Ni
Associate Professor of Electrical Engineering

¹⁸ Stephanie Wissel
Associate Professor of Physics

¹⁹ *Signatures are on file in the Graduate School.

²⁰ Abstract

²¹ Neutrinos are fundamental particles in the standard model and play an important role
²² in the current understanding of the universe, however, the masses of the neutrinos, one
²³ of the most fundamental parameters for any particles, is currently unknown. This fact
²⁴ represents a gaping hole in our current knowledge of the universe that may provide clues
²⁵ to the energy scale of possible physics beyond the standard model. This dissertation
²⁶ summarizes research and development as a member of the Project 8 collaboration towards
²⁷ an experiment to measure the neutrino mass to a sensitivity below $50 \text{ meV}/c^2$, which
²⁸ is an order of magnitude below the most sensitive direct measurements of the neutrino
²⁹ mass to date. Project 8 will perform this measurement using Cyclotron Radiation
³⁰ Emission Spectroscopy (CRES) to measure the beta-decay endpoint spectrum of atomic
³¹ tritium. I present an analysis of the signal reconstruction performance of an antenna
³² array system designed to perform large-scale CRES measurements. Next, I discuss an
³³ approach to calibrating an antenna array CRES experiment using a unique probe antenna
³⁴ designed to mimic radiation from CRES events. Finally, I present design studies for a
³⁵ resonant cavity that could be used to perform a CRES experiment with atomic tritium
³⁶ at multi-cubic-meter scales.

Table of Contents

38	List of Figures	viii
39	List of Tables	xxvii
40	Chapter 1	
41	Introduction	1
42	1.1 Summary	1
43	1.2 Outline	4
44	Chapter 2	
45	Neutrinos and Neutrino Masses	6
46	2.1 Introduction	6
47	2.2 Neutrinos and Beta-decay	6
48	2.3 Neutrino Oscillations	8
49	2.4 Neutrino Masses in the Standard Model	11
50	2.5 Neutrino Absolute Mass Scale	13
51	2.5.1 Limits from Cosmology	13
52	2.5.2 Limits from Neutrinoless Double Beta-decay Searches	15
53	2.5.3 Limits from Beta-decay	17
54	Chapter 3	
55	Direct Measurement of the Neutrino Mass with Project 8	21
56	3.1 Introduction	21
57	3.2 Cyclotron Radiation Emission Spectroscopy and Project 8	22
58	3.2.1 Cyclotron Radiation Emission Spectroscopy — CRES	22
59	3.2.2 The Project 8 Collaboration	26
60	3.2.3 The Project 8 Phased Development Plan	30
61	3.3 Phase II: First Tritium Beta Decay Spectrum and Neutrino Mass Mea- surement with CRES	33
62	3.3.1 The Phase II CRES Apparatus	34
63	3.3.2 CRES Track and Event Reconstruction	38
64	3.3.3 Results from Phase II	42
65	3.4 Phase III R&D: Antenna Array CRES	46
66	3.4.1 The Basic Approach	46

68	3.4.2 The FSCD: Free-space CRES Demonstrator	48
69	3.5 Pilot-scale Experiments	53
70	3.5.1 Choice of Frequency	53
71	3.5.2 Pilot-scale Experiment Concepts	56
72	3.6 Phase IV	58

73	Chapter 4	
74	Signal Reconstruction Techniques for Antenna Array CRES and the	
75	FSCD	60
76	4.1 Introduction	60
77	4.2 FSCD Simulations	61
78	4.2.1 Kassiopeia	62
79	4.2.2 Locust	66
80	4.2.3 CRESana	70
81	4.3 Signal Detection and Reconstruction Techniques for Antenna Array CRES	71
82	4.3.1 Digital Beamforming	75
83	4.3.2 Matched Filtering	85
84	4.3.3 Machine Learning	97
85	4.4 Analysis of Signal Detection Algorithms for the Antenna Array Demonstrator	104
86	4.4.1 Introduction	104
87	4.4.2 Signal Detection with Antenna Array CRES	106
88	4.4.2.1 Antenna Array and DAQ System	106
89	4.4.2.2 Real-time Signal Detection	109
90	4.4.3 Signal Detection Algorithms	113
91	4.4.3.1 Power Threshold	113
92	4.4.3.2 Matched Filtering	114
93	4.4.3.3 Machine Learning	119
94	4.4.4 Methods	120
95	4.4.4.1 Data Generation	120
96	4.4.4.2 Template Number and Match Estimation	121
97	4.4.4.3 CNN Training and Data Augmentation	122
98	4.4.5 Results and Discussion	124
99	4.4.5.1 Trigger Classification Performance	124
100	4.4.5.2 Computational Cost and Hardware Requirements	125
101	4.4.6 Conclusion	128

102	Chapter 5	
103	Antenna and Antenna Measurement System Development for the	
104	Project 8 Experiment	129
105	5.1 Introduction	129
106	5.2 Antenna Measurements for CRES experiments	130
107	5.2.1 Antenna Parameters	130
108	5.2.1.1 Radiation Patterns	130
109	5.2.1.2 Directivity and Gain	131

110	5.2.1.3	Far-field and Near-field	132
111	5.2.1.4	Polarization	133
112	5.2.1.5	Antenna Factor and Effective Aperture	134
113	5.2.2	Antenna Measurement Fundamentals	136
114	5.2.2.1	Friis Transmission Equation	136
115	5.2.2.2	S-Parameters and Network Analyzers	137
116	5.2.2.3	Antenna Array Commissioning and Calibration Measurements	138
117	5.2.3	The Penn State Antenna Measurement System	140
118	5.3	Development of a Synthetic Cyclotron Antenna (SYNCA) for Antenna Array Calibration	143
119	5.3.1	Introduction	143
120	5.3.2	Cyclotron Radiation Phenomenology	146
121	5.3.3	SYNCA Simulations and Design	152
122	5.3.4	Characterization of the SYNCA	156
123	5.3.5	Beamforming Measurements with the SYNCA	160
124	5.3.6	Conclusions	163
125	5.4	SYNCA Development Discussion	164
126	5.5	FSCD Antenna Array Measurements with the SYNCA	167
127	5.5.1	Introduction	167
128	5.5.2	Measurement Setups	168
129	5.5.2.1	FSCD Array Setup	168
130	5.5.2.2	Synthetic Array Setup	170
131	5.5.3	Simulations, Analysis, and Results	171
132	5.5.3.1	Simulations	171
133	5.5.3.2	Phase Analysis	172
134	5.5.3.3	Magnitude Analysis	177
135	5.5.3.4	Beamforming Characterization	179
136	5.5.4	Conclusions	182

139	Chapter 6		
140	Development of Resonant Cavities for Large Volume CRES Measurements		184
141	6.1	Introduction	184
142	6.2	Cylindrical Resonant Cavities	185
143	6.2.1	General Field Solutions	185
144	6.2.2	TE and TM Modes	186
145	6.2.3	Resonant Frequencies of a Cylindrical Cavity	188
146	6.2.4	Cavity Q-factors	190
147	6.3	The Cavity Approach to CRES	194
148	6.3.1	A Sketch of a Molecular Tritium Cavity CRES Experiment	194
149	6.3.2	Magnetic Field, Cavity Geometry, and Resonant Modes	196
150	6.3.3	Trade-offs Between the Antenna and Cavity Approaches	199
151	6.4	Single-mode Resonant Cavity Design and Simulations	201

153	6.4.1	Open Cylindrical Cavities with Coaxial Terminations	201
154	6.4.2	Mode Filtering	204
155	6.4.3	Simulations of Open, Mode-filtered Cavities	206
156	6.5	Single-mode Resonant Cavity Measurements	209
157	6.5.1	Cavities and Setup	209
158	6.5.2	Results and Discussion	212
159	Chapter 7		
160	Conclusion and Future Prospects		216
161	Bibliography		218

List of Figures

162	2.1	A diagram of two different neutrino mass ordering scenarios. In the inverted hierarchy (inverted mass ordering) the lightest neutrino mass is m_3 , whereas, in the normal hierarchy (normal mass ordering) m_1 is the lightest neutrino. What cannot be measured by neutrino oscillations is the neutrino absolute mass scale, which is essentially the mass of the lightest neutrino mass eigenstate.	9
163	2.2	The masses of the neutrinos as a function of the lightest neutrino mass in both the normal (a) and inverted (b) mass ordering regimes.	10
164	2.3	The neutrino mass observable measured by cosmology as a function of the lightest neutrino mass eigenstate.	14
165	2.4	Feynman diagrams for double beta-decay (a) and $0\nu\beta\beta$ (b).	15
166	2.5	The discovery probabilities for the future generation of $0\nu\beta\beta$ experiments as a function of $m_{\beta\beta}$ and m_{least} . Figure from [1].	16
167	2.6	A Feynman diagram of beta decay	17
168	2.7	A figure from Fermi's 1934 paper on a theory of beta-decay depicting the kinetic energy spectrum of the emitted electron. The effect of the neutrino mass, written as μ , is to distort the shape of the spectrum near the endpoint from the zero-mass spectrum.	17
169	2.8	The tritium beta-decay spectrum. The effect of a massive neutrino on the spectrum is to change its shape near the endpoint by an amount proportional to the size of the neutrino mass. A sufficiently high-statistic and high-resolution measurement of the spectrum endpoint would be able to measure the neutrino mass.	19
170			
171			
172			
173			
174			
175			
176			
177			
178			
179			
180			
181			
182			
183			
184			
185			

186	3.1	A cartoon illustration of the CRES technique. An electron is contained in a magnetic trap so that it's cyclotron radiation can be detected by an array of antennas. Detecting the cyclotron radiation allows us to measure its cyclotron frequency and determine its kinetic energy.	23
190	3.2	An illustration of an electron in a bathtub magnetic trap generated by two well-separated coils.	24
192	3.3	A plot of the main components of an electron's trajectory in a cylindrically symmetric trap.	26
194	3.4	A plot of the final state distributions of atomic and molecular tritium. The final state distribution provides the primary contribution to the width of the molecular spectrum whereas thermal doppler broadening is responsible for the width of the atomic spectrum.	27
198	3.5	Neutrino mass exclusion plot including limits from cosmological measure- ments and the KATRIN experiment. Allowed ranges for neutrino masses under the normal and inverted hierarchies are shown as the blue and orange lines respectively. The black dashed line shows Project 8's goal neutrino mass sensitivity for the Phase IV experiment.	30
203	3.6	Sensitivity calculations for a cavity based CRES experiment that demon- strate the neutrino mass measurement goals of the Project 8 collaboration throughout the phased development plan. The blue curves indicate molec- ular tritium sources and the red curves indicate atomic tritium sources. In the current plan Phase III contains two tritium experiments. The first is the Low-frequency Apparatus (LFA) which is a molecular tritium experiment and the second is the atomic tritium pilot-scale experiment that ends Phase III. The sensitivity of these experiments is primarily a function of statistics, however, there is a critical density beyond which CRES electrons do not have enough time to radiate between collisions for a high-resolution frequency measurement leading to worse sensitivity. . .	31
214	3.7	The Phase II CRES apparatus used to perform the first measurement of the tritium beta-decay spectrum using CRES.	34
216	3.8	Diagram of the CRES cell portion of the Phase II apparatus.	36
217	3.9	RF system diagram for the Phase II apparatus.	37
218	3.10	The time-frequency spectrogram of a tritium CRES event in the Phase II apparatus.	39

220	3.11 The sparse spectrogram obtained by placing a power cut on the raw 221 spectrogram shown in Figure 3.10.	41
222	3.12 Fits to the measured 17.8-keV ^{83m}Kr conversion line using the deep and 223 shallow trap configurations.	43
224	3.13 Measurements of the 17.8-keV ^{83m}Kr line using the deep trap configuration 225 for different values of the magnetic field from the field shifting solenoid.	44
226	3.14 The measured tritium spectrum from Phase II with Bayesian and frequen- 227 tist fits.	45
228	3.15 A cartoon illustration of the basics of the antenna array CREES technique.	47
229	3.16 An image of the MRI magnet installed in the Project 8 laboratory at the 230 University of Washington, Seattle.	49
231	3.17 (a) A model of the FSCD antenna array, magnetic trap, and tritium 232 containment vessel design.(b) A more detailed model of a prototype 233 design for the 5-slot waveguide antenna design.	50
234	3.18 (a) A plot of the decay rate for the two-body dipolar spin exchange 235 interaction for cc and dd state. (b) A plot of the decay rate of the dipolar 236 spin exchange interaction for d+d states as a function of magnetic field 237 magnitude. Lowering the magnetic field is key for reducing the losses 238 from this interaction.	55
239	3.19 A conceptual sketch of a large-volume antenna array based CREES experi- 240 ment to measure the neutrino mass.	56
241	3.20 A conceptual sketch of a pilot-scale cavity CREES experiment with an 242 atomic tritium beamline.	57

243	3.21 An illustration of a possible arrangement of ten pilot-scale cavity experiments for Phase IV. The experiments are arranged in a circle with an approximate diameter of 50 meters. Each atomic beamline connected to the bottom of each cavity is approximately 10 m in length. The cavities themselves are designed to operate at 325 MHz and are approximately 11 m tall. The circular arrangement of cavities has some advantages when it comes to cancellation of fringe fields from neighboring magnets, which is important due to the small magnetic field magnitudes consistent with these CRES frequencies. The advantage of ten independent atomic sources and cavities is that there is no single point of failure for the experiment. If an experiment goes down for repairs the other nine may continue running. Figure courtesy of Michael Huehn at UW-Seattle.	59
255	4.1 The geometry and parameters of the coils used to simulate the FSCD magnetic trap in Kassiopeia. Some axial profiles of the magnetic trap at different radial positions are show to demonstrate the shape of the magnetic field and trap depth as a function of position. Calulation of the magnetic field profiles was graciously done by René Reimann.	63
260	4.2 A map of the average ∇B -drift frequency for electrons trapped in the prototype FSCD trap shown in Figure 4.1. Negative drift frequencies indicate electrons that are drifting opposite to the standard direction, which means that they are close to escaping the magnetic trap.	65
264	4.3 The receiver chain used by Locust when simulating CRES events in the FSCD.	68
266	4.4 A high-level diagram depicting the process of CRES event reconstruction. The first step consists of identifying the presence of a signal in the data. This step is necessary to avoid the danger of performing a reconstruction of a false event, which would constitute a background contribution to the tritium spectrum measured by CRES.	72
271	4.5 An illustration of two PDFs associated a binary hypothesis test. The decision threshold is represented by the vertical line that partitions both distributions. The orange and red areas correspond to the true negative and false positive probabilities and the blue and green areas correspond to the false negative and true positive probabilities respectively. To decided between the two hypotheses we perform the likelihood ratio test specified by the Neyman-Pearson theorem. This approach achieves the highest true positive probability for a given false positive probability.	74

279	4.6 An example ROC curve formed by computing the P_{FP} and the P_{TP} for 280 a given likelihood ratio test. As the decision threshold is increased P_{FP} 281 decreases at the expense of a lower P_{TP} . The black dashed line indicates 282 the lower bound ROC curve obtained by randomly deciding between \mathcal{H}_0 283 and \mathcal{H}_1	75
284	4.7 An illustration of the constructive interference condition which is the 285 operating principle of digital beamforming using a uniform linear array 286 as an example.	76
287	4.8 System level diagram of the laboratory setup used for beamforming 288 demonstrations at Penn State. For more information on this system see 289 Chapter 5. Signals near 26 GHz are fed to a dipole antenna using an 290 arbitrary waveform generator (AWG) and vector network analyzer (VNA), 291 which drive a mixer. The dipole radiation is collected by an array of 292 antennas connected to the digitizer data acquisition (DAQ) system. . . .	78
293	4.9 Photographs of the beamforming demonstration setup. In (a) I show a 294 top-down view of the dipole antenna and the array of eight horn antennas. 295 Manual repositioning of the horn antennas allows one to synthesize a full- 296 circular antenna array. The dipole antenna is mounted on a camera tripod 297 mount that allows for manual position tuning. (b) is a close up image of 298 the dipole, which is manufactured from two segments of semi-rigid coaxial 299 cable. (c) is another image of the dipole and array.	79
300	4.10 An example of digital beamforming reconstruction of a dipole antenna 301 using a synthetic array of horn antennas. The beamforming image on 302 the right is constructed by computing the time-averaged power of the 303 summed signals for a two-dimensional grid of beamforming positions. In 304 the image one can see a clear maximum that corresponds to the position 305 of the dipole antenna. On the left I show the frequency spectrum of the 306 time-series at the maximum power pixel. White gaussian noise is added 307 to the signal to mimic a more realistic signal-to-noise-ratio. The signal 308 emitted by the dipole is clearly visible as the high power peak in the 309 frequency spectrum.	79
310	4.11 Beamforming images visualizing the reconstruction of an electron without 311 (a) and with (b) the cyclotron phase correction. The images were generated 312 using data from Locust simulations. The cyclotron phase refers to a phase 313 offset equal to the relative azimuthal position of an antenna in the array. 314 This phase offset is caused by the circular electron orbit and must be 315 corrected for during reconstruction.	81

316	4.12 Beamforming images visualizing the reconstruction of an electron located 317 off the central axis of the FSCD trap. In (a) we performing beamforming 318 without the ∇B -drift correction, and in (b) we include the ∇B -drift 319 correction.	82
320	4.13 A plot of a typical frequency spectrum obtained by applying a Fourier 321 transform to the time-series obtained from beamforming. The frequency 322 spectra are plotted without noise on top of an example of a typical noise 323 spectrum to visualize a realistic signal-to-noise ratio. In the example we 324 see that without beamforming it would not be possible to detect anything 325 since the signal amplitudes would be reduced by a factor of sixty relative 326 to the noise. Additionally, we see that the ∇B -drift correction is needed 327 to detect this electron since it comes from a simulation of an electron with 328 a significant off-axis position.	83
329	4.14 A plot of the total signal power received by the FSCD array from trapped 330 electrons with different radial positions and pitch angles generated using 331 Locust simulations. The lines on the plot indicate a 10 dB detection 332 threshold above the mean value of the noise in the frequency spectrum. 333 With static beamforming electrons with radial positions larger than about 334 two centimeters are undetectable due to the change in the electron's 335 position over time causing losses from beamforming phase mismatch. This 336 is corrected by including ∇B -drift frequencies in the beamforming phases. 337 Both beamforming techniques fail to detect electrons below $\approx 88.0^\circ$, since 338 these signal are composed of several relatively weak sidebands that are 339 comparable to the noise.	84
340	4.15 Example of a convolution of a CRES signal template with a segment of 341 noisy data. A simulated CRES signal was simulated using Locust and 342 normalized to create a matched filter template. When this template is 343 convolved with noisy data the contains the matching signal the con- 344 volution output increases dramatically compared to data with only noise. 345 The decreasing convolution output as the time offset of the convolution 346 increases is caused by zero-padding of the data and template.	87

385	4.21 Two example illustrations of the correlation between kinetic energy and	
386	pitch angle imparted by the shape of the FSCD magnetic trap. The	
387	correlations manifest themselves as degeneracies in the matched filter	
388	score where multiple matched filter templates have the same matched filter	
389	for a particular signal. These degeneracies are a sign that the magnetic	
390	trap must be redesigned in order to break the correlation between pitch	
391	angle and kinetic energy.	97
392	4.22 A visualization of the correlation between energy and pitch angle in the	
393	FSCD magnetic trap. The image is formed by computing the match of the	
394	best template from a grid consisting of pitch angles from 84 to 90 degrees	
395	in steps of 0.05 degrees, kinetic energies from 17574 to 18574 eV, located	
396	at 2 cm from the central axis, and simulated for a length of three FSCD	
397	time-slices. The signals used to compute the best matching template	
398	consisted of a grid from 84 to 90 degrees in steps of 0.05 degrees, kinetic	
399	energies from 18550 to 18575 eV in steps of 0.25 eV, located 2 cm from	
400	the central axis, and simulated for three FSCD time-slices. The colored	
401	regions of the plot show how well signals with lower energy can match	
402	those of higher energy for the FSCD magnetic trap, which is proportional	
403	to the achievable energy resolution of the FSCD design.	98
404	4.23 A representation of a matched filter template bank as a convolutional	
405	neural network. The network has a single layer composed of the templates,	
406	which act as convolutional filters. The activation of the neural network is	
407	an absolute value followed by a max operator.	100
408	4.24 A graphical depiction of CRES signal detection using a CNN. A noisy	
409	segment of data is converted to a frequency series using digital beamforming	
410	and a FFT. The complex-valued frequency series is input into a trained	
411	CNN model that classifies the data as signal or noise using a decision	
412	threshold on the CNN output.	102
413	4.25 The detection efficiency and false alarm rate (false positive rate) as	
414	a function of the decision threshold for different values of the noise	
415	temperature. The model is trained to output a value close to one for	
416	data that contains a signal and outputs a value near zero when the data	
417	contains only noise. One sees that a lower decision threshold will have a	
418	high detection efficiency at the cost of a high rate of false alarms.	103
419	4.26 ROC curves for a CNN model classifying CRES signals. One can see	
420	that the area under the curve, which is a figure of merit that describes the	
421	performance of the classifier, is roughly linearly dependent with the noise	
422	temperature.	103

423	4.27 An illustration of the conceptual design for an antenna array CRES tritium beta-decay spectrum measurement. The antenna array geometry consists of a 20 cm interior diameter with 60 independent antenna channels arranged evenly around the circumference. The nominal antenna design is sensitive to radiation in the frequency range of 25-26 GHz, which corresponds to the cyclotron frequency of electrons emitted near the tritium beta-spectrum endpoint in a 1 T magnetic field. The array is located at the center of the magnetic trap produced by a set of current- carrying coils. The nominal magnetic trap design is capable of trapping electrons up to 5 cm away from the central axis of the array and traps electrons within an approximately 6 cm long axial region centered on the antenna array.	106
435	4.28 A high-level diagram of the DAQ system architecture envisioned for the FSCD.	107
437	4.29 A block diagram illustration of the real-time triggering algorithm proposed for antenna array CRES reconstruction.	108
439	4.30 An illustration of the digital beamforming procedure. The blue lines indicate the various distances from the beamforming position to the antenna. In the situation depicted the actual position of the electron matches the beamforming position, so we should expect constructive interference when the phase shifted signals are summed. To prevent the electron's ∇B -motion from moving the electron off of the beamforming position, the beamforming phase include a time-dependence to follow the trajectory of the electron in the magnetic trap.	109
447	4.31 Frequency spectra of simulated CRES signals post-beamforming. The signal of a 90° electron consists of a single frequency component that is easy to detect with a power threshold on the frequency spectrum. This power threshold is still effective for signals with relatively large pitch angles such as 89.0° and 88.75°, which are composed of a main carrier and a few small sidebands. Signals with smaller pitch angles, below about 88.5°, tend to be dominated by sidebands such that no single frequency component can be reliably distinguished from the noise with a power threshold.	111

456	4.32 PDFs of the power threshold test statistic for CRES signals with various 457 pitch angles as well as the PDF for the noise-only signal case. The average 458 PDF computed for pitch angles ranging from 85.5 to 88.5° is also shown. 459 As the pitch angle is decreased the signal PDF converges towards the 460 noise PDF which indicates that the power threshold trigger is unable to 461 distinguish between small pitch angle signals and noise.	114
462	4.33 Plots of the estimated PDFs for the matched filter template bank test 463 statistic for CRES signals with various pitch angles as well as the estimated 464 PDF for the noise only signal case. We assume an estimated number 465 of templates of 10^5 and perfect match between signal and template i.e. 466 $\Gamma_{\text{best}} = 1$. The mean PDF includes signals ranging from 85.5 – 88.5° in 467 pitch angle. There is a much larger distinction between the signal PDFs 468 at small pitch angle compared to the power threshold indicating a higher 469 detection efficiency for these signals.	118
470	4.34 The mean match of the matched filter template bank to a test set of 471 randomly parameterized signals as a function of the number or density of 472 templates. The parameter space includes pitch angles from 85.5 – 88.5° 473 and energies from 18575 – 18580 eV.	122
474	4.35 Histograms of the trained CNN model output from the test dataset. The 475 blue histogram shows the model outputs for signal data. The oddly shaped 476 peak near the end is the result of the softmax function mapping the long 477 tail of the raw output distribution to the range [0, 1].	123
478	4.36 ROC curves describing the detection efficiency or true positive rates for 479 the three signal classification algorithms examined in this paper.	124
480	5.1 An example radiation pattern generated using HFSS simulations. The 481 color and radial distance of the surface from the origin indicate the 482 relative magnitude of radiation power emitted by the antenna in that 483 direction. The primary goal of most antenna measurements is typically to 484 measure the antenna pattern, which is used to derive many useful antenna 485 performance parameters.	130

486	5.2 An illustration of the three field regions important for the analysis of 487 an antenna system. Very close to the antenna the electric fields are 488 primarily reactive so there is no radiation. If a receiving antenna were 489 placed in this region most of the energy would be reflected back to the 490 transmitter. Outside of the reactive near-field is the radiative near field. 491 At these distances the antenna does radiate, but the radiation pattern is 492 not well-defined since it changes based on the distance of the receiving 493 antenna. It is only in the far-field region where the radiation pattern 494 becomes constant as a function of distance, which is where the majority 495 of antenna engineering is assumed to take place. The antenna arrays 496 developed by Project 8 for CRES measurements operate in the radiative 497 near-field due to the importance of limiting power loss from free-space 498 propagation, which complicates the design of the antenna system.	132
499	5.3 An illustration of the Friis measurement technique commonly used for 500 antenna characterization measurements.	136
501	5.4 Illustration of a two-port S-parameter measurement setup. S-parameters 502 characterize how incoming waves of voltage or power scatter off of the RF 503 device under test. This allows you to measure important properties of the 504 device. In particular, we can use this framework to model a two antenna 505 radiation pattern measurement, which we can then automate using a VNA.	138
506	5.5 Two measurement approaches to characterizing an antenna array for CRES 507 measurements. The full-array approach (a) requires a complete antenna 508 array with all the associated hardware. The synthetic array approach 509 (b) utilizes a single antenna and a set of rotation/translation stages to 510 reposition the transmitter or the receiving antenna to synthesize the signals 511 that would be received by the full-array. This approach reduces the cost 512 and complexity of array measurements. A down-side of the synthetic 513 array approach is that multi-channel effects such as reflections cannot 514 be measured. Utilizing both the full-array and the synthetic array is a 515 powerful way to quantify the impact of errors from the multi-channel array.	139
516	5.6 Illustration of the antenna measurement system developed for the Project 517 8 Collaboration. The reference and test antennas can be connected to 518 different data acquisition configurations depending on the measurement 519 goals. The reference antenna is typically a standard horn antenna and 520 the test antenna is mounted on a set of translation stages for positioning. 521 Automated translation stages allow for relatively painless data-taking enabling 522 synthetic antenna array measurements using only a single receiving 523 antenna. Anechoic form designed to mitigate RF reflections surrounds 524 the setup.	140

525	5.7	Diagrams of two measurement system configurations. Configuration (a) utilizes a VNA and is more suited to antenna characterization. Configuration (b) utilizes an AWG and VNA as a signal generation system and digitizer to collect measurement data, which is more suited to simulating CRES measurements. The transmission chain utilizes a quadrature hybrid and a pair of baluns to drive the cross-dipole variant test antenna developed for synthetic CRES measurements.	141
532	5.8	A sketch of an antenna array large-volume CRES experiment. Electrons from β -decays are confined in a magnetic field using a set of trap coils. The cyclotron radiation produced by the motion of the trapped electrons can be detected by a surrounding antenna array to determine the electron energies. Measuring the energies of many electrons produces a β -decay spectrum.	144
538	5.9	A schematic of the antenna array test stand. The circular antenna array has a radius of 10 cm with 60 independent channels (limited number shown for clarity). The test stand includes an arbitrary waveform generator (AWG), local oscillator (LO), and data acquisition (DAQ) hardware. Finally, a specialized Synthetic Cyclotron Antenna (SYNCA) is used to inject signals to test the antenna array.	145
544	5.10	An electron (red dot) performing cyclotron motion in the x-y plane. The resulting cyclotron radiation is observed by an antenna located at the field point of interest.	146
547	5.11	A plot of the numeric solution to Equation 5.31. The time-domain representation of the signal (a) is composed of a zero frequency term and a series of harmonics separated by the main cyclotron frequency as shown in the plot of the frequency spectrum (b). We can see that the relative amplitude of the harmonics beyond $k = 7$ are smaller than the main carrier by a factor of about 10^{-5} and are completely negligible.	149
553	5.12	The amplitude maxima of the cyclotron radiation form an Archimedean spiral as the radiation propagates outward from the cyclotron orbit center (a). A circular antenna array located at a fixed radius from the orbit center will receive electric fields with equal magnitude in each of its channels, but the phase of the electric field incident on each array channel will be linearly out of phase from its neighbor antennas by an amount equal to the angular separation of the two channels (b).	151

560	5.13 An idealized crossed-dipole antenna consists of two electric dipole antennas oriented perpendicular to each other and is fed with four signals with a quadrature phase relationship. An example antenna feed circuit is shown which is composed of a chained combination of a quadrature hybrid-coupler (Quad) and two baluns.	152
565	5.14 A model of the PCB crossed-dipole antenna with dimensions. The design has an inside diameter of 2.16 mm for the central circular trace, which is 0.13 mm wide. The dipole arms each have a width of 1.27 mm and protrude beyond the circular trace by 1.40 mm, which gives an overall width of 4.96 mm for the length of the antenna PCB trace from end-to-end. The overall size of the antenna is 20.0 mm the majority of which is the PCB dielectric material. This design was observed in simulation to maintain the field characteristics of the idealized crossed-dipole while being simpler to fabricate due to the increased size of the antenna.	153
574	5.15 A comparison of the electric field magnitudes, normalized by the maximum value of the electric field in each simulation, plotted on a 10 cm square to visualize the Archimedean spirals formed by the electron (a), the crossed-dipole antenna (b), and a PCB crossed-dipole antenna (c). The matching patterns indicate that the electric fields have similar phase characteristics. These images were generated using Locust simulations for the electron and ANSYS HFSS for both antennas.	154
581	5.16 A comparison of the normalized electric field magnitudes for the ideal crossed-dipole, PCB crossed-dipole, and a simulated electron as a function of the polar angle (θ). (a) Shows the total electric field, (b) shows the ϕ -polarized electric field component, and (c) shows the θ -polarized electric field component. These images were generated using Locust simulations for the electron and ANSYS HFSS for both antennas.	155
587	5.17 A comparison of the normalized electric field magnitudes for the crossed-dipole, PCB crossed-dipole, and a simulated electron as a function of the azimuthal angle (ϕ) evaluated at $\theta = 90^\circ$. This image was generated using Locust simulations for the electron and ANSYS HFSS for both antennas.	156

591	5.18 (a) A cartoon schematic which highlights the routing of the semi-rigid 592 coax transmission lines. (b) A photograph of a SYNCA constructed 593 using the modified crossed-dipole PCB antenna design. Visible in the 594 photograph of the SYNCA are four blobs of solder which are an artifact 595 of the SYNCA's hand-soldered construction. These solder blobs are the 596 most significant deviation from the SYNCA design shown in Figure 5.14 597 and are responsible for a significant fraction of the irregularities seen in 598 the antenna pattern.	157
599	5.19 A schematic of the VNA characterization measurements (a). This setup 600 allows for antenna gain and phase measurements across a full 360° of 601 azimuthal angles using a motorized rotation stage and control of the radial 602 position of the SYNCA using a translation stage. A photo of the setup in 603 the lab is shown in (b).	158
604	5.20 Linear interpolations of the measured electric field magnitude (a) and 605 phase (b). The data was acquired using a VNA at 120 points spaced 606 by 3 degrees from 0 to 357 degrees of azimuthal angle. The different 607 color lines indicate the vertical offset of the horn antenna relative to the 608 SYNCA PCB and the dashed line shows the expected shape from electron 609 simulations. No significant difference in the antenna pattern is observed 610 for the measured vertical offsets.	159
611	5.21 (a) A depiction of the relative phase differences for signals received by a 612 circular antenna array from an isotropic source. The phases correspond to 613 a unique spatial position. (b) A schematic of the setup used to perform 614 digital beamforming.	160
615	5.22 Digital beamforming maps generated using a simulated 60 channel array 616 and electron simulated using the Locust package. (a) and (b) show the 617 beamforming maps for simulated electrons without the cyclotron spiral 618 phases and with the cyclotron spiral phases respectively. (c) and (d) 619 show the beamforming maps produced from SYNCA measurements. We 620 observe good agreement between simulated electrons and the SYNCA 621 measurements.	161

622	5.23 A plot of the SYNCA's reconstructed position using the synthesized horn-	
623	antenna array and digital beamforming. (a) Shows the reconstructed	
624	position of the SYNCA compared with the target position indicated by	
625	the positioning system readout. (b) Shows the reconstruction error, which	
626	is the difference between the target and reconstructed positions. The error	
627	bars in (b) are the uncertainty in the mean position of the 2D Gaussian	
628	used to fit the digital beamforming reconstruction peak obtained from	
629	the fit covariance matrix. The mean fit position uncertainty of 0.02 mm	
630	is an order of magnitude smaller than the typical reconstruction error of	
631	0.3 mm obtained by calculating the standard deviation of the difference	
632	between the reconstructed and target position.	163
633	5.24 Images of an early prototype crossed-dipole antenna manufactured by	
634	hand and the first measurement setup. The antenna was constructed	
635	by hand using four stripped coaxial cables. The antenna was connected	
636	to one port of the VNA, and the remaining three ports on the VNA	
637	were connected to horn antenna arranged with 90 deg offsets around the	
638	crossed-dipole. The measured unwrapped S-parameter phases exhibit the	
639	desired relative phase behavior for a SYNCA. These early measurements	
640	were the first laboratory proof-of-principle for the crossed-dipole SYNCA.	165
641	5.25 An early iteration of a crossed-dipole SYNCA antenna simulated in HFSS.	
642	The antenna is electrically small at 26 GHz, which requires dipole arms on	
643	the order of 1 mm long. This design is limited by the minimum achievable	
644	distance between the dipole arms caused by the available diameters of	
645	coaxial cables. The assumed termination scheme for the coaxial cables to	
646	the antenna is hand-soldering, which introduces random variation in the	
647	antenna pattern from the inevitable blobs of solder left on the surface of	
648	the PCB.	166
649	5.26 A diagram of the array measurement system used to test the prototype	
650	FSCD antenna array. A VNA is used as the primary measurement tool,	
651	which is connected to the array through a series of switches. The other port	
652	of the VNA connects to the SYNCA through the quad-balun chain used	
653	to provide the SYNCA feed signals. During measurements the SYNCA	
654	is positioned inside the center of the antenna array and translated to	
655	different radial and axial positions using a 3-axis manual translation stage	
656	setup.	167
657	5.27 Photos of the prototype FSCD antenna (a), the FSCD array and SYNCA	
658	(b), and the translation stages and coordinate system used to position the	
659	SYNCA (c).	169

660	5.28 A photo of the FSCD antenna and the SYNCA in the synthetic array 661 measurement setup at Penn State.	171
662	5.29 The unwrapped phases of signals received by the FSCD antenna array 663 from an electron with a 90° pitch angle located in the plane of the antenna 664 array. The data points indicated the phases extracted from simulation 665 and the dashed lines show the model predictions.	172
666	5.30 Plots of the measured unwrapped phases from the FSCD array (a) and the 667 synthetic array (b) compared to the model predictions for a series of radial 668 positions. The different phases of the sinusoidal phase oscillations in the 669 two plots reflects differences in the coordinate systems of the measurements.	174
670	5.31 The phase errors between the measurement and model for the synthetic 671 array (blue) and the FSCD array (orange) for a series of radial positions. 672 The label JUGAAD refers to an alternative name for the FSCD array 673 setup. As the SYNCA is translated off-axis phase errors with progressively 674 higher oscillation frequency enter into the measurements.	175
675	5.32 Two dimensional plots of the phase errors for the synthetic array (a) 676 and the FSCD (JUGAAD) array (b). In both plots we observe evidence 677 of a similar diffraction pattern with bilateral symmetry, but the FSCD 678 array measurements have an additional phase error contribution from the 679 different antennas and paths through the switch network.	176
680	5.33 The amplitude of the signals from CRESana for the FSCD array from a 681 90° electron. As the electron is moved from $R = 0$ the signals begin to 682 have unequal amplitudes depending on the distance from the electron to 683 the antenna.	177
684	5.34 The normalized magnitudes of the S21 parameters measured in the FSCD 685 (orange) and synthetic array (blue) setups. The dominant observed 686 behavior as a function of radius is the increase in the number of magnitude 687 peaks, which was noted in the phase error curves. There does not appear 688 to be a strong change in the relative amplitude of a group of antennas as 689 predicted by CRESana.	178
690	5.35	179

691	5.36 Beamforming images from the synthetic array (a) and FSCD array (b) 692 setups with the SYNCA positioned 15 mm off the central axis. In both 693 images we see a clear maxima that corresponds to the true SYNCA 694 position. However, in the FSCD array there is an additional faint peak 695 located at the opposite position of the beamforming maximum. This 696 additional peak is the mirror of the true peak and is the result of reflections 697 between antennas in the FSCD array.	180
698	5.37 A comparison of the maximum signal amplitude obtained by beamforming 699 to the signal amplitude obtained with an ideal summation as a function 700 of the radial position of the SYNCA. The amplitudes for the synthetic 701 array are shown in (a) and the FSCD array are shown in (b). In both 702 setups we observe that the signal amplitudes obtained from beamforming 703 are smaller than the signal amplitude that could be attained with the 704 ideal summation without phase mismatch.	181
705	5.38 The ratio of the beamforming signal amplitude to the ideal signal amplitude 706 for the FSCD and synthetic arrays. We see that the FSCD array has 707 a larger power loss from phase error compare to the synthetic array which 708 indicates that calibration errors associated with the multiple channels as 709 well as reflections are impacting the signal reconstruction.	182
710	6.1 Geometry of a cylindrical waveguide with radius b	185
711	6.2 The geometry of a cylindrical cavity with length L and radius b	188
712	6.3 Relation of mode frequency to cavity length for a cylindrical cavity with 713 a radius of 18.32 cm.	189
714	6.4 A series RLC circuit.	190
715	6.5 Illustration of the behavior of the input impedance of the series RLC 716 circuit as a function of the driving frequency. The BW is proportion to 717 the width of the resonance, which is inversely proportional to Q.	192
718	6.6 A series RLC circuit coupled to an external circuit with input impedance 719 R_L	193

720	6.7 A cartoon depiction of a cavity CRES experiment. A metallic cavity filled 721 with tritium gas is inserted into a uniform background magnetic field 722 to perform CRES measurements. Electrons from beta-decays inside the 723 cavity can be trapped and used to excite a resonant mode(s). By coupling 724 to the cavity mode with a suitable probe one can measure the cyclotron 725 frequency of the electron and perform CRES.	194
726	6.8 Examples of the resonant mode frequencies of a cylindrical cavity. This 727 cavity has a radius of 18.32 cm and a length to diameter ratio of 4.55.	198
728	6.9 An image of an open cavity with coaxial terminations used for dielectric 729 constant measurements. Figure from [2].	202
730	6.10 The simplified geometry of an open cavity with coaxial terminations. 731 Figure from [3].	203
732	6.11 Electric field regions for the open cavity boundary value problem. Figure 733 from [3].	203
734	6.12 Two mode filtering concepts to break the degeneracy of TE_{01} and TM_{11} 735 modes. The resistive approach uses dielectric materials to impede currents 736 that travel vertically along the cavity while leaving azimuthal currents 737 unperturbed. An alternative approach is to impede the currents using 738 grooves cut into the cavity wall, which achieve the same effect with an 739 inductive impedance.	206
740	6.13 Four cavity design variations. (a) is a standard sealed cylindrical cavity, 741 (b) is an open cavity with smooth walls, (c) is an open cavity with resistive 742 walls, and (d) is an open cavity with grooved walls. The main cavity and 743 coaxial terminator parameter are identical for all four cavities.	207
744	6.14 The frequencies and Q-factors of the resonant modes identified by HFSS 745 for the cavity variations shown in Figure 6.13. The fully-sealed cavity with 746 smooth walls has several high-Q modes near the TE_{011} resonance. Intro- 747 ducing the open-termination preserves the Q-factors of the $TE_{01\ell}$ modes 748 and suppresses the Q-factors of the modes whose boundary conditions do 749 not match the cylindrical partition. Both the resistive and grooved wall 750 perturbations shift the resonant frequencies of the TM modes away from 751 the TE_{011} mode. By properly tuning the geometry of the grooves or the 752 resistive spacers several MHz of frequency separation can be achieved.	208

753	6.15 A cartoon depicting the design of the open-ended cavity prototype designed 754 to operate at approximately 6 GHz. The main cavity wall was composed of 755 a single copper pipe. A mode-filtered version of this cavity was constructed 756 by	210
757	6.16 Images depicting the measurement of the filtered and non-filtered open 758 cavities using the VNA. The coupling loop in the figure is shown in the 759 TE orientation.	211
760	6.17 HFSS simulation results for a the as-built cavity with the coaxial termi- 761 nators removed. The TE_{011}/TM_{111} frequency is approximately 5.78 GHz.	212
762	6.18 Measurements of the filtered and non-filtered prototype cavities acquired 763 with the VNA.	213

List of Tables

764	4.1	A summary of the CNN model layers and parameters. The output of each 1D-Convolution and Fully Connected layer is passed through a LeakyReLU activation function and re-normalized using batch normalization before being passed to the next layer in the model. The output of the final Fully Connected layer in the model is left without activation so that the model outputs can be directly passed to the Binary Cross-entropy loss function used during training.	120
765	6.1	A table of the values of p'_{nm}	187
766	6.2	A table of the values of p_{nm}	188
767	6.3	A table of cavity design parameters used for HFSS simulations.	207
768	6.4	A table of parameters describing the cavity prototypes. Certain values such as the cavity length and the distance between dielectric spacers are approximate due to variation in the machining of the copper. In particular, the filtered cavity was constructed from conducting copper segments that varied in size from 1.50" to 1.85".	210
770			
771			
772			
773			
774			
775			
776			
777			
778			
779			

780 **Chapter 1** |
781 **Introduction**

782 **1.1 Summary**

783 Neutrinos are one of the fundamental particles that comprise the standard model of
784 particle physics and account for a significant fraction of the matter in the universe.
785 Neutrinos are the most abundant fermions in the universe, but due to their weak
786 interactions neutrinos seldom interact with other particles. Regardless, neutrinos play a
787 unique role in the evolution of the early-universe, therefore, a detailed understanding of
788 the properties of the neutrino is key to understanding the universe at the cosmological
789 scale as well as the smallest particle physics regime.

790 It was uncertain that neutrinos had nonzero mass until vacuum neutrino flavor
791 oscillations were observed in the late 90's and early 00's. A simple relativistic argument
792 as to why oscillations are evidence for neutrino masses is that oscillations imply neutrinos
793 experience time, which means that they do not propagate at the speed of light, therefore
794 the masses of the neutrinos must be non-zero. Current neutrino oscillation data supports
795 that neutrino flavor states are actually a superposition of three separate neutrino states
796 with well-defined masses. Measurements of neutrino oscillations that have taken place
797 over the past couple of decades have measured the differences between neutrino mass
798 eigenstates with increasing precision. However, oscillation measurements cannot tell
799 us the mass scale of the neutrinos, which is required in order to measure the absolute
800 neutrino masses.

801 The neutrino mass scale remains an unknown quantity in the standard model of
802 particle physics. The value of the neutrino mass influences the evolution of the early
803 universe and is likely relevant to the energy-scale of new physics responsible for the factor
804 of 10^{-6} difference between the neutrino and electron masses. A model-independent way
805 to measure the neutrino mass is to measure the tritium beta-decay spectrum near its
806 endpoint. Energy conservation requires that the neutrino mass carry away some kinetic

807 energy from the beta-decay electron in the form of its mass, which causes a distortion in
808 the shape of the tritium beta-decay spectrum near the endpoint. The isotope tritium has
809 many advantages for this measurement, and has been used by the KATRIN collaboration
810 to perform the most sensitive direct neutrino mass measurement to date.

811 KATRIN represents the state-of-the-art in the current generation of neutrino mass
812 direct measurement experiments with a projected neutrino mass sensitivity of $m_\nu < 200$ meV.
813 This sensitivity does not fully exhaust the allowed parameter space of neutrino
814 masses under the normal and inverted neutrino mass ordering scenarios, which motivates
815 the development of a next generation of neutrino mass measurement experiments.

816 The Project 8 collaboration is developing a next-generation neutrino mass experiment
817 with a goal neutrino mass sensitivity of $m_\nu < 40$ meV. This sensitivity is sufficient to
818 exhaust the range of neutrino masses allowed under the inverted mass ordering regime.
819 Project 8 intends to achieve its sensitivity goal utilizing two technologies that are novel
820 to the space of direct neutrino mass measurements — atomic tritium and cyclotron
821 radiation emission spectroscopy (CRES). Atomic tritium is required in order to avoid
822 systematic broadening the tritium beta-decay spectrum caused by the final state of the
823 $^3\text{He}^+ \text{-T}$ molecule, and the CRES technique enables a differential measurement of the
824 tritium spectrum that is background-free and able to be directly integrated with the
825 atomic tritium source.

826 The Project 8 collaboration is currently engaged in a research and development
827 program intended to simultaneously develop the atomic tritium and CRES technologies
828 so that they can be combined in a next-generation experiment. This past year (2022)
829 Project 8 has used the CRES technique to measure the molecular tritium beta-decay
830 spectrum and place an upper limit on the neutrino mass: $m_\beta \leq 152$ eV. This measurement,
831 while not competitive scientifically, represents the first proof-of-principle that the CRES
832 technique can be used to measure the neutrino mass.

833 The future goals of the Project 8 collaboration are to develop the technologies
834 and techniques necessary to scale-up the volume in which CRES measurements can
835 be performed. Project 8's first neutrino mass measurement with CRES utilized a
836 measurement volume on the cubic-centimeter scale, however, sensitivity calculations
837 estimate that an experiment sensitive to neutrino masses of 40 meV will require several
838 tens of cubic-meters of experiment volume filled with atomic tritium. Developing a new
839 approach to performing CRES measurements that can be successfully scaled to these
840 volumes is a necessary step towards Project 8's neutrino mass measurement goal, and is
841 the primary topic of my dissertation research.

842 A parallel development is the technology necessary to produce, cool, trap, and
843 recirculate a supply of atomic tritium that is compatible with CRES measurements. The
844 atomic tritium system is equally important as the large-volume CRES measurement
845 technology, but will not be discussed at depth here.

846 The Project 8 collaboration has identified two scalable approaches to neutrino mass
847 measurement using the CRES technique. One approach is to use an array of antennas
848 that surrounds a volume of trapped atomic tritium that can perform CRES measurements
849 by collection the cyclotron radiation emitted by beta-decay electrons into free-space. The
850 other approach uses a resonant cavity filled with atomic tritium to perform CRES by
851 measuring the excitation of resonant cavity modes caused by the motion of electrons
852 trapped inside the cavity volume.

853 The cavity and antenna approaches to CRES have been studied in detail over the past
854 five years, and, while both approaches offer a physically viable path towards a 40 meV
855 neutrino mass measurement the collaboration has elected to pursue the cavity approach
856 for the foreseeable future. The major advantage of the cavity approach is a significant
857 reduction in the cost and complexity of the experiment design and data analysis, which
858 provides a lower risk path to Project 8’s scientific goals.

859 In this dissertation I summarize my most impactful contributions to the research and
860 development of antenna array and cavity CRES. In short these contributions are

- 861 • the development and analysis of signal reconstruction algorithms for antenna array
862 CRES, which provide key inputs to sensitivity analyses of antenna array CRES
863 experiments.
- 864 • The development of a specialized antenna, designed to synthesize fake CRES
865 radiation, which enables bench-top testing and validation of the antenna array
866 CRES technique.
- 867 • The development of an open-cavity design for CRES measurement, whose mode
868 structure can be tuned using perturbations that modify the impedance of the cavity
869 walls. The development of this cavity concept was one of many developments that
870 eventually lead to the adoption of cavities as the CRES technology of choice for
871 the future of Project 8.

872 1.2 Outline

873 The outline of this dissertation is as follows. In Chapter 2 I provide an introduction to
874 the basic physics of neutrinos and beta-decay, which provides context for a discussion of
875 various methods to measure the neutrino absolute mass scale.

876 Chapter 3 is an overview of the CRES technique and the Project 8 collaboration.
877 I highlight the Project 8 Phase II experiment, which was the first measurement of
878 the tritium beta-decay spectrum with CRES, and I discuss the planned research and
879 development for an antenna array CRES experiment in Phase III of the Project 8
880 collaboration’s experiment plan. I end Chapter 3 with a discussion of the pilot-scale and
881 Phase IV experiments, that will combine a scalable CRES measurement technology with
882 atomic tritium and measure the neutrino mass with 40 meV sensitivity.

883 Chapter 4 discusses the first of my contributions mentioned above, which is the
884 development of signal reconstruction techniques for antenna array CRES and an antenna
885 array demonstrator experiment called the FSCD. I discuss the key tools that Project 8
886 uses to simulate antenna array CRES before introducing signal reconstruction algorithms
887 that can be used to detect CRES signals using the array. I end Chapter 4 with a paper
888 that summarizes a detailed analysis and comparison of the signal detection performance
889 of each algorithm.

890 Chapter 5 describes my contributions to the development of antennas and an antenna
891 measurement system for Project 8, which is the second major contribution of this
892 dissertation. I begin with a general overview of basic principle of antennas and antenna
893 measurements, before including a paper that describes the development of unique antenna
894 designed to mimic the cyclotron radiation emitted by electrons in free-space when trapped
895 in a magnetic field. I call this antenna the synthetic cyclotron radiation antenna (SYNCA)
896 and its main purpose is to serve as a fake electron for laboratory validation measurements
897 of Project 8’s antenna array CRES simulations. Chapter 5 ends with an overview of
898 laboratory measurements of a prototype antenna array using the SYNCA, which were
899 compared with simulations to provide upper bounds on reconstruction errors caused by
900 imperfections in real-life measurements.

901 Chapter 6 discusses the cavity approach to CRES, which was adopted as the preferred
902 CRES technology for Phase IV late into my dissertation work. The chapter stars by
903 discussing resonant cavities in general before introducing the operating principles of the
904 cavity approach to CRES. I end the chapter by discussing a study of and open-cavity
905 design that could be used for CRES measurements and integrated with atomic tritium

906 and an electron gun calibration source for the pilot-scale and Phase IV experiments.

907 Finally, in Chapter 7 I conclude by briefly discussing the future directions of the
908 Project 8 collaboration as we continue towards a direct measurement of the neutrino
909 mass.

910 **Chapter 2 |**

911 **Neutrinos and Neutrino Masses**

912 **2.1 Introduction**

913 In this chapter I provide a cursory overview of background information relevant to
914 neutrinos and neutrino mass measurements.

915 In Section 2.2 I provide background information on the history of neutrinos and beta-
916 decay. In Section 2.3 I describe the discovery of neutrino oscillations, which demonstrated
917 unambiguously that neutrinos have non-zero masses. In Section 2.4 I discuss the current
918 state of the theoretical understanding of neutrino masses in the standard model. Lastly,
919 in Section 2.5 I discuss a few methods for measuring the absolute scale of the neutrino
920 mass.

921 **2.2 Neutrinos and Beta-decay**

922 Late in the 19th century the phenomena of radioactivity was first observed in experiments
923 performed by Henri Becquerel with uranium, and further studied using thorium and
924 radium by Marie and Pierre Curie [4, 5]. Early work in radioactivity classified different
925 forms of radiation based on it's ability to penetrate different materials. Rutherford was
926 the first to separate radioactive emissions into two types, alpha and beta radiation [6].
927 Alpha rays were easily stopped by a piece of paper or thin foil of metal, whereas beta
928 radiation could penetrate metal several millimeters thick. Later a third form of radiation
929 was identified by Villard [7], which was still more penetrating, later termed gamma
930 radiation by Rutherford.

931 When these forms of radioactivity were first discovered it was unclear what physically
932 constituted an alpha, beta, or gamma particle. Experiments with radioactivity in magnetic
933 fields were eventually able to identify the charge composition of the different forms of

radiation. In particular, experiments by Becquerel identified [8] that beta radiation had an identical charge-to-mass ratio to the electron. This was strongly suggestive that beta particles were indeed electrons.

Studies of beta radiation lead to the discovery that radioactivity resulted in the transmutation of elements [9] caused by the decay of a heavier nucleus to a lighter species. One feature of beta radiation, which we will refer to now as beta-decay, that differentiated it from alpha and gamma radiation is that the electrons produced by beta-decay have a continuous spectrum of kinetic energies, whereas, alpha and gamma particles are emitted with discrete energies. This feature of beta-decay was first observed by Chadwick in 1914 [10], and was extremely puzzling at the time, since the continuous spectrum apparently violates energy conservation [11].

Famously, in 1930 Pauli proposed the existence of a new neutral particle, which he termed the "neutron", that was also produced during beta-decay to resolve the missing energy problem posed by the beta-decay spectrum [12]. Because this particle carried no charge, it was hypothesized that it had simply not been observed in any previous experiments. This "neutron", which was initially estimated to have a mass no larger than that of an electron, was eventually renamed the "neutrino" by Fermi [13] after the discovery of the neutron by Chadwick in 1932 [14]. Later, in 1933, Fermi developed a quantum mechanical theory for beta-decay in which an electron and neutrino are produced by the decay of a neutron to a proton inside the radioactive nucleus [15].

Little more than a speculation when first introduced, indirect evidence for the existence of neutrinos was obtained in 1938 by the simultaneous observation of the electron and recoiling nucleus in cloud chambers by Crane and Halpern [16]. However, it wasn't until the Cowan-Reines experiment [17] in 1956 that direct evidence for the existence of neutrinos was observed through the observation of inverse beta-decays caused by neutrinos from a nuclear reactor interacting with protons contained in water molecules. The difficulty in detecting neutrinos is caused by their weak interactions with other particles. Later experiments revealed the existence of different types or flavors of neutrinos based on the nature of the leptons produced in neutrino charged-current interactions [18], but the existence of a neutrino mass remained an open question that would take more than 40 years to resolve.

965 2.3 Neutrino Oscillations

966 One of the first clues that neutrino flavor transitions or neutrino oscillations were occurring
 967 was the solar neutrino problem. The solar neutrino problem is a discrepancy between
 968 the measured and predicted flux of ν_e from the sum. The solar neutrino problem was
 969 famously observed by Ray Davis Jr. and collaborators in the 1960's [19] at the Homestake
 970 mine in South Dakota. In the early 2000's, the SNO experiment was able to resolve the
 971 solar neutrino problem by identifying neutrino oscillations as the cause of the observed
 972 deficit [20]. Furthermore, measurements of the atmospheric flux of neutrinos by the
 973 Super-Kamiokande experiment and others revealed that fewer muon-type neutrinos
 974 survived passage through the earth than expected providing strong evidence for neutrino
 975 oscillations for both flavors [21].

976 Neutrino oscillations occur because the weakly-interacting neutrino eigenstates are
 977 distinct from the mass eigenstates [22]. The neutrino mass eigenstates represent physical
 978 particles in that they are solutions to the free-particle Hamiltonian, whereas, the neutrino
 979 weak eigenstates correspond to the neutrino states that interact via the weak charged-
 980 current interaction. The neutrino weak eigenstates are a linear superposition of the
 981 neutrino mass eigenstates

$$982 \quad \nu_\ell = \sum_i U_{\ell i} \nu_i, \quad (2.1)$$

983 where $\ell = e, \mu, \tau$ and $i = 1, 2, 3$. The matrix elements $U_{\ell i}$ are the elements of the
 984 Pontecorvo-Maki-Nakagawa-Sakata (PMNS) matrix that describes the mixing between
 the neutrino flavor and mass states.

985 A standard parameterization [23] of the PMNS matrix is

$$986 \quad U_{PMNS} = \begin{bmatrix} U_{e1} & U_{e2} & U_{e3} \\ U_{\mu 1} & U_{\mu 2} & U_{\mu 3} \\ U_{\tau 1} & U_{\tau 2} & U_{\tau 3} \end{bmatrix} \\ 987 \quad = \begin{bmatrix} 1 & 0 & 0 \\ 0 & c_{23} & s_{23} \\ 0 & -s_{23} & c_{23} \end{bmatrix} \begin{bmatrix} c_{13} & 0 & s_{13}e^{-i\delta} \\ 0 & 1 & 0 \\ -s_{13}e^{i\delta} & 0 & c_{13} \end{bmatrix} \begin{bmatrix} c_{12} & s_{12} & 0 \\ -s_{12} & c_{12} & 0 \\ 0 & 0 & 1 \end{bmatrix} \quad (2.2) \\ 988 \quad \times \begin{bmatrix} e^{i\alpha_1/2} & 0 & 0 \\ 0 & e^{i\alpha_2/2} & 0 \\ 0 & 0 & 1 \end{bmatrix},$$

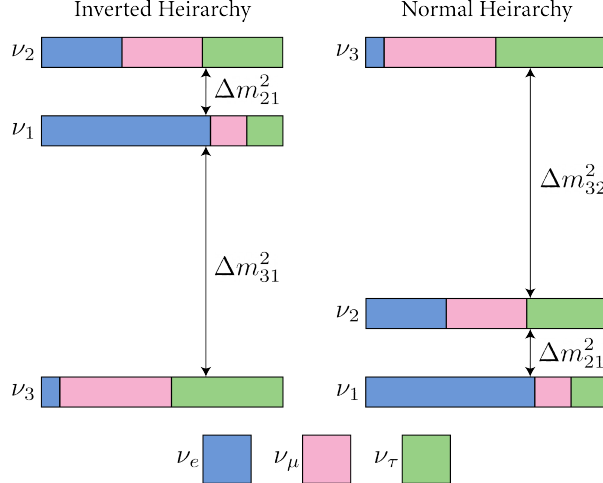


Figure 2.1. A diagram of two different neutrino mass ordering scenarios. In the inverted hierarchy (inverted mass ordering) the lightest neutrino mass is m_3 , whereas, in the normal hierarchy (normal mass ordering) m_1 is the lightest neutrino. What cannot be measured by neutrino oscillations is the neutrino absolute mass scale, which is essentially the mass of the lightest neutrino mass eigenstate.

where $c_{ij} = \cos \theta_{ij}$ and $s_{ij} = \sin \theta_{ij}$. The parameters α_1 and α_2 are only included in the PNMS matrix if neutrinos are Majorana particles, something which represents a current area of research in neutrino physics. The phase δ quantifies the degree of CP-violation in the neutrino sector. Including the Majorana phases the PMNS matrix contains six independent parameters. Neutrino oscillation probabilities also depend on the squared mass differences between neutrino mass eigenstates

$$\Delta m_{ij}^2 = m_i^2 - m_j^2, \quad (2.3)$$

where $ij = 12, 32, 31$ respectively. Because $\Delta m_{32}^2 = \Delta m_{31}^2 - \Delta m_{21}^2$, this adds an additional two parameters that must be constrained by neutrino oscillations.

A large experimental effort over the past couple decades has greatly contained the majority of parameters in the PMNS matrix, many to relative uncertainties of only a few percent. However, certain ambiguities remain, which is the origin of the current uncertainty in the ordering of the neutrino masses (see Figure 2.1). The neutrino masses can be arranged by their relative masses. Current neutrino oscillation data supports that $m_2 > m_1$, however, the sign of Δm_{32}^2 is still unknown. Therefore, two mass-ordering scenarios are allowed, one where neutrino masses are arranged $m_3 > m_2 > m_1$, which is called the normal mass ordering (NMO), or alternatively neutrino masses may be ordered $m_2 > m_1 > m_3$, which is called the inverted mass ordering (IMO). Next-

1003 generation neutrino oscillation experiments such as JUNO [24], Hyper-Kamiokande [25],
 1004 and DUNE [26] are poised to resolve this ambiguity in the coming years.

1005 Neutrino oscillation probabilities are sensitive to the neutrino masses via the squared
 1006 mass differences. Therefore, oscillation probabilities are unaffected by the absolute scale
 1007 of the neutrino mass. However, oscillations can be used to obtain a lower bound on the
 1008 neutrino masses by setting the mass of the lightest neutrino mass state to zero. This
 1009 results in different lower limits depending on the ordering of the neutrino mass states.
 1010 Current best-fit values [23] with 1σ -uncertainties for the squared mass differences are

$$\Delta m_{21}^2 = (7.42^{+0.21}_{-0.20}) \times 10^{-5} \text{ eV}^2, \quad (2.4)$$

$$\Delta m_{31}^2 = (2.5176^{+0.026}_{-0.028}) \times 10^{-3} \text{ eV}^2 \text{ (NMO)}, \quad (2.5)$$

1011 for the normal mass ordering, and for the inverted ordering the limit is

$$\Delta m_{32}^2 = (-2.498^{+0.028}_{-0.028}) \times 10^{-3} \text{ eV}^2 \text{ (IMO).} \quad (2.6)$$

1012 The parameter Δm_{21}^2 is the same in the NMO and the IMO. Allowing the lightest neutrino
 1013 mass in each ordering scenario (m_{least}) to take on a range of values one can visualize the
 1014 relative masses of the neutrinos as a function of m_{least} (see Figure 2.2). The absolute
 1015 neutrino mass scale is effectively the value of this m_{least} parameter.

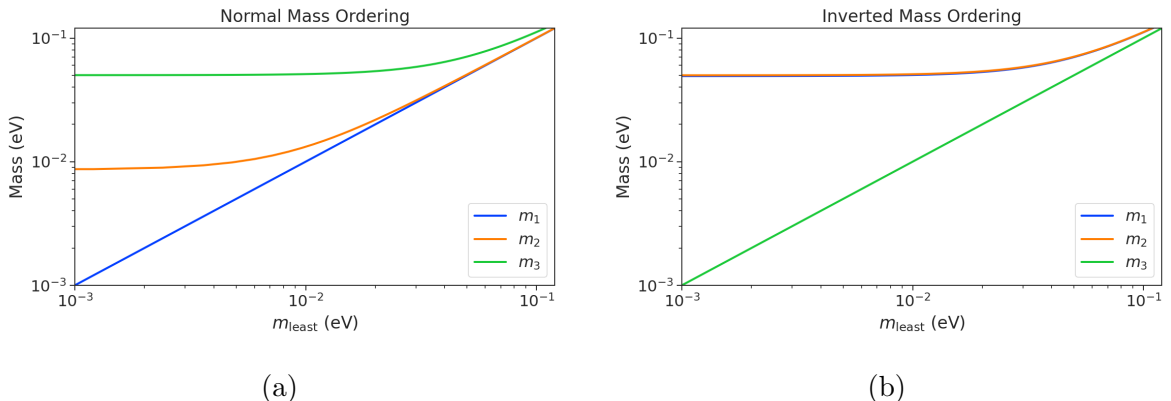


Figure 2.2. The masses of the neutrinos as a function of the lightest neutrino mass in both the normal (a) and inverted (b) mass ordering regimes.

2.4 Neutrino Masses in the Standard Model

In this section, I briefly summarize the current theoretical understanding of neutrino masses in the standard model [27–29]. Neutrinos are spin 1/2 particles, which are described using the Dirac equation.

$$(i\hbar\gamma^\mu\partial_\mu - mc)\psi(x) = 0, \quad (2.7)$$

where the field that describes the particle is denoted as $\psi(x)$. In the standard model fermions acquire mass through the Yukawa interaction, which add to the standard model Lagrangian terms of the form

$$\mathcal{L}_{\text{Yukawa}} = -Y_{ij}^\ell \bar{L}_{Li} \phi E_{Rj} + \text{h.c.}, \quad (2.8)$$

where Y_{ij}^ℓ is an element of the 3×3 Yukawa coupling matrix for leptons, L_{Li} is the left-handed lepton doublet for generation i , ϕ is the Higgs doublet, and E_{Rj} is the right-handed lepton field for generation j . Neutrinos are represented only as left-handed neutrinos and right-handed antineutrinos in the standard model, which is consistent with experimental observations. Since there are no right-handed neutrino singlet fields, there are no Yukawa interaction terms, thus neutrinos in the standard model are strictly massless. Therefore, non-zero neutrino mass is evidence for physics beyond the standard model.

For the charged leptons, the Yukawa interaction leads to masses of the form

$$m_{ij}^\ell = Y_{ij}^\ell \frac{v}{\sqrt{2}}, \quad (2.9)$$

where v is the Higgs vacuum expectation value. The observation of massive neutrinos motivates the extension of the standard model to explain the origin of neutrino masses, which can be approached in different ways, but all approaches add additional degrees of freedom to the standard model.

One approach is to introduce to the standard model a right-handed neutrino field that allows one to include Yukawa terms of the form

$$\mathcal{L}_{\nu \text{Yukawa}} = -Y_{ij}^\ell \bar{L}_{Li} \phi \nu_{Rj} + \text{h.c.} \quad (2.10)$$

where ν_{Rj} is the right-handed neutrino singlet. Because experimental evidence strongly

1039 predicts only three active neutrinos, these additional neutrinos are sterile and do not in-
1040 teract via the strong, weak, or electromagnetic interactions. After spontaneous symmetry
1041 breaking, the Yukawa interaction leads to mass terms given by

$$\mathcal{L}_D = -M_{Dij}\bar{\nu}_{Ri}\nu_{Lj} + \text{h.c.}, \quad (2.11)$$

1042 which is called a Dirac mass term. One of the issues with constructing neutrino masses
1043 in this way is that the required Yukawa couplings are at least a factor of 10^6 smaller than
1044 that of an electron, which begs the question: why are the Yukawa couplings so small for
1045 the neutrinos?

1046 An alternative approach is to allow the neutrinos to have a Majorana mass, which is
1047 possible because neutrinos are electrically neutral particles. The Majorana mass terms
1048 for neutrinos have the form

$$\mathcal{L}_M = -\frac{1}{2}(M_{Rij}\bar{\nu}_{Ri}\nu_{Rj}^c M_{Lij}\bar{\nu}_{Li}\nu_{Lj}^c) + \text{h.c.}, \quad (2.12)$$

1049 where M_{Rij} and M_{Lij} are right-handed and left-handed Majorana mass matrices. A
1050 consequence of neutrinos being Majorana particles is lepton number violation, which
1051 predicts the occurrence of neutrino-less double beta-decay at a rate proportional to the
1052 neutrino mass.

1053 In the most general case neutrinos have both Dirac and Majorana mass terms, which
1054 allows one to generate neutrino masses with Yukawa couplings similar to the rest of the
1055 standard model. Considering a single generation of neutrinos for demonstration, the
1056 combined neutrino mass Lagrangian can be written as

$$\mathcal{L}_{D+M} = -m_D\bar{\nu}_R\nu_L - \frac{1}{2}(m_L\bar{\nu}_L\nu_L^c + m_R\bar{\nu}_R\nu_R^c) + \text{h.c.}, \quad (2.13)$$

1057 or equivalently,

$$\mathcal{L}_{D+M} = -\frac{1}{2} \begin{bmatrix} \bar{\nu}_L & \bar{\nu}_R^c \end{bmatrix} \begin{bmatrix} m_L & m_D \\ m_D & m_R \end{bmatrix} \begin{bmatrix} \nu_L^c \\ \nu_R \end{bmatrix} + \text{h.c..} \quad (2.14)$$

1058 An example mass generation mechanism with this approach is the Type-I see-saw
1059 mechanism [30], in which we take $m_L = 0$ and $m_R \gg m_D$. By diagonalizing Equation
1060 2.14 one obtains the mass eigenvalues that represent the physical masses of the neutrinos.
1061 The light neutrino mass eigenstate, which represents the observed neutrino mass, has a
1062 mass given by

$$m_1 \approx \frac{m_D^2}{m_R}, \quad (2.15)$$

1063 and the heavy neutrino mass eigenstate, which represents the unobserved sterile neutrino,
1064 has a mass

$$m_2 \approx m_R. \quad (2.16)$$

1065 For m_D similar to the other quark or lepton masses, one obtains physical neutrino masses
1066 consistent with observations from sterile neutrino masses of $m_R \approx O(10^{15})$ GeV. This
1067 mass scale is well beyond the capabilities of modern particle accelerators to probe.

1068 2.5 Neutrino Absolute Mass Scale

1069 The neutrino absolute mass scale or simply "neutrino mass" cannot be probed with
1070 neutrino oscillations, since oscillation probabilities are determined by the squared mass
1071 differences between neutrino mass eigenstates, therefore, alternative techniques are needed
1072 to perform an effective measurement of the neutrino mass.

1073 2.5.1 Limits from Cosmology

1074 The Λ CDM model summarizes the current cosmological understanding of the universe [23].
1075 Λ CDM predicts that the universe originated from a single expansion event colloquially
1076 called the "Big Bang". During the Big Bang, the universe originated as a hot spacetime
1077 singularity, which abruptly experienced rapid expansion in a process known as inflation.
1078 After expansion the inflationary field eventually decayed into a population of quarks,
1079 gluons, leptons, and photons, which were kept in thermal equilibrium by the high-
1080 temperatures of the early universe.

1081 As the universe continued to expand it's density and temperature decreased until
1082 the formation of neutral atoms, primarily hydrogen, was possible. At which point the
1083 population of photons produced during the Big Bang decoupled from the primordial
1084 universe and began to freely propagate. A direct prediction of the Λ CDM model is that
1085 this population of photons is still present, but with a significantly reduced temperature
1086 due to the subsequent expansion of the universe. This is consistent with the observation of
1087 the CMB (cosmic microwave background), which is a population of microwave radiation
1088 with a blackbody temperature of 2.7 K. The CMB is extremely uniform in all directions
1089 with slight anisotropies that can be analyzed to study the evolution of the early universe.
1090 A series of experiments have measured the CMB with increasing levels of precision, which
1091 has lead to a significant increase in our current understanding of cosmology.

1092 In addition to the CMB, inflation predicts the existence of a $C\nu B$ (cosmic neutrino

background) [31], which are the remnant neutrinos produced during the Big Bang. Since neutrinos only interact via the weak force, they decouple from the Big Bang plasma at an earlier time than the CMB photons. The temperature at which the C ν B decouples depends on the neutrino rest mass. Neutrinos play a unique role in the Λ CDM model, due to the fact that neutrinos act as radiation early in the universe but as matter in the late universe. This leads to specific signatures that impact the expected anisotropies of the CMB as well as the distribution of matter in the universe [32]. By combining measurements of the CMB with measurements of the large-scale structure (LSS) of the universe one can constrain the neutrino mass scale by fitting these datasets with the Λ CDM model. This analysis results in some of the most stringent constraints on the neutrino mass. Recent analyses [23] have been able to constrain the neutrino mass scale to

$$\Sigma_{m_\nu} \equiv \sum_i m_i < 0.11 \text{ eV}, \quad (2.17)$$

where m_i are the neutrino mass eigenstates.

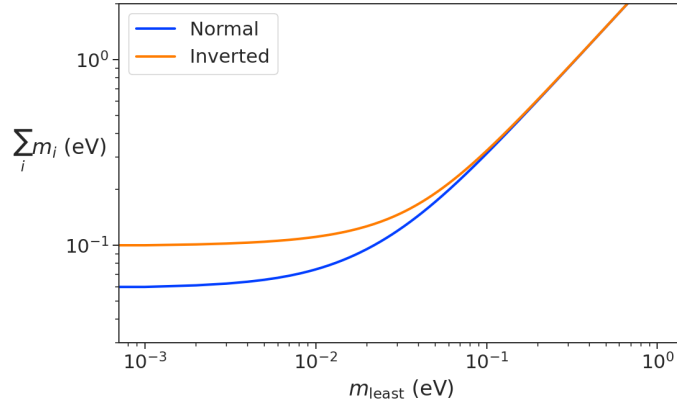


Figure 2.3. The neutrino mass observable measured by cosmology as a function of the lightest neutrino mass eigenstate.

The observable Σ_{m_ν} constrains the neutrino mass by setting the mass of the lightest neutrino mass eigenstate (m_{least}) (see Figure 2.3). In the normal mass ordering Σ_{m_ν} can be rewritten in the form

$$\Sigma_{m_\nu} = m_{\text{least}} + \sqrt{\Delta m_{21}^2 + m_{\text{least}}^2} + \sqrt{\Delta m_{32}^2 + m_{\text{least}}^2}, \quad (2.18)$$

where it is clear that a measurement of Σ_{m_ν} effectively sets the neutrino mass scale

1110 through m_{least} . The analogous formula for the inverted mass ordering is

$$\Sigma_{m_\nu} = m_{\text{least}} + \sqrt{-\Delta m_{32}^2 + m_{\text{least}}^2} + \sqrt{-\Delta m_{31}^2 + m_{\text{least}}^2}. \quad (2.19)$$

1111 Upcoming experiments [33] are planned to refine measurements of the CMB, LSS,
 1112 and other cosmological observables. With this additional data it is possible that in the
 1113 near future cosmological measurements will be able to positively constrain the neutrino
 1114 absolute mass scale. However, the strength of these limits strictly depend on the accuracy
 1115 of the Λ CDM model, which highlights the need for direct experimental measurements of
 1116 the neutrino mass to confirm the predictions of cosmology and to fix the neutrino mass
 1117 parameter in future cosmological analyses.

1118 2.5.2 Limits from Neutrinoless Double Beta-decay Searches

1119 If neutrinos are Majorana fermions, then the neutrino is equivalent to its own antiparticle
 1120 and lepton conservation is not an exact law of nature [34]. Limits on the rate of
 1121 neutrinoless double beta-decay ($0\nu\beta\beta$), are some of the most powerful current tests of
 1122 lepton number conservation [23]. If $0\nu\beta\beta$ were observed, it would direct evidence that
 1123 neutrinos are Majorana fermions and provide a method for measuring the neutrino mass
 1124 scale.

1125 Standard double beta-decay occurs when two neutrons in an unstable nucleus spon-
 1126 taneously decay into two protons, which results in the production of two electrons and
 1127 two neutrinos (see Figure 2.4). Whereas, during $0\nu\beta\beta$ the two neutrinos self-annihilate

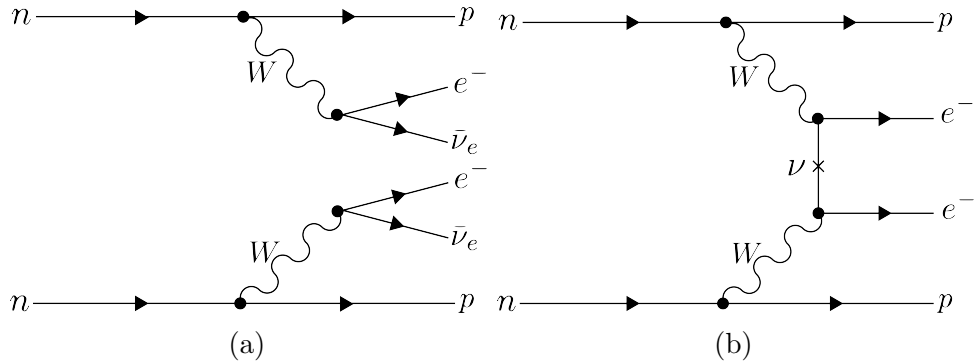


Figure 2.4. Feynman diagrams for double beta-decay (a) and $0\nu\beta\beta$ (b).

1127
 1128 producing only two electrons, which violates lepton number by two.

1129 Assuming that the exchange of two Majorana neutrinos is the dominant channel for
 1130 $0\nu\beta\beta$, then a measurement of the $0\nu\beta\beta$ half-life for a particular isotope can be used to

1131 set the neutrino absolute mass scale [35]. The half-life is written in terms of the effective
 1132 neutrino mass for $0\nu\beta\beta$ ($m_{\beta\beta}$) using the equation

$$T_{1/2}^{0\nu} = \frac{1}{G|\mathcal{M}|^2 m_{\beta\beta}^2}, \quad (2.20)$$

1133 where G is the phase-space factor for the decay and \mathcal{M} is the relevant nuclear matrix
 1134 element. $m_{\beta\beta}$ is given by an incoherent sum of the neutrino mass eigenstates weighted
 1135 by the PMNS mixing matrix parameters,

$$m_{\beta\beta} = \left| \sum_i U_{ei}^2 m_i \right|. \quad (2.21)$$

1136 The information provided from $0\nu\beta\beta$ on the neutrino mass scale can be visualized by
 1137 expressing the value of $m_{\beta\beta}$ in terms of m_{least} and two relative Majorana phases [1]. The
 1138 allowed regions for $m_{\beta\beta}$ as a function of m_{least} are shown in Figure 2.5 as the regions
 1139 bounded by the black curves overlayed with the discovery probabilities of future $0\nu\beta\beta$
 decay experiments based on current neutrino data.

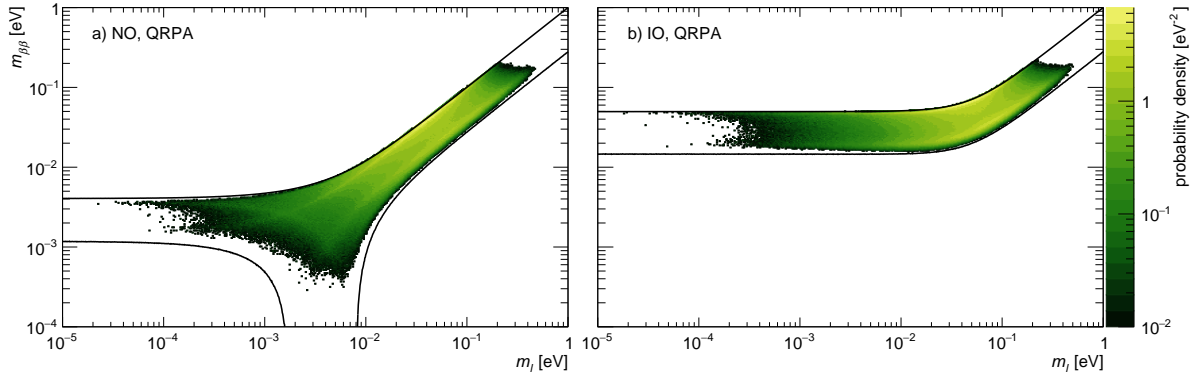


Figure 2.5. The discovery probabilities for the future generation of $0\nu\beta\beta$ experiments as a function of $m_{\beta\beta}$ and m_{least} . Figure from [1].

1140
 1141 Because of the possibility of cancellation due to the unknown Majorana phases included
 1142 in the sum specified by Equation 2.21, the neutrino mass information gained from $0\nu\beta\beta$
 1143 is necessarily imperfect. Additionally, theoretical uncertainties in the calculation of the
 1144 nuclear matrix elements complicates the calculation of $m_{\beta\beta}$ from a measurement of $0\nu\beta\beta$
 1145 half-life. Similar to cosmology, there is a high degree of complementarity between direct
 1146 measurements of the neutrino mass and $0\nu\beta\beta$. In particular, a measurement of m_{least} to
 1147 less than 0.1 eV sensitivity provides significant information for $0\nu\beta\beta$ searches based on
 1148 the discovery probabilities displayed in Figure 2.5.

2.5.3 Limits from Beta-decay

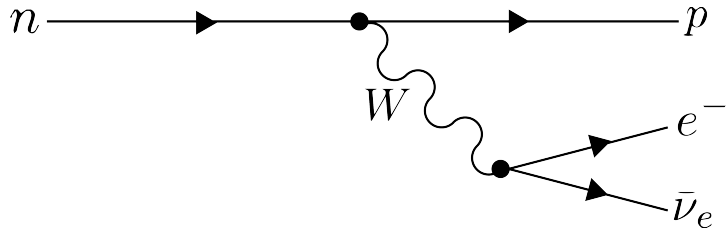


Figure 2.6. A Feynman diagram of beta decay

Certain processes involving neutrinos, in particular beta-decay (see Figure 2.6), have initial states with well-defined total energies and final states that can be measured with high accuracy and precision. Beta-decay involves the decay of an unstable isotope where a neutron spontaneously converts to a proton and emits an electron and anti-neutrino ("neutrino" for brevity) to conserve charge and lepton number [4]. Therefore, by applying the principles of energy and momentum conservation, a measurement of the kinematics of the final state can be used to constrain the neutrino mass [36].

Using beta-decay to measure the neutrino mass can be tied back to Fermi's original 1934 theory of nuclear beta-decay [15] (see Figure 2.7). Because the constraints on the

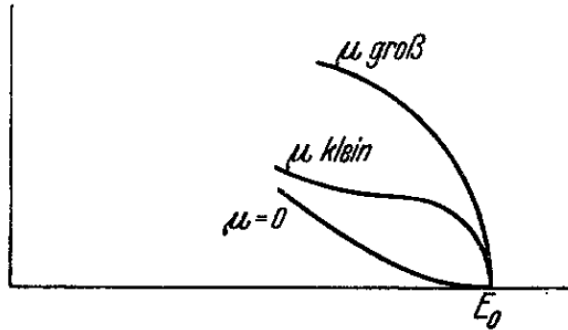


Figure 2.7. A figure from Fermi's 1934 paper on a theory of beta-decay depicting the kinetic energy spectrum of the emitted electron. The effect of the neutrino mass, written as μ , is to distort the shape of the spectrum near the endpoint from the zero-mass spectrum.

neutrino mass from beta-decay depend only on the final state measurement capabilities and the principles of energy and momentum conservation, neutrino mass measurements with beta-decay are called direct measurements. A direct measurement like beta-decay contrasts with other neutrino mass measurements approaches that are model-dependent such as cosmology and $0\nu\beta\beta$, which provide complementary ways to study the physics of massive neutrinos.

1165 The isotope of choice for direct neutrino mass measurements with beta-decay has
 1166 been tritium (3H_2) for many decades, because it conveniently fulfills many experimental
 1167 requirements. Of upmost importance is a decay with a low Q-value, which is the available
 1168 kinetic energy based on the mass difference between the initial and final states. The
 1169 effect of a massive neutrino on the shape of the spectrum is magnified for low Q-values
 1170 and tritium has an unusually low Q-value of 18.6 keV.

1171 Additionally, tritium beta-decay is super-allowed, which results in a relatively short
 1172 half-life of 12.3 years. Therefore, high source activity can be obtained with a relatively
 1173 small source mass. High-activity is desirable because of the low-activity near the tritium
 1174 spectrum endpoint. For tritium beta-decays, only a factor of 3×10^{-13} of the decays
 1175 occur in the last 1 eV of the spectrum. Isotopes with Q-values lower than tritium are
 1176 known [36], but this is outweighed by exceedingly long half-lives leading to unobtainable
 1177 source masses.

1178 The endpoint measurement approach involves quantifying the effect of the neutrino's
 1179 mass on shape of the electron's kinetic energy spectrum near the endpoint. The shape of
 1180 the kinetic energy spectrum (see Figure 2.8) is given by

$$\frac{d\Gamma}{dE} = \frac{G_F^2 |V_{ud}|^2}{2\pi^3} (G_V^2 + 3G_A^2) F(Z, \beta) \beta (E + m_e)^2 (E_0 - E) \\ \times \sum_{i=1,2,3} |U_{ei}|^2 [(E_0 - E)^2 - m_i^2]^{1/2} \Theta(E_0 - E - m_i), \quad (2.22)$$

1181 where G_F is the Fermi coupling constant, V_{ud} is an element of the CKM matrix, E
 1182 is the kinetic energy of the electron, β is the velocity of the electron divided by the
 1183 speed of light, E_0 is the endpoint energy assuming zero neutrino mass, $F(Z, \beta)$ is the
 1184 Fermi function, and $\Theta(E_0 - E - m_i)$ is the Heaviside function, which enforces energy
 1185 conservation. One can see that the decay spectrum is actually a combination of three
 1186 spectra with different endpoints based on the values of the neutrino mass eigenstates, m_i .
 1187 This produces "kinks" in the spectrum shape due to overlapping spectra with different
 1188 endpoint values, but such an effect would be nearly impossible to resolve given the finite
 1189 energy resolution of a real experiment.

1190 The neutrino mass scale variable measured by beta-decay is given by

$$m_\beta^2 = \sum_i |U_{ei}|^2 m_i^2, \quad (2.23)$$

1191 where m_β is the electron-weighted neutrino mass or simply "neutrino mass" for brevity.

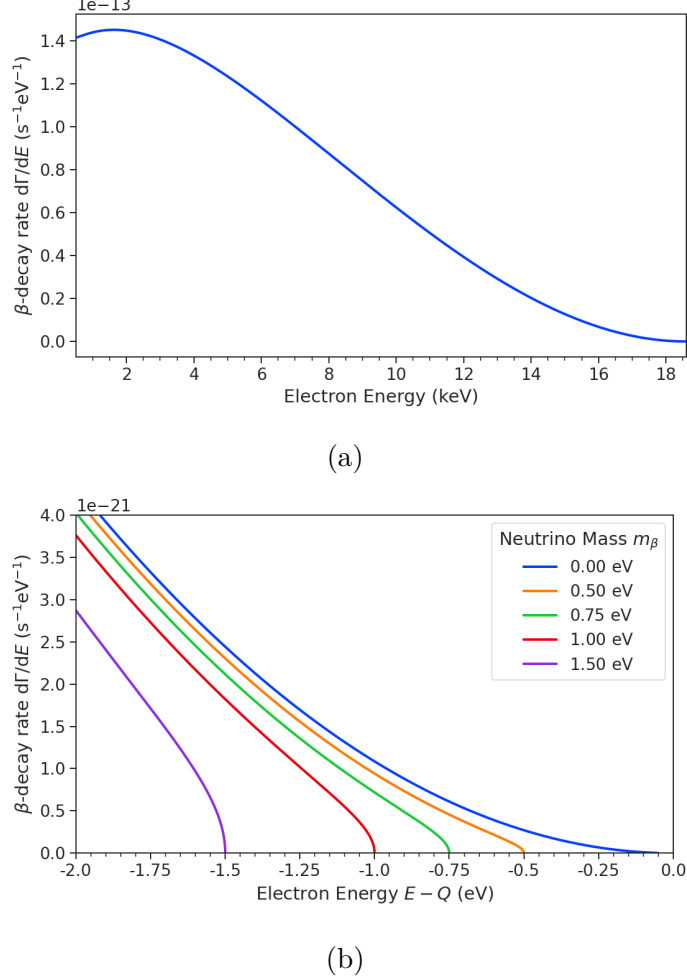


Figure 2.8. The tritium beta-decay spectrum. The effect of a massive neutrino on the spectrum is to change its shape near the endpoint by an amount proportional to the size of the neutrino mass. A sufficiently high-statistic and high-resolution measurement of the spectrum endpoint would be able to measure the neutrino mass.

1192 m_β corresponds to a particular weighted sum of the neutrino masses, which is distinct
 1193 from effective neutrino masses such as $m_{\beta\beta}$ [36]. Assuming unitarity, the neutrino mass
 1194 can be expressed in terms of the PMNS matrix elements, squared mass differences, and
 1195 the lightest neutrino mass eigenstate. For the normal mass ordering the equation is

$$m_\beta^2 = m_{\text{least}}^2 + |U_{e2}|^2 \Delta m_{21}^2 + |U_{e3}|^2 \Delta m_{31}^2, \quad (2.24)$$

1196 and for the inverted ordering the equation is

$$m_\beta^2 = m_{\text{least}}^2 + |U_{e1}|^2 (-\Delta m_{32}^2 - \Delta m_{21}^2) + |U_{e2}|^2 (-\Delta m_{32}^2). \quad (2.25)$$

1197 Therefore, a measurement of the neutrino mass in combination with neutrino mixing
1198 parameters is effectively a measurement of m_{least} .

1199 Since the neutrino mass is small (< 1 eV), it's effect on the spectrum is limited to
1200 the endpoint region. The affect of a non-zero neutrino mass on the endpoint spectrum is
1201 plotted for the reader in Figure 2.8. Resolving the small changes in the spectrum shape
1202 requires an experimental technique with high statistics, excellent energy resolution, and
1203 low background activity.

Chapter 3

Direct Measurement of the Neutrino Mass with Project 8

3.1 Introduction

A promising technique for direct measurements of the neutrino mass beyond the projected limit of the ongoing KATRIN experiment [37] is tritium beta-decay spectroscopy with an atomic tritium source [38]. Atomic tritium, combined with a large-volume, high-resolution energy measurement technique, is capable of measuring the neutrino mass with sensitivity below the 50 meV limit allowed by neutrino oscillations.

Cyclotron Radiation Emission Spectroscopy or CRES is a high-resolution energy measurement technique compatible with atomic tritium production and storage that can enable the next-generation of neutrino mass direct measurement experiments [39]. The Project 8 collaboration is currently engaged in a program of research and development (R&D) aimed at developing the technology necessary for a 40 meV sensitivity measurement of the neutrino mass using CRES and atomic tritium [40].

In Section 3.2 I provide an introduction to the basics of the CRES technique as well as the goals of the Project 8 experiment. Additionally, I sketch out the phased experiment development plan being implemented by Project 8 to build towards a next-generation neutrino mass experiment.

In Section 3.3 I give a brief overview of Phase II of the Project 8 experiment [41, 42], which completed early in 2023. Although the bulk of the work presented in this thesis is relevant to designs of future Project 8 experiments, a description of the work in Phase II provides useful context for the rest of the work.

In Section 3.4 I introduce a CRES measurement concept based on antenna arrays [43], which could be the basis for the ultimate Project 8 neutrino mass experiment. A significant portion of the R&D efforts of Project 8 in Phase III were directed towards

1230 simulating and modeling this experimental concept in order to understand the achievable
1231 sensitivity to the neutrino mass.

1232 Lastly, in Section 3.5 I introduce conceptual designs of pilot-scale experiments and
1233 Phase IV that combine atomic CRES with a large-volume CRES detection technique.
1234 This includes a design concept for an antenna array based experiment, but also a design
1235 for a resonant cavity based experiment. Resonant cavities are discussed in more depth in
1236 Chapter 6 and have become the default choice for the Phase IV experiment.

1237 **3.2 Cyclotron Radiation Emission Spectroscopy and Project** 1238 **8**

1239 **3.2.1 Cyclotron Radiation Emission Spectroscopy — CRES**

1240 Time and frequency are two of the most precisely measured quantities in physics. It is
1241 often advantageous to convert measurements of other physical quantities like mass or
1242 length into frequency measurements due to the digital nature of frequency measurements
1243 that make them immune to many sources of noise. Atomic clocks, which operate by
1244 measuring the frequencies of various atomic transitions, have been used to measure
1245 time with astounding relative uncertainties of 10^{-18} seconds [44]. The extreme precision
1246 possible with frequency measurements is often summarized using the a quote from the
1247 Physicist Arthur Schawlow who said advise his students to "Never measure anything but
1248 frequency!" [45].

1249 Neutrino mass measurements using tritium beta-decay require us to measure pertur-
1250 bations of the 18600 eV tritium endpoint to a precision as low as 0.1 eV, therefore, a
1251 spectroscopic technique with extremely high resolution is required for this measurement.
1252 The intuitive explanation for why frequency measurements are capable of such high reso-
1253 lutions is that they are essentially counting measurements, which average the number of
1254 oscillations of a physical system over time. By observing a rapidly oscillating system over
1255 a sufficient length of time one can obtain essentially arbitrary precision on a frequency
1256 limited only by the time available for measurement and the SNR of the system.

1257 What is required is that one translate the kinetic energy of the electron into a frequency,
1258 and a straightforward way to accomplish this is to place a gaseous supply of tritium into
1259 a magnetic field. When an atom decays the resulting electron will immediately begin
1260 to orbit around a magnetic field line at the cyclotron frequency, which is proportional
1261 to its kinetic energy (see Figure 3.1). The acceleration caused by the orbit leads to the

1262 emission of cyclotron radiation that can be detected using an array of antennas or a
 1263 different RF sensor such as a resonant cavity. The frequency of the radiation gives the
 1264 electron's kinetic energy, which is used to build the beta-decay spectrum and measure
 1265 the neutrino mass. The name for this measurement technique is Cyclotron Radiation
 1266 Emission Spectroscopy or CREs [39].

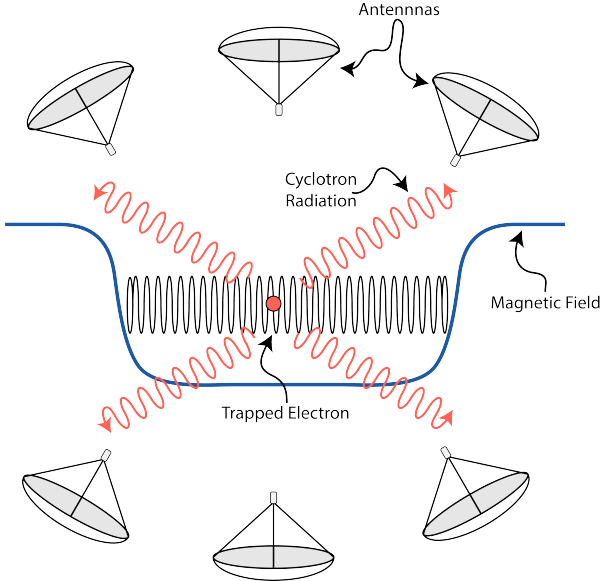


Figure 3.1. A cartoon illustration of the CREs technique. An electron is contained in a magnetic trap so that it's cyclotron radiation can be detected by an array of antennas. Detecting the cyclotron radiation allows us to measure its cyclotron frequency and determine its kinetic energy.

1267 For non-relativistic particles the cyclotron frequency is simply a function of the
 1268 charge-to-mass ratio of the particle, however, from the relativistic form of the cyclotron
 1269 frequency

$$f_c = \frac{qB}{2\pi m_e \gamma} = \frac{1}{2\pi} \frac{qB}{m_e + E_{\text{kin}}/c^2}, \quad (3.1)$$

1270 one can see that the kinetic energy (E_{kin}) of the electron is directly proportional to the
 1271 inverse of the cyclotron frequency (f_c). Electrons with kinetic energies of 18.6 keV are in
 1272 the weakly relativistic regime with $\beta = \frac{v}{c} = 0.263$ and $\gamma = 1.036$.

1273 The required frequency resolution needed for neutrino mass measurement can be
 1274 obtained by differentiating Equation 3.1,

$$\frac{df_c}{dE_{\text{kin}}} = \frac{1}{2\pi} \frac{-qBc^2}{(m_e c^2 + E_{\text{kin}})^2}, \quad (3.2)$$

1275 from which we can obtain the relationship between fractional differences in energy and

1276 frequency,

$$\frac{df_c}{f_c} = \frac{1 - \gamma}{\gamma} \frac{dE_{\text{kin}}}{E_{\text{kin}}}. \quad (3.3)$$

1277 Therefore, an energy precision of 1 eV for an 18.6 keV electron requires a frequency
1278 precision of approximately 2 ppm.

1279 The minimum observation time required to achieve this resolution can be estimated
1280 using the uncertainty principle as formulated by Gabor [46]. Electrons from tritium
1281 beta-decay experience random collisions with the background gas particles, which limits
1282 the uninterrupted radiation lifetime. The time between collision events, referred to
1283 as track length in the context of CRES measurements, is an exponentially distributed
1284 variable. Differences in the track lengths of a population of mono-energetic electrons leads
1285 to uncertainty or broadening in the distribution of measured frequencies proportional to
1286 the mean track length, τ_λ . The resulting frequency distribution has a Lorentzian profile,
1287 whose width is given by the Gabor limit,

$$\tau_\lambda \Delta f_c = \frac{1}{2\pi} \implies \Delta f_c = \frac{1}{2\pi\tau_\lambda}. \quad (3.4)$$

1288 The cyclotron frequency for a 18.6-keV electron in a 1 T field is approximately
1289 27 GHz, from which one can estimate the minimum observation time for 2 ppm frequency
1290 resolution at approximately 3 μ sec. The Gabor limit is not the true lower bound on the
1291 frequency resolution for a CRES signal, since it is based on the details of the Fourier
1292 representation of a time-series with a fixed length. If one takes the approach of fitting
1293 the CRES signal in the time-domain, then one finds that the limit on frequency precision
1294 is given by the Cramér-Rao lower bound (CRLB) [47], which depends on the track length
1295 and SNR. The CRLB allows for better precision on the cyclotron frequency, however,
1296 the Gabor limit provides an intuitive limit with the correct order of magnitude.

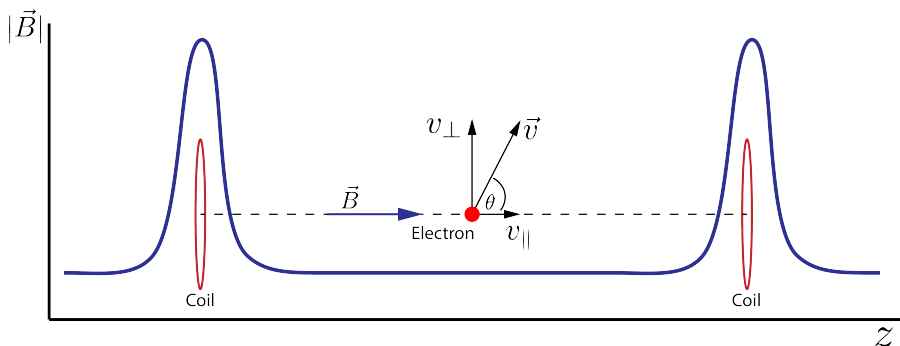


Figure 3.2. An illustration of an electron in a bathtub magnetic trap generated by two well-separated coils.

Ensuring that an electron remains under observation long enough so that it's frequency can be precisely measured requires a magnetic trap. A magnetic trap is a local minimum in a background magnetic field generated an appropriate configuration of electromagnetic coils. Since magnetic fields can do no work, there is no danger of the magnetic trap affecting the kinetic energy electron after it is emitted from the beta-decay. One common approach to creating a magnetic trap is the "bathtub" trap configuration, which in it's simplest form consists of two high magnetic field pinch coils aligned on a central axis that are well separated (see Figure 3.2). This configuration produces a trap with a flat uniform bottom and relatively steep walls, which is ideal for CRES measurements.

Electrons produced in the trap oscillate back and forth between the trap walls at a frequency that depends upon the pitch angle, unless they are produced with pitch angles too small to be contained in the trap. Pitch angle is defined as the angle between the component of the electron's velocity perpendicular to the magnetic field and the component parallel to the magnetic field,

$$\tan \theta = \frac{v_{\perp}}{v_{\parallel}}. \quad (3.5)$$

The axial motion of the electron leads to variation in the cyclotron frequency due to the changing value of the magnetic fields. This leads to frequency modulation that generate sidebands in the cyclotron radiation spectrum. Resolving these sideband frequency components is necessary for a complete reconstruction of the CRES signal in the experiment.

Electrons trapped in a cylindrically symmetric trap have three primary components of motion (see Figure 3.3). The dominant component, typically with the highest frequency, is the electron's cyclotron orbit, which encodes information on the electron's kinetic energy. Axial motion from the electron's pitch angle leads to frequency modulation but also a shift in the average magnetic field experienced by an electron. This leads to a correlation between the kinetic energy of the electron and the pitch angle depending on the particular shape of the magnetic trap, which can negatively impact energy resolution. To reduce this correlation one must engineer the trap to have a flat bottom with very steep wall both of which are more easily achieved with a small aspect ratio bathtub trap. Radial gradients in the trap leads to a third component of motion called grad-B drift [48]. The equation for the drift velocity is

$$\mathbf{v}_{\nabla B} = \frac{m_e v_{\perp}^2}{2qB} \frac{\mathbf{B} \times \nabla B}{B^2}. \quad (3.6)$$

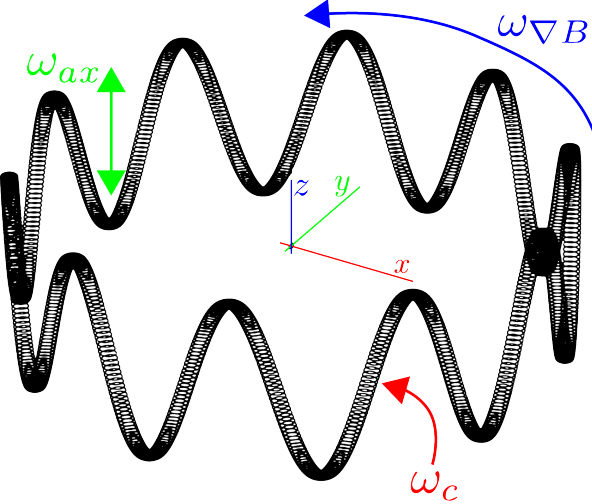


Figure 3.3. A plot of the main components of an electron's trajectory in a cylindrically symmetric trap.

1327 These additional components of motion all influence the shape of the CRES signal so
 1328 modeling their effects is critical to proper measurement of the kinetic energy.

1329 The total power of the radiation emitted by an electron in a free-space environment
 1330 is given by the Larmor equation [49]

$$P(\gamma, \theta_p) = \frac{1}{4\pi\epsilon_0} \frac{2}{3} \frac{q^2 \omega_c^2}{c} (\gamma^2 - 1) \sin^2 \theta_p, \quad (3.7)$$

1331 where ω_c is the cyclotron frequency multiplied by 2π and θ_p is the pitch angle to distinguish
 1332 it from the spherical angle coordinate. A single electron with a 90° pitch angle and
 1333 18.6 keV of kinetic energy in a 1 T magnetic field emits a total radiation power of 1.2 fW,
 1334 which is quite small compared with typical RF systems, furthermore, one is typically
 1335 only able to receive a fraction of this total power with an antenna or other detection
 1336 system. Therefore, RF systems in CRES experiments must be operated at cryogenic
 1337 temperatures to limit the noise power such that adequate SNR can be achieved for signal
 1338 detection and reconstruction. Alternatively, longer tracks enable detection of weaker
 1339 signals due to the increase in the total signal energy available for the detection algorithm.

1340 3.2.2 The Project 8 Collaboration

1341 The Project 8 collaboration¹ is a group of institutions in the United States and Germany
 1342 aiming to measure the neutrino mass by developing a novel spectrometer technology

¹<https://www.project8.org/>

1343 based on CRES. In the ultimate Project 8 experiment the CRES technique will be used
1344 to measure the beta-decay spectrum using a large source of atomic tritium sufficient to
1345 achieve the required statistics in the last $O(10)$ eV of the decay spectrum. Project 8 is
1346 targeting a neutrino mass sensitivity below 50 meV [50], which exhausts the range of
1347 possible neutrino masses under the inverted hierarchy and is a factor of four less than
1348 sensitivity projections for the ongoing KATRIN experiment.

1349 Project 8's proposed experiment requires the development of two novel technologies:
1350 the production and trapping of a source of atomic tritium on cubic-meter scales and
1351 technology to enable CRES measurements of individual electrons in the same volume.

1352 Atomic Tritium

1353 Previous measurements of the tritium beta-decay spectrum for neutrino mass measure-
1354 ments have relied on sources of molecular tritium for their measurements [37, 51, 52] due
1355 to the technical challenges associated with the production and storage of atomic tritium.

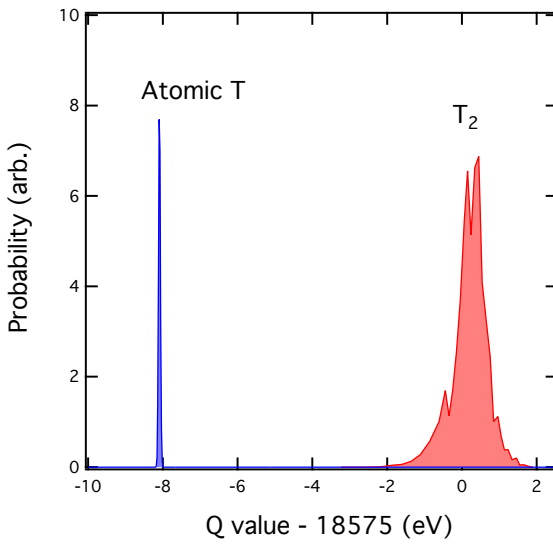


Figure 3.4. A plot of the final state distributions of atomic and molecular tritium. The final state distribution provides the primary contribution to the width of the molecular spectrum whereas thermal doppler broadening is responsible for the width of the atomic spectrum.

1356 One must supply sufficient energy to the tritium molecules to break the molecular
1357 bond and create atomic tritium. Common approaches to this include the use of hot
1358 coaxial filament atom crackers as well as plasma atom sources. Both involve heating the
1359 tritium atoms to temperatures of > 2500 K, which must then be cooled to temperatures
1360 on the order of a few mK so that the tritium atoms can be trapped. Cooling the atoms

1361 requires the construction of a large tritium infrastructure and cooling system that can
1362 supply a source of cold atoms to the trap.

1363 Once cold tritium atoms are produced they cannot make contact with any surfaces
1364 to avoid recombination of the atoms to molecules. Therefore, a magnetic trap is required
1365 to store the atoms for a sufficient length of time that they have a chance to decay before
1366 escaping the trap. Trapping the atoms requires the construction of a large and complex
1367 magnet system that must be cooled to cryogenic temperatures.

1368 The significant experimental complexity caused by atomic tritium makes a molecular
1369 source the obvious choice from practical considerations. However, the drawback of
1370 molecular tritium for neutrino mass measurement is the irreducible broadening in the
1371 electron's kinetic energy due to the final state spectrum of molecular tritium (see Figure
1372 3.4). The broadening of the final state spectra has a RMS amplitude of 436 meV [53, 54]
1373 caused by variation in the final vibrational state of the daughter molecule. For atomic
1374 tritium the primary sources of broadening in the final state spectrum are magnetic
1375 hyperfine splittings (magnitude of $O(10^{-5})$ eV) and thermal Doppler broadening caused
1376 by the motion of the trapped atom. For atomic tritium at a temperature of 1 mK thermal
1377 broadening is the dominant contribution, providing about 1 meV RMS of broadening to
1378 the electron's kinetic energy.

1379 The larger energy broadening with molecular tritium leads to an irreducible statistical
1380 uncertainty that limits the achievable sensitivity to approximately 100 meV at 90%
1381 confidence. For previous direct measurements of the neutrino mass this uncertainty is an
1382 insignificant contribution to the overall uncertainty budget, however, for experiments
1383 like Project 8 atomic tritium is a key component to the success of the experiment.

1384 **CRES for Neutrino Mass Measurement**

1385 Several features of the CRES technique make it an attractive choice for a next generation
1386 neutrino mass measurement experiment. For example, with a CRES experiment the
1387 volume of the source gas can be the same as the volume of the CRES spectrometer.
1388 This is due to the fact that CRES is a remote-sensing technique that can observe the
1389 energy of the electron without altering its trajectory or directly interacting with the
1390 electron. Given that tritium gas is transparent to cyclotron radiation the kinetic energies
1391 of electrons can be measured with an appropriate sensing technology, such as a cavity or
1392 antenna array, located directly outside the atom trapping volume.

1393 The current state-of-the-art tritium beta-decay spectroscopy experiment, KATRIN,
1394 utilizes the magnetic adiabatic collimation with an electrostatic filter (MAC-E filter)

1395 technique to measure the beta-decay spectrum of molecular tritium. In this approach,
1396 a source of molecular tritium is located outside the spectrometer. When a beta-decay
1397 occurs the electron must exit the tritium source and travel through the MAC-E filter
1398 before it can be detected on the other side of the filter using a charge sensor. The
1399 measurement statistics of the MAC-E filter are limited by the transverse areas of the
1400 tritium source and the filter due to the need to travel through the experiment without
1401 scattering. This scaling is less favorable than the volumetric scaling of CRES due to the
1402 ability to co-locate source and detector.

1403 Another promising aspect of the CRES technique is the inherently high precision
1404 of frequency based measurements. The endpoint of the molecular tritium beta-decay
1405 spectrum is approximately 18.6 keV, which dwarfs the neutrino mass scale of $< 1 \text{ eV}/c^2$
1406 by at least a factor of 10^5 . Measuring the effect of such a small mass on a high energy
1407 electron requires excellent energy resolution. Since frequency measurements are essentially
1408 counting measurements they are intrinsically quite accurate due to the ability to measure
1409 the cyclotron frequency by effectively averaging over millions of cyclotron orbits. Using
1410 off-the-shelf RF components its is possible to achieve part-per-million accuracy on the
1411 kinetic energy with the CRES technique.

1412 CRES is also nearly immune to typical sources of backgrounds that plague other
1413 experiments. Since CRES operates via non-destructive measurements of the electron's
1414 cyclotron frequency potential sources of background electrons are effectively filtered out
1415 by limiting the frequency bandwidth of the measurement. The fiducial volume of the
1416 experiment is free from any surfaces that could introduce stray electrons and electrons
1417 from sources outside the fiducial volume can be prevented from entering the experiment.

1418 Neutrino Mass Sensitivity Goals

1419 Project 8's ultimate goal is to combine CRES with atomic tritium to measure the neutrino
1420 mass with 40 meV sensitivity at the 90% confidence level (see Figure 3.5). This sensitivity
1421 is sufficient to fully exhaust the range of allowable neutrino masses under the inverted
1422 neutrino mass ordering regime and is approximately an order of magnitude less than the
1423 projected final sensitivity of the KATRIN experiment. Excluding the full neutrino mass
1424 parameter space would require a sensitivity an order of magnitude lower than what is
1425 proposed by Project 8, which would require an experiment whose size and complexity
1426 are currently well beyond proposals for the next-generation of neutrino mass direct
1427 measurement experiments.

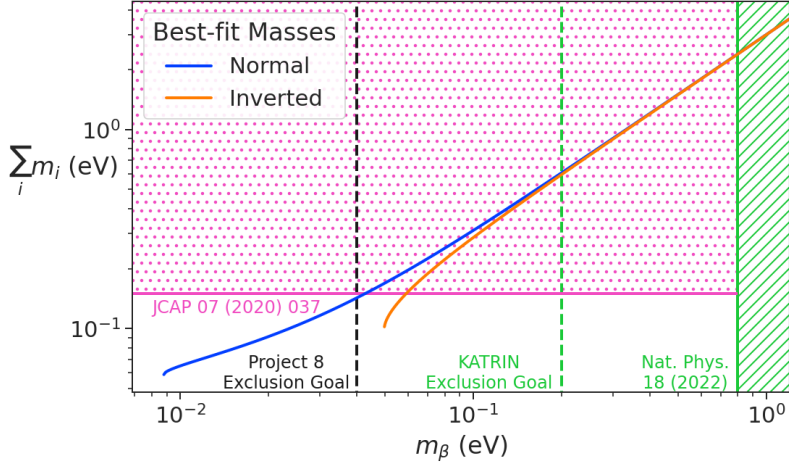


Figure 3.5. Neutrino mass exclusion plot including limits from cosmological measurements and the KATRIN experiment. Allowed ranges for neutrino masses under the normal and inverted hierarchies are shown as the blue and orange lines respectively. The black dashed line shows Project 8’s goal neutrino mass sensitivity for the Phase IV experiment.

1428 **3.2.3 The Project 8 Phased Development Plan**

1429 Reaching 40 meV sensitivity requires the simultaneous development and eventually
 1430 combination of CRES and atomic tritium. These technologies require a significant up-
 1431 front research and development (R&D) investment to build-out the required capabilities
 1432 for a 40 meV CRES experiment. Therefore, Project 8 is following a phased experiment
 1433 plan in which incremental progress can be made towards the ultimate goal of a 40 meV
 1434 neutrino mass measurement with CRES.

1435 **Phase I and II: Proof of Principle and First Tritium Measurements**

1436 The earlier phases of the Project 8 experiment, Phase I and II, were focused on demon-
 1437 stration and development of the CRES technique itself as well as a proof-of-principle
 1438 measurement of the neutrino mass using the CRES technique.

1439 In Phase I, Project 8 performed a proof-of-principle measurement of the ^{83m}Kr
 1440 spectrum using CRES, which marked the first ever energy spectrum measurement with
 1441 CRES. The experiment included all of the main components expected for the full-scale
 1442 version of the experiment. An electron source consisting of a gas of ^{83m}Kr was supplied
 1443 to a waveguide gas cell constructed out of a segment of WR-42 waveguide and sealed
 1444 with Kapton windows at the top and bottom. A magnetic trapping region was created
 1445 in the waveguide cell using a single electromagnetic coil wrapped around the waveguide

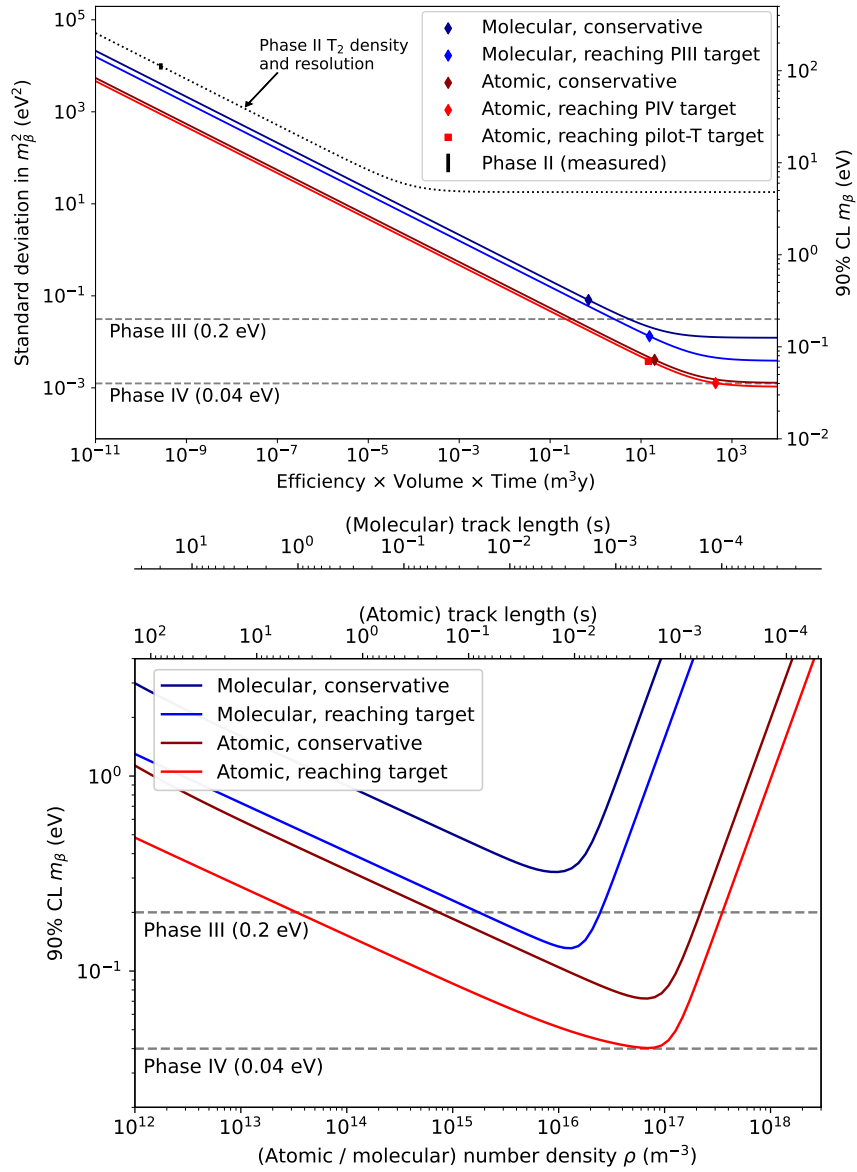


Figure 3.6. Sensitivity calculations for a cavity based CRES experiment that demonstrate the neutrino mass measurement goals of the Project 8 collaboration throughout the phased development plan. The blue curves indicate molecular tritium sources and the red curves indicate atomic tritium sources. In the current plan Phase III contains two tritium experiments. The first is the Low-frequency Apparatus (LFA) which is a molecular tritium experiment and the second is the atomic tritium pilot-scale experiment that ends Phase III. The sensitivity of these experiments is primarily a function of statistics, however, there is a critical density beyond which CRES electrons do not have enough time to radiate between collisions for a high-resolution frequency measurement leading to worse sensitivity.

1446 which provided a trapping volume on the order of a few cubic-millimeters. Detection of
1447 the cyclotron radiation was performed by connecting the waveguide cell to an additional
1448 segment of waveguide that transmitted the radiation to a cryogenic amplifier.

1449 Success in Phase I was achieved with the 2014 publication of the measured ^{83m}Kr
1450 conversion spectrum [55], which contains a mono-energetic 17.8-keV as well as several
1451 other conversion lines at higher energies. Publication of this result marked the official
1452 end of Phase I and the start of Phase II in which Project 8 shifted its focus to the
1453 demonstration of the first tritium beta-decay spectrum using CRES. Phase II successfully
1454 concluded in 2023 with the submission of the papers demonstrating the first tritium
1455 beta-decay spectrum endpoint and neutrino mass measurement using CRES. For more
1456 information on Phase II please see Section 3.3.

1457 **Phase III: Research and Development and a Pilot-scale Experiment**

1458 After Phase II Project 8 has shifted focus to R&D towards the construction of an
1459 experiment that demonstrates all the technologies required for a 40 meV measurement of
1460 the neutrino mass. The goal for this pilot-scale experiment is to successfully retire all
1461 technological and engineering risks associated with the Phase IV experiment, while being
1462 a scientifically interesting experiment in its own right that has sensitivity to neutrino
1463 masses on par with KATRIN’s final projected sensitivity.

1464 Phase III R&D is divided into two equally important efforts — atomic tritium
1465 and CRES detection techniques. Atomic tritium development in Phase III includes
1466 the development of all aspects of the tritium system. This includes the production of
1467 tritium atoms, atomic cooling and recirculation systems, purity and isotope concentration
1468 monitoring, and atom trapping. Currently, Project 8 is operating small scale demonstrator
1469 systems developing atom crackers to show that atom production at the estimated rates
1470 needed for Phase IV is achievable. Future efforts will continue the current developments
1471 on atom production and expand to include demonstrations of atomic cooling with an
1472 evaporative beam line as well as atom trapping using Halbach magnet arrays.

1473 The need for new CRES detection techniques is driven by the drastic increase in scale
1474 from Phase II to the Phase IV and the pilot-scale experiments. The physical volume
1475 used for CRES in Phase II was on the order of a few cubic-centimeters, and achieving
1476 Project 8’s sensitivity target of 40 meV requires an experiment volume on the multi-cubic
1477 meter scale. Therefore, the waveguide gas cell CRES detection technique used in Phase
1478 II is not a feasible option for the future of Project 8 due to it’s inability to scale to the
1479 required size.

1480 Two alternative CRES detection techniques have been proposed for the pilot-scale
1481 experiment — antenna arrays and resonant cavities (see Section 3.4 and Chapter 6).
1482 Both approaches have relative advantages and disadvantages, however, the improved
1483 understanding of the antenna array and cavity approaches to CRES in the recent years
1484 has led to cavities being the preferred technology for the pilot-scale experiment and
1485 Phase IV due to the estimated reduced cost and complexity of this approach. Since a
1486 large degree of the work presented in this thesis is focused on the development of the
1487 antenna array CRES technique as well as the design of demonstrator experiments, we
1488 described the proposed R&D plan for antenna array CRES in Phase III in Section 3.4.

1489 Cavity CRES R&D in Phase III consists of a series of demonstrator experiments
1490 intended to demonstrate cavity CRES at a variety of scales and magnetic fields using
1491 electrons from ^{83m}Kr , an electron gun, and potentially molecular tritium sources. The
1492 near-term cavity effort in Project 8 is the cavity CRES apparatus (CCA), which is a
1493 small-scale cavity experiment operating near 26 GHz, that will perform the first CRES
1494 measurements using a small cavity. This experiment will pave the way towards larger
1495 scale cavity experiments in preparation for the eventual pilot-scale tritium experiment.

1496 The pilot-scale experiment is the first experiment, which will combine atomic tritium
1497 and large-volume CRES detection in the same experiment. It will directly demonstrate
1498 all the technologies required for Phase IV such that no technical risks remain for scaling
1499 the experiment to required scale. A robust approach to scaling the pilot-scale experiment
1500 is to simply build multiple copies of it for the Phase IV experiment.

1501 **Phase IV: Project 8’s Ultimate Neutrino Mass Experiment**

1502 The design of Phase IV should be a direct extension of the pilot-scale CRES experiment
1503 that marks the official end of Phase III (see Section 3.5). The Phase IV experiment
1504 represents the final experiment in the Project 8 neutrino mass measurement experiment
1505 plan and will have sensitivity to neutrino masses of 40 meV.

1506 **3.3 Phase II: First Tritium Beta Decay Spectrum and** 1507 **Neutrino Mass Measurement with CRES**

1508 In Phase II Project 8 demonstrated the first ever measurement of the tritium beta-decay
1509 spectrum endpoint using the CRES technique, which lead to the first neutrino mass
1510 measurement by the Project 8 collaboration. This milestone was made possible by many

improvements in the CRES technique and in the understanding of CRES systematics, which takes an important first step towards larger scale measurements of the tritium beta-decay spectrum with CRES. In this section, I briefly describe some important elements of the Phase II experiment, with the goal of contextualizing the research and development efforts for Phases III and IV of Project 8. For more complete descriptions of the work that lead to Project 8’s Phase II results please refer to the relevant publications by the collaboration [41, 42].

3.3.1 The Phase II CRES Apparatus

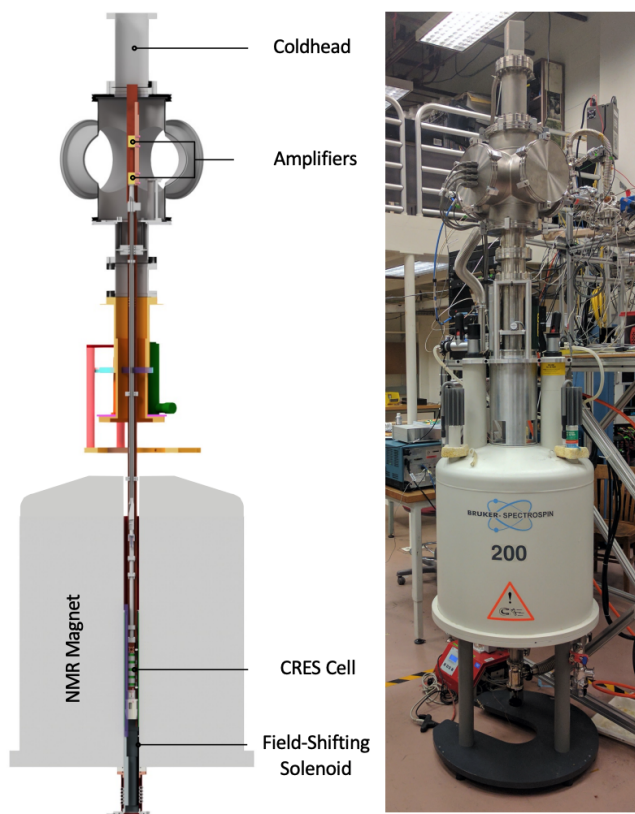


Figure 3.7. The Phase II CRES apparatus used to perform the first measurement of the tritium beta-decay spectrum using CRES.

1519 Magnet and Cryogenics

1520 The magnetic field for the the Phase II experiment is provided by a nuclear magnetic
1521 resonance (NMR) spectroscopy magnet with a central bore diameter of 52 mm (see Figure

1522 3.7). The magnet produces a background magnetic field with an average value of 0.959 T
1523 and a 10 ppm variation across the bore diameter achieved using several shim coils built
1524 into the magnet. Using an external NMR field probe the variation of the magnetic field
1525 along the vertical axis of the magnet bore was measured to obtain an accurate model of
1526 the magnetic field so that the CRES cell could be positioned for optimal magnetic field
1527 uniformity.

1528 An external solenoid magnet was installed inside the magnet bore to provide the
1529 ability to shift the magnitude of the background magnetic field by values on the order of
1530 a few mT. The solenoid has inside diameter of 46 mm and a length of 350 mm, which
1531 terminates in a vacuum flange that allows it to be inserted into the NMR magnet bore
1532 from the bottom. By shifting the value of the magnetic field by a few mT, the cyclotron
1533 frequencies of electrons produced by the 17.8 keV ^{83m}Kr internal-conversion line [56]
1534 can be shifted over a range of frequencies on the order of 100 MHz. This allows one to
1535 study the frequency dependent behavior of multiple CRES systematics such as detection
1536 efficiency that directly affect the measured shape of the tritium spectrum.

1537 The inside of the magnet bore diameter was pumped down to a vacuum of less than
1538 10 μtorr using a turbomolecular pump, which allows for cryogenic cooling of the CRES
1539 cell and RF system. Cooling power was supplied to the Phase II apparatus using a
1540 cryopump with its coldhead mounted above the primary magnet and CRES cell. This
1541 arrangement allowed for sufficient cooling power to be delivered to the amplifiers to cool
1542 them to a temperature of \approx 40 K, while keeping the amplifiers far enough from the
1543 magnet so as not to be damaged by the large field strength. Thermal contact between
1544 the coldhead, amplifiers, RF system, and CRES cell is achieved using a copper bar that
1545 runs the full length of the apparatus. To prevent freeze-out of ^{83m}Kr on the walls of the
1546 CRES cell a separate heater was installed to keep the CRES cell near a temperature of
1547 85 K during the operation of the experiment.

1548 **CRES Cell**

1549 Located in the most uniform region of the magnetic field is the CRES cell, which is the
1550 region of the apparatus where radioactive decays of ^{83m}Kr and T_2 emit electrons that can
1551 be trapped and measured using CRES (see Figure 3.8). The CRES cell is manufactured
1552 from a segment of cylindrical waveguide designed to operate at K-band frequencies
1553 near 26 GHz. The diameter of the waveguide determines which resonant modes of the
1554 waveguide will couple to the electron and transmit its radiation to the amplifiers. For
1555 Phase II a waveguide diameter of 1 cm was selected, which allows electrons to couple to

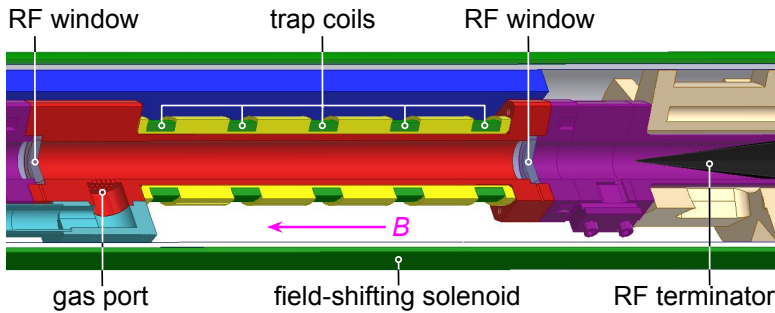


Figure 3.8. Diagram of the CRES cell portion of the Phase II apparatus.

1556 the TE₁₁ and TM₀₁ cylindrical waveguide modes. To reduce complexity in modeling and
 1557 analyzing the CRES data, it is ideal to select a diameter that prevents electrons from
 1558 coupling to higher-order waveguide modes beyond the fundamental TE and TM modes.

1559 Around the exterior of the cylindrical waveguide are several magnetic coils used to
 1560 produce magnetic traps inside the CRES cell volume. Without a magnetic trap electrons
 1561 produced from decays inside the CRES cell quickly impact the cell wall, which prevents
 1562 a measurement of their cyclotron frequency using CRES. Each coil along the length of
 1563 the waveguide produces a separate trap that is approximately harmonic in shape. By
 1564 independently controlling the currents provided to each coil the traps can be configured
 1565 to have equal values of the magnetic field at the trap bottom despite a non-uniform field
 1566 from the NMR magnet.

1567 Two primary magnetic trap configurations were used during the Phase II experiment.
 1568 The first was a shallow trap configuration used primarily for its high energy resolution to
 1569 study systematics using ^{83m}Kr decays, and the second was a deeper trap that could trap a
 1570 higher percentage of pitch angles. The trade-off with this trap is that the higher trapping
 1571 efficiency comes at the cost of lower energy resolution due to the greater variation in pitch
 1572 angle. The deep trap was the trap used to measure the tritium beta-decay spectrum in
 1573 Phase II.

1574 The source gases were delivered into the CRES cell through a gas port located near the
 1575 top end of the cylindrical waveguide. To prevent the gases from escaping the cell, vacuum
 1576 tight RF transparent windows are needed to contain the tritium and krypton source
 1577 gas across a 1 atm pressure differential, while still transmitting the cyclotron radiation
 1578 without distortion. The crystalline material, CaF₂, which has a thermal expansion
 1579 coefficient similar to that of copper, was used for this purpose in the CRES cell. Two
 1580 windows, each 2.4 mm thick, were used to seal off the ends of the CRES cell. The
 1581 thickness of 2.4 mm corresponds to half of a cyclotron wavelength when one accounts for

1582 the permittivity of CaF_2 .

1583 **RF System**

1584 The RF system in the Phase II apparatus transferred the cyclotron radiation from the
1585 CRES cell to the receiver chain. The receiver chain performs the down-conversion and
1586 digitization required to obtain signals that can be analyzed to determine the cyclotron
frequencies of electrons in the CRES cell (see Figure 3.9).

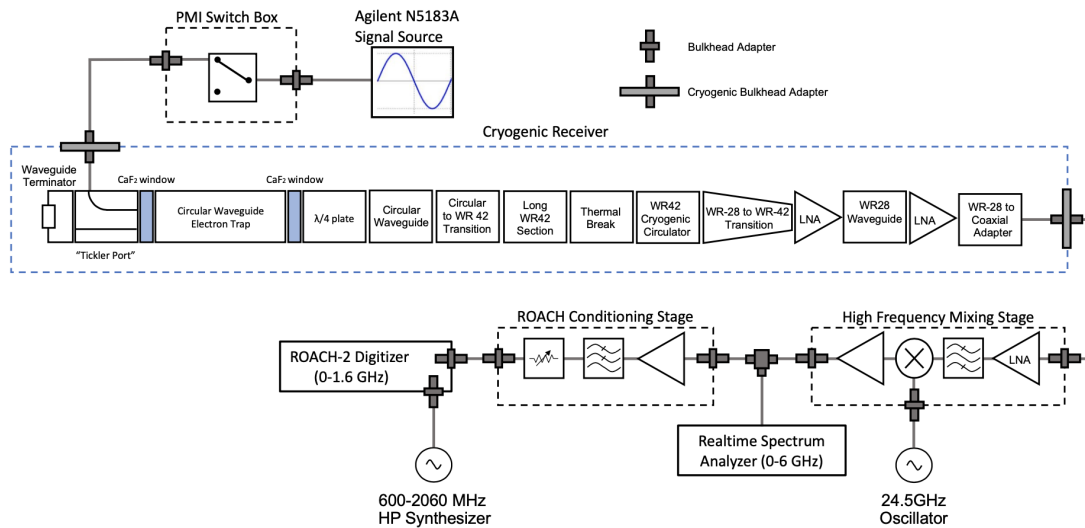


Figure 3.9. RF system diagram for the Phase II apparatus.

1587
1588 Below the CRES cell, at the bottom of the Phase II apparatus, is a tickler port and
1589 waveguide terminator. The tickler port is used to inject signals into the CRES cell and
1590 RF system for testing and calibration purposes. The waveguide terminator is designed to
1591 absorb cyclotron radiation emitted by electrons that transmits out of the bottom of the
1592 CRES cell. This lowers the total power received from electrons in the CRES cell, since all
1593 the energy radiated downwards is absorbed into the terminator. Earlier iterations of the
1594 Phase II apparatus used an RF short in this location that reflected this power up towards
1595 the amplifiers, however, interference between the upward traveling and reflected radiation
1596 led to a disappearance in the signal carrier that made reconstruction impossible.

1597 Radiation traveling upward passes through the CaF_2 window passes through a $\lambda/4$
1598 plate, which transforms the circularly polarized cyclotron radiation into linear polarization.
1599 The linearly polarized fields next travel through a segment of circular waveguide that
1600 transitions into a long segment of WR-42 waveguide that carries the fields out of the
1601 high magnetic field region. A thermal break segment is included, which consists of a a

1602 segment of gold-plated stainless steel WR-42 waveguide, to help thermally isolate the
1603 relatively warm CRES cell from the colder amplifiers. The radiation then passes through
1604 a cryogenic circular, which prevents signals reflected from the amplifiers from interfering
1605 with the CRES cell before a WR-42 to WR-28 transition connects the waveguide to the
1606 first of the cryogenic amplifiers. The radiation passes through two cryogenic amplifiers
1607 before being coupled to a coaxial termination at the top of the Phase II apparatus.

1608 The coaxial cable transfers the cyclotron radiation signals to a high-frequency mixing
1609 stage that performs an analog frequency down-conversion using a 24.5 GHz LO. Two forms
1610 of digitization can be used at this stage to readout the CRES data. One is a real-time
1611 spectrum analyzer that digitizes the CRES signal data in time-domain and computes the
1612 frequency spectrum in real-time, which allows for direct visualization of CRES signal
1613 spectrograms as the experiment is running. The real-time spectrum analyzer is most
1614 useful for taking small amount of streamed data for debugging and analysis of the system.
1615 The other method, which was used to collect the majority of the CRES data in Phase II,
1616 is a ROACH-2 FPGA and digitizer system. The ROACH system consists of a fast ADC
1617 that samples the CRES signal data at 3.2 GSps. Internal digital down-conversion stages
1618 implemented in the FPGA perform a mixing operation that reduces the bandwidth of the
1619 CRES signals to 100 MHz. The FPGA implements a 8192 sample FFT and packetizes
1620 time and frequency domain records in parallel. The packetized data is then transferred
1621 from the ROACH to be analyzed by the data-processing pipeline.

1622 **CRES Track and Event Reconstruction**

1623 **Time-Frequency Spectrogram**

1624 The online data-processing is intended to identify interesting data that could contain
1625 CRES signals using a software real-time triggering algorithm. Interesting segments of
1626 data identified by this algorithm are collected into files that are transferred to a server for
1627 offline processing and analysis. The data files contain a continuous series of time-domain
1628 samples, broken into a set of records, which are 4096 samples long. The time-series is
1629 made up of 8-bit IQ samples acquired at 100 MHz.

1630 Each time-series record is accompanied by an associated frequency spectrum consisting
1631 of 4096 frequency bins approximately 24.4 kHz wide, which is represented as a power
1632 spectral density. The individual frequency spectra can be organized temporally to create
1633 a time-frequency spectrogram that represents the evolution of the cyclotron frequency
1634 spectrum over the course of the CRES event (see Figure 3.10). The time-frequency

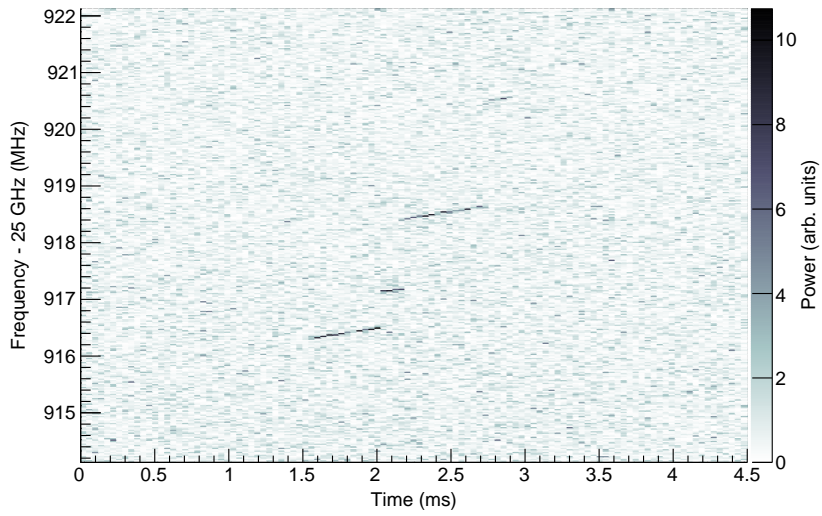


Figure 3.10. The time-frequency spectrogram of a tritium CRES event in the Phase II apparatus.

1635 spectrogram is represented as a two-dimensional image where the color of each pixel is
 1636 proportional to the power spectral density. Each vertical slice of pixels in the image
 1637 represents a frequency spectrum, therefore, each horizontal bin represents the data
 1638 obtained over a duration of $4096 \times 0.01 \text{ MHz}^{-1} = 40.96 \mu\text{sec}$.

1639 CRE Event Data Features

1640 Phenomenologically, a CRES signal appears as a sinusoidal signal whose frequency slow
 1641 increases ("chirps") over time. Axial motion of the electron in the trap leads to the
 1642 formation of frequency sidebands that surround the more powerful carrier frequency, due
 1643 to Doppler modulation of the electron's frequency as it bounces between the walls of the
 1644 magnetic trap. The critical piece of information that must be extracted from the track
 1645 and event reconstruction procedure is the carrier frequency, since it is this frequency
 1646 that gives the cyclotron frequency and thus the kinetic energy. While axial motion from
 1647 non- 90° pitch angles does change the average magnetic field experienced by an electron
 1648 and, therefore, changes the cyclotron frequency. Because of low-SNR sidebands were
 1649 unable to be observed in Phase II, so a correction for the effect of the pitch angle on the
 1650 cyclotron frequency was not possible.

1651 In the time-frequency spectrogram representation the chirping carrier frequency
 1652 appears as a linear track of high-power frequency bins (see Figure 3.10). The vertical
 1653 slope of the tracks is caused by the emission of energy from the electron in the form of

1654 cyclotron radiation, therefore, the size of the slope parameter is directly proportional
1655 to the Larmour power. The continuous track is periodically interrupted by random
1656 jumps to higher frequency and lower energy caused by random inelastic collisions with
1657 background gas molecules. The length of a track is an exponentially distributed variable
1658 whose mean value is inversely proportional to the gas density. The size of the frequency
1659 discontinuities is directly proportional to the energies of the rotational and vibrational
1660 states of background gas molecules.

1661 A CRES event refers to the collection of tracks produced by a trapped electron until
1662 it inevitably scatters into a pitch angle that can no longer be trapped. The goal of track
1663 and event reconstruction is to first identify the set of tracks present in a time-frequency
1664 spectrogram that represents a segment of data acquired in the Phase II apparatus. These
1665 tracks must then be clustered into events from which we can determine the first track
1666 produced by the electron and thus estimate it's starting cyclotron frequency and kinetic
1667 energy.

1668 **Track Reconstruction**

1669 The first step in CRES event reconstruction is the identification of tracks in the time-
1670 frequency spectrogram, which is essentially an image processing task. Track finding
1671 starts by normalizing the power spectral density based on the average noise power.
1672 Next a power threshold is applied to the normalized spectrogram where only bins that
1673 have a signal-to-noise ratio greater than five are selected to build tracks. In this case
1674 signal-to-noise ratio is defined as the ratio between the normalized, unitless power of a
1675 bin divided by the average normalized power across the full frequency spectrum.

1676 The sparse spectrogram produced by this power cut consists only of a sparse collection
1677 of high-power frequency bins that could be part of a CRES signal track (see Figure
1678 3.11). In this form is it much easier to identify tracks "by eye", however, for the Phase II
1679 analysis Project 8 developed its own custom-made track finding algorithm, called the
1680 sequential track finder (STF).

1681 The STF algorithm processes the sparse spectrogram in sequential fashion, processing
1682 each time-slice one-by-one until the end of the spectrogram is reached. Tracks are found
1683 by searching for points in the sparse spectrogram that appear to fall on a straight line.
1684 Multiple configurable parameters are built into the STF algorithm that allow the user to
1685 tune the criteria for adding a point to an existing track or creating a new track. These
1686 include parameters such as maximum time and frequency differences between subsequent
1687 points in a track as well as minimum SNR values for the start and endpoints of the track.

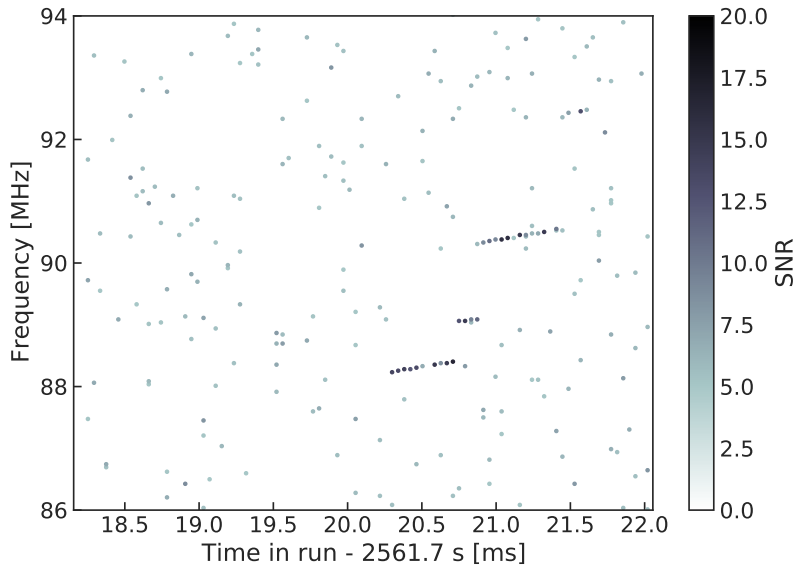


Figure 3.11. The sparse spectrogram obtained by placing a power cut on the raw spectrogram shown in Figure 3.10.

1688 Additionally, tracks are required to have a minimum length and slope to be considered
 1689 potential CRES tracks rather than random noise fluctuations.

1690 The resulting output of the STF is a collection of track objects that consist of the track
 1691 point objects and their properties. The final step is to calculate track-level properties
 1692 and apply cuts to reject false tracks found by the STF. This involves the fitting of a
 1693 line to the collection of track points as well as the total and average power of the track
 1694 obtained by computing the sum and mean of the points powers. The starting frequency
 1695 of the track is determined by calculating the time coordinate that intersects with the
 1696 linear fit. A cut is performed to remove all tracks that do not have a specified average
 1697 power over their duration, which helps to remove the majority of noise fluctuations that
 1698 have passed all previous cuts up to this point.

1699 Event Reconstruction

1700 After track reconstruction comes event reconstruction where the identified tracks are
 1701 grouped into events that correspond to the trajectory of a single electron in the trap. This
 1702 procedure attempts to match tracks head to tail by checking if the start and end times
 1703 of a pair of tracks falls within a certain tolerance. This tolerance is a configurable
 1704 parameter that can be tuned to an optimal value using Monte Carlo simulations of events
 1705 in the Phase II apparatus.

1706 After the event building procedure has completed there remains a small likelihood
1707 that false tracks have made it through to the event reconstruction stage. Typically, cuts
1708 at the track level are able to remove 95% of the false tracks identified by the STF, which
1709 leads to a significant number of false tracks at the event building stage. However, the
1710 additional event-level information makes it possible to reject events that contain these
1711 false tracks with a high degree of confidence.

1712 Two event level features are associated with events caused by real electrons — the
1713 duration of the first track as well as the number of tracks in the event. Real electrons
1714 tend to have event structures with longer first tracks and a higher number of total tracks.
1715 Based on the values of these two criteria, a minimum threshold on the average power in
1716 the first track was configured to reject false events. The average power in the first track
1717 was chosen due to the critical nature of the starting frequency of the first track in an
1718 event to the krypton and tritium spectrum analyses.

1719 **3.3.3 Results from Phase II**

1720 The main result from Phase II was the measurement of the tritium beta-decay spectrum
1721 using CRES, which lead to the first neutrino mass limit with CRES. However, Phase
1722 II also included a significant ^{83m}Kr measurement campaign to understand important
1723 systematics relevant to the tritium spectrum measurement, but also to understanding the
1724 fundamentals of the CRES technique itself. This required high-resolution measurements
1725 of the ^{83m}Kr internal-conversion spectrum [56], which is an interesting science result in
1726 its own right.

1727 The results from Phase II represents a significant effort from the entire Project 8
1728 collaboration over several years. Because the focus of my contributions to Project 8 is
1729 directed towards the research and development efforts for the Phase III experiments, the
1730 goal in this section is not to provide a detailed description of the analyses that lead to
1731 the Phase II results. Rather, I will provide brief descriptions of a few plots representative
1732 of the main results from Phase II.

1733 **Measurements with Krypton**

1734 Measurements with krypton were a key calibration tool for Phase II of the experiment and
1735 will continue to be useful in Phase III. In the context of Project 8 krypton measurements
1736 refers to CRES measurements of the internal-conversion spectrum of the metastable state
1737 of krypton-83, ^{83m}Kr , produced by electron capture decays of ^{83}Rb . A supply of ^{83}Rb

1738 was built into the Phase II apparatus gas system that supplied the CRES cell with ^{83m}Kr
1739 via emanation.

1740 The ^{83m}Kr internal-conversion spectrum consists of several lines based on the orbital
1741 of the electron ejected during the decay. The conversion lines useful to Project 8 are
1742 those that emit electrons with kinetic energies that fall inside the detectable frequency
1743 bandwidth of the Phase II apparatus. These are the K; L2 and L3; M2 and M3; and N2
1744 and N3 lines with kinetic energies of 17.8 keV, \approx 30.4 keV, \approx 31.9 keV, and \approx 32.1 keV,
1745 respectively. The different energies of the lines allow a onw to test the linearity of the
1746 relationship between kinetic energy and frequency across the range of frequencies covered
1747 by the continuous tritium spectrum.

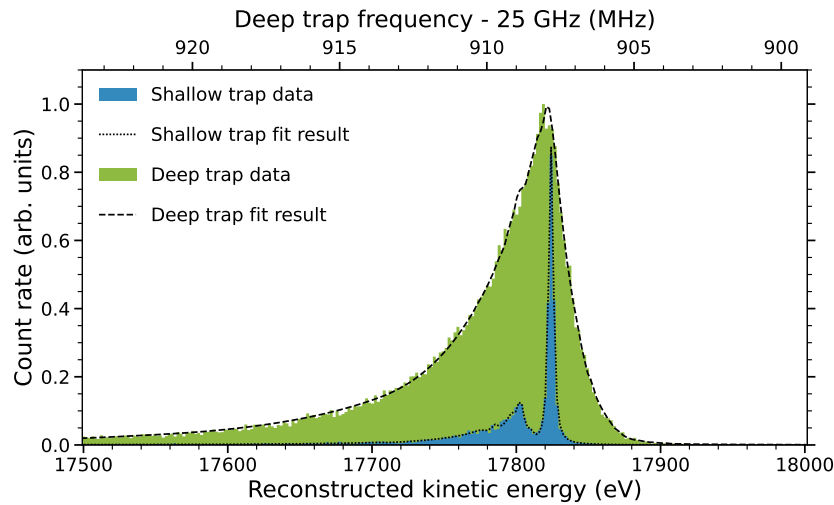


Figure 3.12. Fits to the measured 17.8-keV ^{83m}Kr conversion line using the deep and shallow trap configurations.

1748 Numerous detector related effects relevant to the tritium analysis can be characterized
1749 by measuring the shape of the krypton spectrum. Specific examples include variations
1750 in the magnetic field as a function of the radial position of the electron, variation in
1751 the magnetic field caused by the trap shape, variation in the average magnetic field for
1752 electrons with different pitch angles, and the effect of missing tracks due to scattering.
1753 These spectrum shape measurements focused on the 17.8-keV krypton line and utilized
1754 different trap geometries based on the particular goal of the dataset (see Figure 3.12).

1755 Krypton measurements with a shallow trap allow for high energy resolution, since
1756 variation in frequency due to pitch angle differences is sharply reduced in the shallow
1757 trap configuration. With this trap the main 17.8-keV peak of the conversion spectrum is
1758 clearly visible along with additional satellite peaks at lower energy, which correspond to

1759 the shakeup/shakeoff spectrum of the decay. The high accuracy of the fit demonstrates a
 1760 high degree of understanding of the CRES systematics.

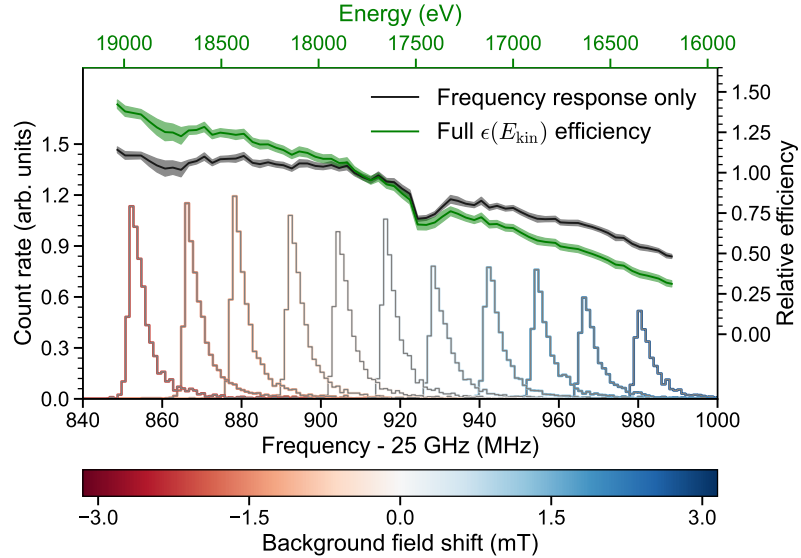


Figure 3.13. Measurements of the 17.8-keV ^{83m}Kr line using the deep trap configuration for different values of the magnetic field from the field shifting solenoid.

1761 The broadening of the krypton spectrum seen for the deeper track is due to the large
 1762 range of electron pitch angles that can be trapped. Furthermore, with a deeper trap
 1763 there is a larger parameter space of electron that could be produced with pitch angles
 1764 that are trappable but not visible in the time-frequency spectrogram. These electrons
 1765 live in the trap and can scatter multiple times before randomly scattering to a visible
 1766 pitch angle. This leads to one or more missing tracks earlier in the event, which leads to
 1767 a misreconstruction of the true starting frequency. By measuring the krypton spectrum
 1768 shape in the same trap used to detect tritium events, the effect this has on the spectrum
 1769 shape can be characterized to mitigate its impact on the tritium measurements.

1770 Changes in the Krypton spectrum shape as a function of CRES frequency were
 1771 used to study the detection efficiency of the Phase II apparatus. Variations in the
 1772 detection efficiency as a function of frequency directly influences the measured shape of
 1773 the continuous tritium spectrum, which can lead to errors in the neutrino mass estimate
 1774 if not modeled appropriately. Using the field shifting solenoid the cyclotron frequency
 1775 of the krypton 17.83 keV line was shifted across the full frequency range of the tritium
 1776 spectrum data (see Figure 3.13). Variations in the deep trap krypton spectrum shape
 1777 can be used to infer the detection efficiency as a function of frequency and correct for

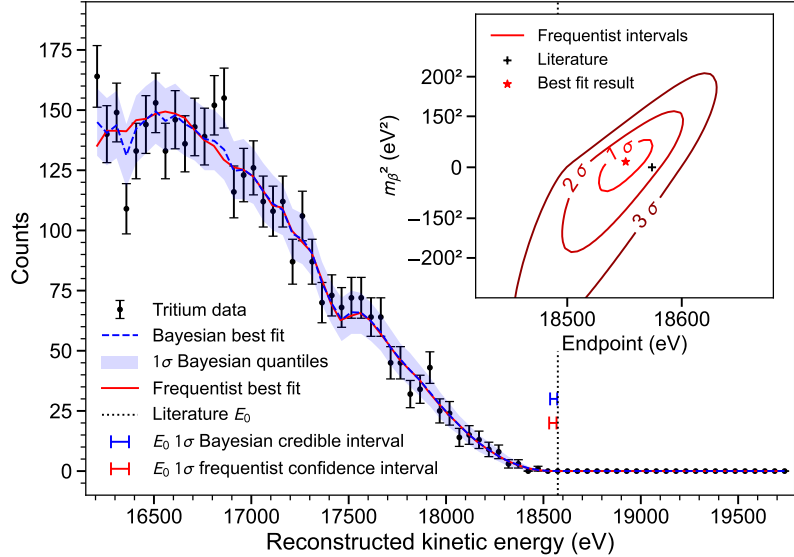


Figure 3.14. The measured tritium spectrum from Phase II with Bayesian and frequentist fits.

1778 this affect in the tritium measurements.

1779 Tritium Spectrum and Neutrino Mass Results

1780 The tritium measurement campaign resulted in the collection of 82 days of detector
 1781 live time during which 3770 total tritium events were detected. The track and event
 1782 reconstruction analysis extracted the starting frequencies of these tritium events, which
 1783 were used to build a frequency spectrum of tritium beta-decays. The resulting frequency
 1784 spectrum was then converted to an energy spectrum using the information gleaned from
 1785 the krypton measurement campaign to obtain the tritium beta-decay spectrum (see
 1786 Figure 3.14).

1787 CRES is inherently a very low background technique with the dominant source of
 1788 noise being random RF fluctuations. Monte Carlo simulations backed validated using
 1789 measurements of the RF noise background were used to set track and event cuts to
 1790 guarantee that zero false events would occur over the duration of the experiment with
 1791 90% confidence. Notably, the measured spectrum has zero events beyond the tritium
 1792 spectrum endpoint, which allows us to constrain the background rate in the Phase II
 1793 apparatus to less than 3×10^{-10} counts/ev/s. Achieving a low background is critical for
 1794 future neutrino mass experiments that seek to measure the neutrino mass with less than
 1795 100 meV sensitivity.

1796 Bayesian and frequentist based fits to the measured tritium spectrum, incorporating

1797 information gained about CRES systematics from the krypton measurements, were
1798 performed to extract upper limits on the tritium beta-decay spectrum endpoint as well as
1799 the neutrino mass. The estimated spectrum endpoints are 18553^{+18}_{-19} eV for the Bayesian
1800 analysis and 18548^{+19}_{-19} eV for the frequentist analysis. The quoted uncertainties are
1801 $1-\sigma$, and both results are within $2-\sigma$ of the literature endpoint value of 15574 eV. The
1802 estimated neutrino mass for both results is consistent with $m_\beta^2 = 0$. The 90% confidence
1803 upper limits for the Bayesian analysis is $m_\beta < 155$ eV/c² and $m_\beta < 152$ eV/c for the
1804 frequentist analysis.

1805 Though the neutrino mass results from Phase II are not competitive with KATRIN
1806 the experiment was a promising first step towards the development of more precise
1807 neutrino mass measurements using CRES. The low-background and high-resolution
1808 achievable with krypton measurements are promising features of the technique that were
1809 demonstrated with the Phase II apparatus. As new technologies are developed to enable
1810 CRES measurements in larger volume, many of the lessons learned from Phase II will
1811 continue to influence the operation and design of future experiments.

1812 **3.4 Phase III R&D: Antenna Array CRES**

1813 The goal of Phase III in the Project 8 experimental program is to develop the technologies
1814 and expertise required to build an experiment that uses CRES to measure the neutrino
1815 mass with a target sensitivity of 40 meV. One of the key technologies is a method for
1816 performing high resolution CRES measurements in a large volume, which allows one to
1817 observe a sufficient quantity of tritium to measure the low-activity endpoint region of
1818 the tritium spectrum.

1819 **3.4.1 The Basic Approach**

1820 One possible approach, suggested in the original CRES publication [39], is to use many
1821 antennas to surround a volume of tritium gas in a magnetic field (see Figure 3.15). When
1822 a decay occurs the electron will begin to emit cyclotron radiation that can be collected
1823 by the array and used to perform CRES. Each antenna in the array collects only a small
1824 fraction of the electron's signal power, which is less than 1 fW for a 18.6 keV kinetic
1825 energy electron in a 1 T magnetic field. Scaling to large volumes with the antenna
1826 array approach is accomplished by increasing the number of antennas in the array, which
1827 increases the volume under observation proportionally, so that a sufficient population of

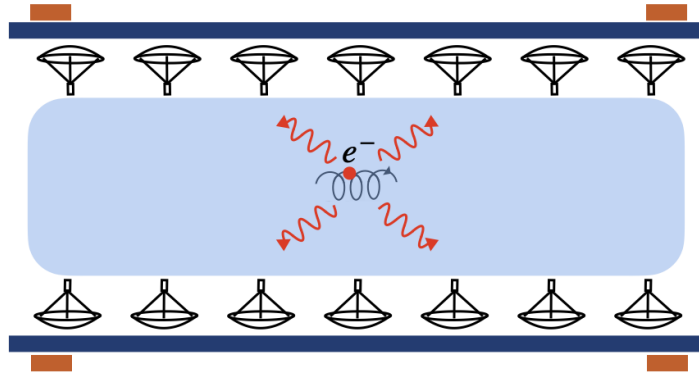


Figure 3.15. A cartoon illustration of the basics of the antenna array CRES technique.

1828 tritium atoms can be observed to measure the tritium spectrum endpoint shape.

1829 Several features of the antenna array approach make it an attractive candidate technol-
 1830 ogy for a large volume experiment. One example is the accurate position reconstruction
 1831 made possible by the multichannel nature of the array. Using techniques like digital
 1832 beamforming it is possible to estimate the radial and azimuthal positions of the electron
 1833 in the magnetic trap with a precision significantly less than the size of the cyclotron
 1834 wavelength. This capability allows one to perform event-by-event estimations of the
 1835 magnetic field experienced by an electron, which is crucial to achieving high energy
 1836 resolution with the CRES technique.

1837 The easy availability of position information with the antennas array approach
 1838 is potentially a unique advantage that provides significant flexibility in the magnetic
 1839 field uniformity requirements compared to other proposed approaches to large volume
 1840 CRES (see Chapter 6). Spatial discrimination using digital beamforming leads to pileup
 1841 reduction, which helps to reduce the potential of background events caused by missing
 1842 tracks or by incorrectly clustering a group of tracks into an event. Limits on the
 1843 background rate for a neutrino mass measurement with 40 meV sensitivity are stringent
 1844 and the total activity of the tritium source for such an experiment is gigantic relative to
 1845 the activity near the endpoint. Thus, pileup discrimination could be an important tool
 1846 for a large scale CRES experiment.

1847 Another beneficial quality of the antenna array approach is that the volume of the
 1848 experiment can be scaled independent of frequency by simply adding more antennas to
 1849 the array (see Figure 3.19). Resonant cavities, the proposed alternative large volume
 1850 CRES technology, are ideally operated in magnetic fields that cause electrons to move
 1851 with cyclotron frequencies near the fundamental cavity resonance, to avoid complex
 1852 coupling of the electron to many cavity modes simultaneously. This leads to a coupling

1853 between the cavity volume and the magnetic field magnitude, which forces one to lower
1854 the magnetic field in order to increase the experiment scale. Whereas, for antenna arrays,
1855 in principle there is no physical limitation on the size of the antenna array that can be
1856 used at a particular magnetic field. However, the nature of scaling an antenna array
1857 based experiment leads to rapidly increasing cost and complexity due to the large number
1858 of antennas, amplifiers, and data streams that require substantial computer processing
1859 power to effectively analyze.

1860 **3.4.2 The FSCD: Free-space CRES Demonstrator**

1861 The complexity of the antenna array CRES technique requires the construction of a
1862 small scale demonstration experiment to develop an understanding of technique itself and
1863 relevant systematics. Without a demonstrator experiment it is not possible to sufficiently
1864 retire the technical risks associated with the full-scale experiment. Therefore, Phase
1865 III of the Project 8 experimental program is primarily focused on the development and
1866 operation of demonstrator experiments to inform the design of the Phase IV experiment.

1867 The demonstrator experiment developed for antenna array CRES in Phase III is called
1868 the Free-space CRES Demonstrator or FSCD. The FSCD is intended as a demonstration
1869 of antenna array CRES, but is also a capable neutrino mass measurement experiment
1870 in its own right, with a target neutrino mass sensitivity of a few eV using a molecular
1871 tritium source.

1872 **Magnetic Field**

1873 The background magnetic field for the FSCD is provided by a hospital-grade MRI magnet
1874 (see Figure 3.16). The magnet produces a magnetic field of approximately 0.958 T, which
1875 corresponds to a tritium spectrum endpoint frequency of approximately 25.86 GHz. The
1876 magnet is installed in the Project 8 laboratory located at the University of Washington,
1877 Seattle, and is shimmed to produce a uniform magnetic field with variations on the
1878 ppm-level. Measurements of the magnetic field non-uniformities are performed using a
1879 NMR probe and rotational gantry to capture measurements of the magnetic field around
1880 an elliptical surface in the center of the MRI magnet. During the operation of the FSCD
1881 an array of Hall or NMR magnetometers would be used to periodically measure the
1882 magnetic field to monitor its time stability.

1883 Inside the field of the MRI magnet additional electromagnets would be installed that
1884 provide the capability to shift the value of the background magnetic field and produce



Figure 3.16. An image of the MRI magnet installed in the Project 8 laboratory at the University of Washington, Seattle.

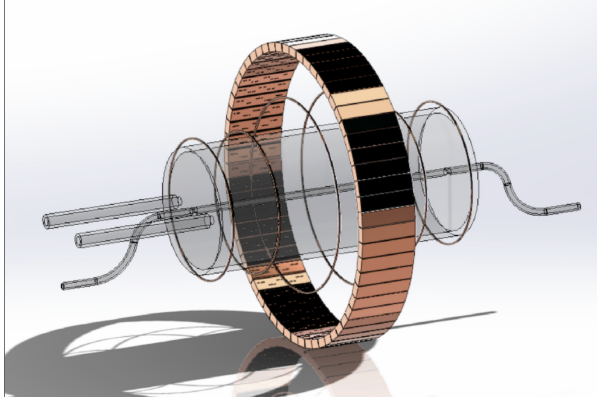
1885 a magnetic trap. Shifting the background magnetic field by a few μ T lets one control
 1886 the cyclotron frequencies of electrons with a fixed kinetic energy, which is key to an
 1887 effective calibration of the FSCD. The preferred calibration method for the FSCD is
 1888 a mono-energetic electron gun that can inject electrons into the magnetic trap with a
 1889 known kinetic energy. In combination with the field shifting magnet, one can vary the
 1890 cyclotron frequencies of the electrons to measure the response of the antenna array as a
 1891 function of the radiation frequency and electron position. This procedure characterizes
 1892 the response of the antenna array and provides further information on magnetic field
 1893 uniformity, which is important to achieving good energy resolution.

1894 The design of the magnetic trap is absolutely critical to the success of a CRES
 1895 experiment. The ideal shape is the perfect magnetic box, which has a flat bottom and
 1896 step function walls. Any variation in the average magnetic field experienced by an
 1897 electron leads to changes in the cyclotron frequency that can make determining the true
 1898 starting kinetic energy more difficult. This includes changes in the magnetic field caused
 1899 by the walls of the magnetic trap as well as radial magnetic field variations.

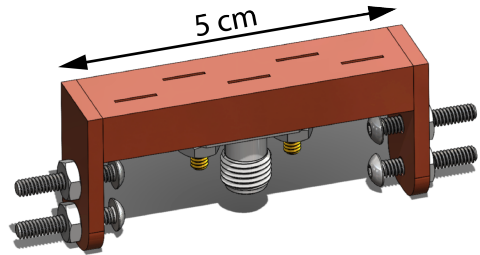
1900 The ideal box trap is completely uniform and has infinitely steep walls that cause
 1901 no change in the electron's cyclotron frequency as it is reflected from the trap wall,
 1902 however, such a trap cannot be made from any combination of magnetic coils since it
 1903 violates Maxwell's equations. One of the goals of magnetic trap design is to identify the
 1904 configuration of coils that produces a trap that approximates the perfect box trap as
 1905 closely as possible.

1906 **Antenna Array**

1907 The canonical antenna array design for CRES is a uniform cylindrical array of antennas
1908 that surrounds the magnetic trap volume. Since the FSCD is a demonstrator experiment,
1909 the antenna array design is the simplest form of the uniform cylindrical array, which is a
single circular ring of antennas with a diameter of 20 cm (see Figure 3.17). Along this



(a)



(b)

Figure 3.17. (a) A model of the FSCD antenna array, magnetic trap, and tritium containment vessel design.(b) A more detailed model of a prototype design for the 5-slot waveguide antenna design.

1910
1911 circle are sixty slotted waveguide antennas that fully populate the available space around
1912 the array circumference. In order to maximize the power collected from each electron
1913 it is optimal to cover as large a fraction of the solid angle around the magnetic trap as
1914 possible.

1915 The distance between antennas around the circumference of the array is proportional
1916 to the wavelength of the cyclotron radiation. Therefore, maximizing the solid angle
1917 coverage of the array, while minimizing channel count to keep the hardware and data
1918 acquisition costs manageable, biases one towards smaller array diameters. Antenna
1919 near-field effects limit the minimum diameter of the array for a given antenna design
1920 since the radiation from electrons that are too close to the array cannot be detected
1921 due to destructive interference caused by path-length differences from the electron to
1922 different points on the antenna surface.

1923 Slotted waveguide antennas are used in the FSCD antenna array due to their high
1924 efficiency and low loss, which comes from the lack of dielectric materials in the antenna
1925 structure. Coupling to the waveguide can be performed with a coaxial cable connected
1926 at the center or on either end of the waveguide. One of the drawbacks of waveguide

1927 antennas is the large amount of space required to fit them inside the limited MRI magnet
1928 volume. Alternative antenna designs, constructed from microstrip printed circuit boards
1929 require significantly less space at the cost of slightly higher energy loss in the antenna
1930 structure.

1931 The FSCD antenna design is a 5 cm long segment of WR-34 waveguide with 5 vertical
1932 slots cut into the side. The distance between slots along the length of the waveguide is
1933 a half wavelength for optimal power combination between the individual antenna slots.
1934 Each slot is offset from the center of the antenna face a small distance in order to most
1935 effectively couple the slot to waveguide modes inside the antenna.

1936 The passive power combination achieved by placing 5 slots in a single waveguide is a
1937 compromise intended to reduce the cost and complexity of the antenna array system.
1938 Each additional channel in the array requires it's own cryogenic amplifier and also increase
1939 the required computer power to process the raw data collected by digitizing each channel.
1940 Passive summation, achieved by combining antennas into arrays axially, reduces the array
1941 channel count at the cost of losses from imperfect passive combination. Imperfect passive
1942 combination is caused by effects such as re-radiation of energy from and destructive
1943 interference between slots in the waveguide antenna.

1944 Interference and re-radiation eventually limit the achievable the axial extent of passive
1945 power combination. The 5-slot designed developed for the FSCD is optimized to minimize
1946 the impact of these losses while achieving the maximum amount of axial coverage with a
1947 single ring of antennas. Scaling beyond the volume covered by a single ring of antennas is
1948 achieved by stacking additional rings of antennas together to cover a larger trap volume
1949 for a higher statistics measurement of the tritium spectrum endpoint region. A likely
1950 scenario for the FSCD experiment involves a staged experiment approach, where first
1951 a series of measurements is performed using only a single ring of antennas followed by
1952 experiments that add additional rings to the FSCD. The goal would be to first understand
1953 the principles of antenna array CRES using the simplest possible experiment, before
1954 attempting to scale the technique by expanding the antenna array size.

1955 **Tritium Source**

1956 While the primary purpose of the FSCD is as a technology demonstrator, it is unlikely
1957 for the collaboration to gain the required confidence in the antenna array CRES tech-
1958 nique to perform neutrino mass measurements at the 40 meV sensitivity level without
1959 an intermediate scale measurement of the neutrino mass using antenna array CRES.
1960 Therefore, the FSCD has an additional scientific goal of measuring the neutrino mass

1961 with a rough sensitivity goal of a few eV. This level of precision is achievable using a
1962 source of molecular tritium with a volume of approximately 1 L at a density comparable
1963 to potential Phase IV scenarios.

1964 Unlike previous CRES experiments, where the tritium source could be co-located
1965 with the receiving antenna inside a waveguide transmission line, the tritium source
1966 in the FSCD is thermally isolated from the antenna array to avoid freeze-out of the
1967 tritium molecules. The tiny radiation power emitted by electrons requires a system noise
1968 temperature of ≈ 10 K or less, in order to detect events at a high enough efficiency to
1969 reach the neutrino mass sensitivity goals of the experiment. Achieving a system noise of
1970 10 K requires that the antenna array and amplifiers operate at cryogenic, liquid helium
1971 temperatures of ≈ 4 K, which significantly lowers the vapor pressure of molecular tritium.
1972 By keeping the molecular tritium isolated in an RF-transparent vessel the tritium gas can
1973 be kept at a relatively warmer temperature in the range of 30 K to avoid the accumulation
1974 of tritium on the experiment surfaces.

1975 Data Acquisition and Reconstruction

1976 A fundamental change in the data acquisition system for the FSCD is the shift from
1977 single to multi-channel reconstruction. This transition results in a significant increase in
1978 the data-generation rate, which is linearly related to the number of independent channels
1979 in the array. The larger data volume coincides with an increased demand for computer
1980 processing power based on the need for more precise signal reconstruction algorithms
1981 driven by the FSCD and Phase IV sensitivity goals. Therefore, the data acquisition
1982 system for the FSCD is likely to represent a significantly larger fraction of the experiment
1983 cost and complexity than previous CRES experiments.

1984 Each antenna in the array is connected to a cryogenic amplifier and down-converted
1985 from the 26 GHz CRES frequency using an IQ-mixer to reduce the size of the analysis
1986 window in which the tritium spectrum is measured. Using an LO with a frequency of
1987 approximately 25.80 GHz the antenna array signals can be digitized at a rate of 200 MHz,
1988 which is sufficient bandwidth to resolve the complete sideband spectrum produced by
1989 axial oscillations of electrons in the FSCD magnetic trap.

1990 Direct storage of the raw FSCD antenna array data is undesirable, since the estimated
1991 amount of raw data generated is $O(1)$ exabyte per year. The management and storage
1992 of such a large dataset is infeasible for a demonstrator experiment on the scale of the
1993 FSCD and would represent a large fraction of the budget for a Phase IV scale antenna
1994 array based CRES experiment. Therefore, a sub-goal of the FSCD experiment is the

1995 development of real-time reconstruction methods that could reduce the raw data volume
1996 by detecting and reconstructing CRES events in real-time. The ultimate goal would be
1997 a complete real-time reconstruction pipeline that takes raw voltages samples from the
1998 antenna array and returns estimates for the starting kinetic energies of CRES events in
1999 the data.

2000 The feasibility of a real-time reconstruction pipeline rests on the development of
2001 computationally efficient algorithms that can be implemented without the need for
2002 enormous computing resources. One challenge with the antenna array approach is that
2003 the small radiation power of a single electron is distributed between each channel in
2004 the array, such that reconstruction using only the information in a single channel is not
2005 possible. Therefore, the simply performing the initial step in reconstruction — signal
2006 detection — requires orders of magnitude more computational power than previous CRES
2007 experiments. This operation will then be followed by other, potentially more expensive,
2008 reconstruction steps that are required in order to determine the kinetic energy of the
2009 electron.

2010 **3.5 Pilot-scale Experiments**

2011 **3.5.1 Choice of Frequency**

2012 The optimal CRES frequency for Project 8 is that which can reach our target sensitivity
2013 of 40 meV, while minimizing the cost and complexity of the overall experiment. The
2014 magnitude of the background magnetic field determines the cyclotron frequency, which
2015 affects the entirety of the CRES detection system design, specifying the operating
2016 frequency of the CRES experiments is one of the first steps towards developing a full
2017 design.

2018 **Scaling Laws**

2019 The Phase I and II experiments utilized a background magnetic field of 0.959 T provided
2020 by an NMR magnet. This magnetic field was selected primarily for convenience, however,
2021 the cyclotron frequencies for electrons near the tritium endpoint in a 0.959 T field ranges
2022 from 25 to 26 GHz, which is within the standard RF Ka-band. Therefore, microwave
2023 electronics specialized for these frequencies are easily obtainable for relatively low cost.
2024 The operating frequency for the large-scale experiments must be selected in a more
2025 rigorous manner due to the increased scale and complexity of the systems as well as the

2026 requirements of the 40 meV neutrino mass science goal.

2027 There is a bias towards lower frequencies in a large-volume experiment, due to the
2028 direct relationship between wavelength and the physical size of the compatible RF
2029 components like antennas and cavities. With a longer wavelength more volume can
2030 be surrounded by an array with fewer antennas, which reduces hardware and data-
2031 processing costs. Additionally, the size of a cavity experiment is directly proportional
2032 to the wavelength since this sets the physical dimensions of the cavity. Furthermore,
2033 it is easier to engineer a magnet that provides a uniform magnetic field across several
2034 cubic-meters of space at lower magnetic fields, which provides advantages in terms of
2035 cost-reduction and field uniformity.

2036 A concern with lower magnetic fields and frequencies is the scaling of the Larmour
2037 power equation, which is proportional to the square of the frequency. Naively, one would
2038 predict that the SNR would decrease with lower fields, however, two additional scaling
2039 laws that affect the noise power also come into play. Noise power is directly proportional
2040 to the required bandwidth, which decreases linearly with the magnetic field. Furthermore,
2041 at lower frequencies it is possible to purchase amplifiers with lower noise temperatures
2042 until approximately 300 MHz at which point this relationship tends to flatten. Therefore,
2043 it is expected that the SNR remains approximately constant as the frequency decreases.

2044 The SNR directly impacts the overall efficiency of the experiment through its effects
2045 on signal detection and energy resolution. Thus, the expectation that SNR remains the
2046 same at lower frequencies clearly biases large-scale experiments in this direction. One
2047 drawback of lower magnetic fields is the increased influence of external magnetic fields
2048 on the experiment. This includes magnetic fields from the building materials as well as
2049 variations in the earth's magnetic field. To deal with these affects a suitable magnetic
2050 field correction system will need to be devised, which includes constant monitoring of
2051 external fields.

2052 **Atomic Tritium Considerations**

2053 The pilot-scale experiments will be the first Project 8 experiments to combine CRES with
2054 atomic tritium, therefore, the optimal frequency should take into account the affect of the
2055 background magnetic field on the atom trap. The primary influence of the background
2056 field magnitude is through the rate of dipolar spin-flips caused by a spin exchange
2057 interaction between trapped atoms [57].

2058 Atomic tritium is a simple quantum system with a hyperfine structure given by the
2059 addition of the nuclear and atomic spins. The addition of two spins leads to a hyperfine

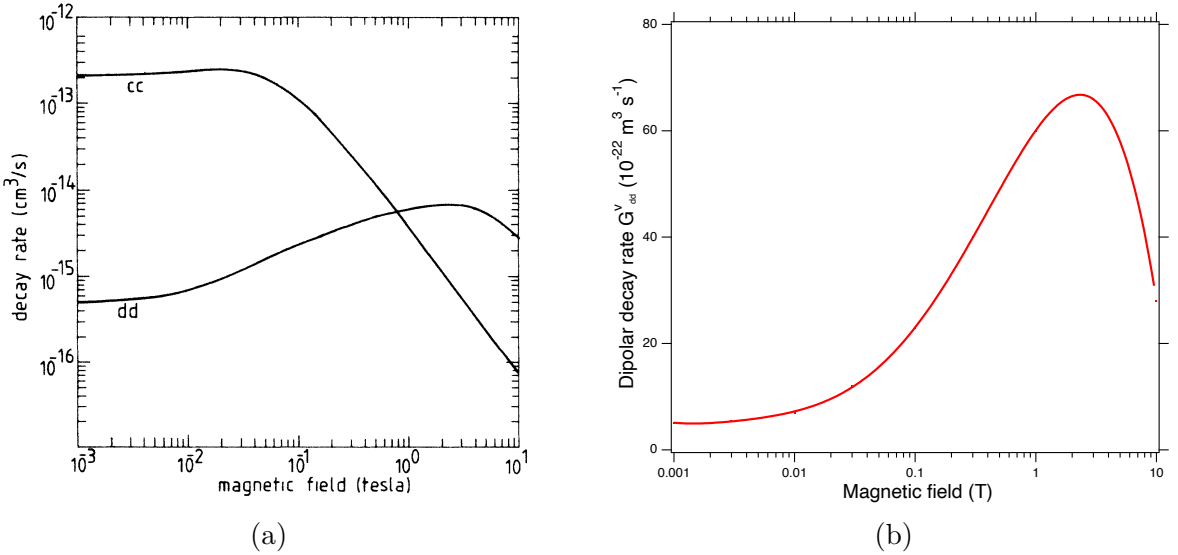


Figure 3.18. (a) A plot of the decay rate for the two-body dipolar spin exchange interaction for cc and dd state. (b) A plot of the decay rate of the dipolar spin exchange interaction for d+d states as a function of magnetic field magnitude. Lowering the magnetic field is key for reducing the losses from this interaction.

2060 structure with four states in the (m_s, m_I) basis [58]. The states with atomic spins directed
 2061 anti-parallel to the magnetic field have $m_s = -1/2$ and are labeled as the a and b states.
 2062 The a and b states are colloquially known as high-field seeking states, since their energy is
 2063 minimized when in regions of higher magnetic field. This leads to losses in the magnetic
 2064 trap as these atoms are drawn to higher fields away from the trap center. Alternatively,
 2065 the c and d states, with atomic spin $m_s = +1/2$, minimize their energy in low magnetic
 2066 fields because of the parallel alignment between spin and the magnetic field. Therefore,
 2067 these low-field seeking states tend to stay trapped significantly longer than the high-field
 2068 seeking states.

2069 It would be advantageous to prepare tritium atoms in purely c and d states before
 2070 trapping, however, even in this case losses still occur due to dipolar interactions between
 2071 pairs of c and d states leading to flipped atomic spins and subsequent losses from high-field
 2072 seeking atoms. The rate of these interactions depends on the magnitude of the background
 2073 magnetic field and is maximal for dd interactions around 1 T (see Figure 3.18). The rate
 2074 of losses from these interactions at 1 T requires atomic tritium production at a rate two
 2075 orders of magnitude larger than at 0.1 T, thus, requirements on the whole atomic tritium
 2076 system are significantly relaxed at lower magnetic fields, which provides an additional
 2077 argument for transitioning to lower frequencies with the pilot-scale experiments.

2078 **3.5.2 Pilot-scale Experiment Concepts**

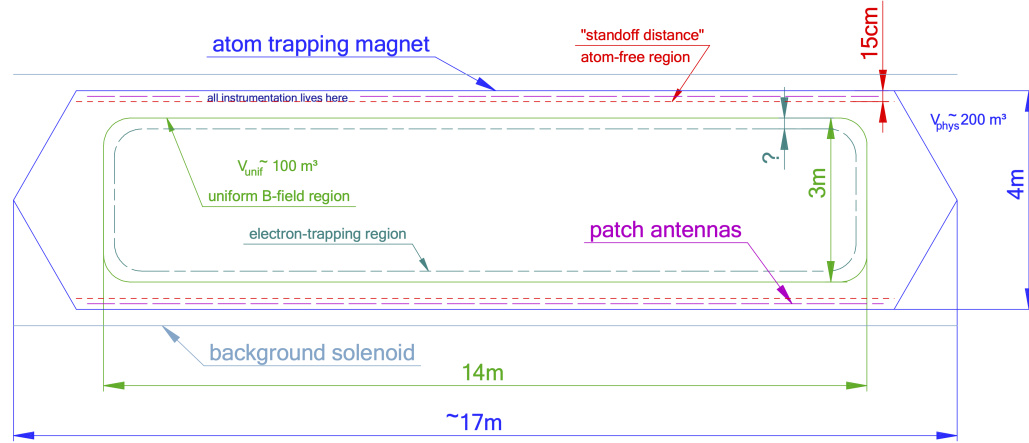


Figure 3.19. A conceptual sketch of a large-volume antenna array based CRES experiment to measure the neutrino mass.

2079 While the pilot-scale experiments are still in the early stages, enough is known to
2080 sketch the general features of these experiments at the conceptual level.

2081 **Pilot-scale Antenna Array CRES Experiment Concept**

2082 A conceptual design for an antenna-based CRES experiment is shown in Figure 3.19.
2083 A large solenoid magnet provides a uniform background magnetic field less than 0.1 T
2084 in magnitude. Inside this region is the atom trapping magnet that generates a high
2085 magnetic field at the walls, which decays exponentially towards the central region. Known
2086 magnet designs that produce suitable atom trapping fields include Ioffe-Prichard traps,
2087 which use conducting coils, as well as a Halbach array made from permanent magnets.
2088 Either magnet choice produces a region of high magnetic fields, which excludes atoms
2089 and allows for the placement of antennas inside the experiment.

2090 Inside this region an array of microstrip patch antennas is inserted to collect the
2091 cyclotron radiation without providing a surface for atomic tritium recombination. Due
2092 to the lower frequency of cyclotron radiation antennas of a larger size can be used,
2093 which lowers the total number of antennas required to observe the experiment volume.
2094 Because of this scaling, the lower frequency experiment uses a similar number of antennas
2095 compared to a much smaller demonstrator experiment with a 1 T magnetic field.

2096 The atomic tritium beamline that supplies fresh tritium atoms to the experiment is
2097 not shown in the figure. The general configuration would matches the one shown for the
2098 pilot-scale cavity experiment (see Figure 3.20).

2099 **Pilot-scale Cavity CRES Experiment Concept**

2100 The pilot-scale cavity experiment includes both an atomic tritium system and cavity
2101 CRES system. The atomic system consists of a thermal atom cracker located at the
2102 start of an evaporatively cooled atomic beamline. The atomic tritium system provides a
2103 supply of tritium atoms to the trap with temperatures on the order of a few mK. Atoms
2104 at this temperature can be trapped magneto-gravitationally, which is the reason for the
2105 vertical orientation of the cavity. At these low magnetic fields the trapping requirements
2106 for electrons and atoms differ enough such that it is advantageous to decouple the the
2107 trapping potentials to avoid radioactive heating of the tritium atoms from excess trapped
2108 electrons. Electron trapping is provided by a set of magnetic pinch coils at the top and
2109 bottom of the cavity and a multi-pole Ioffe or Halbach magnet serves to contain the
2110 atoms.

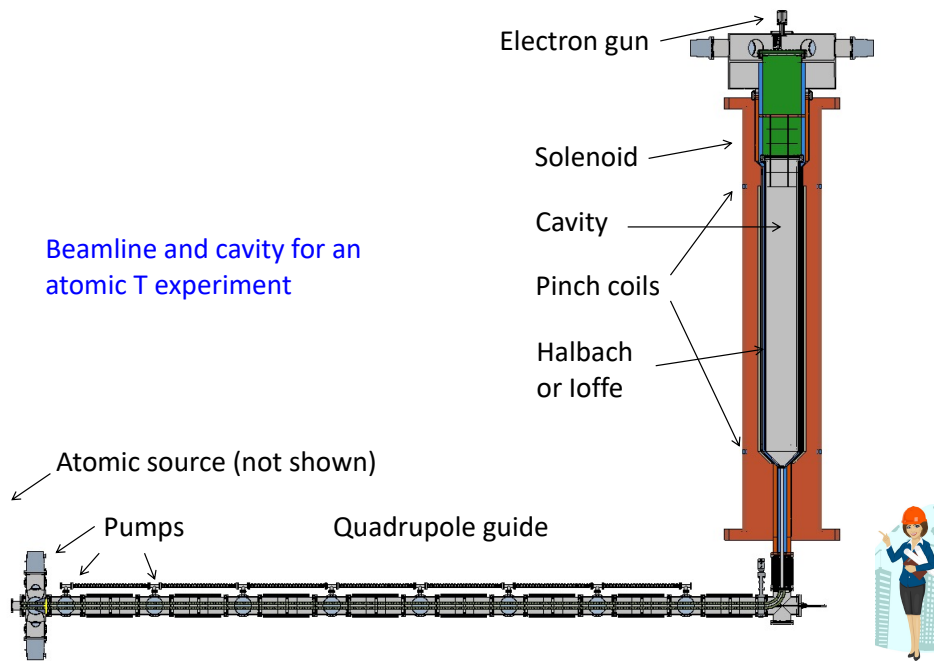


Figure 3.20. A conceptual sketch of a pilot-scale cavity CRES experiment with an atomic tritium beamline.

2111 The cavity design for the pilot-scale experiment consists of a large cylindrical cavity
2112 with a TE011 resonance of 325 MHz. Such a cavity is truly enormous, with a diameter
2113 of approximately 1.2 m and a height of 11 m. When an electron is produced inside
2114 the cavity with a cyclotron frequency that matches the TE011 resonant frequency it's
2115 cyclotron orbit couples the electron to the TE011, which drives a resonance in the cavity.
2116 These resonant fields can be read-out using an appropriate cavity coupling mechanism

2117 located at the center of the cavity. For more information on the cavity approach to
2118 CRES see Chapter 6.

2119 The bottom of the cavity has a cone termination to match the contour of the atom
2120 trapping magnet. This shape still allows for TE011 resonances with high internal Qs,
2121 which are required for good SNR in the cavity experiment. A small opening in the bottom
2122 of the cone serves as an entry point for the tritium atoms. To allow for calibration of
2123 the magnetic field inhomogeneities with an electron gun, the top of the cavity is left
2124 nearly completely open. Normally, this would drastically lower the Q-factor of the TE011
2125 mode, but a specially configured coaxial partition is inserted at the top. This termination
2126 scheme is designed to act as a perfect short for the TE011 mode since the circular shape
2127 of the partition matches the electric field boundary conditions for the TE011 mode.
2128 Simulations with HFSS have confirmed that this design results in a high quality TE011
2129 resonance despite the nearly completely open end.

2130 3.6 Phase IV

2131 The baseline CRES technology being pursued by the Project 8 collaboration are resonant
2132 cavities, which, due to their geometric properties, simple CRES signal structure, and low
2133 channel count, appear to be the better option for Phase IV. The current knowledge of the
2134 antenna array CRES approach reveals no technical obstacles that would preclude it as a
2135 baseline technology for Phase IV though it would most certainly be significantly more
2136 expensive. Therefore, antenna arrays represent a fallback approach if resonant cavities
2137 prove infeasible.

2138 The sensitivity of the pilot-scale atomic tritium experiment is estimated to be on
2139 the order of 0.1 eV, which means that increasing the sensitivity to reach the Phase IV
2140 goal will require an even larger experiment. Because of the direct coupling between the
2141 RF characteristics of a cavity and its geometry, the baseline plan is to build multiple
2142 copies of the pilot-scale experiment (see Figure 3.21) to obtain the required amount of
2143 volume rather than increase the size of the cavity beyond the pilot-scale. The built-in
2144 redundancy of this approach is useful in the sense that the experiment has no single
2145 point of failure, additionally, building several copies of the a pilot-scale experiment will
2146 minimize new engineering and design effort.

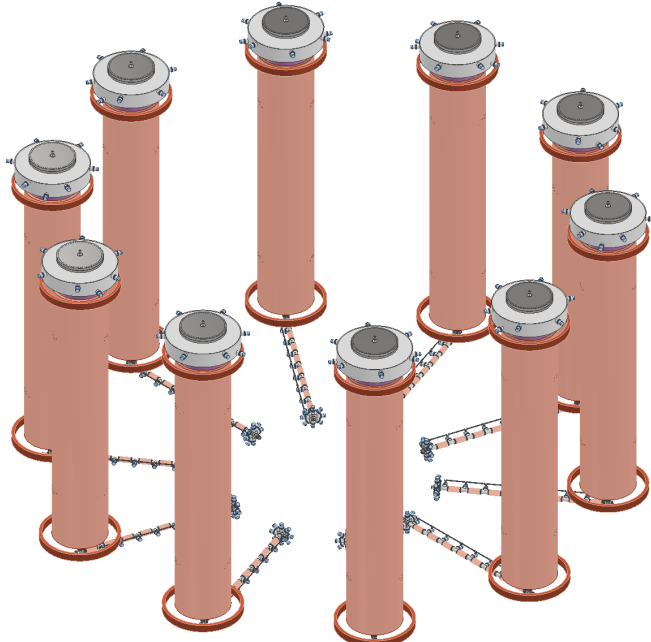


Figure 3.21. An illustration of a possible arrangement of ten pilot-scale cavity experiments for Phase IV. The experiments are arranged in a circle with an approximate diameter of 50 meters. Each atomic beamline connected to the bottom of each cavity is approximately 10 m in length. The cavities themselves are designed to operate at 325 MHz and are approximately 11 m tall. The circular arrangement of cavities has some advantages when it comes to cancellation of fringe fields from neighboring magnets, which is important due to the small magnetic field magnitudes consistent with these CRES frequencies. The advantage of ten independent atomic sources and cavities is that there is no single point of failure for the experiment. If an experiment goes down for repairs the other nine may continue running. Figure courtesy of Michael Huehn at UW-Seattle.

Chapter 4

Signal Reconstruction Techniques for Antenna Array CRES and the FSCD

4.1 Introduction

The transition from a waveguide CRES experiment to an antenna array CRES experiment introduces new challenges related to data acquisition, signal detection, and signal reconstruction caused by the multi-channel nature of the data. The development of signal reconstruction algorithms is crucial to the design of antenna array based experiments like the FSCD, because these algorithms directly influence the detection efficiency and energy resolution of the CRES experiment. In this Chapter I summarize my contributions to the development and analysis of signal reconstruction and detection algorithms for the FSCD experiment.

In Section 4.2 I discuss the primary tool for this work, which is the Locust simulations package developed by the Project 8 experiment. Locust is used to simulate CRES events in the detector. Locust uses Kassiopeia to calculate particle trajectory solutions for electrons in the magnetic trap. The trajectories are then used to calculate the response of the antenna array to the cyclotron radiation produced by the electron, which results in signals that can be used to analyze the performance of different signal reconstruction algorithms. More recently, Project 8 has developed CREsana, which is a new simulations package that takes a more analytical approach to CRES signal simulations for antenna arrays. Although CREsana signals were not used for the signal reconstruction algorithm development detailed here, we introduce the software as it plays a role in the antenna array measurements presented in Section 5.5.

In Section 4.3 I discuss the signal reconstruction and detection approaches analyzed for the FSCD experiment. In general there are two steps to signal reconstruction — detection and parameter estimation. With signal detection one is primarily concerned

2173 only with distinguishing between data that contains a signal versus data that contains only
2174 noise, whereas, with parameter estimation one is interested in extracting the kinematic
2175 parameters of the electron encoded in the cyclotron radiation signal shape. Due to
2176 the low signal power of electrons near the spectrum endpoint in the FSCD experiment,
2177 signal detection is a non-trivial problem. This is magnified by the need to maximize the
2178 detection efficiency of the experiment in order to achieve the neutrino mass sensitivity
2179 goals. My contributions to signal reconstruction analysis for the FSCD are focused on
2180 this signal detection component of reconstruction.

2181 After the discussion of various signal detection approaches, in Section 4.4 I present a
2182 more detailed analysis of the detection performance of three algorithms, which could be
2183 used to signal detection in the FSCD. This section was originally prepared for publication
2184 in JINST as a separate paper. The algorithms include a digital beamforming algorithm,
2185 a matched filter algorithm, and a neural network algorithm, which I analyze in terms of
2186 classification accuracy and estimated computational cost.

2187 **4.2 FSCD Simulations**

2188 Antenna array CRES and the FSCD requires a combination of different capabilities
2189 not often found in a single simulation tool. First of all, accurate calculations of the
2190 magneto-static fields produced by current-carrying coils are required in order to accurately
2191 model the magnetic trap and background magnets. The resulting magnetic fields must
2192 then be used to calculate the exact relativistic trajectory of electrons, which is required
2193 in order to calculate the electro-magnetic (EM) fields produced by the acceleration of
2194 the electron. Finally, the simulation has to model the interaction of the antenna and
2195 RF receiver chain with these EM-fields in order to produce the simulated voltage signals
2196 produced by the antenna array during the CRES event. At the time when Project 8 was
2197 developing this simulation capability, no single available simulation tool was known to
2198 adequately perform this suite of calculations, which prompted the development of custom
2199 simulation framework to simulate the FSCD. This simulation framework includes custom
2200 simulation tools developed by Project 8 as well as other open-source and proprietary
2201 software developed by third-parties.

2202 **4.2.1 Kassiopeia**

2203 Kassiopeia¹ is a particle tracking and static EM-field solver developed by the KATRIN
2204 collaboration for simulations of their spectrometer based on magnetic adiabatic collimation
2205 with an electrostatic filter [59]. Due to the measurement technique employed by the
2206 KATRIN collaboration, Kassiopeia is not designed to solve for the EM-fields produced by
2207 electrons in magnetic fields. However, it does provide efficient solvers for static electric
2208 and magnetic fields and charged particle trajectory solvers. Because of this, Project 8
2209 has incorporated parts of Kassiopeia into its own simulation framework.

2210 **Magnetostatic Field Solutions**

2211 The solutions to the electric and magnetic fields generated by a static configuration of
2212 charges and currents is given by Maxwell's equations in the limit where the time-dependent
2213 terms go to zero. In their static form Maxwell's equations [48] are

$$\nabla \cdot \mathbf{E} = \frac{\rho}{\epsilon_0} \quad (4.1)$$

$$\nabla \times \mathbf{E} = 0 \quad (4.2)$$

$$\nabla \cdot \mathbf{B} = 0 \quad (4.3)$$

$$\nabla \times \mathbf{B} = \mu_0 \mathbf{J}, \quad (4.4)$$

2214 where we can see that the electric and magnetic fields are now completely decoupled
2215 from each other. The solution for the magnetic field in this boundary value problem is
2216 given by the Biot-Savart law

$$\mathbf{B}(\mathbf{r}) = \frac{\mu_0}{4\pi} \int dr' \frac{r'^3 \mathbf{J}(\mathbf{r}') \times (\mathbf{r} - \mathbf{r}')}{|\mathbf{r}' - \mathbf{r}|^3}, \quad (4.5)$$

2217 which Kassiopeia uses a variety of numeric integration techniques to solve for a user
2218 defined current distribution.

2219 **Kassiopeia Simulation of the FSCD Magnetic Trap**

2220 The trap developed for the FSCD experiment utilizes six current carrying coils, which
2221 surround a cylindrical tritium containment vessel (see Figure 4.1). Some critical aspects
2222 of the trap design include the total trapping volume, the maximum trap depth, the

¹<https://github.com/KATRIN-Experiment/Kassiopeia>

steepness of the trap walls, as well as the radial and azimuthal uniformity of the magnetic fields.

The volume of the FSCD trap is a cylindrically shaped region with a radius of 5 cm and a length of 15 cm resulting in a roughly 1 L total trap volume. The trap volume is an important design feature, because it sets the volume of the experiment that is potentially usable for CRES measurements. Trapping a larger volume allows one to observe a larger number of tritium atoms, which increases the statistical power and sensitivity of the neutrino mass measurement. Due to the cost of constructing magnets with large and uniform magnetic fields it is important that the trap use as much of the available volume as possible to limit the overall cost of the experiment.

Coil	Radius (mm)	Z Pos. (mm)	Current (A×Turns)
1	50.0	-92.3	750.0
2	50.1	-56.9	-220.3
3	68.5	-19.5	-250.0
4	68.5	19.5	-250.0
5	50.1	56.9	-220.3
6	50.0	92.3	750.0

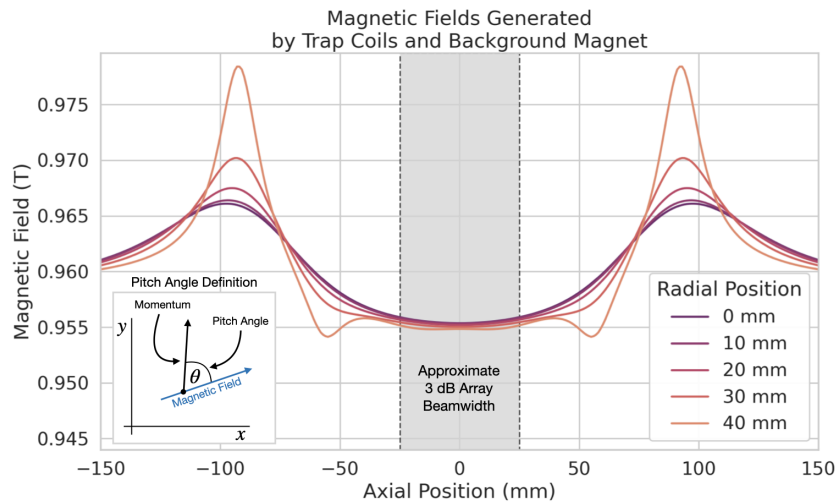
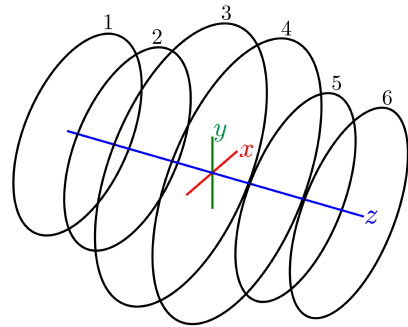


Figure 4.1. The geometry and parameters of the coils used to simulate the FSCD magnetic trap in Kassiopéia. Some axial profiles of the magnetic trap at different radial positions are shown to demonstrate the shape of the magnetic field and trap depth as a function of position. Calculation of the magnetic field profiles was graciously done by René Reimann.

The depth of the FSCD trap is approximately 10 mT when measured along the central axis, which is sufficient to trap electrons with pitch angles as small as 84° . The trap depth factors into the efficiency of the experiment by directly controlling the range

of electron pitch angles that can be trapped. If a higher fraction of pitch angles are trapped then, in principle, more decay events can be observed. However, the signals from electrons with small pitch angles are typically significantly harder to detect than larger pitch angles when using an antenna array, which increases the likelihood of not detecting the first track of the CRES event and harms the energy resolution of the experiment.

The steepness of the trap walls as well as any non-uniformities in the magnetic field contribute to the total energy resolution of the CRES measurement by causing uncertainty in the relationship between an electron's kinetic energy and it's cyclotron frequency. When an electron is trapped, it oscillates back and forth along the trap z-axis (see Figure 4.1) unless it is produced with a pitch angle of exactly 90° [60]. As the electron is reflected from the trap walls it experiences a change in the total magnetic field, which causes a modulation in the cyclotron frequency. This change in magnetic field from the trap introduces a correlation between the pitch angle and kinetic energy parameters of the electron that can reduce energy resolution. In order to mitigate this effect it is important to make the trap walls as steep as possible.

Particle Trajectory Solutions

The magnetic fields solved by direct integration of the electron's current density can be used by Kassiopeia to solve for the trajectory of electrons based on user specified initial conditions. Various distributions are available within Kassiopeia that can be sampled in order to replicate realistic event statistics, including uniform, Gaussian, and Lorentzian among others. In general, an electron has six kinematic parameters that define its trajectory, which are the three-dimensional coordinates of the initial position and the three components of the electron's momentum vector. However, when simulating CRES events it is more common to parameterize the electron's trajectory in terms of it's initial position, the kinetic energy, the pitch angle, and the initial direction of the component of the electron's momentum perpendicular to the magnetic field. This parameterization is completely equivalent to specify each component of the electrons initial position and momentum vectors.

From the initial parameters of the electron and the magnetic field, Kassiopeia solves for the trajectory of the electron. The direct approach proceeds by solving the motion of the electron using the Lorentz force equation, which takes the form of a set of differential equations

$$\frac{d\mathbf{r}}{dt} = \frac{\mathbf{p}}{\gamma m} \quad (4.6)$$

$$\frac{d\mathbf{p}}{dt} = e(\mathbf{E} + \frac{\mathbf{p} \times \mathbf{B}}{\gamma m}), \quad (4.7)$$

where \mathbf{r} is the position of the electron, \mathbf{p} is the electron's momentum, e is the charge of the electron, m is the electron's mass, and γ is the relativistic Lorentz term. To account for kinetic energy losses from radiation Kassiopeia includes an additional term in the momentum differential equation, which calculates the change in the electron's momentum induced by synchrotron radiation. Kassiopeia solves this pair of differential equations using numerical integration, however, the exact trajectory can be computationally intensive to solve. If the adiabatic approximation can be applied, then Kassiopeia can make use of a simpler set of equations that can be more readily solved numerically.

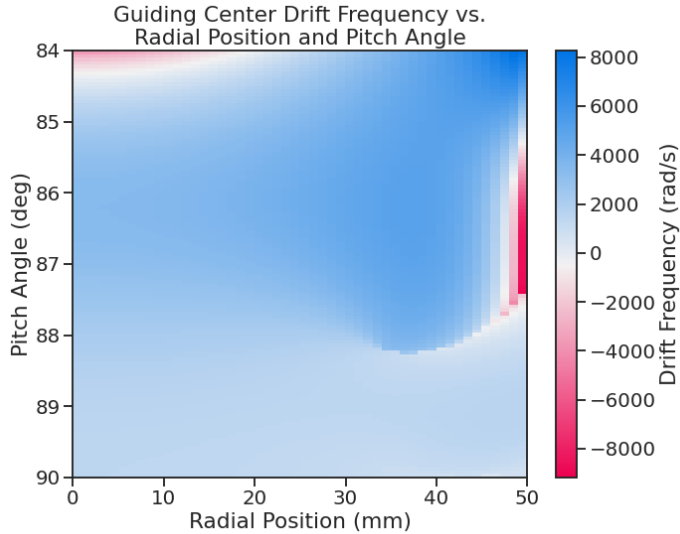


Figure 4.2. A map of the average ∇B -drift frequency for electrons trapped in the prototype FSCD trap shown in Figure 4.1. Negative drift frequencies indicate electrons that are drifting opposite to the standard direction, which means that they are close to escaping the magnetic trap.

Even though Kassiopeia is not directly capable of simulating the cyclotron radiation, it is still an invaluable CRES simulation tool, due to the accurate trajectory solutions for electrons in magnetic traps. With Kassiopeia it is possible to test the efficiency of a particular trap design and analyze features of the electron trajectories that are important to the position, track, and event reconstruction algorithms (see Section 4.3). One example of this for the FSCD is the analysis of the average ∇B -drift frequency as a function of the electrons radial position and pitch angle in the magnetic trap (see Figure 4.2). Radial gradients in the trap cause the guiding center of the electron to drift around the center of

the magnetic trap with an average frequency on the order of 10^3 rad/s. This frequency, while slow compared to the length of a typical CRES time-slice, is large enough to cause a significant loss in efficiency of certain signal reconstruction algorithms. Therefore, it is important to model the drift of the electron in the reconstruction algorithm in order to mitigate the effects of this motion on the reconstruction.

4.2.2 Locust

The Locust² software package [61] is the primary simulation tool developed and used by the Project 8 collaboration for CRES experiments. Locust simulates the responses of antennas and receiver electronics chain to rapidly time-varying electric fields using a flexible approach that allows one to choose from a variety of electric field sources and antennas. Similarly, one can simulate the receiver chain using a series of modular generators that include standard signal processing operations such as down-mixing and fast Fourier transforms (FFT). Since the primary focus of this chapter is the application of Locust to analyses of the FSCD, we shall describe only the most relevant aspects of the software rather than provide a comprehensive description.

Cyclotron Radiation Field Solutions

Simulating CRES events in the FSCD requires that we calculate the electric fields produced by the acceleration of the electron. In the general case, this can be a complicated question to answer, due to back-reaction forces on the electron from its own electric fields that occur when the electron is surrounded by conductive material such as a waveguide or cavity. However, in the case of the FSCD it is possible to ignore such effects and approximate the electron as radiating into a free-space environment.

The equations that describe the electromagnetic fields from a relativistic moving point particle are the Liénard-Wiechert field equations [62, 63], which are obtained by differentiating the Liénard-Wiechert potentials. In their full form the Liénard-Wiechert field equations are

$$\mathbf{E} = e \left[\frac{\hat{n} - \boldsymbol{\beta}}{\gamma^2(1 - \boldsymbol{\beta} \cdot \hat{n})^3 |\mathbf{R}|^2} \right]_{t_r} + \frac{e}{c} \left[\frac{\hat{n} \times [(\hat{n} - \boldsymbol{\beta}) \times \dot{\boldsymbol{\beta}}]}{(1 - \boldsymbol{\beta} \cdot \hat{n})^3 |\mathbf{R}|} \right]_{t_r} \quad (4.8)$$

$$\mathbf{B} = [\hat{n} \times \mathbf{E}]_{t_r}, \quad (4.9)$$

²https://github.com/project8/locust_mc/tree/master

2310 where e is the charge of the particle, \hat{n} is the unit vector pointing from the particle to the
 2311 position where the fields are calculated, β and $\dot{\beta}$ are the velocity and acceleration of the
 2312 particle divided by the speed of light (c), \mathbf{R} is the distance from the particle to the field
 2313 calculation position, and γ is the relativistic Lorentz term. The subscript t_r indicates
 2314 that the equations must be evaluated at the retarded time so that the time-delay from
 2315 the travel time of the electromagnetic radiation is correctly accounted for.

2316 The only required input to calculate the electric field at the position of an FSCD
 2317 antenna is the velocity and acceleration of the electron, which can be obtained from
 2318 Kassiopeia simulations. Therefore, when simulating a CRES event Locust first runs a
 2319 Kassiopeia simulation of the electron and calculates the electric field incident on the
 2320 antenna. The only difficulty with this approach is the determination of the retarded time.
 2321 The retarded time corresponds to the time that a photon, which has just arrived at an
 2322 antenna at the space-time position (t, \mathbf{r}) , was actually emitted by the electron at the
 2323 space-time position of $(t_r, \mathbf{r}_e(t_r))$. Defined in this way, finding the retarded time requires
 2324 solving

$$c(t - t_r) = |\mathbf{r} - \mathbf{r}_e(t_r)|, \quad (4.10)$$

2325 where the distance traveled by the photon between the measurement and retarded times
 2326 is equal to the distance between the antenna and the electron at the retarded time.
 2327 Locust solves Equation 4.10 using a built-in root finding algorithm to find the retarded
 2328 time, and thus the electric field produced by the electron at the position of each antenna
 2329 in the FSCD array.

2330 Antenna Response Modeling

2331 With the electric field it is possible, in principle, to calculate the resulting voltages pro-
 2332 duced in the antenna. However, direct simulation of the antenna itself is computationally
 2333 expensive since it would require the modeling of complex interactions of the electron's
 2334 electric fields with charge carriers in the conductive elements of the antenna. Direct
 2335 simulation of the antenna in Locust can be avoided by modeling the antenna response
 2336 using the antenna factor, or antenna transfer function, approach. The antenna factor
 2337 defines the voltage produced in the antenna terminal for an incident electric field [64],

$$A_F = \frac{V}{|\mathbf{E}|}, \quad (4.11)$$

2338 where V is the voltage and $|\mathbf{E}|$ is the magnitude of the incident electric field. To obtain the
 2339 antenna factor for the antennas developed for the FSCD Project 8 employs Ansys HFSS.
 2340 HFSS is a commercially available finite element method electromagnetic solver widely
 2341 used throughout the antenna engineering industry [65]. HFSS is capable of calculating
 2342 the antenna factor and gain patterns for complex antenna designs and outputting the
 2343 resulting quantities in the form of a text file that can be used as an input to the Locust
 2344 simulation.

2345 The antenna factor defines the steady-state response of the antenna to electromagnetic
 2346 plane waves and is a function of the frequency of the radiation. Therefore, in order to
 2347 apply the transfer function for the calculation of the antenna voltage response in the
 2348 time domain, Locust models the antenna as a linear time-invariant system [66]. In this
 2349 formalism the response of the system to the driving force is given by

$$y[n] = h * x = \sum_k h[k]x[n - k], \quad (4.12)$$

2350 where $y[n]$ is the discretely sampled response, x is the driving force stimulus, and h is
 2351 the finite impulse response (FIR) filter. When applied to the FSCD array, this formalism
 2352 calculates the voltage time-series produced in each antenna by convolving the electric
 2353 field time-series with the antenna FIR filter, which is obtained by performing a inverse
 2354 Fourier transform on the transfer function from HFSS.

2355 Radio-frequency Receiver and Signal Processing

2356 After obtaining the voltage time-series by computing the electron trajectory and antenna
 2357 response, Locust simulates the signal processing associated with the radio-frequency
 2358 receiver chain. The standard receiver chain used in Locust simulations of the FSCD
 2359 attempts to mimic the operations that would actually occur in hardware (see Figure 4.3).

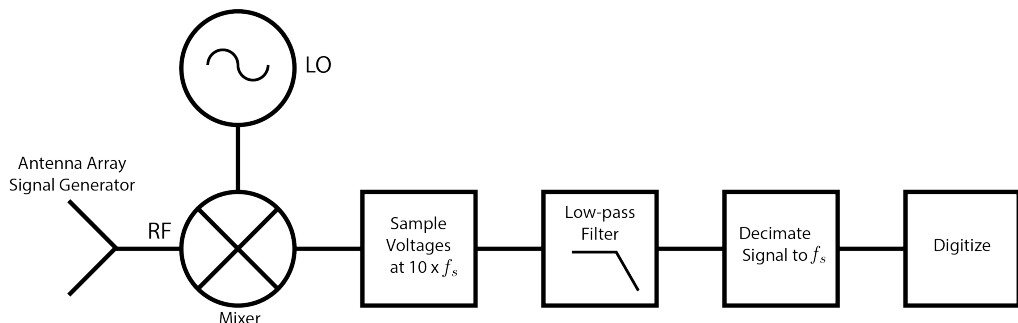


Figure 4.3. The receiver chain used by Locust when simulating CRES events in the FSCD.

2360 Frequency down-conversion is used in the FSCD to reduce the digitization bandwidth
 2361 required to read-out CRES data. According to the Nyquist sampling theorem [67], the
 2362 minimal sampling rate that guarantees no information loss for a signal with a bandwidth
 2363 Δf is given by

$$f_{\text{Nyq}} = 2\Delta f. \quad (4.13)$$

2364 The total bandwidth of CRES signal frequencies from tritium beta-decay ranges from 0
 2365 to 26 GHz in a 0.95 T magnetic field, therefore, direct digitization of CRES signals from
 2366 the FSCD would require sampling frequencies greater than 50 GHz, which is infeasible for
 2367 a real experiment. However, for the purposes of neutrino mass measurement we are only
 2368 interested in measuring the shape of the spectrum in the last 100 eV, which corresponds
 2369 to a frequency bandwidth of 5 MHz. Down-conversion is a technique for reducing the
 2370 base frequencies of signals in a bandwidth given by $[f_{\text{LO}}, f_{\text{LO}} + \Delta f]$ to the bandwidth
 2371 $[0, \Delta f]$, by performing the following multiplication

$$x(t) \rightarrow x(t)e^{-2\pi f_{\text{LO}} t}. \quad (4.14)$$

2372 In down-conversion the signal ($x(t)$) is multiplied by a sinusoidal signal with frequency
 2373 f_{LO} to reduce the absolute frequencies of the signals in the bandwidth. In the FSCD this
 2374 allows us to detect events in the last 100 eV of the tritium spectrum while sampling the
 2375 data far below 50 GHz. The standard bandwidth used in the FSCD is 200 MHz, which
 2376 allows for higher frequency resolution than the minimum sampling frequency for 100 eV
 2377 of energy bandwidth.

2378 Trying to directly simulate down-conversion with a frequency multiplication in Locust
 2379 would require the sampling of the electric fields at each antenna in the FSCD array with
 2380 a period of ≈ 20 ps, which is extremely slow computationally. To avoid this Locust
 2381 performs the down-conversion by intentionally under-sampling the electric fields with
 2382 a frequency of 2 GHz. Sampling below the Nyquist limit causes the higher frequency
 2383 components of the CRES signal to alias, however, Locust can remove these aliased
 2384 frequency peaks using a combination of low-pass filtering and decimation to recreate
 2385 frequency down-conversion. After filtering and decimation, Locust simulates digitization
 2386 by an 8-bit digitizer at a sampling frequency of 200 MHz to recreate the conditions of
 2387 the FSCD. The voltage offset and the digitizer range must be configured by the user
 2388 based on the characteristics of the simulation.

2389 **Data**

2390 The output of Locust simulations for the FSCD primarily consists of two data files. The
2391 first is the electron trajectory information calculated by Kassiopiea, which is output in
2392 the form of a `.root` file [68]. This file contains important kinematic information about
2393 the electron such as it's position and pitch angle as a function of time. The other file is
2394 produced by Locust and it contains the digitized signals acquired from each antenna in
2395 the FSCD array. The Locust output files conform to the Monarch specification developed
2396 by Project 8, which is based on the commonly used HDF5 file format, and matches the
2397 format of the files produced by the Project 8 data acquisition software. This makes it
2398 possible to use the same data analysis code to analyze both simulated and real data.

2399 **4.2.3 CRESana**

2400 Locust is the primary simulation tool used by Project 8 in the development and simulation
2401 of the FSCD. However, simulations of CRES events in larger antenna arrays (≥ 100
2402 antennas) using Locust can take several hours to complete, which is prohibitively long
2403 when one is performing a sensitivity analysis for a large scale antenna experiment. One
2404 of the reasons for Locust's slow operation is that the electric fields from the electron
2405 must be solved numerically for each time-step for each of the antennas in the array.
2406 These numerical solutions allow Locust to accurately simulate the electric fields from
2407 arbitrarily complicated electron trajectories at the cost of more computations and slower
2408 simulations. Therefore, an additional simulation tool that sacrifices some accuracy for
2409 computational efficiency would be extremely useful simulations and sensitivity analyses
2410 of larger antenna array experiments.

2411 To fill this need, Project has developed a new simulations package called CRESana³,
2412 specifically designed to perform analytical simulations of antenna array based CRES
2413 experiments. CRESana is not as flexible as Locust, but it provides a significant increase
2414 in simulation speed. It does this by using well-justified analytical approximations of the
2415 electrons motion in the magnetic field and the resulting electric fields from the electron's
2416 acceleration. The electric fields and signals generated by CRESana are consistent with
2417 theoretical calculations of the electron's radiation, and are test for accuracy using
2418 well-known test-case simulations and consistency checks.

³<https://github.com/MCFlowMace/CRESana>

2419 4.3 Signal Detection and Reconstruction Techniques for 2420 Antenna Array CRES

2421 Antenna Array CRES Signal Reconstruction

2422 A robust set of FSCD simulation tools are vital to the development of the analysis
2423 algorithms necessary for antenna array CRES to succeed. In order to perform CRES
2424 measurements using an antenna array, one must develop an algorithm that uses the
2425 multi-channel time-series obtained by digitizing the array to estimate the starting kinetic
2426 energies of electrons produced in the magnetic trap. This procedure consists of a multi-
2427 stage process of detecting a CRES signal then estimating the parameters of the electron
2428 that produced and is often referred to as simply CRES signal reconstruction.

2429 Compared with the signal reconstruction approaches of the Phase I and II CRES
2430 experiments, antenna array CRES requires a significantly different approach to signal
2431 reconstruction. In Phase I and II, CRES was performed using a waveguide gas cell that
2432 could be directly connected to a waveguide transmission line. The transmission line
2433 efficiently transmits the cyclotron radiation along it's length to an antenna at either end
2434 of the waveguide. However, with an antenna array the electron is essentially radiating
2435 into free-space, therefore, the cyclotron radiation power collected by the array is directly
2436 proportional to the solid angle surrounding the electron that is covered with antennas.
2437 Because it is not practical to fully surround the magnetic trap with antennas, some of the
2438 cyclotron radiation power that would have been collected by the waveguide escapes into
2439 free-space. Furthermore, the power that is collected by the antenna array is split between
2440 every channel in the antenna array, which significantly lowers the signal-to-noise ratio
2441 (SNR) of CRES signals in a single antenna channel compared to a waveguide apparatus.
2442 Therefore, a suite of completely new signal reconstruction techniques are needed in order
2443 to perform CRES in the FSCD.

2444 Changes to the approach to CRES signal reconstruction are also motivated by the
2445 more ambitious scientific goals of the FSCD experiment. A measurement of the tritium
2446 beta-decay spectrum that is sensitive to neutrino masses as small as 40 meV requires that
2447 we measure the kinetic energies of individual electrons with a total energy broadening
2448 of 115 meV [69]. This resolution includes all sources of uncertainty in the electron's
2449 kinetic energy such as magnetic field inhomogeneities. This level of energy resolution is
2450 compatible only with an event-by-event signal reconstruction approach where the kinetic
2451 energies, pitch angles, and other parameters of the CRES events are estimated before

2452 constructing the beta-decay spectrum.

2453 The event-by-event approach is distinct from the analysis done for the Phase I and
2454 Phase II experiments where only the starting cyclotron frequency of the event was
2455 estimated by analyzing the tracks formed by the carrier frequency in the time-frequency
2456 spectrogram. These frequencies were then combined into a frequency spectrogram, which
2457 was converted to the beta-decay energy spectrum using an ensemble approach that
2458 averaged over all other event parameters. The ensemble approach to signal reconstruction
2459 results in poor energy resolution because other kinematic parameters such as pitch angle
2460 change the cyclotron carrier frequency due to changes in the average magnetic field
2461 experience by the electron, and it is therefore incompatible with the future goals of the
2462 Project 8 collaboration.

2463 Components of Reconstruction: Signal Detection and Parameter Estimation

2464 CRES signal reconstruction can be viewed as a two-step procedure consisting of signal
2465 detection followed by parameter estimation. In the former, one is concerned with
2466 identifying CRES signals in the data regardless of the signal parameters, whereas, in the
2467 latter one operates under the assumption that a signal is present and then estimates its
2468 parameters.

2469 More formally, signal detection is essentially a binary hypothesis test between the
2470 signal and noise data classes and parameter estimation describes a procedure of fitting a
2471 model to the observed data. While both of these processes are required for a complete
2472 reconstruction (see Figure 4.4), the focus of my work and this chapter is on the signal
2473 detection aspect of antenna array CRES signal reconstruction.

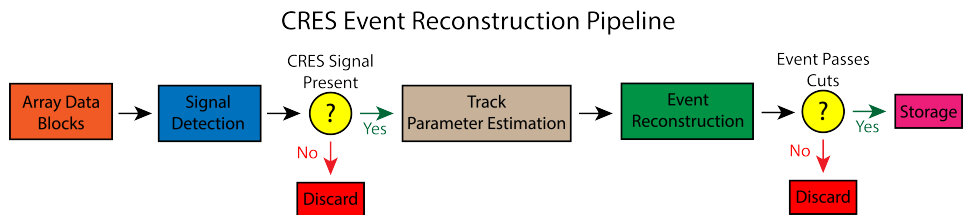


Figure 4.4. A high-level diagram depicting the process of CRES event reconstruction. The first step consists of identifying the presence of a signal in the data. This step is necessary to avoid the danger of performing a reconstruction of a false event, which would constitute a background contribution to the tritium spectrum measured by CRES.

2474 **Detection Theory**

2475 The problem of signal detection can be posed as a statistical hypothesis test [70]. For
2476 CRES signals, which are essentially vectors with added white Gaussian noise (WGN),
2477 one needs to choose between two hypotheses

$$\mathcal{H}_0 : \mathbf{y} = \boldsymbol{\nu} \quad (4.15)$$

$$\mathcal{H}_1 : \mathbf{y} = \mathbf{x} + \boldsymbol{\nu}, \quad (4.16)$$

2478 where \mathbf{y} is the CRES data vector, $\boldsymbol{\nu}$ is a sample of WGN, and \mathbf{x} represents the CRES
2479 signal. The hypothesis that the data contains only noise is labeled \mathcal{H}_0 and the hypothesis
2480 that the data contains a signal is labeled \mathcal{H}_1 .

2481 For illustrative purposes one can examine the case where one the first sample of
2482 data is used to distinguish between \mathcal{H}_0 and \mathcal{H}_1 . The value of the first data sample is
2483 distributed according to two gaussian distributions corresponding to \mathcal{H}_0 and \mathcal{H}_1 (see
2484 Figure 4.5). By setting a decision threshold on the value of this sample, one can choose
2485 the correct hypothesis with a probability given by the areas underneath the probability
2486 distribution curves. A true positive corresponds to correctly identifying that the data
2487 contains signal, whereas, a true negative means that one has correctly identified the data
2488 as noise. The rate at which the detector performs a true positive classification is given
2489 by the green region underneath $p(\mathbf{y}[0]; \mathcal{H}_0)$, and the rate at which the detector performs
2490 a true negative classification is given by the orange region underneath $p(\mathbf{y}[0]; \mathcal{H}_1)$. Two
2491 types of misclassifications are possible. Either we declare noise data as signal, which is
2492 call a false positive, or we declare signal data as noise, which is a false negative. Note
2493 that it is only possible to trade off these two types of errors by tuning the detection
2494 threshold. One cannot simultaneously reduce the rate of false positives without also
2495 increasing the rate of false negatives.

2496 The approach taken with CRES signals is to fix the rate of false positives by setting
2497 a minimum value for a detection threshold. The rate of false positives that is acceptable
2498 at the detection stage depends upon the rate of background events compatible with the
2499 sensitivity goals of the experiment. The ultimate goal of a neutrino mass measurement
2500 with 40 meV sensitivity in general has strict requirements on the number of background
2501 events, which requires a relatively high detection threshold to achieve. Consequently,
2502 the ideal signal detection algorithm is the one that achieves the maximum rate of true
2503 positives for a fixed rate of false positives, so that the detection efficiency of the experiment
2504 is maximized and potential sources of background are kept to a minimum.

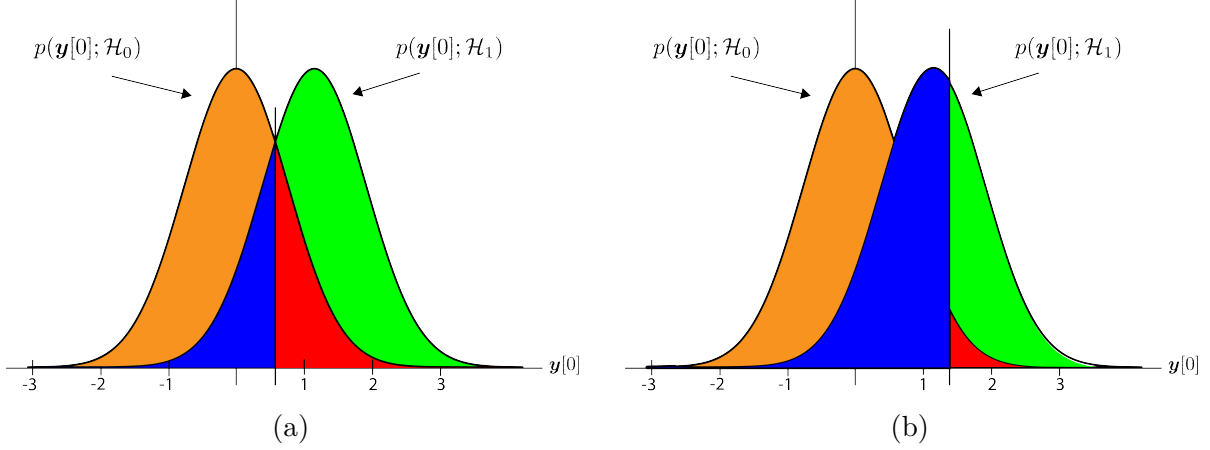


Figure 4.5. An illustration of two PDFs associated with a binary hypothesis test. The decision threshold is represented by the vertical line that partitions both distributions. The orange and red areas correspond to the true negative and false positive probabilities and the blue and green areas correspond to the false negative and true positive probabilities respectively. To decide between the two hypotheses we perform the likelihood ratio test specified by the Neyman-Pearson theorem. This approach achieves the highest true positive probability for a given false positive probability.

According to the Neyman-Pearson theorem [71], the statistical hypothesis test that maximizes the probability of detection for a fixed rate of false positives is the likelihood ratio test, which is formed by computing the ratio of the signal likelihood to the noise likelihood,

$$L(x) = \frac{P(\mathbf{y}; \mathcal{H}_1)}{P(\mathbf{y}; \mathcal{H}_0)} > \gamma. \quad (4.17)$$

Here, the likelihood of the hypotheses \mathcal{H}_0 and \mathcal{H}_1 are described by the probability distributions $P(\mathbf{y}; \mathcal{H}_0)$ and $P(\mathbf{y}; \mathcal{H}_1)$ respectively, and γ is the threshold for deciding \mathcal{H}_1 . The decision threshold is determined by integrating $P(\mathbf{y}; \mathcal{H}_0)$ such that

$$P_{\text{FP}} = \int_{\gamma}^{\infty} P(\tilde{\mathbf{y}}; \mathcal{H}_0) d\tilde{\mathbf{y}} = \alpha, \quad (4.18)$$

where α is the desired false positive detection rate given by the red colored areas shown in Figure 4.5. The true positive detection rate is given by the similar integral

$$P_{\text{TP}} = \int_{\gamma}^{\infty} P(\tilde{\mathbf{y}}; \mathcal{H}_1) d\tilde{\mathbf{y}}, \quad (4.19)$$

which corresponds to the green areas in Figure 4.5.

Changing the decision threshold allows one to trade-off between P_{TP} and P_{FP} as

2516 appropriate for the given situation. It is common to summarize the relationship between
 2517 P_{TP} and P_{FP} using the receiver operating characteristic (ROC) curve, which is obtained
 2518 by evaluating the true positive and false positive probabilities as a function of the decision
 threshold value (see Figure 4.6). The ROC curve provides a convenient way to compare

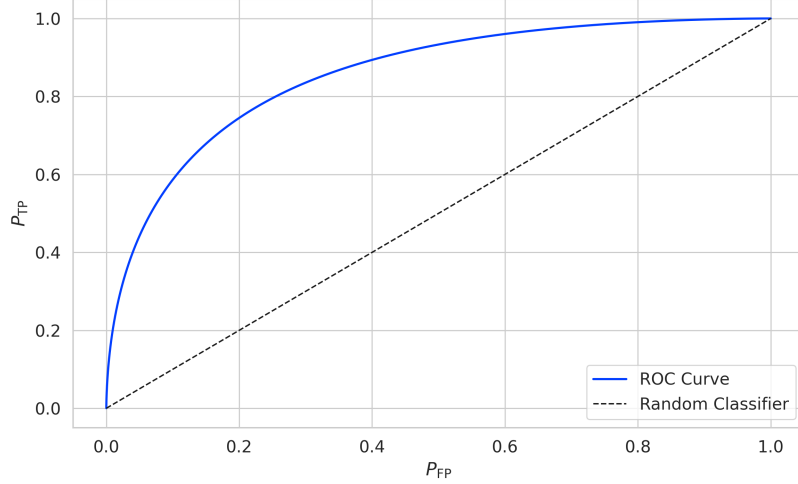


Figure 4.6. An example ROC curve formed by computing the P_{FP} and the P_{TP} for a given likelihood ratio test. As the decision threshold is increased P_{FP} decreases at the expense of a lower P_{TP} . The black dashed line indicates the lower bound ROC curve obtained by randomly deciding between \mathcal{H}_0 and \mathcal{H}_1 .

2519
 2520 the performance of different signal detection algorithms. In general, a classifier with
 2521 a higher the P_{TP} as a function of P_{FP} is desirable, which corresponds to a larger area
 2522 underneath the respective ROC curve. A perfect classifier has an area underneath the
 2523 curve of 1.0, however, such a classifier is almost never achievable in practice.

2524 **4.3.1 Digital Beamforming**

2525 **Introduction to Beamforming**

2526 Beamforming refers to a suite of antenna array signal processing techniques that are
 2527 designed to enhance the radiation or gain of the array in certain directions and suppress
 2528 it in other direction [64]. Beamforming is of interest to Project 8 as a first level of signal
 2529 reconstruction for the FSCD and other antenna array CRES experiments, which operates
 2530 at the signal detection stage of reconstruction.

2531 Beamforming is accomplished by performing a phased summation of the signals
 2532 received by the antenna array. The beamforming phases are chosen such that the signals

2533 emitted by the array will constructively interfere at the point of interest (see Figure
 2534 4.7). As a consequence of the principle of reciprocity [72], when the array is operating in
 2535 receive mode, the signals emitted from a source at the same point will constructively
 interfere when summed. The origin of the phase delays in beamforming is the path-

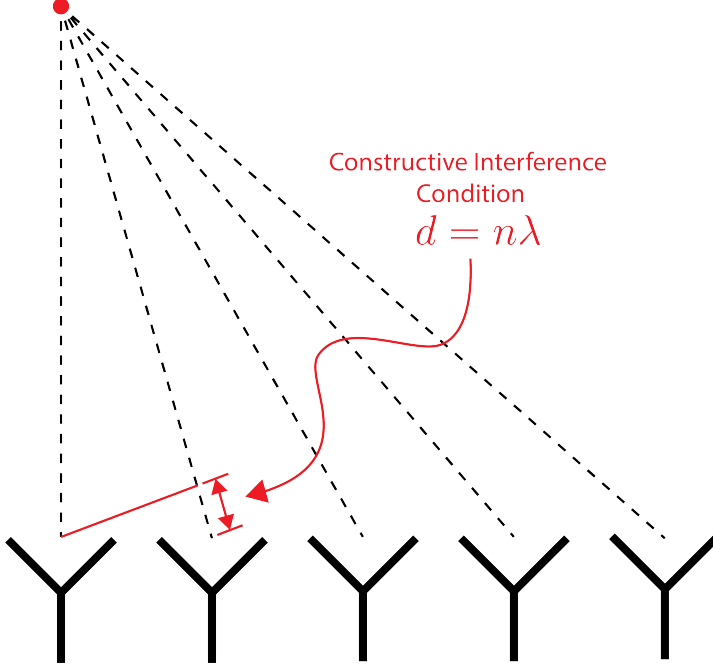


Figure 4.7. An illustration of the constructive interference condition which is the operating principle of digital beamforming using a uniform linear array as an example.

2536
 2537 length difference to the beamforming point between different antennas in the array. The
 2538 relationship between the phase delay and the path-length difference is given by the
 2539 familiar equation

$$\phi = \frac{2\pi d}{\lambda}, \quad (4.20)$$

2540 where ϕ is the phase delay, d is the path-length difference, and λ is the wavelength of
 2541 the radiation. In practice, one chooses the values of d by specifying the beamforming
 2542 positions of interest and then calculates the beamforming phases using Equation 4.20,
 2543 which is guaranteed to follow the constructive interference condition shown in Figure 4.7.

2544 Beamforming can be neatly expressed mathematically using the vector equation

$$y[n] = \Phi^T[n] \mathbf{x}[n], \quad (4.21)$$

2545 where $\mathbf{x}[n]$ is the array snapshot vector, $\Phi[n]$ is a vector of beamforming shifts, and
 2546 $y[n]$ is the resulting summed signal. The beamforming shifts consist of a set of complex

2547 numbers that contain the beamforming phase shift and an amplitude weighting factor,

$$\Phi[n] = [A_0[n]e^{-2\pi i \phi_0[n]}, A_1[n]e^{-2\pi i \phi_1[n]}, \dots, A_{N-1}[n]e^{-2\pi i \phi_{N-1}[n]}], \quad (4.22)$$

2548 where the set of magnitudes $A_i[n]$ are amplitude weighting factors and $\phi_i[n]$ are the phase
2549 shifts from the path-length differences. The index i is used to denote the antenna channel
2550 number. The amplitude weighting factor is the relative magnitude of the signal received
2551 by a particular antenna to the other antennas in the array, such that the antennas that
2552 receive signals with higher amplitude, due to being closer to the source, have more
2553 weight in the beamforming summation. The input and outputs signals beamforming
2554 are naturally expected to be functions of time as indicated by the index $[n]$, however, it
2555 is also possible to use time dependent beamforming phases that shift the beamforming
2556 position of the array over time.

2557 Digital beamforming is the type of beamforming algorithm of interest to Project 8 for
2558 CRES. Specifically, digital beamforming means that the beamforming phases are applied
2559 to the array signals in software rather than employing fixed beamforming phase shifts in
2560 the receiver chain hardware. The advantage of digital beamforming is that for a given
2561 series of array snapshots one can specify a large number of beamforming positions and
2562 effectively search for electrons by performing the beamforming summation associated
2563 with each point and applying a signal detection algorithm to identify the presence of a
2564 CRES signal.

2565 One of the most attractive features of digital beamforming is the spatial filtering
2566 effect, which is a direct consequence of the constructive interference condition used to
2567 define the beamforming phases. Spatial filtering allows for signals from multiple electrons
2568 at different positions in the trap to be effectively separated, because the constructive
2569 interference condition will force the signals from electrons at positions different from the
2570 beamforming position to cancel. This helps to reduce signal pile-up that could become
2571 an issue for large scale CRES experiments using a dense tritium source.

2572 The digital beamforming positions can be specified with arbitrary densities limited
2573 only by the available computational resources. This provides a very straight-forward way
2574 to estimate the position of the electron in the trap by using a dense grid of beamforming
2575 positions and maximizing the output power of the beamforming summation over this
2576 grid. This natural approach to position reconstruction is attractive due the requirements
2577 of an event-by-event signal reconstruction, which needs an accurate estimation of the
2578 exact magnetic field experienced by the electron in order to correctly estimate it's kinetic

2579 energy. Combined with an accurate map of the magnetic field inhomogeneities of the
 2580 trap obtained from calibrations, beamforming allows one to apply this magnetic field
 2581 correction with a spatial resolution that is a fraction of the cyclotron wavelength.

2582 **Laboratory Beamforming Demonstrations**

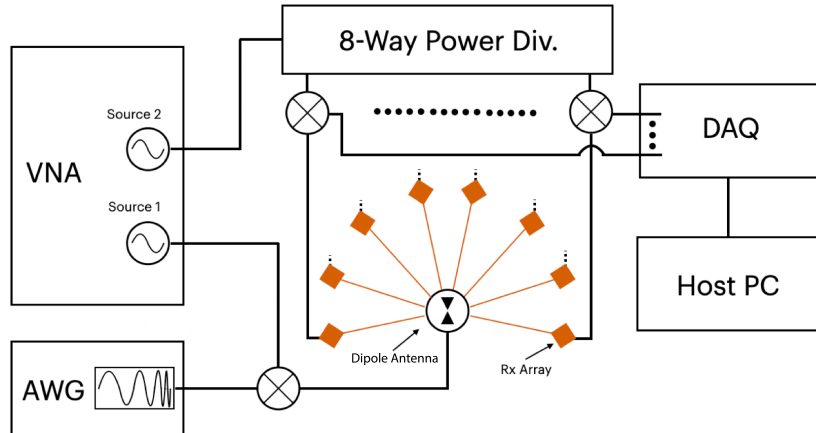


Figure 4.8. System level diagram of the laboratory setup used for beamforming demonstrations at Penn State. For more information on this system see Chapter 5. Signals near 26 GHz are fed to a dipole antenna using an arbitrary waveform generator (AWG) and vector network analyzer (VNA), which drive a mixer. The dipole radiation is collected by an array of antennas connected to the digitizer data acquisition (DAQ) system.

2583 As part of the development of antenna array CRES for the FSCD, an antenna
 2584 measurement setup was constructed at Penn State to serve as a testbed for antenna
 2585 prototypes and to perform laboratory validations of array simulations. This system
 2586 is discussed in more detail in Chapter 5. Early versions of the antenna measurement
 2587 system (see Figure 4.8 and Figure 4.9) were used to perform beamforming reconstruction
 2588 studies of a simple probe antenna to better understand the principles of beamforming
 2589 and confirm the estimated beamforming performance of Locust.

2590 Signals from an arbitrary waveform generator were up-converted to 26 GHz using a
 2591 mixer and a high-frequency source from a vector network analyzer and fed to the dipole
 2592 antenna through a balun. The radiation from the dipole antenna was received by an
 2593 array of horn antennas. The signals from the horn antennas were then down-converted
 2594 to baseband using a collection of mixers and an 8-way power divider. The signals were
 2595 then digitized and saved to a host computer for analysis.

2596 The data collected using the dipole and horn antenna array is reconstructed using the
 2597 beamforming reconstruction approach specified in Section 4.3.1. A two-dimensional grid

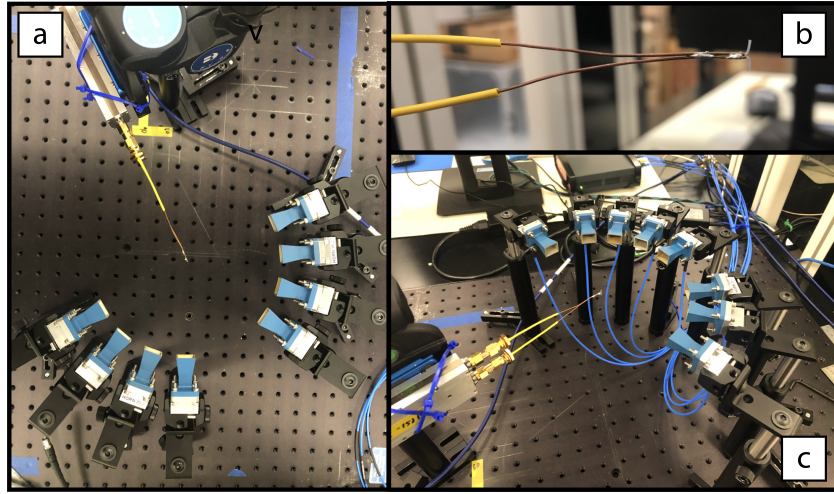


Figure 4.9. Photographs of the beamforming demonstration setup. In (a) I show a top-down view of the dipole antenna and the array of eight horn antennas. Manual repositioning of the horn antennas allows one to synthesize a full-circular antenna array. The dipole antenna is mounted on a camera tripod mount that allows for manual position tuning. (b) is a close up image of the dipole, which is manufactured from two segments of semi-rigid coaxial cable. (c) is another image of the dipole and array.

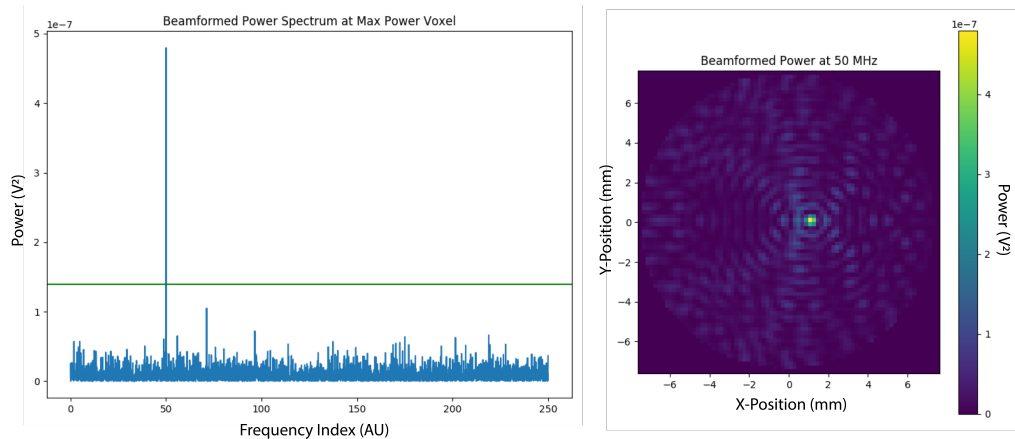


Figure 4.10. An example of digital beamforming reconstruction of a dipole antenna using a synthetic array of horn antennas. The beamforming image on the right is constructed by computing the time-averaged power of the summed signals for a two-dimensional grid of beamforming positions. In the image one can see a clear maximum that corresponds to the position of the dipole antenna. On the left I show the frequency spectrum of the time-series at the maximum power pixel. White gaussian noise is added to the signal to mimic a more realistic signal-to-noise-ratio. The signal emitted by the dipole is clearly visible as the high power peak in the frequency spectrum.

of xy-positions is defined and the beamforming phase shifts for each of these positions is calculated. The phased summation can be visualized by plotting the time-averaged power for each of the summations as a pixel in the resulting beamforming image (see Figure 4.10). White Gaussian noise (WGN) can be added to the data at this stage to simulate more realistic signal-to-noise ratios (SNR) if desired. The beamforming peak maxima is expected to have a Bessel function shape due to the circular symmetry of the array, and by analyzing the size of the beamforming maxima one can confirm that the beamforming reconstruction measurement has similar position resolution as expected from Locust simulations. Additionally, signal detection rates can be estimated from the data by comparing the magnitude of the beamforming signal peak in the frequency spectra to simulation.

FSCD Beamforming Simulations

Using Locust simulations of the FSCD one can perform beamforming reconstruction studies using the simulated CRES signal data. As we mentioned in the previous section, the beamforming procedure begins by specifying a set of beamforming positions and corresponding beamforming shifts. The beamforming positions form a grid that covers the region of interest in the field of view of the antenna array. There are effectively an infinite number of ways to specify the grid positions, however, uniform square grids are the most commonly used due to their simplicity. In the FSCD experiment the number and pattern of the grid positions would be optimized to cover the most important regions of the trap volume to maximize detection efficiency while minimizing superfluous calculations.

The beamforming grids used for signal reconstruction with the FSCD consist of a set of points that cover a region of the two-dimensional plane formed by the perimeter of the antenna array. The axial dimension is left out of the beamforming grid because the electrons are assumed to occupy only an average axial position, which corresponds to the center of the magnetic trap. This is because it is impossible to resolve the axial position of the electron as a function of time due to the rapid axial oscillation frequencies of trapped electrons relative to the FSCD time-slice duration.

After beamforming, a summed time-series is obtained for each beamforming position that can be evaluated for the presence of a signal using a detection algorithm. A beamforming image is a visualization method that is equivalent to arranging the beamforming grid points according to their physical locations to form a three-dimensional matrix where the first two dimensions encode the XY-position of the beamforming point and the third dimension contains the summed time-series. The image is formed by taking the

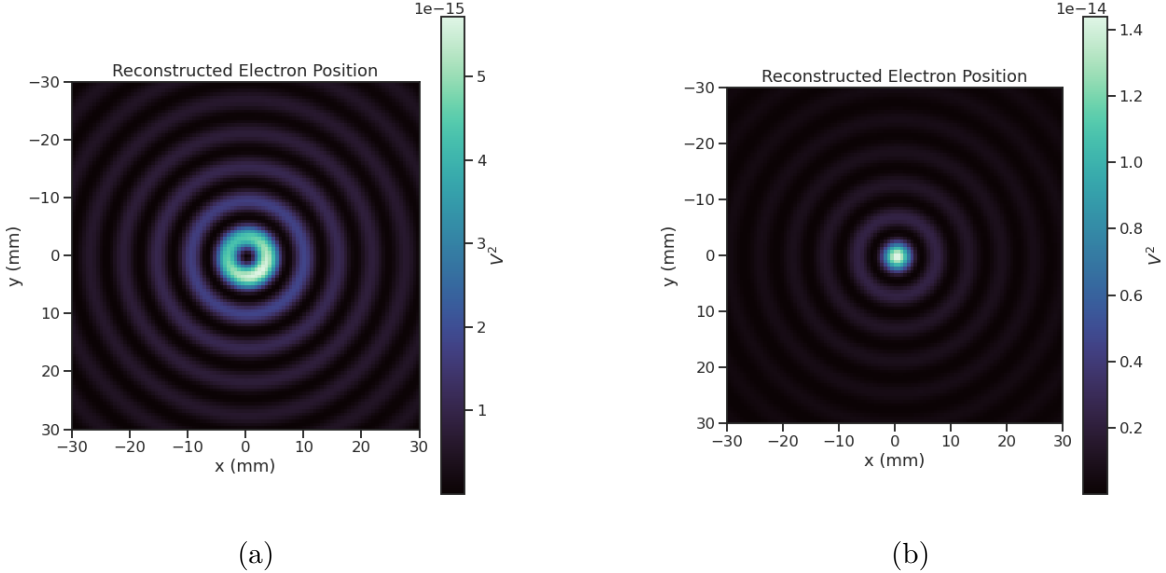


Figure 4.11. Beamforming images visualizing the reconstruction of an electron without (a) and with (b) the cyclotron phase correction. The images were generated using data from Locust simulations. The cyclotron phase refers to a phase offset equal to the relative azimuthal position of an antenna in the array. This phase offset is caused by the circular electron orbit and must be corrected for during reconstruction.

time-averaged power (see Figure 4.11). Beamforming images are purely for the purposes of visualization and are not particularly useful for signal detection or reconstruction.

If the beamforming phases consist only of the spatial phase component from Equation 4.20, then the resulting beamforming image contains a relatively high-power ring-shaped region that is centered on the position of the electron (see Figure 4.11a). The origin of this shape is an additional phase offset particular to a cyclotron radiation source. Essentially, the circular motion that produces the cyclotron radiation introduces a relative phase offset to the electric fields that is equal to the azimuthal position of the field measurement point. For example, if we have two antennas, one located at an azimuthal position of 0° and another located at an azimuthal position of 90° , then the CRES signals received by these antennas will be out of phase by 90° , which is the difference in their azimuthal positions. This phase offset can be corrected by adding an additional term to the beamforming phase equation that is equal to the azimuthal position of the antenna relative to the electron,

$$\phi_i[n] = \frac{2\pi d_i[n]}{\lambda} + \Delta\varphi_i[n], \quad (4.23)$$

where $\Delta\varphi_i$ is difference between the azimuthal position of the electron and the i -th antenna channel. Using the updated beamforming phases in the summation changes the

ring feature into a Bessel function peak whose maximum corresponds to the position of the electron. Including this cyclotron phase correction significantly improves the signal detection and reconstruction capabilities of beamforming by more than doubling the summed signal power and shrinking the beamforming maxima feature size.

The beamforming image examples in Figure 4.11 were produced using an electron located on the central axis of the magnetic trap, which do not experience ∇B -drift. However, for electrons produced at non-zero radial position the beamforming phases must be made time-dependent in order to track the position of the electron's guiding center over time. Without this correction the ∇B -drift causes the electron to move between beamforming positions, which effectively spreads the cyclotron radiation power over a wider area in the beamforming image (see Figure 4.12). This effect significantly

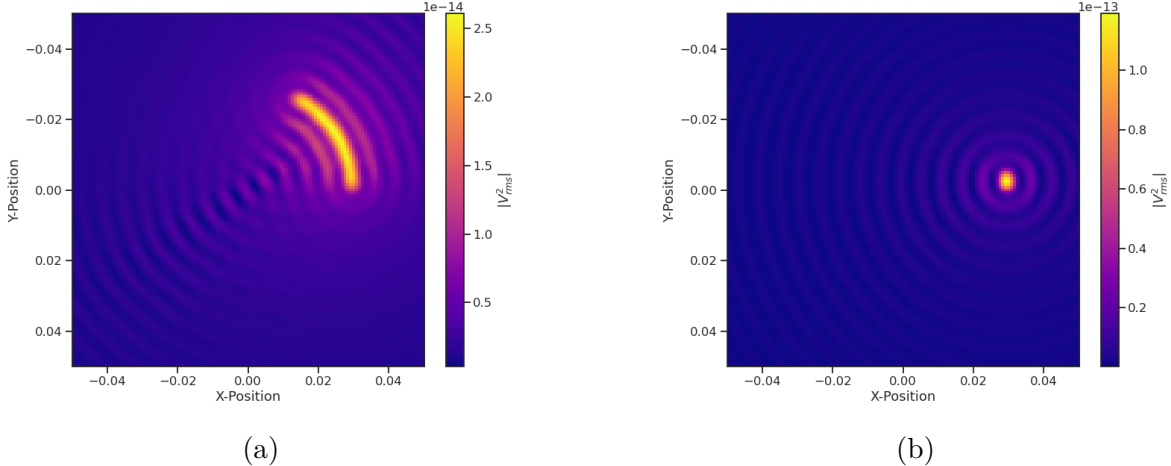


Figure 4.12. Beamforming images visualizing the reconstruction of an electron located off the central axis of the FSCD trap. In (a) we performing beamforming without the ∇B -drift correction, and in (b) we include the ∇B -drift correction.

reduces the power of the beamforming maxima and increases the size of the beamforming features, simultaneously harming detection efficiency and position reconstruction.

The ∇B -drift correction simply adds a circular time-dependence to the beamforming positions as a function of time,

$$r[n] = r_0 \quad (4.24)$$

$$\varphi[n] = \varphi_0 + \omega_{\nabla B} t[n], \quad (4.25)$$

where $\omega_{\nabla B}$ is the drift frequency and $t[n]$ is the time vector. In the ideal case the ∇B -drift frequencies from Figure 4.2 for the correct pitch angle and radial position would be used,

however, it is not possible to know the electron's pitch angle a priori. In principle, one could perform multiple beamforming summations for a given beamforming position using different drift frequencies and choose the one that maximizes the summed power, but this approach leads to a huge computational burden that would be impractical for a real FSCD experiment. A compromise is to use an average value of $\omega_{\nabla B}$ obtained by averaging over the drift frequencies for electrons of different pitch angle at a particular radius. This approach keeps the computational cost of time-dependent beamforming to a minimum while still providing a significant increase in the detection efficiency of digital beamforming.

Signal Detection with Beamforming and a Power Threshold

Up to this point we have neglected any specific discussion of how digital beamforming is used for signal detection and reconstruction. This is because, strictly speaking, digital beamforming consists only of the phased summation of the array signals and cannot be used alone for signal detection. The example beamforming images shown in Figure 4.11 and Figure 4.12 were produced using simulated data that contained no noise, which significantly degrades the utility of analyzing the beamforming images for signal detection and reconstruction.

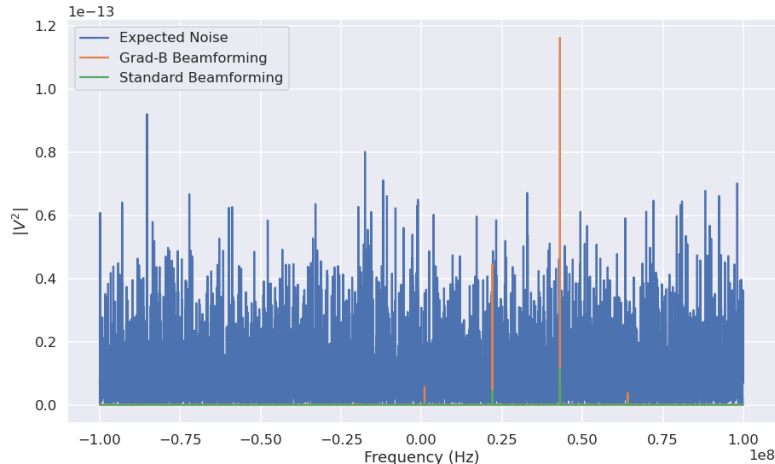


Figure 4.13. A plot of a typical frequency spectrum obtained by applying a Fourier transform to the time-series obtained from beamforming. The frequency spectra are plotted without noise on top of an example of a typical noise spectrum to visualize a realistic signal-to-noise ratio. In the example we see that without beamforming it would not be possible to detect anything since the signal amplitudes would be reduced by a factor of sixty relative to the noise. Additionally, we see that the ∇B -drift correction is needed to detect this electron since it comes from a simulation of an electron with a significant off-axis position.

2682 Digital beamforming as a detection algorithm is understood to mean digital beam-
 2683 forming plus a detection threshold placed on the amplitude of the frequency spectrum
 2684 obtained by applying a fast Fourier transform (FFT) to the summed time-series (see
 2685 Figure 4.13). This approach is most similar to the time-frequency spectrogram analysis
 2686 employed in previous CRES experiments, however, in principle any signal detection
 2687 algorithm could be used after the beamforming procedure. In Section 4.4 I analyze the
 2688 signal detection performance of the power threshold approach in detail.

2689 From the example frequency spectra in Figure 4.13 it is clear that without a re-
 2690 construction technique that coherently combines the signals from the full antenna our
 2691 ability to detect CRES signals will be drastically reduced. Because the CRES signals are
 2692 in-phase at the correct beamforming position the summed power increases as a function
 2693 of N^2 compared to a single antenna channel, where N is the number of antennas. It
 2694 is true that the noise power is also increased by beamforming, but, because the noise
 2695 is incoherent, its power only increases linearly. Consequently, the signal-to-noise ratio
 2696 (SNR) of the CRES signal increases linearly with the number of antennas, which greatly
 2697 improves detection efficiency compared to using only the information in a single antenna.

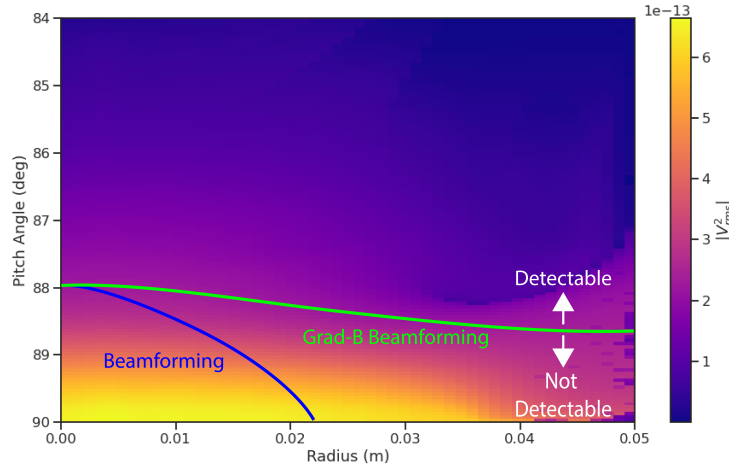


Figure 4.14. A plot of the total signal power received by the FSCD array from trapped electrons with different radial positions and pitch angles generated using Locust simulations. The lines on the plot indicate a 10 dB detection threshold above the mean value of the noise in the frequency spectrum. With static beamforming electrons with radial positions larger than about two centimeters are undetectable due to the change in the electron's position over time causing losses from beamforming phase mismatch. This is corrected by including ∇B -drift frequencies in the beamforming phases. Both beamforming techniques fail to detect electrons below $\approx 88.0^\circ$, since these signal are composed of several relatively weak sidebands that are comparable to the noise.

2698 The power threshold detection algorithm searches for high-power frequency bins that
 2699 should correspond to a frequency component of the CRES signal. In order to prevent
 2700 random noise fluctuations from being mistaken as CRES signals the power threshold
 2701 must be set high enough so that it is unlikely that random noise could be responsible. A
 2702 consequence of this is that many electrons that can be trapped will go undetected because
 2703 the modulation caused by axial oscillations leads to the cyclotron carrier power to falling
 2704 below the decision threshold. The time-dependent beamforming used to correct for the
 2705 ∇B -drift increases the volume of the magnetic trap where electrons can be detected,
 2706 but it is ineffective at increasing the range of detectable pitch angles (see Figure 4.14).
 2707 Fundamentally, this is because the power threshold only uses a fraction of the signal
 2708 power to detect electrons and ignores the power present in the frequency sidebands. In
 2709 the subsequent sections I examine two other signal detection algorithms that seek to
 2710 improve the detection efficiency of the FSCD by utilizing the more of the signal shape to
 2711 compute the detection test statistics.

2712 **4.3.2 Matched Filtering**

2713 **Introduction to Matched Filtering**

2714 The problem of CRES signal detection is the problem of detecting a signal buried in
 2715 WGN, which has been examined at great depth in the signal processing literature [70].
 2716 For a fully known signal in WGN the optimal detector is the matched filter, which means
 2717 that it achieves the highest true positive rate for a fixed rate of false positives. The
 2718 matched filter test statistic is calculated by taking the inner product of the data with
 2719 the matched filter template

$$\mathcal{T} = \left| \sum_n h^\dagger[n] y[n] \right|, \quad (4.26)$$

2720 where $h[n]$ is the matched filter template and $y[n]$ is the data. The matched filter test
 2721 statistic defines a binary hypothesis test in which the data vector is assumed to be an
 2722 instance of two possible data classes. By setting a decision threshold on the value of \mathcal{T} ,
 2723 one can classify a given data vector as belonging to two distinct hypotheses. Under the
 2724 first hypothesis the data is composed of pure WGN, and under the second hypothesis the
 2725 data is composed of the known signal with additive WGN. The matched filter template

2726 is obtained by rescaling the known signal in the following way

$$h[n] = \frac{x[n]}{\sqrt{\tau \sum_n x^\dagger[n]x[n]}}, \quad (4.27)$$

2727 where τ is the variance of the WGN and $x[n]$ is the known signal. Strictly speaking,
2728 Equation 4.27 is only true for noise with a diagonal covariance matrix, however, in the
2729 context of the FSCD we are justified in assuming this to be true. Defining the matched
2730 filter templates in this way guarantees that the expectation value of \mathcal{T} is equal to one
2731 when the data contains only noise, which is the standard matched filter normalization in
2732 the signal processing literature.

2733 Although matched filters are canonically formulated in terms of a perfectly known
2734 signal, it is still possible to apply the matched filter technique given imperfect information
2735 about the signal provided that the signal is deterministic. From our discussion of CRES
2736 simulation tools for the FSCD (see Section 4.2) we know that the shape of CRES signals
2737 are completely determined by the initial parameters of the electron. The random collisions
2738 with background gas molecules which cause the formation of signal tracks are the only
2739 stochastic component of the CRES event after the initial beta-decay, therefore, it is
2740 possible to develop a matched filter for the detection of CRES signal tracks which are fully
2741 determined by the parameters of the electron after the initial beta-decay or subsequent
2742 collision events.

2743 The matched filter test statistic for CRES signals is a modified version of Equation
2744 4.26

$$\mathcal{T} = \max_{\mathbf{h}, m} |\mathbf{h} * \mathbf{y}| = \max_{\mathbf{h}, m} \left| \sum_k h^\dagger[k]x[m - k] \right|, \quad (4.28)$$

2745 where the matched filter inner product has been replaced with a convolution operation
2746 and a maximization over the template and convolution delay (m). Replacing the inner
2747 product with a convolution accounts for the fact that the start time of the CRES signal is
2748 now an unknown parameter, in addition, we now perform a maximization of the matched
2749 filter convolution over a number of different templates. Because the shape of the signal is
2750 unknown we are forced to guess a number of different signal shapes to create a template
2751 bank with which we can identify unknown signals by performing an exhaustive search.

2752 The template bank approach to matched filtering, while quite powerful, can quickly
2753 become computationally intractable. This is especially true in the case of the FSCD
2754 because of the large amount of raw data produced by the array that must be analyzed.
2755 Specifically, the time-domain convolution specified by Equation 4.28 is particularly

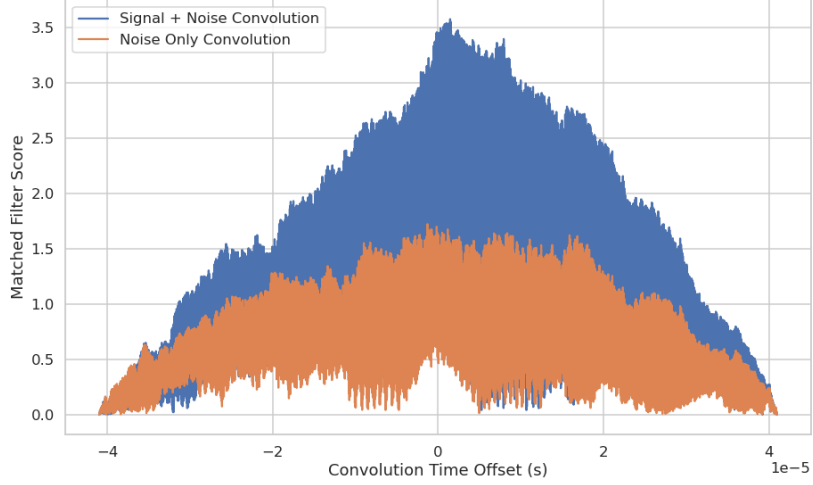


Figure 4.15. Example of a convolution of a CRES signal template with a segment of noisy data. A simulated CRES signal was simulated using Locust and normalized to create a matched filter template. When this template is convolved with noisy data the contains the matching signal the convolution output increases dramatically compared to data with only noise. The decreasing convolution output as the time offset of the convolution increases is caused by zero-padding of the data and template.

2756 computationally intensive and is a major barrier towards the implementation of a
 2757 matched filter for signal detection in an experiment like the FSCD. This can be avoided
 2758 by using the convolution theorem to replace the time-domain convolution with an inner
 2759 product in the frequency domain.

2760 The convolution theorem states that

$$\mathbf{f} * \mathbf{g} = \mathcal{F}^{-1}(\mathbf{F} \cdot \mathbf{G}) \quad (4.29)$$

2761 where \mathbf{f} and \mathbf{g} are discretely sampled time-series, \mathbf{F} and \mathbf{G} are the respective discrete
 2762 Fourier transforms, and \mathcal{F}^{-1} is the inverse discrete Fourier transform operator. The
 2763 convolution theorem allows us to perform the matched filter convolution by first com-
 2764 puting the Fourier transform of the template and data, then performing a point-wise
 2765 multiplication of the two frequency series, and finally performing the inverse Fourier
 2766 transform to obtain the convolution output. Because discrete Fourier transforms can be
 2767 performed extremely efficiently, the convolution theorem is almost always used in lieu of
 2768 directly computing the convolution.

2769 One thing to note here is that the convolution theorem for discrete sequences shown
 2770 here, is technically valid only for circular convolutions, which is not directly specified
 2771 in Equation 4.28. However, because typical CRES track lengths are much longer than

2772 the Fourier analysis window and also that the frequency chirp rates are small compared
2773 to the time-slice duration, it is relatively safe to use circular convolutions to evaluate
2774 matched filter scores for CRES signals, which allows us to apply the convolution theorem
2775 to compute matched filter scores using the frequency representation of the data and
2776 matched filter template.

2777 Matched Filter Analysis of the FSCD

2778 The optimality provided by the matched filter makes it a useful algorithm for analysis
2779 of CRES experiment designs for sensitivity analyses, since it indicates the best possible
2780 detection efficiency achievable by an experiment configuration. The standard approach to
2781 performing these studies involves generating a large number of simulated electron signals
2782 that span the kinematic parameter space of electrons in the magnetic trap. In general,
2783 electrons have six kinematic parameters along with an additional start time parameter.

2784 In order to limit the number of simulations required to evaluate the detection efficiency
2785 the standard approach is to fix the starting axial position, starting azimuthal position,
2786 starting direction of the perpendicular component of the electron's momentum, and event
2787 start time to reduce the parameter space to starting radial position, starting kinetic
2788 energy, and starting pitch angle. The fixed variables are true nuisance parameters that do
2789 not affect the detection efficiency estimates for the FSCD design, because they manifest
2790 as phases which are marginalized during the calculation of the matched filter score.

2791 Across radial position, kinetic energy, and pitch angle one defines a regular grid of
2792 parameters and uses Locust to simulate the corresponding signals (see Figure 4.16). This
2793 grid of simulated signals can be used to estimate the likelihood of detecting signals,
2794 because the matched filter score specifies the shape of the PDF that defines the detection
2795 probability and the size of the template bank influences the likelihood of a good match
2796 between a template and a random signal.

2797 The matched filter approach can also be used to estimate the achievable energy
2798 resolution of the experiment by using a dense grid of templates generated with parameters
2799 close to the unknown signal (see figure 4.17). Because matched filter templates with
2800 similar parameters have signal shapes that are also similar, templates with incorrect
2801 parameters can have nearly identical matched filter scores as the correct template. Since
2802 only one sample of noise is included in a sample of real data, one cannot guarantee that
2803 the best matching template corresponds to the ground truth parameters of the signal.
2804 This introduces uncertainty into the signal parameter estimation that manifests as an
2805 energy broadening. Dense grids of matched filter templates allows one to quantify this

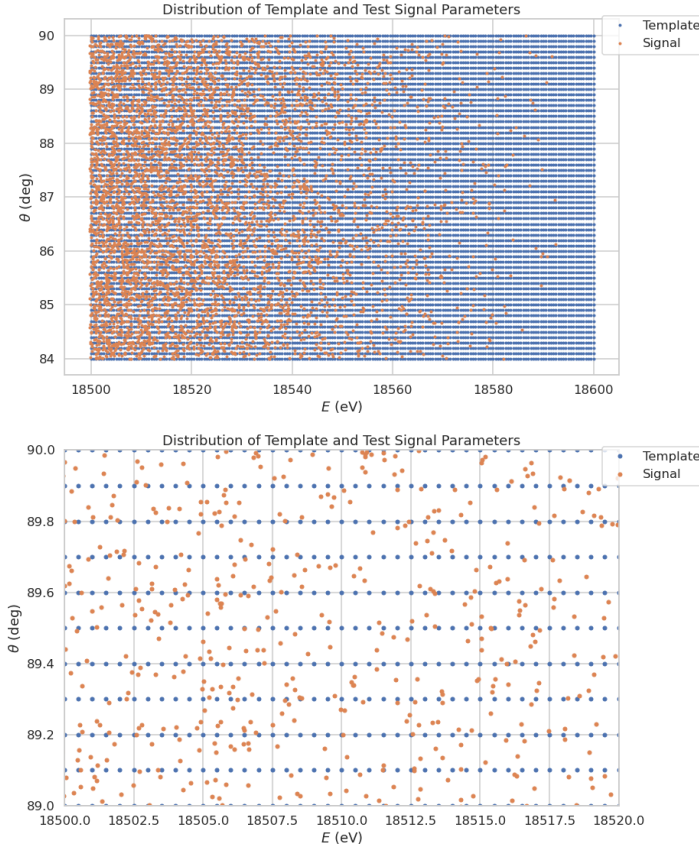


Figure 4.16. An example two-dimensional parameter distribution of a matched filter template bank and random test signals. θ refers to the pitch angle of the electron and E is the kinetic energy. The template bank forms a regular grid of in pitch angle and energy, whereas, the test signals are uniformly distributed in pitch angle and follow the tritium beta-decay kinetic energy distribution. This is why there are fewer test signals at higher energies. The need for high match across the full parameter space prevents one from reducing the density of templates in this low activity region. A zoomed in version of the template bank illustrates the relative density of templates and signals needed for match $> 90\%$.

broadening by analyzing the parameter space of templates with matched filter scores close to the ground truth. This approach is analogous to maximum likelihood estimation and is one key component of a complete sensitivity analysis for an antenna array CRES experiment.

A key parameter for describing the performance of a matched filter template bank at signal detection is match, which we define as the average ratio of the highest matched filter score for a random signal to the matched filter score for a perfectly matching

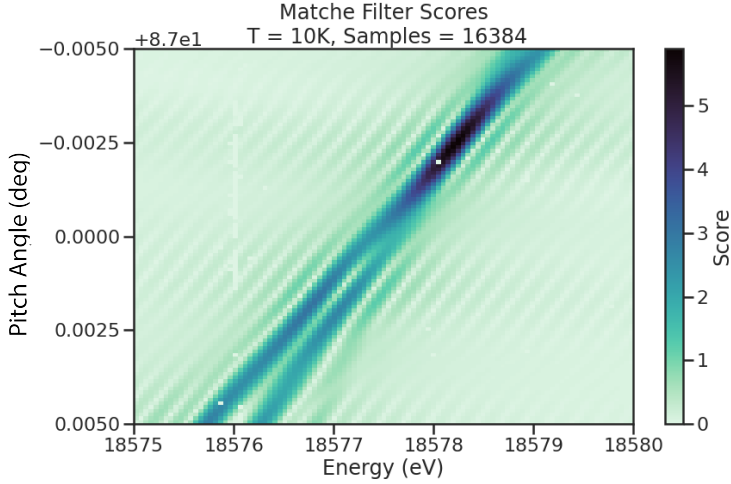


Figure 4.17. The matched filter scores of a dense grid of templates in pitch angle energy space. Dense template grids allow one to estimate the kinetic energy of the electron by identifying the best matching template. The uncertainty on this value is proportional to the space of templates that also match the test signal well. In the worst case matched filter templates can be completely degenerate where templates with different parameters match a signal with equal likelihood.

2813 template. In equation form this is

$$\text{Match} \equiv \Gamma = \frac{\mathcal{T}_{\text{best}}}{\mathcal{T}_{\text{ideal}}}, \quad (4.30)$$

2814 where $\mathcal{T}_{\text{best}}$ is the matched filter score of the best fitting template in the bank and $\mathcal{T}_{\text{ideal}}$ is
 2815 the hypothetical matched filter score one would measure if the signal perfectly matched
 2816 the template. Generally, one desires an average match as close to one as possible, however,
 2817 the average match value is an exponential function of the number of templates in the
 2818 template bank (see Figure 4.18). This behavior is observed for dense matched filter grids
 2819 like the one in Figure 4.17. A dense grid was used to calculate the average value of match
 2820 for different template bank sizes shown in Figure 4.18.

2821 The exponential relationship between match and template bank size is also evident
 2822 for template banks that cover a wide range of parameters, such as the template bank
 2823 visualized in Figure 4.16. Since no prior knowledge of the signal parameters is available,
 2824 one has no choice but to use a template bank that covers a large range of parameters for
 2825 signal detection. Achieving a high average match in this scenario can easily overwhelm
 2826 the available computational resources, so in practice only a limited number of templates
 2827 could be used at the detection stage. Therefore, accurately modeling the effects of match
 2828 is key to correct sensitivity calculations.

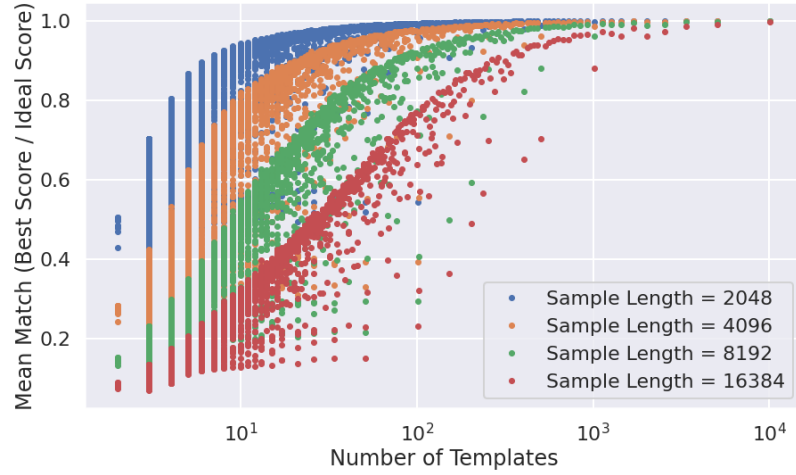


Figure 4.18. The mean match of the dense template grid shown in Figure 4.17 for different numbers of templates. Grids of different sizes were obtained by decimating a dense grid of templates and the average match for each grid was computed using the same set of randomly distributed test signals. Plotting the mean match against the size of the grid allows one to visualize the exponential relationship between match and template bank size. The noise in each curve is caused by sampling effects from the decimation algorithm. In general, longer templates are harder to than shorter templates.

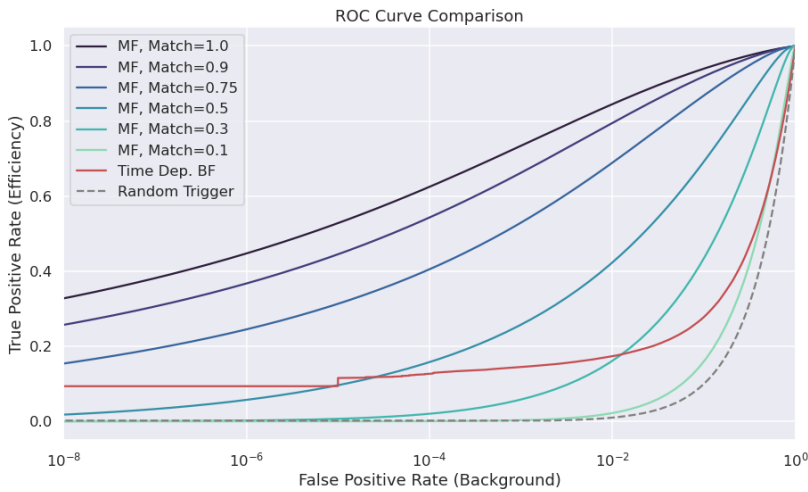


Figure 4.19. Matched filter template bank ROC curves as a function of mean match. One can see that for low match a matched filter is on average worse than the more straight forward beamforming detection approach.

2829 The effect of match on the detection efficiency of the matched filter template bank can
2830 be summarized using the ROC curve (see Figure 4.19). A single ROC curve is obtained
2831 by averaging over the PDFs that describe the detection probabilities of each individual
2832 template. The matched filter score for a template follows a Rician distribution with a
2833 mean value equal to the matched filter score multiplied by the match ratio between the
2834 template and signal. Therefore, the distribution that describes the average matched filter
2835 score when there is a signal in the data is obtained by averaging over the distributions
2836 for every template, whose expectation values are multiplied by the average match ratio.

2837 The distribution of the matched filter score when there is no signal in the data follows
2838 a Rayleigh distribution. Therefore, a trials penalty, which is the statistical penalty one
2839 pays for randomly checking many templates in order to avoid a random match between
2840 noise and a template, is included by computing the joint distribution of N_{template} Rayleigh
2841 distributions, where N_{template} is the size of the template bank. For more information on
2842 the calculation of matched filter template bank ROC curves please refer to Section 4.4.

2843 An alternative way to visualize the detection performance for each algorithm is to
2844 specify a minimum acceptable false positive rate at the trigger level. This is equivalent
2845 to specifying a minimum threshold on the value of the matched filter score or the size of
2846 a frequency peak for a beamforming power threshold trigger. One can then draw regions
2847 of detectable signals as a function of the electron's pitch angle and radial position (see
2848 Figure 4.20). A kinetic energy shift is equivalent to an overall frequency shift of the
2849 signal and should have no effect on the detection probability assuming sufficient density
2850 of matched filter templates in the energy dimension. A electron is declared "detectable"
2851 for the regions in Figure 4.20 if the signal has at least 50% probability of falling above the
2852 decision threshold of the respective classifier. One can see that the parameter space of
2853 detectable signals is greatly expanded beyond the beamforming power threshold trigger
2854 with a matched filter (MF) or deep neural network (DNN) (see Section 4.3.3). Plots such
2855 as Figure 4.20 are useful for visualization, but, since the handling of detection likelihood
2856 is not sufficiently rigorous, the detection probability boundaries are not well-suited to
2857 sensitivity estimates.

2858 **Optimized Matched Filtering Implementation for the FSCD**

2859 The biggest practical obstacle to the implementation of a matched filter template bank
2860 detection approach is oftentimes the computational cost associated with exhaustively
2861 calculating the matched filter scores of the template bank, and the FSCD is no exception
2862 in this regard. At a basic level computing a matched filter score requires the convolution

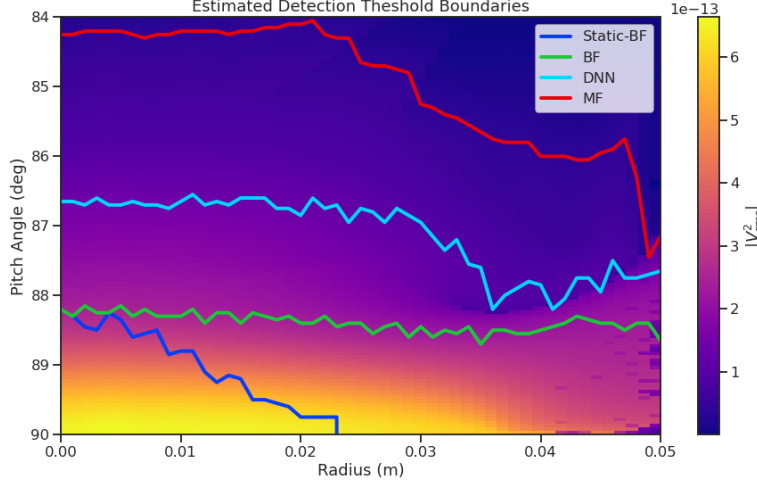


Figure 4.20. Boundaries of detectable electrons in pitch angle kinetic energy space for a series of different signal detection algorithms. A detectable signal is defined as a signal that is above a consistent decision with at least 50% probability. This non-rigorous treatment of detection probability is primarily useful for the visualization the relative increases in detection performance provided by the different algorithms. The static beamforming (Static-BF) algorithm is the digital beamforming algorithm introduced above without the ∇B -drift correction. The DNN algorithm refers to a convolutional neural network classifier trained to detect CRES signals (see Section 4.3.3).

of two vectors, which can be performed very efficiently by computers if the convolution theorem and fast Fourier transforms (FFT) are utilized. Furthermore, one can consider applying digital beamforming as a pre-processing step to reduce the dimensionality of the data before the matched filter is applied. In order to understand the relative gain in computational efficiency offered by these optimizations we analyze the total number of floating-point operations (FLOP) of several matched filter implementations in big O notation that utilize different combinations of optimizations.

A direct implementation of a matched filter as specified by Equation 4.28 involves the convolution of N_{ch} signals of length N_s with template signals of length N_t . As a uniform metric we shall compare the FLOP of the various matched filter implementations on a per-template basis, since each implementation scales linearly with the number of templates. The direct convolution approach to matched filtering costs

$$O(N_{\text{ch}}) \times O(N_s \times N_t) \quad (4.31)$$

FLOP per-template, whose cost is dominated by the $O(M \times N)$ convolution operation. The computational cost of the direct matched filter approach can be significantly

2877 reduced by exploiting the convolution theorem and FFT algorithms. If we restrict
 2878 ourselves to signals and templates that contain equal numbers of samples then the
 2879 convolution can be calculated by Fourier transforming both vectors, performing the
 2880 point-wise multiplication, and then performing the inverse Fourier transform to obtain
 2881 the convolution result. The FFT algorithm is able to compute the Fourier transform
 2882 utilizing only $O(N \log N)$ operations compared to $O(N^2)$ for a naive Fourier transform
 2883 implementation. This optimization results in a computational cost per-template of

$$O(N_{\text{ch}}) \times O(N_s \log N_s) \quad (4.32)$$

2884 A typical signal vector in the FSCD contains $O(10^4)$ samples in which case the FFT
 2885 reduces the computational cost of the matched filter by a factor of $O(10^3)$. This large
 2886 reduction in computational cost implies that a direct implementation of a matched filter
 2887 is completely infeasible in the FSCD due to resource constraints.

2888 Rather than relying solely on the matched filter it is tempting to consider using
 2889 digital beamforming as an initial step in the signal reconstruction for the purposes of
 2890 data reduction. The primary motivation is to reduce the dimensionality of the data by
 2891 a factor of N_{ch} by combining the array outputs coherently into a single channel. One
 2892 can view the beamforming operation as a partial matched filter, in the sense that the
 2893 matched filter convolution contains the beamforming phased summation along with a
 2894 prediction of the signal shape. By separating beamforming from the signal shape one
 2895 hopes to reduce the overall computational cost by effectively shrinking the number of
 2896 templates and reducing the number of operations required to check each one.

2897 The nature of this optimization requires that we account for the number of templates
 2898 used for pure matched filtering versus the hybrid approach. To first order, the total
 2899 number of templates at the trigger stage is a product of the number of guesses for each
 2900 of the electron's parameters

$$N_T = N_E \times N_\theta \times N_r \times N_\varphi, \quad (4.33)$$

2901 where N_E is the number of kinetic energies, N_θ is the number of pitch angles, N_r is the
 2902 number of starting radial positions, and N_φ is the number of starting azimuthal positions.
 2903 The starting axial position and cyclotron motion phase are not necessary to include in
 2904 the template bank since these parameters manifest themselves as the starting phase of
 2905 the signal, which is effectively marginalized when using a FFT to compute the matched
 2906 filter convolution. Therefore, the total number of operations required by a matched filter

2907 to detect a signal in a segment of array data is on the order of

$$O(N_T) \times O(N_{\text{ch}}) \times O(N_s \log N_s) \quad (4.34)$$

2908 With the hybrid approach we attempt to remove the spatial parameters from the
2909 template bank by using beamforming to combine the array signals into a single channel.
2910 Beamforming explicitly assumes a starting position, which allows us to only use matched
2911 filter templates that span the two-dimensional space of kinetic energy and pitch angle.
2912 The total computational cost of the hybrid method is directly proportional to the number
2913 of beamforming positions. For the time-dependent beamforming defined in Section 4.3.1,
2914 the number of beamforming positions is given by

$$N_{\text{BF}} = N_r \times N_\varphi \times N_{\omega_{\nabla B}}, \quad (4.35)$$

2915 where N_r and N_φ are the same spatial parameters encountered in the pure matched
2916 filter template bank and $N_{\omega_{\nabla B}}$ is the number of ∇B -drift frequency assumptions. If a
2917 unique drift frequency is used for each pitch angle then the hybrid approach is effectively
2918 equivalent to a pure matched filter in the number of operations. The key efficiency gain
2919 of the hybrid approach is to exploit the relatively small differences in $\omega_{\nabla B}$ for electrons
2920 of different pitch angles by using only a small number of average drift frequencies.

2921 The total number of operations for the hybrid approach can be expressed as a sum of
2922 the operations required by the beamforming and matched filtering steps,

$$O(N_{\text{BF}}) \times O(N_{\text{ch}} N_s) + O(N_{\text{BF}}) \times O(N_E N_\theta) \times O(N_s \log N_s). \quad (4.36)$$

2923 The first product in the sum is the number of operations required by beamforming,
2924 which is simply the number of beamforming points times the computational cost of the
2925 beamforming matrix multiplication, and the second product is the computational cost
2926 of matched filtering the summed signal generated by each beamforming position. To
2927 compare this to pure matched filtering we take the ratio of Equations 4.34 and 4.36 to
2928 obtain

$$\Gamma_{\text{BFMF}} = \frac{O(N_{\omega_{\nabla B}})}{O(N_E N_\theta) \times O(\log N_s)} + \frac{O(N_{\omega_{\nabla B}})}{O(N_{\text{ch}})}. \quad (4.37)$$

2929 This expression can be simplified by observing that $O(N_E N_\theta) \times O(\log N_s) \gg O(N_{\text{ch}})$,

2930 which means that the ratio of computational cost for the two methods can be reduced to

$$\Gamma_{\text{BFMF}} \approx \frac{O(N_{\omega_{\nabla B}})}{O(N_{\text{ch}})}. \quad (4.38)$$

2931 If we limit ourselves to a number of estimated drift frequencies of $O(1)$ then we see that
2932 the estimated computational cost reduction of the hybrid approach is of $O(N_{\text{ch}})$. This is
2933 quite a large reduction considering that the FSCD antenna array contains sixty antennas
2934 in the baseline design.

2935 The main drawback of the hybrid approach is that the limited number of allowed
2936 drift frequency guesses can lead to detection efficiency loss due to phase mismatch. The
2937 degree of phase error from an incorrect drift frequency is proportional to the length of
2938 the array data vector used by the signal detection algorithm. For signals with lengths
2939 equal to the baseline FSCD Fourier analysis window of 8192 samples, typical phase errors
2940 from using an average versus the exact ∇B -drift frequency are on the order of a few
2941 percent in terms of the signal energy. This has a relatively small impact on the overall
2942 detection efficiency, however, future experiments with antenna array CRES will want to
2943 balance optimizations such as these during the design phase to keep experiment costs to
2944 a minimum while still achieving scientific goals.

2945 Kinetic Energy and Pitch Angle Degeneracy

2946 More accurate modeling of a matched filter requires that we consider the effects of
2947 mismatched signals and template, since this more accurately reflects the real-world usage
2948 of a matched filter where many incorrect templates are convolved with the data until the
2949 matching template is found. One way to study this is to use the grid of simulated signals
2950 to compute the matched filter scores between mismatched signals and templates and
2951 evaluate the matched filter scores under this scenario. What one finds when performing
2952 this analysis is that templates for kinetic energies and pitch angles that do not match
2953 the underlying signal can have matched filter scores that are indistinguishable from the
2954 matched filter score of the correct template (see Figure 4.21 and Figure 4.21).

2955 This degeneracy in matched filter score is the result of correlations between the kinetic
2956 energy of the electron and the pitch angle caused by changes in the average magnetic field
2957 experienced by an electron for different pitch angles. While in principle helpful for the
2958 purposes of signal detection these correlations are unacceptable since they greatly reduce
2959 the energy resolution of the experiment by causing electrons with specific kinetic energy
2960 to templates across a wide range of energies. It is important to emphasize that this

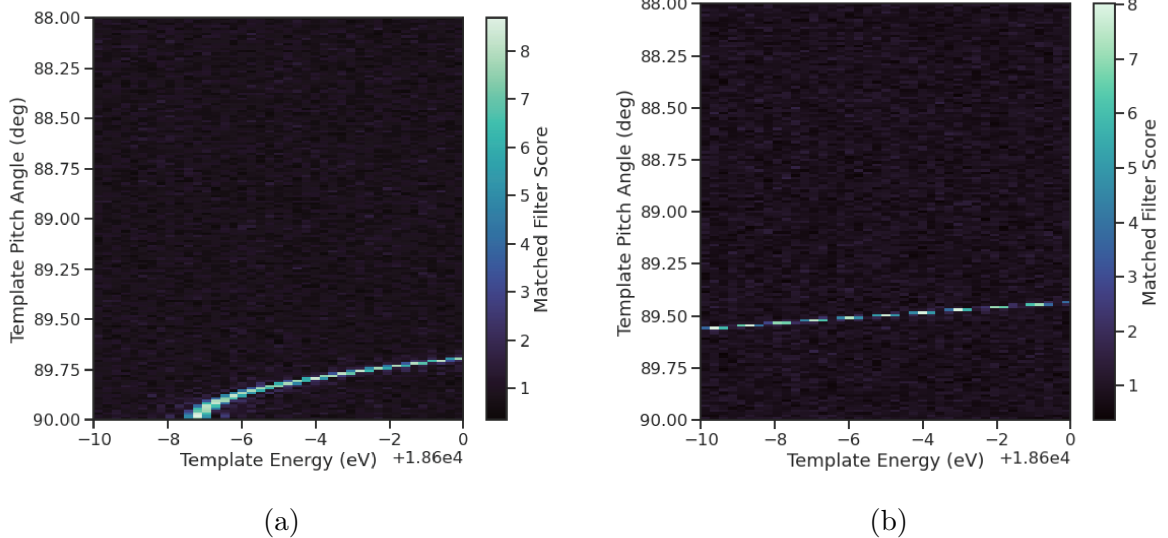


Figure 4.21. Two example illustrations of the correlation between kinetic energy and pitch angle imparted by the shape of the FSCD magnetic trap. The correlations manifest themselves as degeneracies in the matched filter score where multiple matched filter templates have the same matched filter for a particular signal. These degeneracies are a sign that the magnetic trap must be redesigned in order to break the correlation between pitch angle and kinetic energy.

2961 degeneracy cannot be fixed by implementing a different signal reconstruction algorithm.
 2962 As revealed by the matched filter scores the shapes of the signals for different parameters
 2963 are identical. Resolving this degeneracy between pitch angle and energy requires the
 2964 design of a new magnetic trap with steeper walls so that the average magnetic field
 2965 experienced by an electron is less dependent on pitch angle.

2966 4.3.3 Machine Learning

2967 Machine learning is a vast and rapidly developing field of research [73]. In this Section
 2968 we shall attempt to provided a brief introduction to some of the concepts and techniques
 2969 of machine learning that were applied to CRES signal detection rather than attempt a
 2970 comprehensive overview.

2971 Introduction to Machine Learning

2972 Digitization of the FSCD antenna array generates large amounts of data that must be
 2973 rapidly processed to enable real-time signal detection and reconstruction. While digital
 2974 beamforming combined with a power threshold is relatively computationally inexpensive,
 2975 it is relatively ineffective at detecting CRES signal with small pitch angles, since it relies

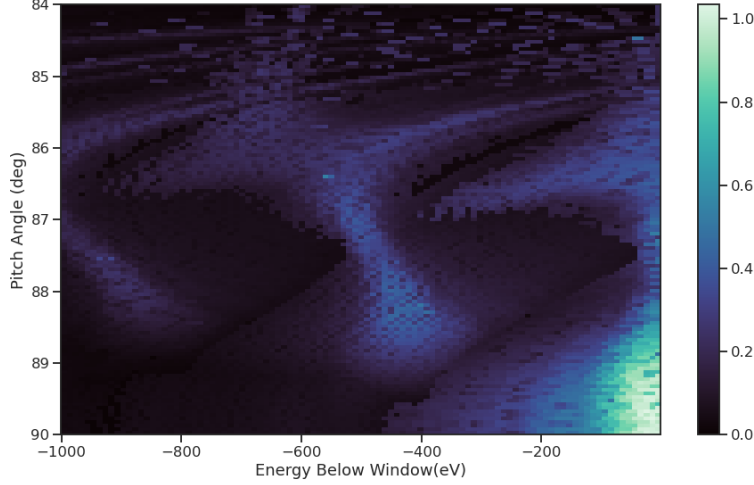


Figure 4.22. A visualization of the correlation between energy and pitch angle in the FSCD magnetic trap. The image is formed by computing the match of the best template from a grid consisting of pitch angles from 84 to 90 degrees in steps of 0.05 degrees, kinetic energies from 17574 to 18574 eV, located at 2 cm from the central axis, and simulated for a length of three FSCD time-slices. The signals used to compute the best matching template consisted of a grid from 84 to 90 degrees in steps of 0.05 degrees, kinetic energies from 18550 to 18575 eV in steps of 0.25 eV, located 2 cm from the central axis, and simulated for three FSCD time-slices. The colored regions of the plot show how well signals with lower energy can match those of higher energy for the FSCD magnetic trap, which is proportional to the achievable energy resolution of the FSCD design.

2976 on a visible frequency peak above the noise. On the other hand, a matched filter is able
 2977 to detect signals with a significantly larger range of parameters, however, the exhaustive
 2978 search of matched filter templates can be computationally expensive. Machine learning
 2979 based triggering algorithms have been used successfully in many different high-energy
 2980 physics experiments [74] and recent developments have shown success in the detection
 2981 of gravitational wave signals using machine learning techniques [75, 76] in place of the
 2982 more traditional matched filtering method. This motivates the exploration of machine
 2983 learning as a potential CRES signal detection algorithm.

2984 There are several different approaches to machine learning, but the one most important
 2985 to our discussion here is the supervised learning approach. In supervised machine learning
 2986 one uses a differentiable model or function that is designed to map the input data to the
 2987 appropriate label [73]. The data is represented as a multidimensional matrix of floating
 2988 point values such as an image or a time-series, and the label is generally a class name
 2989 such as signal or noise for classification problems or a continuous value like kinetic energy
 2990 in the case of regression problems.

2991 In supervised learning the model is trained to map from the data to the correct label
2992 by evaluating the output of the model using a training dataset consisting of a set of
2993 paired data and labels. To evaluate the difference between the model output and the
2994 correct label a loss function is used to quantify the error between the model prediction
2995 and the ground truth. For example, a common loss function in regression problems is the
2996 squared error loss function, which quantifies error using the squared difference between
2997 the model output and label.

2998 Using the outputs of the loss function the next step in supervised learning is to
2999 compute the gradient of error with respect to the model parameters in a process called
3000 backpropagation. Using the model parameter gradients the last step in the supervised
3001 learning process is to perform an update of the parameter values in order to minimize
3002 the error in the model predictions across the whole dataset. This loop is performed many
3003 times while randomly shuffling the dataset until the error converges to a minimum value
3004 at which point the training procedure has finished. It is standard practice to monitor
3005 the training procedure by evaluating the performance of the model using a separate
3006 validation dataset that matches the statistical distribution of the training data and to
3007 check the performance of the model after training using yet another dataset called the
3008 test dataset. These practices help to guard against overtraining which is a concern for
3009 models with many parameters.

3010 Convolutional Neural Networks

3011 A popular class of machine learning models are neural networks. A neural network is
3012 essentially a function composed of a series of linear operations called layers which take a
3013 piece of data typically represented as a matrix, multiplies the elements of the data by a
3014 weight, and then sums these products to produce an output matrix. Neural networks
3015 composed of purely linear operations are unable to model complex non-linear behavior,
3016 therefore, non-linear activation functions are applied to the outputs of each of the layers
3017 to increase the ability of the neural network to model complex relationships between the
3018 data.

3019 Neural networks are typically composed of at least three layers, but with the present
3020 capabilities of computer hardware they more often contain many more than this. The
3021 first layer in a neural network is called the input layer, because it takes the data objects
3022 as input, and the last layer in a neural network is known as the output layer. The
3023 output layer is trained by machine learning to map the data to a desired output using
3024 the supervised learning procedure described in Section 4.3.3. In between the input and

3025 the output layer are typically several hidden layers that receive inputs from and transmit
3026 outputs to other layers in the neural network model. The term deep neural network
3027 (DNN) refers to those neural networks that have at least one hidden layer, which have
3028 proven to be extremely powerful tools for pattern recognition and function approximation.

3029 An important type of DNN are convolutional neural networks (CNN) that typically
3030 contain several layers which perform a convolution of the input with a set of filters. These
3031 convolution operations are typically accompanied by layers that attempt to down-sample
3032 the data along with the standard neural network activation functions. A standard CNN
3033 is composed of several convolutional layers at the beginning of the network and ends
3034 with a series of fully-connected neural network layers at the output. Intuitively, one
3035 can imagine that the convolutional layers are extracting features from the data that
3036 fully-connected layers use to perform the classification or regression task.

3037 **Deep Filtering for Signal Detection in the FSCD**

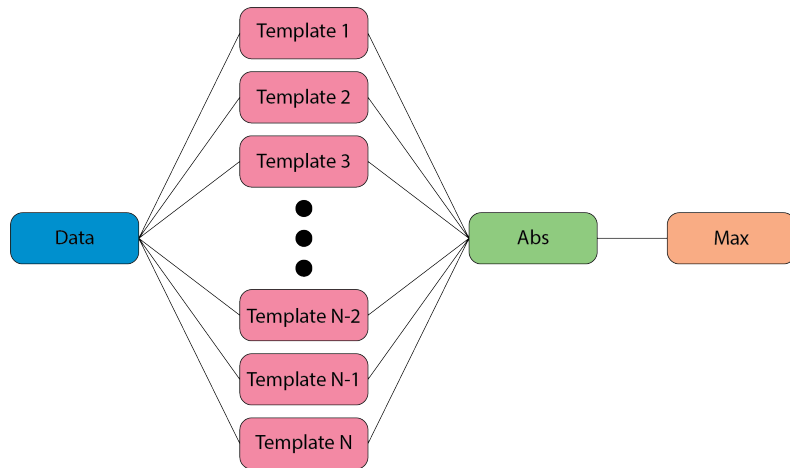


Figure 4.23. A representation of a matched filter template bank as a convolutional neural network. The network has a single layer composed of the templates, which act as convolutional filters. The activation of the neural network is an absolute value followed by a max operator.

3038 CNNs have been extremely influential in the field of computer vision, particularly tasks
3039 such as image segmentation and classification, but have also been applied in numerous
3040 experimental physics contexts. Given the particular challenge posed by signal detection
3041 and reconstruction in the FSCD we are interested in exploring the potential of machine
3042 learning as an effective algorithm for real-time signal detection, since this application
3043 requires both high efficiency and fast evaluation.

3044 In the machine learning paradigm signal detection is equivalent to a binary classifi-

3045 cation problem between the signal and noise data classes, and my investigation focuses
3046 specifically on the application of CNNs to signal detection in the FSCD, which is moti-
3047 vated by relatively recent demonstrations of CNNs achieving classification accuracies for
3048 gravitational wave time-series signals comparable to a matched filter template bank. In
3049 this framework it is possible to interpret the matched filter as a type of CNN composed
3050 of a single convolutional layer with the templates making up the layer filters (see Figure
3051 4.23). Since this neural network has no hidden layers, it is not a DNN like we have
3052 been discussing so far, but we can attempt to construct a proper CNN that attempts to
3053 reproduce the classification performance of the matched filter network.

3054 The name deep filtering refers to this scheme of replacing a matched filter template
3055 bank with a DNN. The reason why one might want to do this is that it may be possible to
3056 exploit redundancies and correlations between templates that may allow one to perform
3057 signal detection with similar accuracy but with fewer computations, which is important
3058 for real-time detection scenarios like the FSCD experiment. In Section 4.4 we perform a
3059 detailed comparison of the signal detection performance of a CNN to beamforming and a
3060 matched filter template bank.

3061 Deep filtering is conceptually a simple technique. Similar to a matched filter template
3062 bank a large number of simulated CREs signals are generated and used to train a model
3063 to distinguish between signal and noise data (see Figure 4.24). In order to reduce the
3064 dimensionality of the input FSCD data a digital beamforming summation is applied
3065 to the raw time-series data generated by Locust to compress the 60-channel data to a
3066 single time-series. CREs signal have a sparse frequency representation and experiments
3067 training CNN's on time-series and frequency series data found that models trained on
3068 frequency spectrum data performed significantly better, therefore, an FFT is applied to
3069 the summed time-series before being normalized and fed to the classification model.

3070 The data used to train the model consists of an equal proportion of signal and noise
3071 frequency spectra. Unique samples of WGN are generated and added to the signals during
3072 training time to avoid having to pre-generate and store large samples of noise data. The
3073 binary cross-entropy loss function combined with the ADAM optimizer proved effective
3074 at training the models to classify CREs data. A simple hyperparameter optimization
3075 was performed by manually tuning model, loss function, and optimizer parameters. The
3076 model and training loops were implemented in python using the PyTorch deep learning
3077 framework. Standard machine learning best practices were followed when training the
3078 models, such as overtraining monitoring using a validation dataset. Models were trained
3079 until the training loss and accuracy converged and then evaluated using a separate test

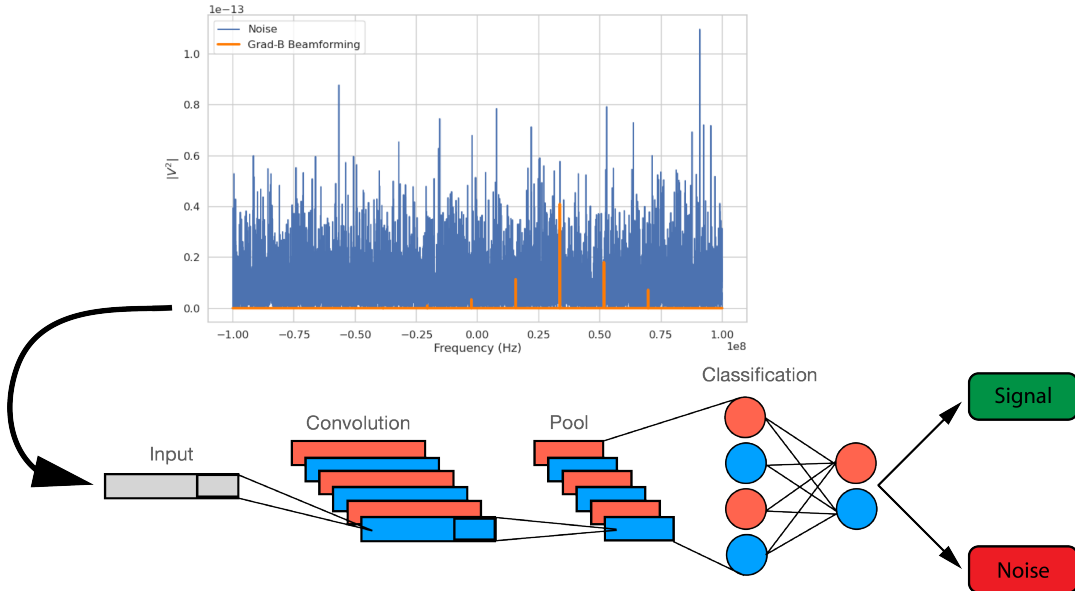


Figure 4.24. A graphical depiction of CRES signal detection using a CNN. A noisy segment of data is converted to a frequency series using digital beamforming and a FFT. The complex-valued frequency series is input into a trained CNN model that classifies the data as signal or noise using a decision threshold on the CNN output.

3080 data set.

3081 The classification results of the test dataset are used to quantify the relationship
 3082 between the true positive rate and the false positive rate for the model. The true positive
 3083 rate is analogous to detection efficiency and the false positive rate is a potential source of
 3084 background in the detector. One can limit the rate of false positives using a sufficiently
 3085 high threshold on the model output at the cost of a lower detection efficiency (see Figure
 3086 4.25 and Figure 4.26). As expected, the performance of the model at signal classification
 3087 is negatively effected the noise power, which is quantified by the noise temperature.

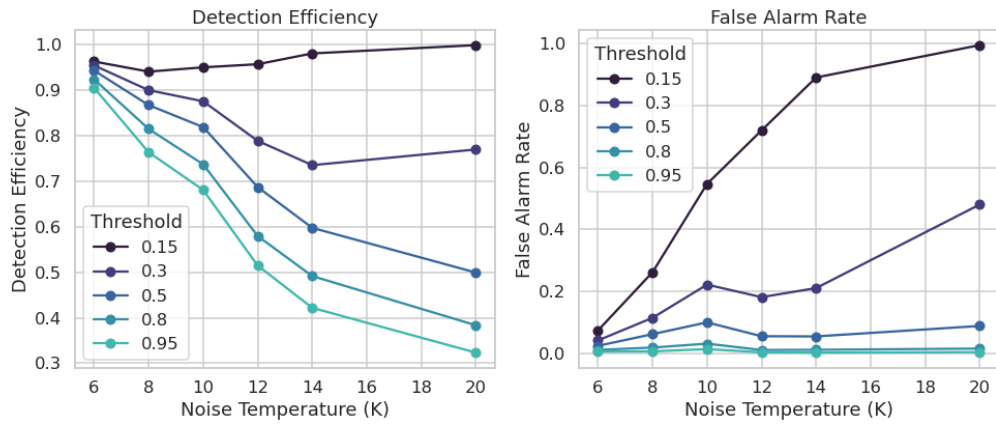


Figure 4.25. The detection efficiency and false alarm rate (false positive rate) as a function of the decision threshold for different values of the noise temperature. The model is trained to output a value close to one for data that contains a signal and outputs a value near zero when the data contains only noise. One sees that a lower decision threshold will have a high detection efficiency at the cost of a high rate of false alarms.

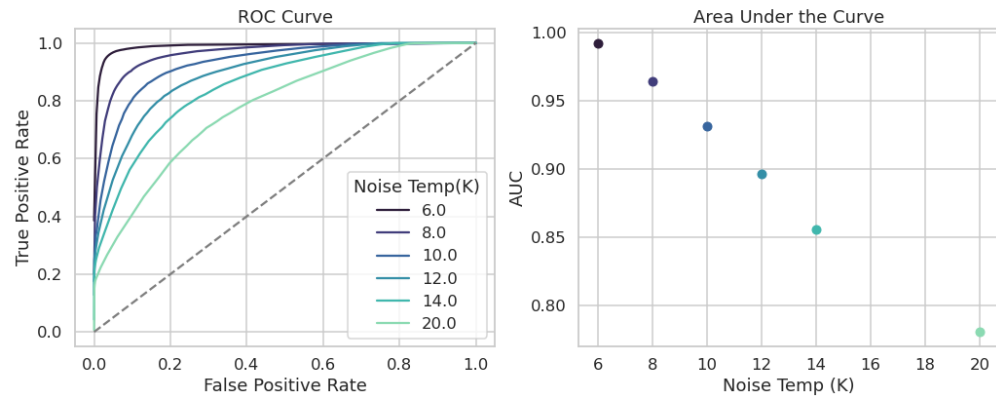


Figure 4.26. ROC curves for a CNN model classifying CRES signals. One can see that the area under the curve, which is a figure of merit that describes the performance of the classifier, is roughly linearly dependent with the noise temperature.

3088 **4.4 Analysis of Signal Detection Algorithms for the An-** 3089 **tenna Array Demonstrator**

3090 This section contains an early version of the manuscript for the triggering paper prepared
3091 for publication in JINST. In it I present a relatively detailed analysis of the signal
3092 detection performance of the three signal detection approaches discussed so far using a
3093 population of simulated CRES signals generated with Locust. The focus of the paper is
3094 on the performance of the signal detection algorithms for pitch angles below 88.5° where
3095 the beamforming power threshold begins to fail.

3096 **4.4.1 Introduction**

3097 Cyclotron Radiation Emission Spectroscopy (CRES) is a technique for measuring the
3098 kinetic energies of charged particles by observing the frequency of the cyclotron radiation
3099 that is emitted as they travel through a magnetic field [39]. The Project 8 Collaboration
3100 is developing the CRES technique as a next-generation approach to tritium beta-decay
3101 endpoint spectroscopy for neutrino mass measurement. Recently, Project 8 has used
3102 CRES to perform the first ever tritium beta-decay energy spectrum and neutrino mass
3103 measurement [41, 42].

3104 Previous CRES measurements have utilized relatively small volumes of gas that are
3105 directly integrated with a waveguide transmission line, which transmits the cyclotron
3106 radiation emitted by the trapped electrons to a cryogenic amplifier. While this technology
3107 has had demonstrable success, it is not a feasible option for scaling up to significantly
3108 larger measurement volumes. In particular, the goal of the Project 8 Collaboration
3109 is to use CRES combined with atomic tritium to measure the neutrino mass with a
3110 40 meV sensitivity. Achieving this sensitivity goal will require a multi-cubic-meter scale
3111 measurement volume in order to obtain the required event statistics in the tritium
3112 beta-spectrum endpoint region; hence, there is a need for new techniques to enable large
3113 volume CRES measurements for future experiments.

3114 One approach is to surround a large volume with an array of antennas that together
3115 collect the cyclotron radiation emitted by trapped electrons [40, 77]. A promising
3116 array design is an inward-facing uniform cylindrical array that surrounds the tritium
3117 containment volume. Increasing the size of the antenna array, by adding additional
3118 rings of antennas along vertical axis, allows one to grow the experimental volume until a
3119 sufficient amount of tritium gas can be observed by the array. A challenging aspect of

3120 this approach is that the total radiated power emitted by an electron near the tritium
3121 spectrum endpoint is on the order of 1 fW or less, which is then distributed between
3122 all the antennas in the array. Consequently, detecting the presence of a CRES signal
3123 and determining the electron's kinetic energy requires reconstructing the entire antenna
3124 array output over the course of the CRES event, posing a significant data acquisition
3125 and signal reconstruction challenge.

3126 Project 8 has developed a triggering system to enable real-time identification of CRES
3127 events using an antenna array [78]. Previous measurements with the CRES technique
3128 have utilized a threshold on the frequency spectrum formed from a segment of CRES
3129 time-series data. This algorithm relies on the detection of a frequency peak above the
3130 thermal noise background, which limits the kinematic parameter space of detectable
3131 electrons. Due to the limitations of this power threshold, Project 8 has been investigating
3132 alternative signal identification approaches, including both matched filtering and machine
3133 learning based classifiers, to improve the detection efficiency of the experiment. In
3134 order to evaluate the relative gains in detection efficiency that come from utilizing
3135 these alternative algorithms, we develop analytical models for the power threshold and
3136 matched filter signal classifier performance applicable to an antenna array based CRES
3137 detector. In addition, we implement and test a basic convolutional neural network (CNN)
3138 as a first step towards the development of neural-network based classifiers for CRES
3139 measurements. These results allow us to compare the estimated detection efficiencies of
3140 each of these methods, which we weigh against the associated computational costs for
3141 real-time applications.

3142 The outline of this paper is as follows. In Section 4.4.2 we give an overview of a
3143 prototypical antenna array CRES experiment, and describe the major steps involved
3144 in the proposed approach to real-time signal identification. In Section 4.4.3 we develop
3145 models for the power threshold and matched filter algorithms, and introduce the machine
3146 learning approach and CNN architecture. In Section 4.4.4 we describe our process for
3147 generating simulated CRES signal data and the details of training the CNN. Finally,
3148 in Section 4.4.5 we perform a comparison of the signal classification accuracy of the
3149 three approaches and discuss the relevant trade-offs in terms of detection efficiency and
3150 computational cost.

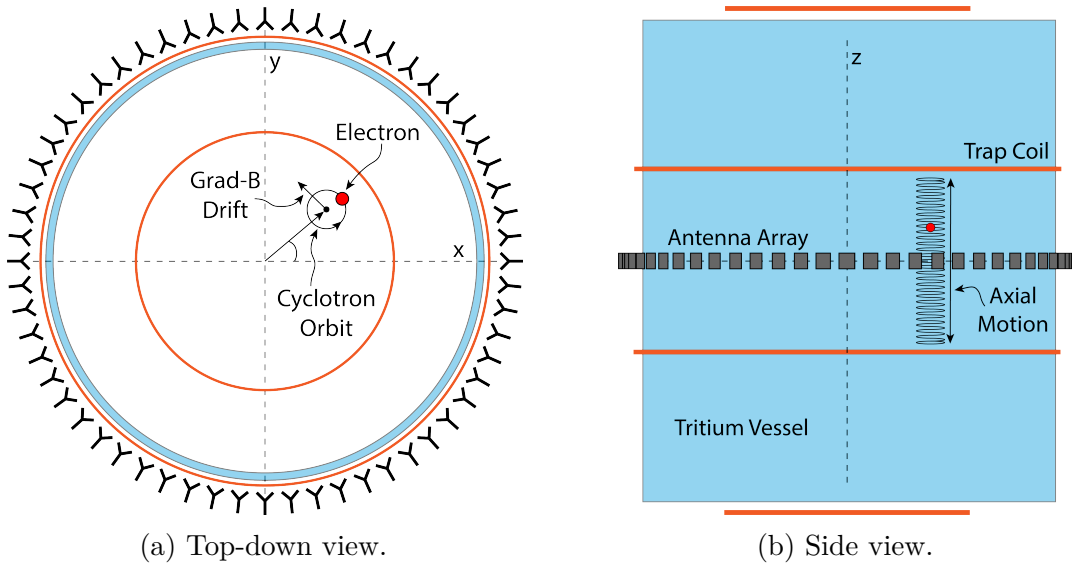


Figure 4.27. An illustration of the conceptual design for an antenna array CRES tritium beta-decay spectrum measurement. The antenna array geometry consists of a 20 cm interior diameter with 60 independent antenna channels arranged evenly around the circumference. The nominal antenna design is sensitive to radiation in the frequency range of 25-26 GHz, which corresponds to the cyclotron frequency of electrons emitted near the tritium beta-spectrum endpoint in a 1 T magnetic field. The array is located at the center of the magnetic trap produced by a set of current-carrying coils. The nominal magnetic trap design is capable of trapping electrons up to 5 cm away from the central axis of the array and traps electrons within an approximately 6 cm long axial region centered on the antenna array.

3151 4.4.2 Signal Detection with Antenna Array CRES

3152 4.4.2.1 Antenna Array and DAQ System

3153 In order to explore the potential of antenna array CRES for neutrino mass measurement,
 3154 the Project 8 Collaboration has developed a conceptual design for a prototype antenna
 3155 array CRES experiment [40, 77], called the Free-space CRES Demonstrator or FSCD,
 3156 which could be used as a demonstration of the antenna array measurement technique
 3157 (see Figure 4.27). The FSCD utilizes a single ring of antennas, which is the simplest
 3158 form of a uniform cylindrical array configuration, to surround a radio-frequency (RF)
 3159 transparent tritium gas vessel. A prototype version of this antenna array has been built
 3160 and tested by the Project 8 collaboration to validate simulations of the array radiation
 3161 pattern and beamforming algorithms [43]. In the FSCD the antenna array is positioned
 3162 at the center of the magnetic trap formed by a set of electro-magnetic coils that are
 3163 designed to produce a magnetic trap with flat central region and steep walls both radially
 3164 and axially.

3165 When a beta-decay electron is trapped its motion consists of three primary components.
 3166 The component with the highest frequency is the cyclotron orbit whose frequency is
 3167 determined by the size of the background magnetic field. The FSCD design assumes
 3168 a background magnetic field value of approximately 0.96 T, which results in cyclotron
 3169 frequencies for electrons with kinetic energies near the tritium beta-spectrum endpoint
 3170 from 25 to 26 GHz. The component with the next highest frequency is the axial oscillation
 3171 experienced by electrons with pitch angles of less than 90° [60]. The flat region of the
 3172 FSCD magnetic trap extends approximately 3 cm above and below the antenna array
 3173 plane causing electrons to move back and forth as they are reflected from the trap walls.
 3174 Typical oscillation frequencies are on the order of 10's of MHz, which results in an
 3175 oscillation period that is $O(10^3)$ smaller than the duration of a typical CRES event.
 3176 Therefore, when reconstructing CRES events we treat the electron as occupying only an
 3177 average axial position at the center of the magnetic trap, since we are not able to resolve
 3178 the axial position as a function of time. The component of motion with the smallest
 3179 frequency is ∇B -drift caused by radial field gradients in the trap, producing an orbit of
 3180 the electron around the central axis of the trap with a frequency on the order of a few
 3181 kHz, dependent on the pitch angle and the radial position of the electron.

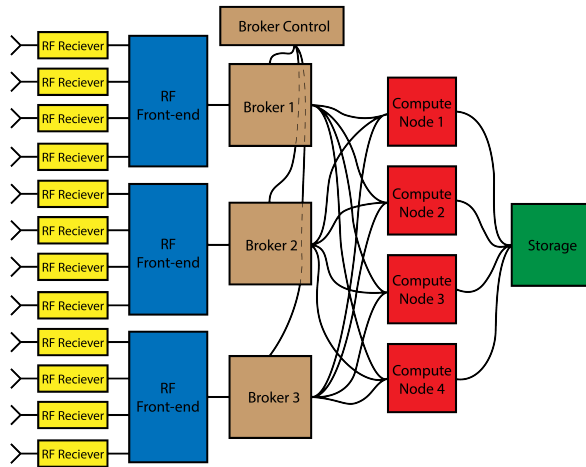


Figure 4.28. A high-level diagram of the DAQ system archctecture envisioned for the FSCD.

3182 The data acquisition (DAQ) system digitizes the signals from the antenna array and
 3183 combines thee data streams into a time-ordered matrix of array snapshots that can be
 3184 used by the reconstruction algorithms. The FSCD DAQ system design [78] is divided into
 3185 three layers 4.28. The first layer is the RF front-end, which includes the antenna array,
 3186 the RF receiver boards, and the digitization electronics. The receiver board contains an
 3187 amplifier, RF mixer, and bandpass filter to enable down-conversion, and is followed by

3188 the digitization electronics that sample the CRES signals at 200 MHz. In order to achieve
 3189 an adequate signal-to-noise ratio to detect CRES events, the DAQ system for the antenna
 3190 array demonstrator must have a total system noise temperature of ≈ 10 K, which we
 3191 can achieve by using low-noise amplifiers and operating at cryogenic temperatures. After
 3192 digitization, the array data must be reorganized from individual data streams sorted
 3193 by channel into array snapshots sorted by time. In order to solve this data transfer
 3194 and networking problem the second layer of the DAQ system consists of a set of broker
 3195 computer nodes that reorganize the array data into time-ordered chunks. This approach
 3196 allows us accommodate different data transfer requirements by scaling the number of
 3197 broker nodes in this layer accordingly. Next, the broker layer distributes these chunks
 3198 of array data to the final layer of the DAQ system, which consists of a set of identical
 3199 reconstruction nodes that perform the calculations required for CRES reconstruction.
 3200 Similar to the broker layer, the number of reconstruction nodes can be increased or
 3201 decreased depending on the amount of computer power required for real-time CRES
 3202 reconstruction.

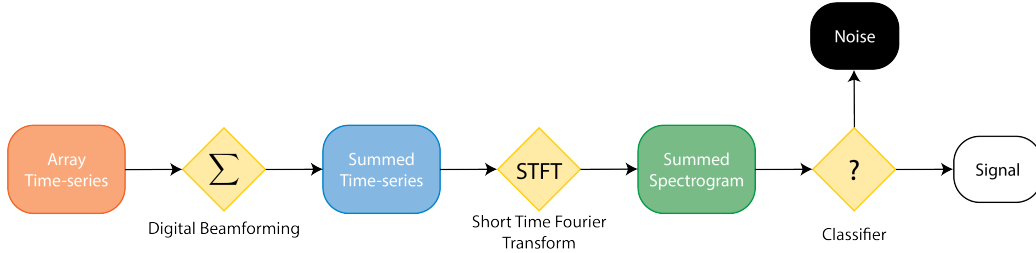


Figure 4.29. A block diagram illustration of the real-time triggering algorithm proposed for antenna array CRES reconstruction.

3203 The design of the FSCD DAQ system is intended to enable a significant portion of
 3204 the CRES event reconstruction to occur in real-time. The motivation for this comes from
 3205 the fact that the FSCD antenna array generates approximately 1 exabyte of raw data
 3206 per year of operation. Therefore, in order to reduce the data-storage requirements, it is
 3207 ideal to perform at least some of the CRES event reconstruction in real-time so that it
 3208 is possible to save a reduced form of the data for offline analysis. The first step of the
 3209 real-time reconstruction would be a real-time signal detection algorithm, which is the
 3210 focus of this paper. Our approach consists of three main operations performed on the
 3211 time-series data blocks including digital beamforming, a short time Fourier transform
 3212 (STFT), and a binary classification algorithm to distinguish between signal and noise
 3213 data (see Figure 4.29).

3214 4.4.2.2 Real-time Signal Detection

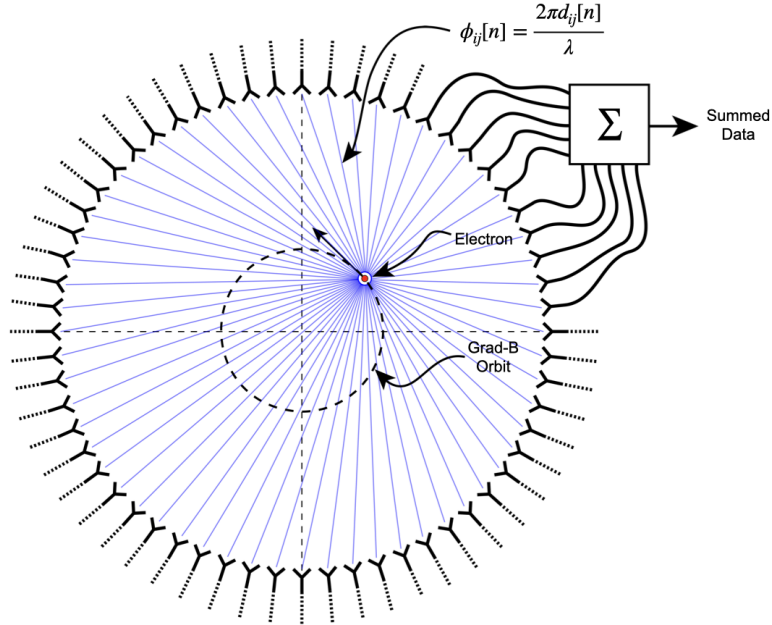


Figure 4.30. An illustration of the digital beamforming procedure. The blue lines indicate the various distances from the beamforming position to the antenna. In the situation depicted the actual position of the electron matches the beamforming position, so we should expect constructive interference when the phase shifted signals are summed. To prevent the electron's ∇B -motion from moving the electron off of the beamforming position, the beamforming phase include a time-dependence to follow the trajectory of the electron in the magnetic trap.

3215 The first step in the real-time detection algorithm is digital beamforming, which is
 3216 a phased summation of the signals received by individual antennas in the array (see
 3217 Figure 5.21). The phase shifts correspond to the path length differences between a spatial
 3218 position and each individual antenna such that, when there is an electron located at
 3219 the beamforming position, all the signals received by the array constructively interfere.
 3220 Since we do not know ahead of time where an electron will be produced in the detector,
 3221 we define a grid of beamforming positions that cover the entire region where electrons
 3222 can be trapped and perform a phased summation for each of these points for every
 3223 time-step in the array data block. As we saw in Section 4.4.2.1, the axial oscillation
 3224 of the electrons prevents us from resolving it's position along the Z-axis of the trap,
 3225 therefore our beamforming grid need only cover the possible positions of the electron in
 3226 the two-dimensional plane defined by the antenna array.

3227 The equation defining digital beamforming can be expressed as

$$\mathbf{y}[n] = \Phi^T[n]\mathbf{x}[n], \quad (4.39)$$

3228 where $\mathbf{x}[n]$ is array snapshot vector at the sampled time n , $\Phi[n]$ is the matrix of
3229 beamforming phase shifts, and $\mathbf{y}[n]$ is summed output vector that contains the voltages
3230 for each of the summed channels that correspond to a particular beamforming position.
3231 The elements of the beamforming phase shift matrix can be expressed as a weighted
3232 complex exponential

$$\Phi_{ij}[n] = A_{ij}[n] \exp(2\pi i \phi_{ij}[n]), \quad (4.40)$$

3233 where the indices i and j label the beamforming and antenna positions respectively. The
3234 weight A_{ij} accounts for the relative power increase for antennas that are closer to the
3235 position of the electron, and ϕ_{ij} is the total beamforming phase shift for the j -th antenna
3236 at the i -th beamforming position.

3237 The beamforming phase shift is a sum of two terms

$$\phi_{ij}[n] = \frac{2\pi d_{ij}[n]}{\lambda} + \theta_{ij}[n], \quad (4.41)$$

3238 where the first term is the phase shift originating from the path length difference ($d_{ij}[n]$)
3239 between the beamforming and antenna positions, which are represented by the vectors
3240 (r_j, θ_j) and $(r_i, \theta_i[n])$, and the second term is the angular separation ($\theta_{ij}[n]$) of the two
3241 positions. The angular separation enters into the beamforming phase due to an effect
3242 caused by the circular orbit of the electron that produces radiation whose phase is linearly
3243 dependent on the relative azimuthal position of the antenna [79, 80]. The time-dependence
3244 of the beamforming phases is intended to correct for the effects of ∇B -drift, which cause
3245 the guiding centers of electrons to orbit the center of the magnetic trap. By including a
3246 linear time-dependence in the azimuthal beamforming position,

$$\theta_i[n] = \omega_{\nabla B} t[n] + \theta_{i,0}, \quad (4.42)$$

3247 where $\omega_{\nabla B}$ is the azimuthal grad-B drift frequency, $t[n]$ is the time vector and, $\theta_{i,0}$ is the
3248 starting azimuthal position, we can configure the beamforming phases to effectively track
3249 the XY-position of the guiding center over the event duration. Predicting accurate values
3250 of $\omega_{\nabla B}$ for a specific trap and set of kinematic parameters will be done by simulations,
3251 which are performed using the Kassiopeia software package [59] by Project 8.

3252 After digital beamforming, we apply a short-time Fourier transform (STFT) to the

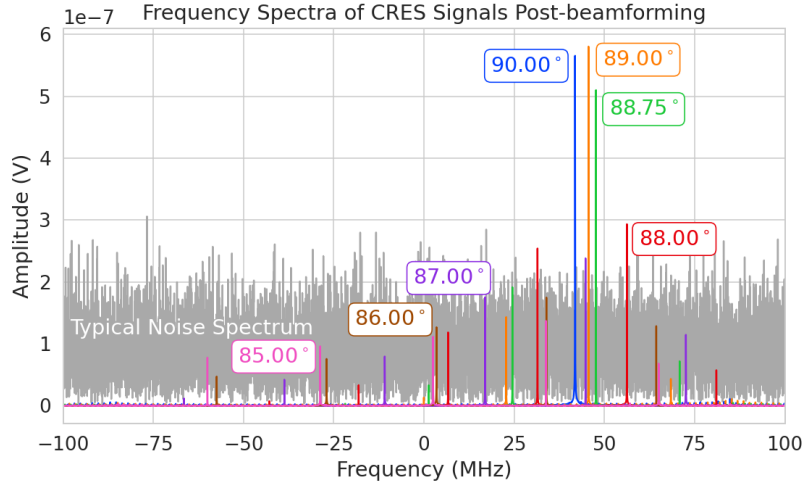


Figure 4.31. Frequency spectra of simulated CRES signals post-beamforming. The signal of a 90° electron consists of a single frequency component that is easy to detect with a power threshold on the frequency spectrum. This power threshold is still effective for signals with relatively large pitch angles such as 89.0° and 88.75° , which are composed of a main carrier and a few small sidebands. Signals with smaller pitch angles, below about 88.5° , tend to be dominated by sidebands such that no single frequency component can be reliably distinguished from the noise with a power threshold.

3253 summed time-series to obtain the frequency spectrum representation of the signals (see
 3254 Figure 4.31). From the detection perspective, the frequency representation of the CRES
 3255 data is advantageous compared to the time domain, because the frequency spectra of
 3256 CRES signals are well-approximated by a frequency and amplitude modulated sinusoidal
 3257 whose carrier frequency increases as a linear chirp. The modulation is caused by the axial
 3258 oscillation of the electron in the magnetic trap and produce frequency spectra that are
 3259 well-described by a small number of frequency components. The linear chirp is caused
 3260 by the energy loss due to cyclotron radiation, which results in a relatively slow increase
 3261 in the frequency components of the CRES signal over time. During the standard Fourier
 3262 analysis window for the FSCD of $40.96 \mu\text{sec}$, we expect a typical CRES signal to increase
 3263 in frequency by approximately 15 kHz, which is smaller than the frequency bin width
 3264 given the 200 MHz sample rate. Therefore when considering a single frequency spectrum
 3265 it is justifiable to neglect the effects of the linear frequency chirp.

3266 In the cases where the electron's pitch angle is $\gtrsim 88.5^\circ$, the majority of the signal
 3267 power is contained in a single frequency component, with the remaining signal power
 3268 contained in a small number of sidebands proportional to the electron's axial modulation
 3269 (see Figure 4.31). In these cases detection is relatively straight-forward by implementing

3270 a power threshold on the STFT, since the amplitude of the main signal peak is distinct
 3271 from the thermal noise spectrum. However, as the pitch angle of the electron is decreased
 3272 below 88.5° , the modulation index of the signal increases causing the maximum amplitude
 3273 of the frequency spectrum to be comparable to typical noise fluctuations. At this point,
 3274 the power threshold trigger is no longer able to distinguish between signal and noise
 3275 leading to a reduction in detection efficiency. The neutrino mass sensitivity of the FSCD
 3276 is directly linked to the overall detection efficiency. And, because the distribution of
 3277 electron pitch angles is effectively uniformly distributed across the range of pitch angles
 3278 that can be trapped, the overall detection efficiency is directly influenced by the range of
 3279 pitch angles that have detectable signals. Therefore, utilizing a signal detection algorithm
 3280 that can more effectively identify signals with pitch angles less than 88.5° will improve
 3281 both detection efficiency and ultimately the neutrino mass sensitivity of the FSCD and
 3282 other CRES experiments.

3283 Modeling the detection performance of alternative signal detection algorithms for
 3284 the FSCD requires that we pose the signal detection problem in a consistent manner.
 3285 The approach we take is to perform a binary hypothesis test on the frequency spectra
 3286 generated by the STFT. Mathematically, this is expressed as,

$$\mathcal{H}_0 : y[n] = \nu[n] \quad (4.43)$$

$$\mathcal{H}_1 : y[n] = x[n] + \nu[n]. \quad (4.44)$$

3287 Where under hypothesis \mathcal{H}_0 , the vector representing the frequency spectrum ($y[n]$) is
 3288 composed of pure white Gaussian noise (WGN) represented by $\nu[n]$, and under hypothesis
 3289 \mathcal{H}_1 the frequency spectrum is composed of a CRES signal ($x[n]$) with added WGN. The
 3290 dominant source of noise in a FSCD-like experiment is expected to be thermal Nyquist-
 3291 Johnson noise, which is well approximated by a WGN distribution. In order to decide
 3292 between these two hypotheses we follow the standard Neyman-Pearson approach by
 3293 performing a log-likelihood ratio test between the probability distributions of the signal
 3294 classifier output under \mathcal{H}_1 and \mathcal{H}_0 [70]. The output of the log-likelihood ratio test is
 3295 called the test statistic, which is used to assign the data as belonging to the noise (\mathcal{H}_0)
 3296 or signal (\mathcal{H}_1) classes by setting a decision threshold on the value of the test statistic.

3297 In practice, we select the decision threshold by finding the value of the test statistic
 3298 that guarantees an acceptable rate of false positives and then attempt to maximize
 3299 the signal detection probability under that fixed false positive rate. Because the signal
 3300 classifier will be used to evaluate the spectra of $O(10^2)$ beamforming positions every

3301 40.96 μ sec, we will require the signal classifiers to operate with decision thresholds that
 3302 provide false positive rates significantly smaller than 1%. This reduces the burden placed
 3303 on later stages of the CRES reconstruction chain to reject these false positives and
 3304 decreases the overall likelihood of reconstructing a false event. Below, we calculate the
 3305 probability distributions that allow us characterize how different detection algorithms
 3306 will perform for CRES signals in an FSCD experiment.

3307 **4.4.3 Signal Detection Algorithms**

3308 **4.4.3.1 Power Threshold**

3309 The power threshold detection algorithm uses the maximum amplitude of the frequency
 3310 spectra as the detection test statistic. To model the performance of this approach,
 3311 consider first the case where the signal is pure WGN. For a single bin in the frequency
 3312 spectrum, the probability that the amplitude falls below a specific threshold value is
 3313 given by the Rayleigh cumulative distribution function (CDF),

$$\text{Ray}(x; \tau) = 1 - \exp(-|x|^2/\tau), \quad (4.45)$$

3314 where the complex amplitude of the frequency bin is x , and τ is the WGN variance.
 3315 Because the noise samples for each frequency bin are independent and identically dis-
 3316 tributed (IID), the probability that every bin in the frequency spectrum falls below the
 3317 threshold is the joint CDF formed by the product of each individual frequency bin CDF,

$$F_0(x; \tau, N_{\text{bin}}) = \text{Ray}(x; \tau)^{N_{\text{bin}}}. \quad (4.46)$$

3318 The PDF for the power threshold classifier can then be obtained by differentiating the
 3319 CDF.

3320 The probability distribution for the power threshold classifier under \mathcal{H}_1 is formed in
 3321 a similar way, but the frequency bins that contain signal must be treated separately. For
 3322 a frequency bin that contains both signal and noise we can describe the probability that
 3323 the amplitude of the bin will fall below our threshold using the Rician CDF,

$$\text{Rice}(x; \tau, \nu) = 1 - Q_1 \left(\frac{|\nu|}{\sqrt{2\tau}}, \frac{|x|}{\sqrt{2\tau}} \right), \quad (4.47)$$

3324 where the parameter $|\nu|$ defines the noise-free amplitude of the signal and Q_1 is the
 3325 Marcum Q-function. This time the CDF that describes the probability that the entire

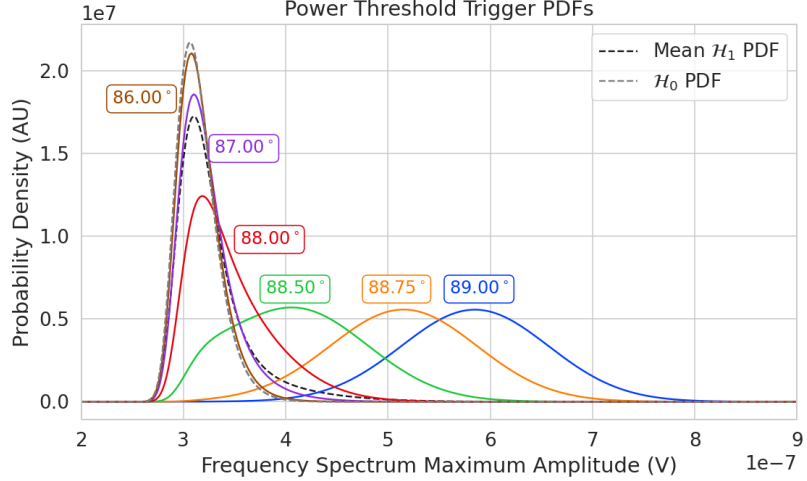


Figure 4.32. PDFs of the power threshold test statistic for CRES signals with various pitch angles as well as the PDF for the noise-only signal case. The average PDF computed for pitch angles ranging from 85.5 to 88.5° is also shown. As the pitch angle is decreased the signal PDF converges towards the noise PDF which indicates that the power threshold trigger is unable to distinguish between small pitch angle signals and noise.

3326 spectrum falls below the decision threshold is the product of both signal and noise CDFs,

$$F_1(x; \tau, \nu, N_{\text{bin}}, N_s) = \text{Ray}(x; \tau)^{N_{\text{bin}} - N_s} \prod_{k=0}^{N_s} \text{Rice}(x; \tau, \nu_k). \quad (4.48)$$

3327 The first half of Equation 4.48 is the contribution from the bins in the frequency spectrum
 3328 that contain only noise, and the second half is the product of the Rician CDFs for the
 3329 frequency bins that contain signal peaks with a noise-free amplitude of $|\nu_k|$. In Figure
 3330 4.32 we show plots of example PDFs under \mathcal{H}_1 and \mathcal{H}_0 .

3331 4.4.3.2 Matched Filtering

3332 The shape of a CRES signal is completely determined by the initial conditions of the
 3333 electron as it is emitted from beta-decay, which implies that it is possible to apply
 3334 matched filtering as a signal detection algorithm. With a matched filter one uses the
 3335 shape of the known signal, which is called a template, to filter the incoming data by
 3336 computing the convolution between the signal and the data [70]. For cases where the
 3337 signal is buried in WGN, the matched filter is the optimal detector in that it achieves
 3338 the maximum probability of a true detection for a fixed false positive rate. Since CRES
 3339 signals have an unknown shape but are deterministic, we can apply a matched filter by

3340 using simulations to generate a large number of signal templates called a template bank,
 3341 which spans the parameter space of possible signals. Then at detection time, we use the
 3342 template bank to identify signals by performing the matched filter convolution for each
 3343 template in an exhaustive search.

3344 As we saw from the frequency spectra in Figure 4.31, CRES signals are highly periodic
 3345 in nature. In such cases, it is advantageous to utilize the convolution theorem to replace
 3346 the matched filter convolution with an inner product in the frequency-domain. With the
 3347 convolution theorem, the matched filter test statistic that describes the detection of a
 3348 signal buried in WGN using a matched filter template bank is given by

$$\mathcal{T} = \max_{\mathbf{h}} \left| \sum_{n=0}^{N_{\text{bin}}} h^\dagger[n] y[n] \right|, \quad (4.49)$$

3349 where $h^\dagger[n]$ is the complex conjugate of the signal template. For the case when our
 3350 template bank consists of only a single template it is possible to derive an exact analytical
 3351 form for the PDF describing the matched filter test statistic. First, we derive PDF under
 3352 the signal hypothesis, where the equation describing the matched filter test statistic, also
 3353 known as the matched filter score, becomes

$$\mathcal{T} = \left| \sum_{n=0}^{N_{\text{bin}}} h^\dagger[n] y[n] \right|. \quad (4.50)$$

3354 Each noisy frequency bin represented by $y[n]$ is the sum between value of the signal
 3355 at that bin and complex WGN, which means that $y[n]$ is itself Gaussian distributed.
 3356 Therefore, the value of the inner product between the template and the data is also a
 3357 complex Gaussian variable; and, since the matched filter score is the magnitude of this
 3358 inner product, it must follow a Rician distribution.

3359 We can derive the equation for the Rician PDF by expressing the matched filter
 3360 template \mathbf{h} in terms of the corresponding simulated signal, which we write as \mathbf{x}_h to
 3361 distinguish from the signal in the data. Using the standard normalization and assuming
 3362 uncorrelated WGN, the matched filter templates can be written as

$$\mathbf{h} = \frac{\mathbf{x}_h}{\sqrt{\tau |\mathbf{x}_h|^2}} \quad (4.51)$$

3363 where τ is the noise variance. Inserting this into Equation 4.49 and expressing the data

3364 as a sum between a signal and a WGN vector yields,

$$\mathcal{T} = \frac{1}{\sqrt{\tau|\mathbf{x}_h|^2}} \left| \sum_{n=1}^{N_{\text{bin}}} x_h[n] (x[n] + \nu[n]) \right|. \quad (4.52)$$

3365 Next, we transform the expression by isolating the randomly distributed components
 3366 giving

$$\mathcal{T} = \frac{\left| \sum_{n=1}^{N_{\text{bin}}} x_h[n] x[n] \right|}{\sqrt{\tau|\mathbf{x}_h|^2}} + \frac{1}{\sqrt{\tau|\mathbf{x}_h|^2}} \left| \sum_{n=1}^{N_{\text{bin}}} x_h[n] \nu[n] \right|. \quad (4.53)$$

3367 The first term of 4.53 can be simplified by using the Cauchy-Schawrz inequality to express
 3368 the magnitude of the inner product in terms of the magnitudes of the signal and template
 3369 as well as an orthogonality constant which we call "match" (Γ). Using this we obtain,

$$\mathcal{T} = |\mathbf{h}| |\mathbf{x}| \Gamma + \frac{1}{\sqrt{\tau|\mathbf{x}_h|^2}} \left| \sum_{n=1}^{N_{\text{bin}}} x_h[n] \nu[n] \right|. \quad (4.54)$$

3370 The second term is a sum of Gaussian distributed variables, which we should expect also
 3371 follows a Gaussian distribution. Each of the samples $\nu[n]$ is described by

$$\nu[n] \sim \mathcal{N}(0, \tau), \quad (4.55)$$

3372 where $\mathcal{N}(0, \tau)$ is a complex Gaussian distribution with zero mean and variance τ . There-
 3373 fore,

$$\frac{x_h[n]}{\sqrt{\tau|\mathbf{x}_h|^2}} \nu[n] \sim \mathcal{N}\left(0, \frac{x_h[n]^2}{|\mathbf{x}_h|^2}\right), \quad (4.56)$$

$$\sum_{n=1}^{N_{\text{bin}}} \frac{x_h[n]}{\sqrt{\tau|\mathbf{x}_h|^2}} \nu[n] \sim \mathcal{N}\left(0, \frac{\sum_{n=1}^{N_{\text{bin}}} x_h[n]^2}{|\mathbf{x}_h|^2}\right) = \mathcal{N}(0, 1), \quad (4.57)$$

$$|\mathbf{h}| |\mathbf{x}| \Gamma + \sum_{n=1}^{N_{\text{bin}}} \frac{x_h[n]}{\sqrt{\tau|\mathbf{x}_h|^2}} \nu[n] \sim \mathcal{N}(|\mathbf{h}| |\mathbf{x}| \Gamma, 1). \quad (4.58)$$

3374 We see that \mathcal{T} is magnitude of a complex variable with mean $|\mathbf{h}| |\mathbf{x}| \Gamma$ and variance one. In
 3375 order to simply the expression a bit further, we define the quantity $\mathcal{T}_{\text{ideal}} = |\mathbf{h}| |\mathbf{x}| \Gamma$, which
 3376 we call the ideal matched filter score, because it represents the value of the matched
 3377 filter inner product that we would expect if no noise was present in the signal. We can
 3378 write the matched filter test statistic as the magnitude of a two-dimensional vector in

3379 the complex plane

$$\mathcal{T} = |(\mathcal{T}_{\text{ideal}} + n_r, n_i)|, \quad (4.59)$$

3380 where n_r and n_i are the real and imaginary components of the noise each with variance
3381 $1/2$, which is modeled by a Rician distribution with shape factor $\mathcal{T}_{\text{ideal}}$. Therefore, the
3382 probability distribution of the matched filter test statistic is given by,

$$P_1(x; \mathcal{T}_{\text{ideal}}) = 2x \exp(- (x^2 + \mathcal{T}_{\text{ideal}}^2)) I_0(2x\mathcal{T}_{\text{ideal}}), \quad (4.60)$$

3383 where I_0 is the zeroth-order modified Bessel function.

3384 The shape of the matched filter score distribution is controlled by the parameter
3385 $\mathcal{T}_{\text{ideal}}$, which is effectively the value of the matched filter score if the data contained no
3386 noise. Without noise, the data vector reduces to the signal, \mathbf{x} , in which case Equation
3387 4.50 becomes the magnitude of an inner product between two vectors. We can write
3388 the magnitude of an inner product in terms of the lengths of the individual vectors and
3389 a constant that describes the degree of orthogonality between them. Applying this to
3390 Equation 4.50, we obtain

$$\mathcal{T}_{\text{ideal}} = |\mathbf{h}^\dagger \cdot \mathbf{x}| = |\mathbf{h}| |\mathbf{x}| \Gamma \quad (4.61)$$

3391 where Γ describes the orthogonality between \mathbf{h} and \mathbf{x} . From the point of view of matched
3392 filtering, we can interpret Γ as describing how well the template matches the underlying
3393 signal in the data.

3394 The matched filter score PDF under the noise hypothesis can be readily obtained
3395 from Equation 4.60 by setting the value of $\mathcal{T}_{\text{ideal}}$ to zero, since the data contains no signal
3396 in the noise case. Doing this, we obtain the Rayleigh distribution that describes the
3397 matched filter score under \mathcal{H}_0 ,

$$P_0(x) = 2x \exp(-x^2). \quad (4.62)$$

3398 Equations 4.60 and 4.62 describe the behavior of the matched filter test statistic
3399 under \mathcal{H}_0 and \mathcal{H}_1 for a single template. However, defining a PDF that describes the
3400 matched filter test statistic in the case of multiple templates is in general a mathematically
3401 intractable problem, since there is no guarantee of orthogonality between matched filter
3402 templates. This leads to correlations between the matched filter scores of different
3403 templates because only one sample of noise is used to compute the matched filter scores
3404 of the template bank. In order to proceed, we need to make the simplifying assumption
3405 that we can treat the matched filter scores as IID variables, which allows to ignore

3406 correlations between templates. The overall effect of this will be an underestimate of the
 3407 performance of the matched filter, since we are under counting the number of templates
 3408 that could contribute a detectable score.

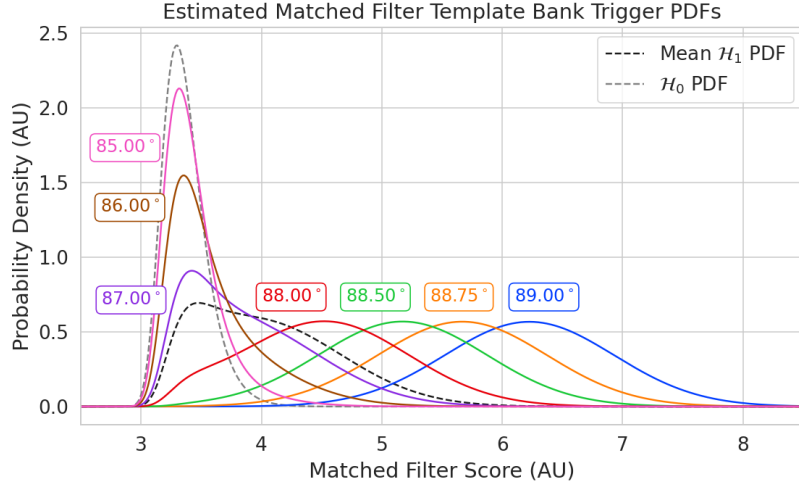


Figure 4.33. Plots of the estimated PDFs for the matched filter template bank test statistic for CRES signals with various pitch angles as well as the estimated PDF for the noise only signal case. We assume an estimated number of templates of 10^5 and perfect match between signal and template i.e. $\Gamma_{\text{best}} = 1$. The mean PDF includes signals ranging from $85.5 - 88.5^\circ$ in pitch angle. There is a much larger distinction between the signal PDFs at small pitch angle compared to the power threshold indicating a higher detection efficiency for these signals.

3409 For \mathcal{H}_0 we model the probability that the matched filter score falls below our threshold
 3410 using the CDF obtained by integrating Equation 4.62. Because we are assuming that
 3411 the matched filter scores using different templates are independent, the probability that
 3412 the matched filter score for all templates falls below a threshold value is the joint CDF
 3413 formed by multiplying the CDF for each template. Under \mathcal{H}_0 this is

$$F_0(x) = \left(1 - e^{-x^2}\right)^{N_t}, \quad (4.63)$$

3414 where x is the matched filter score threshold and N_t is the number of templates. We
 3415 should expect that the distribution describing the matched filter template bank maximum
 3416 score depends on N_t , because with more templates there is a greater chance of a random
 3417 match between the template and data.

3418 For \mathcal{H}_1 , we start by denoting the CDF of the best matching template as $F_{\text{best}}(x; \mathcal{T}_{\text{best}})$,
 3419 and treat the matched filter scores for all other templates as negligible ($\mathcal{T}_{\text{ideal}} \approx 0$). Then
 3420 we form the joint CDF by combining the distributions for all templates used during

3421 detection. Since we are exhaustively checking the matched filter scores, the number of
 3422 templates checked will be a randomly distributed variable that ranges from zero to the
 3423 total number of available templates. If we assume that signals are uniformly distributed
 3424 across the parameter space spanned by the template bank then on average we check
 3425 $(N_t - 1)/2 \approx N_t/2$ templates for each inference. Therefore, the estimated CDF under \mathcal{H}_1
 3426 is

$$F_1(x; \mathcal{T}_{\text{best}}) = F_{\text{best}}(x; \mathcal{T}_{\text{best}}) \left(1 - e^{-x^2}\right)^{N_t/2}. \quad (4.64)$$

3427 In Figure 4.33 we show plots of the estimated matched filter template bank classifier
 3428 PDFs under both \mathcal{H}_0 and \mathcal{H}_1 .

3429 4.4.3.3 Machine Learning

3430 In this paper we focus on Convolutional Neural Networks (CNN) as an example of
 3431 a machine learning based signal classifier. CNNs are constructed using a series of
 3432 convolutional layers, each composed of a set of filters that are convolved with the input
 3433 data. The individual convolutional filters can be viewed as matched filter templates that
 3434 are learned from a set of simulated data rather than being directly generated. This opens
 3435 the possibility of finding a more efficient representation of the matched filter templates
 3436 during the training process that can potentially reduce computational cost at inference
 3437 time while still offering good classification performance.

3438 The machine learning approach is distinct from both the power threshold and matched
 3439 filtering in that we do not attempt to manually engineer a test statistic that is computed
 3440 from the data for classification. Instead, we attempt calculate the test statistic by
 3441 constructing a differentiable function that maps the complex frequency series generated
 3442 by the STFT to a binary classification as either signal or noise. The test statistic for the
 3443 machine learning classifier can be expressed as

$$\mathcal{T} = G(\mathbf{y}; \boldsymbol{\Omega}) \quad (4.65)$$

3444 where \mathbf{y} is the noisy data vector and $G(\mathbf{y}; \boldsymbol{\Omega})$ is the machine learning model parameterized
 3445 by the weights $\boldsymbol{\Omega}$. By using supervised learning on a labeled set of training signals, we
 3446 can modify the function parameters to learn the mapping from the data to the likelihood
 3447 of \mathbf{y} belonging to either \mathcal{H}_1 or \mathcal{H}_0 .

3448 The CNN architecture used for this work is summarized by Table 4.1. No strategic
 3449 hyper-parameter optimization approach was implemented beyond the manual testing
 3450 of different CNN architecture variations, so this particular model is best viewed as a

Table 4.1. A summary of the CNN model layers and parameters. The output of each 1D-Convolution and Fully Connected layer is passed through a LeakyReLU activation function and re-normalized using batch normalization before being passed to the next layer in the model. The output of the final Fully Connected layer in the model is left without activation so that the model outputs can be directly passed to the Binary Cross-entropy loss function used during training.

Layer	Type	Input Channels	Output Channels	Parameters
1	1D-Convolution	2	15	($N_{\text{kernel}} = 4$, $N_{\text{stride}} = 1$)
2	Maximum Pooling	15	15	($N_{\text{kernel}} = 4$, $N_{\text{stride}} = 4$)
3	1D-Convolution	15	20	($N_{\text{kernel}} = 4$, $N_{\text{stride}} = 1$)
4	Maximum Pooling	20	20	($N_{\text{kernel}} = 4$, $N_{\text{stride}} = 4$)
5	1D-Convolution	20	25	($N_{\text{kernel}} = 4$, $N_{\text{stride}} = 1$)
6	Maximum Pooling	25	25	($N_{\text{kernel}} = 4$, $N_{\text{stride}} = 4$)
7	Fully Connected	3200	512	NA
8	Fully Connected	512	64	NA
9	Fully Connected	64	2	NA

³⁴⁵¹ proof-of-concept rather than a rigorously optimized design. Numerous model variations
³⁴⁵² were tested, some with significantly more layers and convolutions filters per layer, as
³⁴⁵³ well as others that were even smaller than the architecture in Table 4.1. Ultimately, the
³⁴⁵⁴ model architecture choice was driven by the motivation to find the minimal model whose
³⁴⁵⁵ classification performance was still comparable to the larger CNN’s tested, because of
³⁴⁵⁶ the importance of minimizing computational cost in real-time applications. It is possible
³⁴⁵⁷ that more sophisticated machine learning models could improve upon the classification
³⁴⁵⁸ results achieved here, but we leave this investigation for future work.

³⁴⁵⁹ 4.4.4 Methods

³⁴⁶⁰ 4.4.4.1 Data Generation

³⁴⁶¹ To test the triggering performance of the classifiers, simulated CRES signals were
³⁴⁶² generated using the Locust simulations package [61, 79] developed by the Project 8
³⁴⁶³ collaboration. Locust uses the separately developed Kassiopeia package to calculate the
³⁴⁶⁴ magnetic fields produced by a user defined set of current carrying coils along with any
³⁴⁶⁵ specified background magnetic fields, resulting in a magnetic trap. Next, Kassiopeia
³⁴⁶⁶ calculates the trajectory of an electron in this magnetic field starting from a set of user
³⁴⁶⁷ specified initial conditions. The Locust software then uses the electron trajectories from
³⁴⁶⁸ Kassiopeia to calculate the resulting electromagnetic fields using the Liénard-Wiechert
³⁴⁶⁹ equations, and determine the voltages generated in the antenna array with the antenna

3470 transfer function. Locust then simulates the down-conversion, filtering, and digitization
3471 steps resulting in the simulated CRES signals for an electron.

3472 The shape of the received CRES signal is determined by the initial kinematic param-
3473 eters, including the starting position of the electron, the starting kinetic energy of the
3474 electron, and the pitch angle. For the studies performed here we constrain ourselves to a
3475 single initial electron position located at $(x, y, z) = (5, 0, 0)$ mm, and using this starting
3476 position we generate two datasets by varying the initial kinetic energy and the starting
3477 pitch angle. The first dataset consists of a two-dimensional square grid of kinetic energy
3478 and pitch angle spanning an energy range from 18575-18580 eV with a spacing of 0.1 eV,
3479 and pitch angles from 85.5-88.5° with a spacing of 0.001°, resulting in 153051 signals with
3480 a unique energy-pitch angle combination. This dataset is intended to represent a matched
3481 filter template bank. The second dataset was generated by randomly sampling uniform
3482 probability distributions covering the same parameter space to produce approximately
3483 50000 signals randomly parameterized in energy and pitch angle. This dataset provides
3484 the training and test data for the machine learning approach, and acts as a representative
3485 sample of signals to evaluate the performance of the matched filter template bank.

3486 Each signal was simulated for a duration of 40.96 μ s, which is equivalent to 8192
3487 samples at the FSCD digitization rate, and begins at time $t = 0$ s for all simulations.
3488 This duration represents a single frequency spectrum generated by the STFT. The output
3489 of the Locust simulation is a matrix of array snapshots with size given by the number of
3490 channels times the event length ($N_{\text{ch}} \times N_{\text{sample}}$), which we pre-process using the digital
3491 beamforming summation and STFT described in Section 4.4.2.2. The ∇B -drift correction
3492 uses the exact value of $\omega_{\nabla B}$, obtained from the Kassiopeia simulation of that electron.
3493 In practice, an average value for $\omega_{\nabla B}$ could be used, because there is limited variation in
3494 drift frequency across this parameter space.

3495 4.4.4.2 Template Number and Match Estimation

3496 The estimated PDF for the matched filter template bank depends on the score of the
3497 best matching template or equivalently the match of the best template (Γ_{best}) as well
3498 as the number of templates. One expects that with a higher number of templates the
3499 average value of Γ_{best} will increase, however, there is a point of diminishing returns at
3500 which more templates will not significantly increase match, but will still increase the
3501 likelihood of false positives. Therefore, it is desirable to use the minimum number of
3502 templates that provide an acceptable mean value of Γ_{best} .

3503 To quantify the relationship between match and template number, we calculated

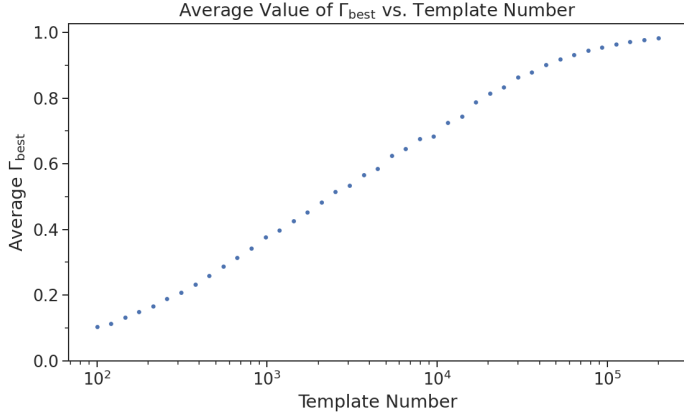


Figure 4.34. The mean match of the matched filter template bank to a test set of randomly parameterized signals as a function of the number or density of templates. The parameter space includes pitch angles from $85.5 - 88.5^\circ$ and energies from 18575 – 18580 eV.

the mean match of the random dataset to a selection of templates obtained from the regularly spaced dataset. The results are shown in Figure 4.34, where we find that the average value of Γ_{best} is an exponential function of the number of templates. From this plot we select the desired value of mean match at which we would like to evaluate the matched filter PDF and can infer the required number of templates.

4.4.4.3 CNN Training and Data Augmentation

To prepare the data for training the model, we split the random dataset in half to create distinct training and test datasets. Additionally, a randomly selected 20% of the training data is isolated for use as a validation set during the training loop. The size of the training, validation, and test datasets are then tripled by appending two additional copies of the data to increase the sample size of the dataset after data augmentation. The data is loaded with no noise, which is added to each data batch during the training phase by generating a new noise sample from a complex WGN distribution. In order to ensure an even split between signal and noise data we append to the noise-free signals an equal number of empty signals composed of all zeros. Therefore, as the data is randomly shuffled during training, on average an equal number of empty signals will be included with the training signals. After adding the sample of WGN to the data batch, the empty signals represent the noise-only data that the model must distinguish from signal data.

As the training signals are loaded we apply a unique random phase shift as the first form of data augmentation. Since the data is generated using the same initial axial position and cyclotron orbit phase, the randomization is an attempt to prevent

3525 overtraining on these features. During each training epoch the data is randomly shuffled
 3526 and split into batches of 2500 signals. Each batch of signals is then circularly shifted
 3527 by a random number of frequency bins to simulate a kinetic energy shift from -75 to
 3528 20 eV to simulate a training dataset with a larger energy range. Next, a sample of
 3529 complex WGN, consistent with the expected 10 K Nyquist-Johnson noise expected for
 3530 the FSCD, is generated and added to the signal, which prevents overtraining on noise
 3531 features. As a final step, the data is renormalized by the standard deviation of the noise
 3532 so that the range of values in the data is close to $[-1, 1]$, which helps ensure well-behaved
 3533 back-propagation.

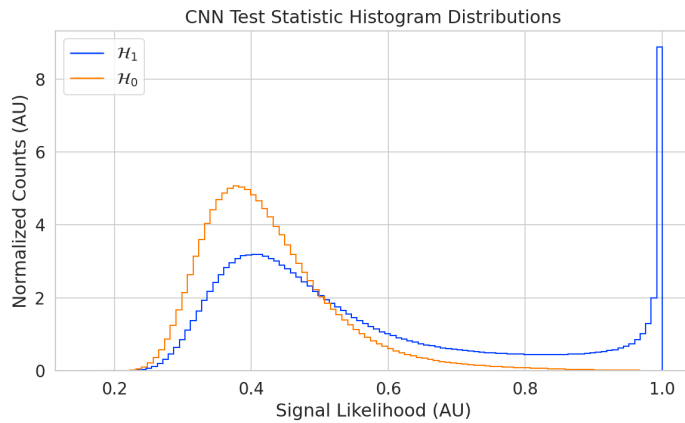


Figure 4.35. Histograms of the trained CNN model output from the test dataset. The blue histogram shows the model outputs for signal data. The oddly shaped peak near the end is the result of the softmax function mapping the long tail of the raw output distribution to the range $[0, 1]$.

3534 The Binary Cross-entropy loss function is used to compute the loss for each batch of
 3535 data and the model weights are updated using the ADAM optimizer with a learning rate
 3536 of 5×10^{-3} . After each training epoch, the loss and classification accuracy of the validation
 3537 dataset are computed to monitor for overtraining. It was noticed that the relatively high
 3538 noise power and the fact that a new sample of noise was used for each batch together
 3539 provided a strong form of regularization, since no evidence of over-training was observed
 3540 even after several thousand epochs. Typically, the loss and classification accuracy of
 3541 the model converged after a few hundred training epochs, but the training loop was
 3542 extended to 3000 epochs to attempt to achieve the best possible performance. The
 3543 training procedure generally took about 24 hrs using a single NVIDIA V100 GPU [81].

3544 After training the model, we use it to classify the test dataset and generate
 3545 histograms of the model outputs for both classes of data. The data augmentation

3546 procedure for the evaluation of the test data mirrors the training procedure without
 3547 the validation split. Since a random circular shift and a new sample of WGN is added
 3548 to each batch, the testing evaluation loop is run for 100 epochs to get a representative
 3549 sample of noise and circular shifts. The model outputs for each batch are passed through
 3550 a softmax activation and then combined into histograms, which we show in Figure 4.35.

3551 4.4.5 Results and Discussion

3552 4.4.5.1 Trigger Classification Performance

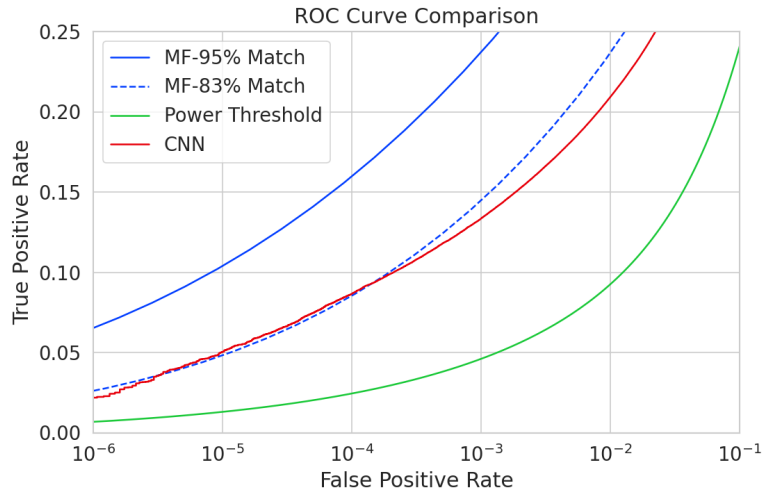


Figure 4.36. ROC curves describing the detection efficiency or true positive rates for the three signal classification algorithms examined in this paper.

3553 Using the matched filter and power threshold CDFs, along with the classification
 3554 results from the CNN, we compare detection performance by computing receiver operating
 3555 characteristic (ROC) curves. Specifically, we compare the detection performance averaged
 3556 over the full signal parameter space in order to get a measure of the overall detection
 3557 efficiency achieved by each algorithm. For the power threshold and matched filter
 3558 algorithms, we obtain the mean ROC curve by taking the average over all signals in the
 3559 regularly spaced dataset. In the case of the matched filter, we examine two cases using
 3560 different numbers of templates, which have different values of mean match. The ROC
 3561 curve describing the CNN is obtained by forming a histogram of the network outputs
 3562 for each class of signal and from this computing the estimated CDFs and ROC curve.
 3563 In Figure 4.36, we show the ROC curves obtained for each of the detection algorithms,
 3564 visualized in terms of true positive rate and false positive rate.

3565 The true positive rate of a signal classifier is equivalent to its detection efficiency, and
3566 we see that for the population of signals with pitch angles $< 88.5^\circ$ the power threshold
3567 has a consistently lower detection efficiency than the CNN and the matched filter. This
3568 result could have been predicted from the visualization of signal spectra in Figure 4.31,
3569 where we see that there is no way to distinguish between a noise peak and a signal peak
3570 with high confidence at small pitch angles. The CNN offers a significant and consistent
3571 increase in detection efficiency over the power threshold approach, with the relative
3572 improvement in detection efficiency increasing as the false positive rate decreases. If
3573 we compare the CNN to the matched filter, we see that the performance of the tested
3574 network is roughly equivalent to a matched filter detector with an average match of
3575 about 83%, which uses approximately 20000 matched filter templates. The overall best
3576 detection efficiency is achieved by the matched filter classifier if a large enough template
3577 bank is used. We show in the plot the ROC curve for a matched filter template bank
3578 with 95% average match, which is achieved with approximately 100000 templates. Since
3579 the matched filter is known to be statistically optimal for detecting a known signal in
3580 WGN, it is somewhat expected that this algorithm has the highest detection efficiency.

3581 A potentially impactful difference between the matched filter and CNN algorithms is
3582 that the CNN relies upon convolutions as its fundamental calculation mechanism, whereas
3583 our implementation of a matched filter utilizes an inner product. Since convolution is
3584 a translation invariant operation, the detection performance of CNN can be extended
3585 to a wider range of CRES event kinetic energies with less cost than the matched filter,
3586 a feature that we exploited during the CNN training by including circular translations
3587 of the CRES frequency spectra in the training loop. Increasing the range of kinetic
3588 energies detectable by a matched filter requires a proportional increase in the number of
3589 templates, which directly translates into increased computational and hardware costs.
3590 From a practical perspective, the detection algorithm is always limited by the available
3591 computational hardware, so estimating the relative costs is a key factor in determining
3592 their feasibility. Below we perform a more detailed analysis of the relative costs of each
3593 of the detection algorithms.

3594 4.4.5.2 Computational Cost and Hardware Requirements

3595 In the process of investigating triggering approaches for an antenna array CRES experi-
3596 ment, we have uncovered a strong tension between detection efficiency and computational
3597 resources. To relate the computational cost estimates to actual costs, we compare the
3598 theoretical amount of computer hardware required to implement the signal classifiers

3599 for real-time detection in an FSCD experiment. To do this we shall utilize order of
3600 magnitude estimates of the theoretical peak performance values for currently available
3601 Graphics Processing Units (GPUs) as a metric. This approach will underestimate the
3602 amount of required hardware, since it is unlikely that any CRES detection algorithm
3603 could reach the theoretical peak performance of the hardware.

3604 Of the three detection algorithms tested, the power threshold classifier is the least
3605 expensive. It requires that we check whether the amplitude of each frequency bin in
3606 the STFT is below or above our decision threshold. The STFT combined with digital
3607 beamforming produces $N_{\text{bin}}N_b$ frequency bins that must be checked every N_{bin}/f_s seconds.
3608 This requires approximately $O(10^{10})$ FLOPS to check in real-time. Current generations of
3609 GPUs have peak theoretical performances in the range of $O(10^{13}) - O(10^{14})$ FLOPS [82],
3610 dependent on the required floating-point precision of the computation. Therefore, the
3611 entire computational needs of a real-time triggering system using a power threshold
3612 classifier, including digital beamforming and generation of the STFT, could be met by a
3613 single high-end GPU or a small number of less powerful GPUs. Since triggering is only
3614 one step of the full real-time signal reconstruction approach, limiting the computational
3615 cost of this stage is ideal. However, we have seen that the power threshold classifier does
3616 not provided sufficient detection efficiency across the entire range of possible signals,
3617 which is the primary motivation for exploring more complicated triggering solutions.

3618 As discussed, the computational cost of the matched filter approach requires counting
3619 the number of templates that must be checked for each frequency spectra produced by the
3620 STFT. Computing the matched filter scores requires $O(N_bN_tN_{\text{bin}})$ operations, since for
3621 each of the N_b beamforming positions we must multiply N_t templates with a data vector
3622 that has length N_{bin} . The time within which we must perform this calculation is equal
3623 to N_{bin}/f_s to keep up with the data generation rate. To cover the 5 eV kinetic energy
3624 range spanned by the template bank, we saw that 10^4 to 10^5 templates are required in
3625 order to match or exceed the detection efficiency of the CNN. If the number of templates
3626 scales linearly with then kinetic energy range of interest as expected, then we would
3627 require 10^5 to 10^6 matched filter templates with this more realistic range of energies.
3628 Considering this, the estimated computational cost of the matched filter is between
3629 $O(10^{15})$ to $O(10^{16})$ FLOPS, which is $O(10^2)$ to $O(10^3)$ high-end GPUs.

3630 Lastly, we have the CNN classifier. To estimate the computational cost we simply
3631 sum the number of convolutions and matrix multiplications specified by the network
3632 architecture shown in Table 4.1. Each convolutional layer consists of $N_{\text{in}}N_{\text{out}}N_{\text{kernel}}L_{\text{input}}$
3633 floating-point operations, where N_{in} is the number of input channels, N_{out} is the number

3634 of output channels, N_{kernel} is the size of the convolutional kernel, and L_{input} is the length
3635 of the input vector, and the fully connected layers each contribute $N_{\text{in}}N_{\text{out}}$ operations.
3636 Summing all the neural network layers we estimate that the CNN would require $O(10^6)$
3637 floating point operations for each frequency spectra; therefore, the total computation
3638 cost of the CNN trigger is this cost times the number of beamforming positions per the
3639 data acquisition time, which is $O(10^{13})$ FLOPS or $O(10^0)$ GPUs.

3640 Compared with the matched filter approach the CNN requires $O(100)$ to $O(1000)$
3641 fewer GPUs to implement, dependent on the exact number of templates used in the
3642 template bank. The 100 eV kinetic energy range is motivated by the application of these
3643 detection algorithms to an FSCD-like neutrino mass measurement experiment. However,
3644 if a significantly larger range of kinetic energies is required, a CNN may be the preferred
3645 detection approach despite the lower average detection efficiency due to computational
3646 cost considerations. The low estimated computational cost of the CNN is directly related
3647 to the small network size.

3648 Additional experiments with larger CNNs, generated by increasing the depth and
3649 width of the neural network, and we observed that these changes provided minimal
3650 ($\lesssim 1\%$) improvement in the classification accuracy of the model. A potential reason
3651 for this could be the sparse nature of the signals in the frequency domain and the low
3652 SNR which makes for a challenging dataset to learn from. Future work could investigate
3653 modifications to the neural network architecture such as sparse convolutions, which may
3654 improve the classification accuracy of the model or further reduce the computational
3655 costs of this approach. Alternatively, more complicated CNN architectures such as a
3656 ResNet [83] or VGG model [84] may provide improved classification performance over a
3657 basic CNN. An additional promising area of investigation are recurrent neural networks,
3658 which may be able to exploit the time-ordered features of the STFT for more accurate
3659 signal detection if the electron signals last for multiple Fourier transform windows.

3660 Our estimate of the computational cost of the matched filter is somewhat naive if
3661 we notice that the majority of the values that make up a CRES frequency spectra are
3662 zero (see Figure 4.31). Therefore, the majority of operations in the matched filter inner
3663 product are unnecessary, and we could instead evaluate the matched filter inner product
3664 using only the $\lesssim 10$ frequency peaks that make up CRES signal. This optimization
3665 reduces the number of operations required to check each template by a factor of $O(100)$
3666 to $O(1000)$, which brings the estimated computational cost of the matched filter in
3667 line with the CNN. Although this level of sparsity results in a multiplication with very
3668 low arithmetic complexity, the resulting sparse matched filter algorithm is still likely

3669 to be constrained by memory access speed rather than compute speed. Ultimately, the
3670 comparison of the relative computational and hardware costs between the matched filter
3671 and CNN will depend on the efficiency of the software implementation and hardware
3672 support for neural network and sparse matrix calculations.

3673 **4.4.6 Conclusion**

3674 Increasing the detection efficiency and overall event rate of the CRES technique represents
3675 a key developmental path towards new scientific results and broader applications of the
3676 CRES technique. It is what motivates both the antenna array detection approach and
3677 the development of real-time signal reconstruction algorithms. We have demonstrated
3678 that significant gains in the detection efficiency of the CRES technique are achievable
3679 by utilizing triggering algorithms that account for the specific shape of CRES signals in
3680 the detector. These algorithms emphasize the need for accurate and fast methods for
3681 CRES simulation, since they directly contribute to the success of matched filter methods
3682 by providing a way to generate expected signal templates and also serve as a source of
3683 training data for machine learning approaches.

3684 The improvements in detection efficiency offered by these alternative approaches to
3685 triggering are crucial to the success of efforts to develop scalable technologies for CRES
3686 measurement, since they provide a significant increase in the detectable parameter space
3687 of CRES events, which allows for a better utilization of the larger detection volume.
3688 While we have focused on the real-time detection of CRES signals from antenna arrays,
3689 these same signal classifiers could be used in CRES experiments utilizing a different
3690 detector technologies, since the same principles of signal detection will apply. For example,
3691 previous CRES measurements by the Project 8 collaboration that utilized a waveguide
3692 gas cell, could have improved their detection efficiency by employing a matched filter
3693 or neural network classifier to identify trapped electrons with pitch angles that are too
3694 small to be detected by the power threshold approach. Furthermore, alternative CRES
3695 detector technologies such as resonant cavities [40] could also see similar improvements
3696 in detection efficiency, which is of crucial importance to future efforts by the Project 8
3697 collaboration to utilize CRES to measure the neutrino mass.

Chapter 5

Antenna and Antenna Measurement System Development for the Project 8 Experiment

5.1 Introduction

The FSCD and antenna array CRES represent an innovative approach to beta-decay spectroscopy. While much can be learned from simulations about the systematics of CRES with antenna arrays, laboratory measurements and demonstrations provide critical inputs to sensitivity and simulation models as well as provide a means for calibration and commissioning of the experiment. Therefore, a robust program of antenna and antenna measurement hardware development is important to the success of the FSCD and the development of antenna array CRES more broadly.

In this chapter we summarize the development of an antenna measurement system at Penn State to implement and test the techniques of antenna array CRES on the bench-top, in order to support the efforts of the Project 8 collaboration. In Section 5.2 we provide an introduction to some fundamental parameters and concepts related to antenna measurements as well as an overview of the Penn State antenna measurement system hardware. In Section 5.3 we include the manuscript of a paper [80] which details the design and characterization of a specialized antenna developed to mimic the electric fields emitted by an electron in a CRES experiment. This antenna, called the Synthetic Cyclotron Antenna (SYNCA), is intended as a calibration tool for antenna arrays developed for CRES measurements. Lastly, in Section 5.5 we summarize a set of prototype FSCD antenna array measurements with the SYNCA [43], which we use to validate the simulated performance of the antenna array and estimate systematic errors associated with the antenna array.

3723 5.2 Antenna Measurements for CRES experiments

3724 5.2.1 Antenna Parameters

3725 Antenna characterization measurements are intended to validate simulations of the
3726 antenna array performance, which ultimately informs the neutrino mass sensitivity of
3727 the experiment. In this section, I shall summarize a few fundamental concepts relating
3728 to antennas and antenna measurement, before introducing how Project 8 uses antenna
3729 measurement for the development of antenna array CRES.

3730 5.2.1.1 Radiation Patterns

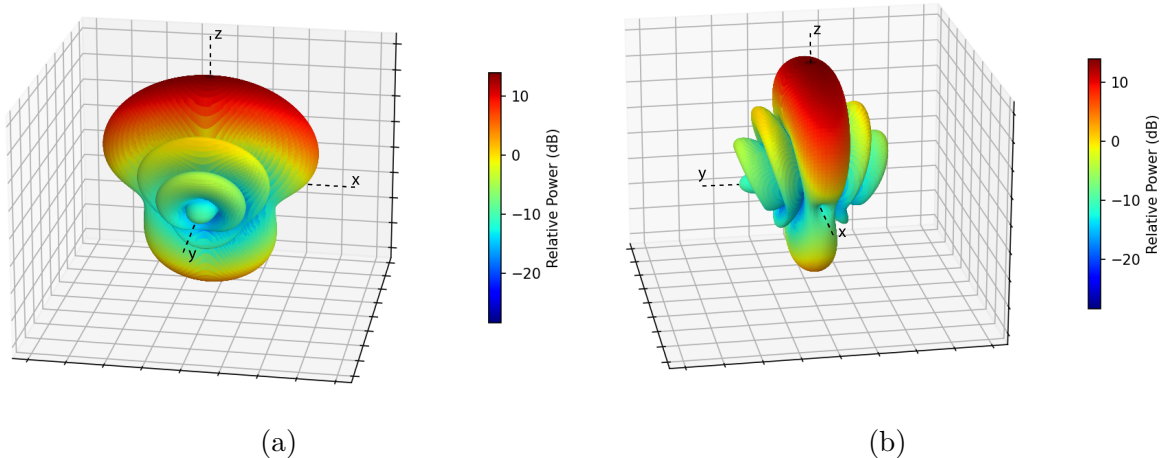


Figure 5.1. An example radiation pattern generated using HFSS simulations. The color and radial distance of the surface from the origin indicate the relative magnitude of radiation power emitted by the antenna in that direction. The primary goal of most antenna measurements is typically to measure the antenna pattern, which is used to derive many useful antenna performance parameters.

3731 Antennas are conductive structures designed to carry alternating electric currents
3732 in order to transmit energy in the form of electro-magnetic (EM) waves [64]. Perhaps
3733 the most fundamental way to characterize an antenna, is to map out the radiated power
3734 density as a function of position, which is called the radiation pattern (see Figure 5.1).
3735 We find the radiation power density by calculating the time-averaged Poynting vector for
3736 all positions surrounding the antenna, which in equation form is

$$\mathbf{W}(x, y, z) = \langle \mathbf{E}(x, y, z, t) \times \mathbf{H}^*(x, y, z, t) \rangle_t, \quad (5.1)$$

3737 where $\mathbf{E}(x, y, z, t)$ and $\mathbf{H}(x, y, z, t)$ are the time-dependent electric and magnetic fields
 3738 produced by the antenna [48]. The radiation power density has units of W/m^2 and is
 3739 more typically called the energy flux density in physics applications, since it is a measure
 3740 of the amount of energy passing through a unit area over time.

3741 Because the radiation power density is a measure of power per unit area, its value
 3742 in a particular direction will depend on the distance from the antenna at which we are
 3743 measuring. This is undesirable for practical applications A related quantity, which is
 3744 distance independent, is the energy flux per unit solid angle or radiation intensity, which
 3745 is computed directly from the radition power density by multiplying by the squared
 3746 distance from the antenna. Specifically,

$$U = r^2 W(x, y, z), \quad (5.2)$$

3747 where r is the distance from the antenna to the field measurement point. The radiation
 3748 intensity is typically defined in regions where the Poynting vector consists only of a radial
 3749 component where it is safe to treat as a scalar quantity.

3750 5.2.1.2 Directivity and Gain

3751 Since the radiation intensity is a measure of average power per unit solid angle, it is
 3752 independent of distance and more useful as feature for antenna measurement. However,
 3753 most antenna measurements are performed in terms of the directly related directivity
 3754 and gain quantities. Directivity is defined as the ratio between the radiation intensity at
 3755 particular point on the radiation pattern to the average radiation intensity computed
 3756 over all solid angles [64]. The equation that relates the radiation intensity to directivity
 3757 is

$$D = \frac{U}{U_0} = \frac{4\pi U}{P_{\text{rad}}}, \quad (5.3)$$

3758 where U_0 is the average radiation intensity over all solid angles, which simply the total
 3759 radiated power (P_{rad}) divided by 4π . Closely related to directivity is concept of gain,
 3760 which accounts for energy losses that occur inside then antenna when attempting to
 3761 transmit or receive a signal. The antenna gain is given by

$$G = \frac{4\pi U}{P_{\text{in}}}, \quad (5.4)$$

3762 where P_{in} is the total power delivered to the antenna. Gain can be thought of as the ratio
 3763 of the antenna's radiation intensity to that of a hypothetical isotropic, lossless radiator.

3764 The maximum values of gain and directivity exhibited by the main lobe of the antenna
 3765 pattern as well as the ratio between the gain of the main lobe and any side-lobes are
 3766 important figures of merit used to evaluate antenna designs.

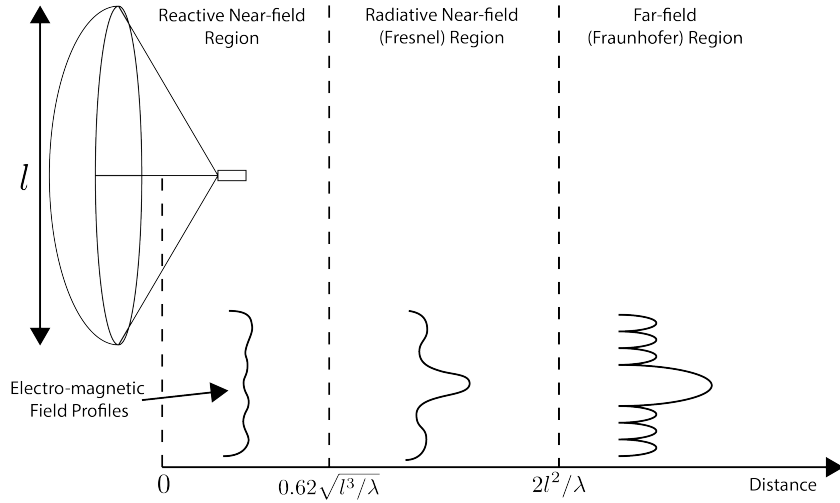


Figure 5.2. An illustration of the three field regions important for the analysis of an antenna system. Very close to the antenna the electric fields are primarily reactive so there is no radiation. If a receiving antenna were placed in this region most of the energy would be reflected back to the transmitter. Outside of the reactive near-field is the radiative near field. At these distances the antenna does radiate, but the radiation pattern is not well-defined since it changes based on the distance of the receiving antenna. It is only in the far-field region where the radiation pattern becomes constant as a function of distance, which is where the majority of antenna engineering is assumed to take place. The antenna arrays developed by Project 8 for CRES measurements operate in the radiative near-field due to the importance of limiting power loss from free-space propagation, which complicates the design of the antenna system.

3767 5.2.1.3 Far-field and Near-field

3768 Radiation patterns are only well-defined in regions where the shape of the radiation
 3769 pattern is independent of distance. The region where this approximation is valid is called
 3770 the "far-field", and in this region we can treat the EM fields from the antenna as spherical
 3771 plane waves. A rule of thumb for antennas is that the far-field approximation is valid
 3772 when the condition

$$R > \frac{2l^2}{\lambda} \quad (5.5)$$

3773 is met. In this expression, R is the distance from the antenna, l is the largest characteristic
 3774 dimension of the antenna, and λ is the wavelength of the radiation (see Figure 5.2).

3775 The region very close to the antenna is called the reactive near-field, because in this
 3776 region the reactive component of the EM field is dominant. Unlike radiative electric

fields, the reactive electric and magnetic fields are out of phase from each other by 3777
 90°, since they are the result of electrostatic and magnetostatic effects coming from the 3778
 self-capacitance and self-inductance of the antenna. The reactive fields are unable to 3779
 transfer energy a significant distance from the antenna and are thus completely negligible 3780
 for most antenna applications. The limit of the reactive near-field for an electrically-large 3781
 antenna is typically taken to be 3782

$$R < 0.62\sqrt{l^3/\lambda}. \quad (5.6)$$

The unique application of antennas by Project 8 is somewhat limited by reactive near- 3783
 field effects in the form of a maximum radial position for electrons inside the uniform 3784
 cylindrical antenna array. If electrons are too close to the edge of the array than reactive 3785
 near-field effects leads to a large reduction in the received power and consequently 3786
 detection efficiency. This leads to a significant volume inside of the antenna array that 3787
 is unsuitable for CRES lowering the volumetric efficiency of the antenna array CRES 3788
 technique relative to a cavity experiment. 3789

In between the reactive near-field and the far-field is the radiative near-field region. 3790
 In this region the fields are primarily radiative, however we are still too close to the 3791
 antenna for the spherical plane wave approximation to apply. Therefore, interference 3792
 effects between EM waves emitted from different points on the antenna occur causing the 3793
 shape of the radiation pattern to change as a function of distance from the antenna. If we 3794
 evaluate the far-field distance limit for the FSCD one finds an estimated far-field distance 3795
 of 43 cm, which is a factor of four larger than the radius of the antenna array designed for 3796
 the experiment. Consequently, we expect near-field effects to influence the performance 3797
 of the antenna array highlighting the importance of calibration and characterization 3798
 measurements. 3799

5.2.1.4 Polarization

The polarization of an EM wave defines the spatial orientation of the electric field 3801
 oscillations in the plane perpendicular to the direction of the propagation, and is defined 3802
 in terms of orthogonal polarization components. In our application, one analyzes the 3803
 properties of radiation propagating along the radial (\hat{r}) direction away from the antenna, 3804
 which implies that the electric fields can be described as a linear combination of orthogonal 3805
 polarization components 3806

$$\mathbf{E}_{\text{tot}} = E_x \hat{x} + E_y \hat{y} + E_z \hat{z}, \quad (5.7)$$

3807 in Cartesian coordinates, or

$$\mathbf{E}_{\text{tot}} = E_\theta \hat{\theta} + E_\phi \hat{\phi}, \quad (5.8)$$

3808 in spherical coordinates.

3809 In general, one defines partial radiation patterns, directivities, and gains so that the
3810 performance of the antenna for the desired polarization can be analyzed. The radiation
3811 pattern defined in terms of partial patterns is

$$U_{\text{tot}} = U_\phi + U_\theta, \quad (5.9)$$

3812 where U_ϕ and U_θ are the radiation intensities in a particular direction for the respective
3813 polarization components. Similarly, a quantity such as gain can be written in terms of
3814 partial gains,

$$G_{\text{tot}} = G_\phi + G_\theta = \frac{2\pi U_\phi}{P_{\text{in}}} + \frac{2\pi U_\theta}{P_{\text{in}}}. \quad (5.10)$$

3815 If we view an electron performing a circular orbit in the XY-plane from the side, that
3816 is, along the X or Y axes, then we would observe the electron to be performing a linear
3817 oscillation perpendicular to the viewing axis. From this intuitive picture, we can predict
3818 that the primary polarization of electric fields from CRES events to be linearly polarized
3819 in the $\hat{\phi}$ direction when viewed with an antenna positioned in the XY-plane.

3820 5.2.1.5 Antenna Factor and Effective Aperture

3821 A useful way to characterize the performance of an antenna is to measure the electric
3822 field magnitude required to produce a signal with an amplitude of one volt in the antenna
3823 terminals. This ratio between the magnitude of the incoming electric field and the
3824 magnitude of the signal produced by the antenna is called the antenna factor, which is
3825 written as

$$A_F = \frac{|\mathbf{E}_{\text{in}}|}{V_{\text{ant}}}, \quad (5.11)$$

3826 where A_F is the antenna factor, E_{in} is the incoming electric field, and V_{ant} is the magnitude
3827 of the voltage produced by the antenna.

3828 The antenna factor can be expressed in terms of the antenna's gain through a related
3829 quantity called the effective aperture. The effective aperture defines for a given incident
3830 radiation power density (W/m^2) the power that is received by the antenna. Therefore,

3831 the effective aperture gives the equivalent area of the antenna,

$$A_{\text{eff}} = \frac{P_{\text{rec}}}{P_{\text{in}}} = \frac{\lambda^2}{4\pi} G, \quad (5.12)$$

3832 where the received power is P_r and the total incoming power is P_{in} .

3833 If we express the incident power in terms of the magnitude of the Poynting vector,
3834 then

$$|\mathbf{S}_{\text{in}}| = |\mathbf{E}_{\text{in}}|^2 / \eta_0, \quad (5.13)$$

3835 where η_0 is the impedance of free-space, which relates the magnitudes of the electric and
3836 magnetic fields in a vacuum, and is defined by

$$\eta_0 = \frac{|\mathbf{E}|}{|\mathbf{H}|} = \sqrt{\frac{\epsilon_0}{\mu_0}}. \quad (5.14)$$

3837 The total received power by the antenna can therefore be expressed as

$$P_{\text{rec}} = |\mathbf{S}_{\text{in}}| A_{\text{eff}} = |\mathbf{S}_{\text{in}}| \frac{\lambda^2}{4\pi} G = \frac{|\mathbf{E}_{\text{in}}|^2 \lambda^2 G}{4\pi \eta_0}. \quad (5.15)$$

3838 To relate this to the antenna factor recall that we can relate the voltage produced by
3839 the antenna to the received power with

$$P_{\text{rec}} = \frac{V_{\text{ant}}^2}{Z} = \frac{|\mathbf{E}_{\text{in}}|^2}{A_F^2 Z}, \quad (5.16)$$

3840 where Z is the system impedance. Setting Equations 5.15 and 5.16 equal to each other,
3841 we obtain the following expression for antenna factor in terms of gain

$$A_F = \sqrt{\frac{4\pi\eta_0}{ZG\lambda^2}} = \frac{9.73}{\lambda\sqrt{G}}. \quad (5.17)$$

3842 The second expression in Equation 5.17 is obtained by evaluating the constant terms
3843 assuming a system impedance of 50Ω .

3844 We have gone through the effort of expressing the antenna factor in terms of gain
3845 to highlight that the majority of antenna parameters that we care to measure for a
3846 CRES experiment can be obtained from the radiation or gain pattern of the antenna.
3847 The antenna factor is a particularly important parameter for CRES measurements
3848 due to its relevance to antenna array simulations with the Locust software [61, 79].
3849 Specifically, Locust simulates the trajectory of an electron in a magnetic trap by running

3850 the Kassiopeia software package [59] and then uses the Liénard-Wiechert equations [62,63]
3851 to calculate the electric fields that are incident on the antenna.

3852 To compute the response of the antenna to the electric field, Locust relies upon
3853 linear time-invariant system theory, which computes the response of the antenna (i.e. the
3854 voltage time series generated by the antenna) using a convolution between the electric field
3855 time-series and the antenna impulse response. This approach is necessary for correctly
3856 modeling the antenna response to the electric field due to the broadband and non-
3857 stationary nature of the electric fields from CRES events. Since antenna measurements
3858 take place under steady-state conditions, parameters such as the radiation pattern, gain,
3859 and antenna factor are defined in the frequency domain. However, by performing an
3860 inverse Fourier transform on the antenna factor we can obtain the antenna impulse
3861 response, which allows us to simulate CRES events in the antenna array demonstrator
3862 experiment.

3863 **5.2.2 Antenna Measurement Fundamentals**

3864 **5.2.2.1 Friis Transmission Equation**

3865 The antenna factor, sometimes called the antenna transfer function, is used to model
3866 how the antenna will respond to electric fields emitted from a CRES event. Therefore,
3867 being able to measure the antenna transfer function of the antenna array is a key step
3868 in the commissioning and calibration phases of an antenna array CRES experiment. A
3869 common approach to antenna characterization is to perform a two antenna transmit-
3870 receive measurement where an antenna with a known gain is used to characterize the
unknown gain of the antenna under test (see Figure 5.3).

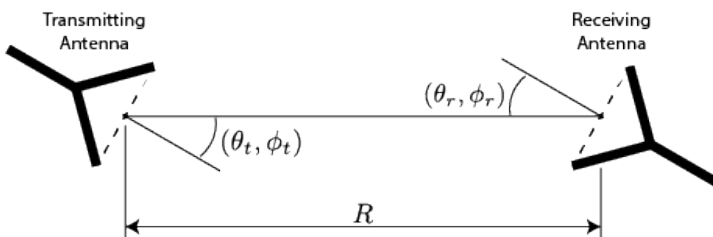


Figure 5.3. An illustration of the Friis measurement technique commonly used for antenna characterization measurements.

3871
3872 To analyze this two antenna setup we seek to calculate the amount of power from
3873 the transmitting antenna that we will detect with the receiving antenna. Using our
3874 understanding of antenna gain, we can calculate the power density transmitted by an

3875 antenna in a direction (θ_t, ϕ_t) at frequency f and distance R , which is given by

$$w_t = \frac{P_t}{4\pi R^2} G_t(\theta_t, \phi_t, f). \quad (5.18)$$

3876 Here, P_t is the total power delivered to the transmitting antenna and $G_t(\theta_t, \phi_t, f)$ is
 3877 the value of the transmitting antenna gain. The power density is the power per unit
 3878 area, so to calculate the total power delivered to the receiving antenna we multiply the
 3879 transmitted power density by the effective area of the receiving antenna,

$$P_r = w_t A_{eff,r} = P_t \frac{G_t(\theta_t, \phi_t, f) G_r(\theta_r, \phi_r, f) c^2}{(4\pi R f)^2}, \quad (5.19)$$

3880 where $G_r(\theta_r, \phi_r, f)$ is the gain of the receiving antenna. Equation 5.19 is called the Friis
 3881 transmission equation [85], which is of fundamental importance for antenna measurements,
 3882 since it allows one to measure the gain of an unknown antenna by measuring the power
 3883 received from an antenna with a known gain pattern. Alternatively, if no antenna with a
 3884 known gain pattern is available, two identical antennas with unknown gain patterns can
 3885 be used.

3886 5.2.2.2 S-Parameters and Network Analyzers

3887 Instead of directly measuring the power received by the antenna under test, it is more
 3888 common to measure the ratio of the received power to the transmitted power,

$$\frac{P_r}{P_t} = \frac{G_t(\theta_t, \phi_t, f) G_r(\theta_r, \phi_r, f) c^2}{(4\pi R f)^2}. \quad (5.20)$$

3889 This power ratio can be easily measured using a vector network analyzer (VNA), which
 3890 automates a significant fraction of the measurement process. Network analyzers are
 3891 used to measure the scattering or S-parameters of a multi-port RF device [86], which
 3892 describes how waves are scattered between the device ports. The antenna measurements
 3893 we have been considering can be modeled as a two-port microwave device that we can
 3894 characterize by measuring how incident voltage waves are transmitted or reflected (see
 3895 Figure 5.4). We can write the scattered waves (V_1^- and V_2^-) in terms of the incident (V_1^+
 3896 and V_2^+) waves using the scattering matrix

$$\begin{pmatrix} V_1^- \\ V_2^- \end{pmatrix} = \begin{pmatrix} S_{11} & S_{12} \\ S_{21} & S_{22} \end{pmatrix} \begin{pmatrix} V_1^+ \\ V_2^+ \end{pmatrix}, \quad (5.21)$$

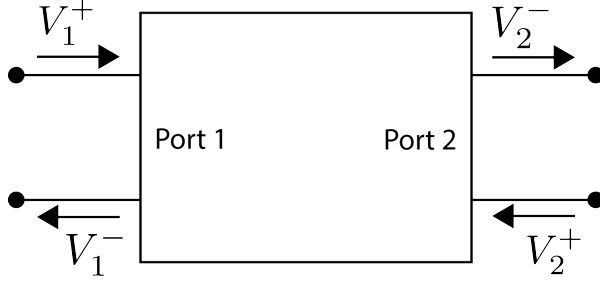


Figure 5.4. Illustration of a two-port S-parameter measurement setup. S-parameters characterize how incoming waves of voltage or power scatter off of the RF device under test. This allows you to measure important properties of the device. In particular, we can use this framework to model a two antenna radiation pattern measurement, which we can then automate using a VNA.

3897 where the elements of the matrix are the device S-parameters. It is assumed that,
 3898 when exciting the device from a particular port, that all other ports in the network are
 3899 terminated at the system impedance. This ensures that the incident waves from other
 3900 ports in the network are zero. Therefore, the S-parameters are the ratios between the
 3901 scattered and incident waves,

$$S_{ij} = \frac{V_i^-}{V_j^+}. \quad (5.22)$$

3902 Alternatively, S-parameters can be defined as the ratio of the scattered and incident
 3903 power, which is proportional to the ratio of the squared voltage waves. Returning to
 3904 our antenna measurement setup, we see that measuring the ratio of the received to the
 3905 transmitted power is equivalent to measuring the ratio of power being scattered from port
 3906 1 to port 2 in a RF network. Therefore, measuring an antenna's gain can be accomplished
 3907 quite easily, by using a VNA to perform a two port S_{21} measurement.

3908 5.2.2.3 Antenna Array Commissioning and Calibration Measurements

3909 Up to this point we have been discussing calibration and commissioning measurements
 3910 as they apply to a single antenna. While these measurements play an important role
 3911 in validating the radiation patterns of the individual array elements, the ultimate goal
 3912 is to use a phased array of these antennas. Therefore, we must also consider antenna
 3913 measurement techniques that apply to the whole array system.

3914 By measuring the gain of each individual array element we can predict the features of
 3915 the signals received during a CRES event using the antenna factor (see Section 5.2.1.5).
 3916 However, unpredictable changes to the antenna performance can be introduced by the
 3917 incorporation of the antennas into the circular array geometry, therefore, we employ both

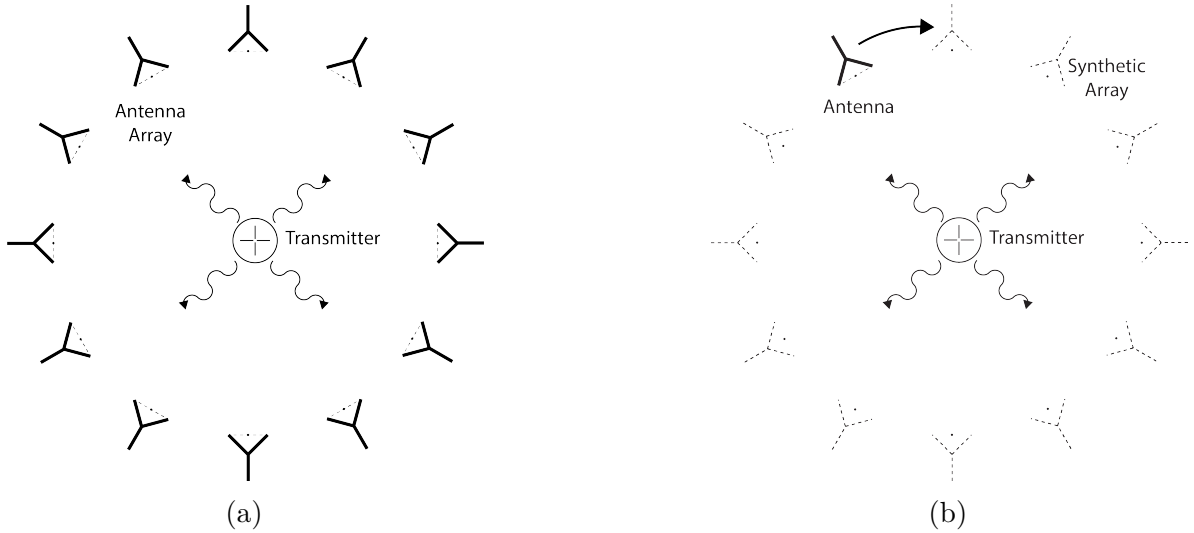


Figure 5.5. Two measurement approaches to characterizing an antenna array for CRES measurements. The full-array approach (a) requires a complete antenna array with all the associated hardware. The synthetic array approach (b) utilizes a single antenna and a set of rotation/translation stages to reposition the transmitter or the receiving antenna to synthesize the signals that would be received by the full-array. This approach reduces the cost and complexity of array measurements. A down-side of the synthetic array approach is that multi-channel effects such as reflections cannot be measured. Utilizing both the full-array and the synthetic array is a powerful way to quantify the impact of errors from the multi-channel array.

3918 individual antenna and full-array measurements in the commissioning of the FSCD to
 3919 account for these effects.

3920 There are two main approaches to array measurements that could be used for
 3921 characterization and calibration (see Figure 5.5). One approach is to construct the
 3922 complete array and use an omni-directional transmitting antenna to measure the power
 3923 received by each channel in the antenna array. In Section 5.3 we describe the development
 3924 of an omni-directional transmitter that also mimics the radiation phase characteristics of a
 3925 CRES event, which is useful because the entire array can be tested without repositioning.
 3926 Alternatively, a full antenna array can be synthesized by repeatedly moving and measuring
 3927 a single array element. This approach is ideal for identifying if different channels in the
 3928 antenna array are affecting each other through multi-path interference by comparing the
 3929 measurement results of the synthetic array to the real array.

5.2.3 The Penn State Antenna Measurement System

The development of antenna array based CRES requires the capability to test and calibrate different antenna array designs to validate the performance of the as-built antenna array before and during the experiment. With these aims in mind we developed an antenna measurement system at Penn State specifically designed to mimic the characteristics of the antenna experiment designed for demonstration of the antenna array CRES technique by the Project 8 collaboration.

The Penn State antenna measurement system utilizes a two antenna measurement configuration with a stationary reference antenna and a test antenna mounted on a set of motorized translation and rotation stages (see Figure 5.6). The antenna measurement system can be operated in two distinct modes, one focused on the characterization of the radiation patterns of prototype antennas and the other focused on the validation of data-acquisition (DAQ) and CRES signal reconstruction techniques to bridge the gap between real measurements and simulation. In both measurement configurations it is critical to isolate the antennas from the environment so that multi-path reflections do not negatively influence the measurement results. For this reason we surround the measurement volume with microwave absorber foam (AEMI AEC-1.5) specifically designed to attenuate microwave radiation near the 26 GHz measurement range of the system.

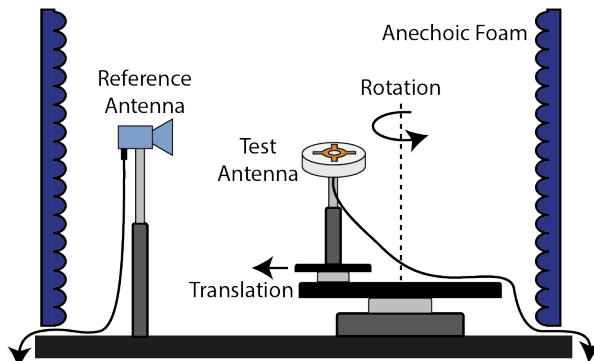


Figure 5.6. Illustration of the antenna measurement system developed for the Project 8 Collaboration. The reference and test antennas can be connected to different data acquisition configurations depending on the measurement goals. The reference antenna is typically a standard horn antenna and the test antenna is mounted on a set of translation stages for positioning. Automated translation stages allow for relatively painless data-taking enabling synthetic antenna array measurements using only a single receiving antenna. Anechoic foam designed to mitigate RF reflections surrounds the setup.

In the first measurement configuration the reference antenna is typically a well-

characterized horn antenna as pictured, since horn antennas have well-known and stable radiation patterns making them ideal as standard references. For characterization measurements, the test antenna represents the antenna-under-test whose pattern we wish to characterize. Mounting the test antenna on motorized rotation and translation stages allows us to automate the procedure significantly speeding up the radiation pattern measurement process.

In the second measurement configuration one is interested in recreating the conditions of an antenna array CRES experiment as it concerns the antenna array and DAQ system. In this case, the reference antenna is a prototype FSCD antenna, which will be used to construct the antenna array in the FSCD experiment, and the test antenna is a specially designed synthetic cyclotron antenna (SYNCA) as picture in Figure 5.6. The SYNCA is designed such that the radiation pattern mimics that of a CRES electron so that the signals received by the prototype CRES array antenna mimic what is expected for a real CRES experiment.

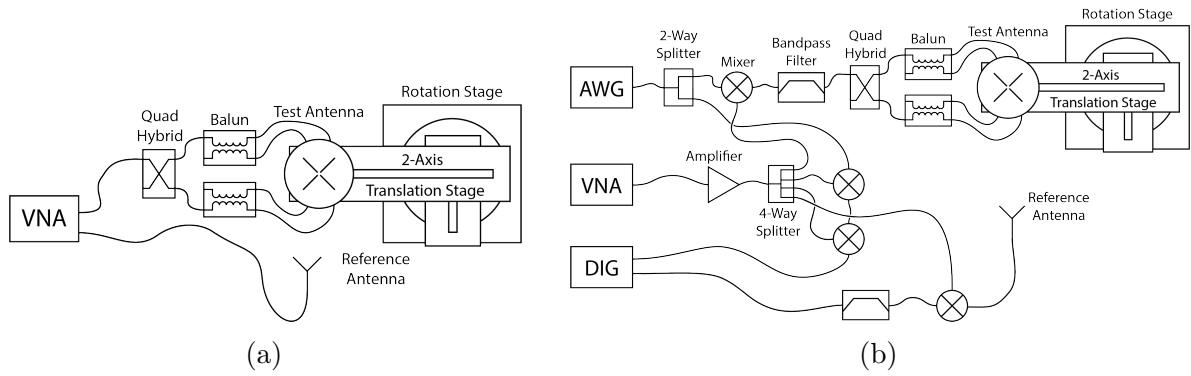


Figure 5.7. Diagrams of two measurement system configurations. Configuration (a) utilizes a VNA and is more suited to antenna characterization. Configuration (b) utilizes an AWG and VNA as a signal generation system and digitizer to collect measurement data, which is more suited to simulating CRES measurements. The transmission chain utilizes a quadrature hybrid and a pair of baluns to drive the cross-dipole variant test antenna developed for synthetic CRES measurements.

In Figure 5.7 we show two high-level system diagrams of the Penn State antenna measurement system that depict the important system components and the connections between them. The two configurations of the measurement system utilize different hardware. For characterization and radiation pattern measurements, one prefers the configuration shown in Figure 5.7a. In this case a vector network analyzer (VNA) is used as both the transmission source and data acquisition system and it is relatively easy to calibrate over a wide range of frequencies. Whereas, if one is more interested

3971 in recreating what would take place in the FSCD experiment then the configuration
3972 shown in Figure 5.7b is preferable, since this system effectively mimics the receiver chain
3973 envisioned for the FSCD experiment.

3974 The characterization configuration utilizes a network analyzer (Keysight N5222A)
3975 with two independent sources and four measurement ports as the primary measurement
3976 tool. A standard reference antenna is connected to one measurement port, and the test
3977 antenna is connected to a separate port. The typical reference antenna used for these
3978 studies is a Pasternack PF9851 horn antenna . In the measurement shown, the test
3979 antenna represents a SYNCA antenna, which requires a transmission chain consisting of
3980 quadrature hybrid coupler (Marki QH-0226) connected to two baluns (Marki BAL-0026)
3981 to generate feed signals with the appropriate phases. The VNA measures the radiation
3982 pattern by performing a transmission S-parameter measurement, which can be used with
3983 the knowledge of the reference antenna's radiation pattern to determine the radiation
3984 pattern of the test antenna (see Section 5.2.1).

3985 The second configuration is more complicated and incorporates more hardware
3986 components in order to more closely mimic the DAQ system envisioned for the FSCD
3987 experiment. The basic approach is to produce CRES-like radiation and use an antenna
3988 combined with a realistic RF receiver chain to acquire the signals. On the transmit side,
3989 an arbitrary waveform generator (AWG, RIGOL DG5252) is used to generate a waveform
3990 that mimics a CRES signal at a baseband frequency up to 250 MHz. This frequency is
3991 then up-converted to the CRES signal frequency band of 25.8 to 26.0 GHz using a mixer
3992 (Marki MM1-0832L) and a bandpass filter (K&L Microwave 3C62-25900/T200-K/K) to
3993 reject unwanted mixing components outside out of the 200 MHz CRES signal band. The
3994 local oscillator signal for mixing is provided by one of the VNA sources configured to run
3995 in a continuous wave setting. On the receive side, a prototype antenna is used to detect
3996 the radiation emitted by the test antenna, which is down-converted and filtered using
3997 the same mixer and bandpass filter as the transmission chain. Lastly, data acquisition is
3998 performed using a 14-bit ADC sampling at 500 MSa/s (CAEN DT530) to digitize the
3999 down-converted signals.

4000 In order to distribute the LO to all mixers a 4-way power splitter (MiniCircuits
4001 ZC4PD-18263-S+) along with an amplifier (Marki APM-6848) is used to drive the four
4002 mixers used in the measurement system. A limitation of using the VNA as an LO source
4003 is that there is no control of the LO phase when a measurement is triggered by the
4004 control script, which leads to a random phase offset between acquisitions. This makes it
4005 impossible to perform synthetic array measurements, which require strict control over

4006 the starting phase of the transmitted signal. In order to monitor the random phase of the
4007 LO, a 2-way power splitter (MiniCircuits Z99SC-62-S+) is used to split the signal from
4008 the AWG between the transmission path and a LO monitoring path. The LO monitoring
4009 path consists of an up-conversion and down conversion using two mixers connected by a
4010 coaxial cable, and monitors the relative phase of the LO using a channel on the digitizer
4011 to sample this path. A phase shift in the LO will lead to a proportional phase shift in
4012 the mixed signal, which is measured and removed from the received signals.

4013 The test antenna is mounted on a set of motorized stages, which are identical for
4014 both measurement configurations. A rotational stage (ThorLabs PRMTZ8) is used as
4015 the base layer with additional translation stages mounted on top of this. The rotational
4016 stage is ideal for measuring a complete azimuthal scan of the test antenna's radiation
4017 pattern as well as for moving a SYNCA antenna in circular motion to recreate the
4018 symmetry of the FSCD antenna array. On top of the rotational stage we mount two
4019 linear translation stages (ThorLabs MTS50-Z8 and MTS25-Z8) in a cross-wise manner
4020 so that the test antenna can be moved along two perpendicular axes. Using the linear
4021 stages in combination with the rotational stage allows one to fine-tune the positioning of
4022 the test antenna so that it can be perfectly aligned with the central axis of the array.
4023 A LabView script was developed to automate the measurement of a full 360° radiation
4024 pattern and control the measurement electronics. Data from these acquisitions is stored
4025 on university provided cloud storage.

4026 **5.3 Development of a Synthetic Cyclotron Antenna (SYNCA)** 4027 **for Antenna Array Calibration**

4028 This section is the manuscript of the publication [80] detailing the development of a
4029 Synthetic Cyclotron Antenna (SYNCA) for antenna array characterization measurements
4030 by the Project 8 collaboration.

4031 **5.3.1 Introduction**

4032 Neutrinos are the most abundant standard model fermions in our universe, but due to
4033 weak interaction cross-sections with other particles, neutrinos are particularly difficult
4034 to study. Consequently, many fundamental properties of neutrinos are still unknown
4035 including the absolute scale of the neutrino mass [23]. Direct, kinematic measurements of
4036 the neutrino mass are particularly valuable due to their model independent nature [36].

4037 To date the most sensitive direct neutrino mass measurements have been performed by
 4038 the KATRIN collaboration [87], which measures the molecular tritium β -decay spectrum
 4039 to infer the neutrino mass. Current data from neutrino oscillation measurements [23]
 4040 allow for neutrino masses significantly smaller than the design sensitivity of the KATRIN
 4041 experiment; therefore, there is a need for new technologies for performing direct neutrino
 4042 mass measurements to probe lower neutrino masses.

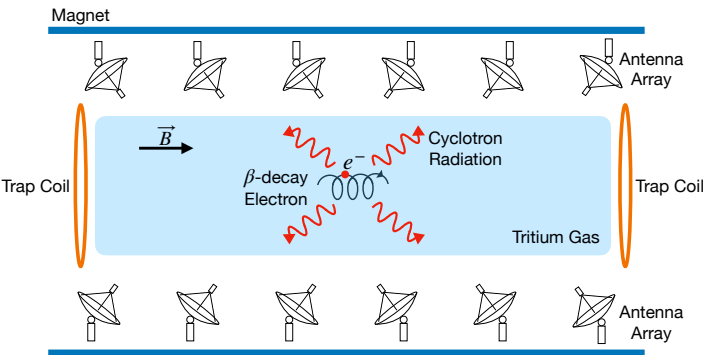


Figure 5.8. A sketch of an antenna array large-volume CRES experiment. Electrons from β -decays are confined in a magnetic field using a set of trap coils. The cyclotron radiation produced by the motion of the trapped electrons can be detected by a surrounding antenna array to determine the electron energies. Measuring the energies of many electrons produces a β -decay spectrum.

4043 The Project 8 collaboration is developing new methods for neutrino mass measurement
 4044 based on Cyclotron Radiation Emission Spectroscopy (CRES) [55, 88–90], with the goal
 4045 of measuring the absolute scale of the neutrino mass with a 40 meV/c² sensitivity [?, 36].
 4046 This sensitivity goal will require the development of two separate technical capabilities.
 4047 First is the development of an atomic tritium source, which avoids significant spectral
 4048 broadening due to molecular final states [54]. Second is the technology for performing
 4049 CRES in a multi-cubic-meter experimental volume with high combined detection and
 4050 reconstruction efficiency, which is required in order to obtain sufficient event statistics
 4051 near the tritium spectrum endpoint.

4052 One approach for a large-volume CRES experiment is to use an array of antennas,
 4053 which surrounds a volume of tritium gas, to detect the cyclotron radiation produced
 4054 by the β -decay electrons when they are trapped in a background magnetic field using a
 4055 set of magnetic trapping coils (see Figure 5.8). Project 8 has developed a conceptual
 4056 experiment design to study the feasibility of this approach. The design consists of a
 4057 single circular array of antennas with a radius of 10 cm and 60 independent channels
 4058 positioned around the center of the magnetic trap. The motivation behind this antenna

array design is to first develop an understanding of the antenna array approach to CRES
 with a small scale experiment before attempting to scale the technique to large volumes
 by using multiple antenna rings to construct the full cylindrical array. The development
 of the antenna array approach to CRES has largely proceeded through simulations using
 the Locust software package [79, 91], which is used to model the fields emitted by CRES
 events and predict the signals received by the surrounding antenna array. To validate
 these simulations, a dedicated test stand is being constructed to perform characterization
 measurements of the prototype antenna array developed by Project 8 (see Figure 5.9)
 and benchmark signal reconstruction methods using a specially designed transmitting
 calibration probe antenna.

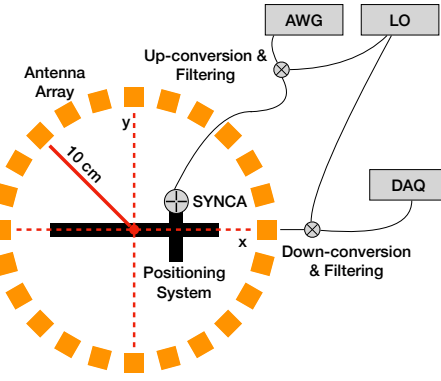


Figure 5.9. A schematic of the antenna array test stand. The circular antenna array has a radius of 10 cm with 60 independent channels (limited number shown for clarity). The test stand includes an arbitrary waveform generator (AWG), local oscillator (LO), and data acquisition (DAQ) hardware. Finally, a specialized Synthetic Cyclotron Antenna (SYNCA) is used to inject signals to test the antenna array.

We call this probe antenna the Synthetic Cyclotron Antenna or SYNCA. The SYNCA
 is a novel antenna design that mimics the cyclotron radiation generated by individual
 charged particles trapped in a magnetic field, which will be used in the antenna test
 stand to perform characterization measurements, simulation validation, and reconstruc-
 tion benchmarking. This paper provides an overview of the design, construction, and
 characterization measurements of the SYNCA performed in preparation for its usage as
 a transmitting calibration probe.

In Section 5.3.2 we provide a description of the cyclotron radiation field characteristics
 that we recreate with the SYNCA. In Section 5.3.3 we give an overview of the simulations
 performed to develop an antenna design that mimics the characteristics of cyclotron
 radiation. In Section 5.3.4 we outline characterization measurements to validate that
 the fields generated by the SYNCA match simulation, and finally in Section 5.3.5 we

4081 demonstrate an application of the SYNCA to test phased array reconstruction techniques
 4082 on the bench-top.

4083 5.3.2 Cyclotron Radiation Phenomenology

4084 To understand the cyclotron radiation phenomenology that the SYNCA should mimic,
 4085 we consider a charged particle moving at relativistic speed in the presence of an external
 4086 magnetic field (see Figure 5.10). In the special case we shall examine, the entirety of
 4087 the electron's momentum is directed perpendicular to the magnetic field; therefore, the
 4088 trajectory of the electron is confined to the cyclotron orbit plane. Because the momentum
 4089 vector is oriented perpendicular to the magnetic field, electrons with these trajectories
 4090 are said to have pitch angles of 90°.

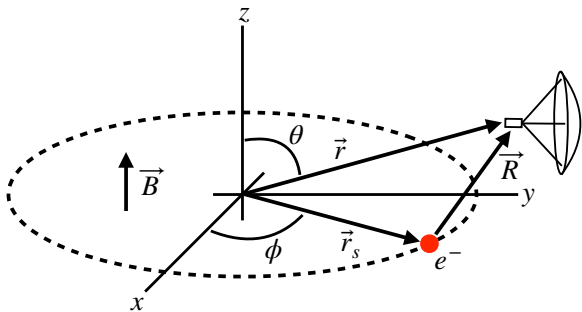


Figure 5.10. An electron (red dot) performing cyclotron motion in the x-y plane. The resulting cyclotron radiation is observed by an antenna located at the field point of interest.

4091 The cyclotron radiation fields generated by this circular trajectory are those which
 4092 we aim to reproduce with the SYNCA. We can describe the electromagnetic (EM) fields
 4093 using the Liénard-Wiechert equations [48, 79], which in non-covariant form express the
 4094 electric field as

$$\vec{E} = e \left[\frac{\hat{n} - \vec{\beta}}{\gamma^2 (1 - \vec{\beta} \cdot \hat{n})^3 |\vec{R}|^2} \right]_{t_r} + \frac{e}{c} \left[\frac{\hat{n} \times [(\hat{n} - \vec{\beta}) \times \dot{\vec{\beta}}]}{(1 - \vec{\beta} \cdot \hat{n})^3 |\vec{R}|} \right]_{t_r}, \quad (5.23)$$

4095 where e is the particle's charge, $\hat{n} = (\vec{r} - \vec{r}_s)/|\vec{r} - \vec{r}_s|$ is the unit vector pointing from the
 4096 electron to the field measurement point, $\vec{\beta} = \dot{\vec{r}}_s/c$ is the velocity of the particle divided
 4097 by the speed of light, and γ is the relativistic Lorentz factor. The equation is meant to
 4098 be evaluated at the retarded time as indicated by $t_r = t - |\vec{R}|/c$, which accounts for the
 4099 time delay due to the finite speed of light between the point where the field was emitted
 4100 and the point where the field is detected.

4101 We would like to simplify Equation 5.23 it at all possible. As a first step we analyze
 4102 the relative magnitudes of the electric field polarization components. Consider an electron
 4103 following a circular cyclotron orbit in a uniform magnetic field whose guiding center
 4104 is positioned at the origin of the coordinate system. The equation of motion can be
 4105 expressed as

$$\vec{r}_s = (r_c \cos \omega_c t_r) \hat{x} + (r_c \sin \omega_c t_r) \hat{y}. \quad (5.24)$$

4106 For single antenna located along the y-axis at position $\vec{r} = r_a \hat{y}$ we are interested in the
 4107 incident electric fields from the electron. The electric field is given by Equation 5.23,
 4108 which we evaluate in the regime where $r_a \gg r_c$. This limit can be justified by comparing
 4109 the radius of the cyclotron orbit for an electron with the tritium beta-spectrum endpoint
 4110 energy of 18.6 keV in a 1 T magnetic field to the typical ($r_a \simeq 100$ mm) radial position
 4111 of the receiving antenna. We find that the cyclotron orbit has a radius of 0.46 mm which
 4112 is approximately a factor of 200 smaller than the typical antenna radial position. In this
 4113 regime we can make the approximation $\vec{R} \simeq r_a \hat{y}$ and the expression for the electric field
 4114 at the antenna's position becomes

$$\vec{E} = \frac{e}{\gamma^2 r_a^2} \frac{\hat{x}(\frac{r_c \omega_c}{c} \sin \omega_c t_r) + \hat{y}(1 - \frac{r_c \omega_c}{c} \cos \omega_c t_r)}{(1 - \frac{r_c \omega_c}{c} \cos \omega_c t_r)^3} - \frac{e}{cr_a} \frac{\hat{x}(\frac{r_c^2 \omega_c^3}{c^2} - \frac{r_c \omega_c^2}{c} \cos \omega_c t_r)}{(1 - \frac{r_c \omega_c}{c} \cos \omega_c t_r)^3}. \quad (5.25)$$

4115 Since the receiving antenna is part of a circular array of antennas, it is useful to rewrite
 4116 Equation 5.25 in terms of the azimuthal ($\hat{\phi}$) and radial (\hat{r}) polarizations. Making use of
 4117 the fact that for an antenna located at $R = r_a \hat{y}$ that $\hat{\phi} = -\hat{x}$ and $\hat{r} = \hat{y}$ we find

$$\vec{E} = \hat{\phi} E_\phi + \hat{r} E_r \quad (5.26)$$

$$E_\phi = \frac{e}{(1 - \frac{r_c \omega_c}{c} \cos \omega_c t_r)^3} \left[-\frac{\frac{r_c \omega_c}{c} \sin \omega_c t_r}{\gamma^2 r_a^2} + \frac{\omega_c \left(\frac{r_c^2 \omega_c^2}{c^2} - \frac{r_c \omega_c}{c} \cos \omega_c t_r \right)}{cr_a} \right] \quad (5.27)$$

$$E_r = \frac{e(1 - \frac{r_c \omega_c}{c} \sin \omega_c t_r)}{\gamma^2 r_a^2 (1 - \frac{r_c \omega_c}{c} \cos \omega_c t_r)^3}. \quad (5.28)$$

4118 For the purposes of designing a synthetic cyclotron radiation antenna we are interested
 4119 in the dominant electric field polarization emitted by the electron. The antenna is being
 4120 designed to mimic the cyclotron radiation produced by electrons with kinetic energies of
 4121 approximately 18.6 keV in a 1 T magnetic field [54]. Since the relativistic beta factor for
 4122 an electron with this kinetic energy is $|\vec{\beta}| \simeq \frac{1}{4}$, the approximations $\gamma \simeq 1$ and $\frac{r_c \omega_c}{c} \simeq \frac{1}{4}$ are
 4123 justified. Inserting these expressions into the equations for the electric field components

4124 above simplifies the comparison of the magnitudes of the two components. Additionally,
4125 we compare the time-averaged magnitudes to evaluate the root mean squared electric
4126 field ratio. The time-averaged ratio of the radial and azimuthally polarized electric fields
4127 with the above simplifications is given by

$$\frac{\langle |E_r| \rangle}{\langle |E_\phi| \rangle} = \frac{8 - \sqrt{2}}{\left| 1 - \frac{r_a}{r_c} \frac{1-2\sqrt{2}}{8} \right|} \simeq \frac{r_c}{r_a} \frac{8(8 - \sqrt{2})}{2\sqrt{2} - 1} = 0.13, \quad (5.29)$$

4128 where we have made use of the fact that for these magnetic fields and kinetic energies
4129 the cyclotron radius is much smaller than the radius of the antenna array.

4130 From Equation 5.29 we see that the time-averaged azimuthal polarization is larger than
4131 the radial polarization by about a factor of 8, which makes it the dominant contribution
4132 to the electric fields at the position of the antenna. We must also consider the directivity
4133 of the receiving antenna which can have a gain that is disproportionately large for a
4134 specific polarization component. Because the E_ϕ component is dominant, the receiving
4135 antenna array is designed with an azimuthal polarization, which negates the voltages
4136 induced in the antenna from the radially polarized fields. Therefore, we conclude that
4137 for the purpose of designing the SYNCA antenna it is acceptable to approximate the
4138 electric fields from Equation 5.23 as purely azimuthally or ϕ -polarized. The simplified
4139 expression for the electric field received by an antenna becomes

$$\vec{E} = E_\phi \hat{\phi} = \frac{e \frac{r_c \omega_c}{c}}{4r_a r_c} \left[\frac{\frac{r_c \omega_c}{c} - \cos \omega_c t - \frac{4r_c}{r_a} \sin \omega_c t}{(1 - \frac{r_c \omega_c}{c} \cos \omega_c t)^3} \right]_{t_r} \hat{\phi}, \quad (5.30)$$

4140 where the radius of the cyclotron orbit is called r_c , the cyclotron frequency is called ω_c ,
4141 and the radial position of the receiving antenna is called r_a . Equation 5.30 has been
4142 evaluated in the non-relativistic limit where $\gamma \simeq 1$, which is justified by the fact that
4143 $|\vec{\beta}| \simeq \frac{c}{4}$ for an electron with an 18.6 keV kinetic energy in a 1 T magnetic field.

4144 This rather complicated expression can be simplified using Fourier analysis. Assuming
4145 a background magnetic field of 1 T and a kinetic energy of 18.6 keV we calculate
4146 numerically the electric field using Equation 5.30 and apply a discrete Fourier Transform
4147 to visualize the frequency spectrum (see Figure 5.11).

4148 We observe that the azimuthally polarized electric field is periodic with a base cyclotron
4149 frequency of 25.898 GHz corresponding to the highest power frequency component in
4150 Figure 5.11. The frequency spectrum reveals that the signal is composed of a constant
4151 term with zero frequency and a series of harmonics separated by 25.898 GHz. Therefore,

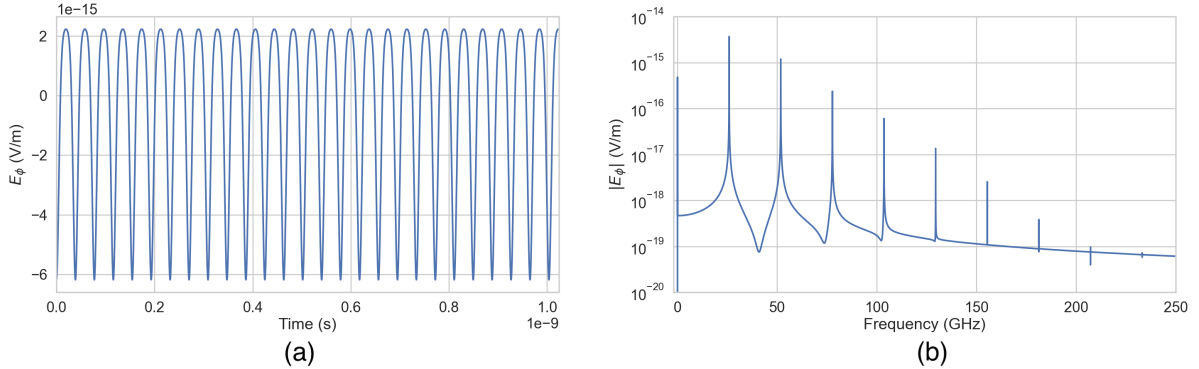


Figure 5.11. A plot of the numeric solution to Equation 5.31. The time-domain representation of the signal (a) is composed of a zero frequency term and a series of harmonics separated by the main cyclotron frequency as shown in the plot of the frequency spectrum (b). We can see that the relative amplitude of the harmonics beyond $k = 7$ are smaller than the main carrier by a factor of about 10^{-5} and are completely negligible.

we can represent the azimuthal electric fields from the electron as a linear combination of pure sinusoids with frequencies given by $\omega_k = k\omega_c$ ($k \in 0, 1, 2, \dots$) and amplitudes extracted from the Fourier representation. Using this representation we can transform the equation for the azimuthally polarized electric fields in Equation 5.30 into

$$E_\phi = \frac{e^{\frac{r_c \omega_c}{c}}}{4r_a r_c} \sum_{k=0}^7 A_k e^{i\omega_k t_r}, \quad (5.31)$$

where we have truncated the sum over harmonics at the 7th order for completeness. The amplitudes A_k are dimensionless complex numbers, which encode the relative powers of the harmonics as well as the starting overall phase of the cyclotron radiation. Because magnitude of the relative amplitudes exponentially decreases for higher harmonics, it is usually sufficient to consider only the terms up to $k = 4$ where the relative amplitude of the harmonics has decreased from the main carrier by a factor of approximately 100. However, for completeness we include harmonics up to 7th order in Equation 5.31. The range of frequencies to which the receiving antenna array in the antenna test stand is sensitive is defined by the antenna's transfer function. The receptive bandwidth for the antennas used in the test stand is a range of frequencies with a bandwidth on the order of a few GHz centered around the main cyclotron carrier frequency of 25.898 GHz. Therefore, the higher order harmonics as well as the zero frequency term can be ignored when considering only the signals that will be received by the antenna array.

Considering only the 1st order harmonic term from Equation 5.31, which represents the portion of the electric field that will be detected by the array, and evaluating this at

4171 the retarded time we obtain the following for the ϕ -polarized electric fields

$$E_\phi \propto \cos \left(\omega_c \left(t - |\vec{R}|/c \right) - \Delta \right), \quad (5.32)$$

4172 where the arbitrary phase Δ is defined by $A_k = |A_k|e^{i\Delta}$. We are interested in the
 4173 characteristics of the amplitude of the electric field as a function of the radial distance
 4174 component ($|\vec{R}|$) of the retarded time. In particular, the maximum of E_ϕ occurs when
 4175 the argument of the cosine function is equal $n\pi$ where $n \in \{0, \pm 2, \pm 4, \dots\}$; however, the
 4176 solutions where n is negative can be discarded since they represent unphysical negative
 4177 overall phases. Applying this condition to Equation 5.32 gives a condition on the radial
 4178 position of the maximum of E_ϕ

$$\omega_c(t - |\vec{R}|/c) - \Delta = n\pi, \quad (5.33a)$$

$$|\vec{R}| = \frac{c}{\omega_c} ((\omega_c t - \Delta) - n\pi), \quad (5.33b)$$

4179 which is a function of time in the frame of the moving electron (t). Equation 5.33 can
 4180 be further simplified by noticing that the azimuthal position of the electron ($\phi_e(t)$) as a
 4181 function of time is defined by $\phi_e(t) = \omega_c t - \Delta$ which reduces Equation 5.33 to

$$|\vec{R}| = \frac{c}{\omega_c} (\phi_e(t) - n\pi). \quad (5.34)$$

4182 Equation 5.34 represents an archimedean spiral which is formed when plotting the
 4183 amplitude of E_ϕ in the x-y plane. The solution where $n = 0$ represents the leading edge
 4184 of the radiation spiral which propagates outward from the electron at the speed of light.
 4185 The additional solutions for $n > 0$ represent the persistent spiral at radii inside the
 4186 leading edge of the radiated fields that have not yet been detected by the receiver at the
 4187 current time. In Figure 5.12a we show the expected spiral pattern for the maxima of the
 4188 cyclotron radiation.

4189 In particular, we note that for the circular array geometry of the test stand, depicted
 4190 as the series of circles in Figure 5.12a, each antenna receives a linearly polarized wave
 4191 with a phase offset that corresponds to the azimuthal angle for that antenna element.
 4192 Therefore, as we show in Figure 5.12b, when the relative phase of the received signal is
 4193 plotted as a function of the receiving antenna's azimuthal position the result is also an
 4194 Archimedean spiral.

4195 Based on these analytical calculations we can characterize the magnitude, polarization,
 4196 and phase of the signals received by the antenna array using three criteria. These criteria

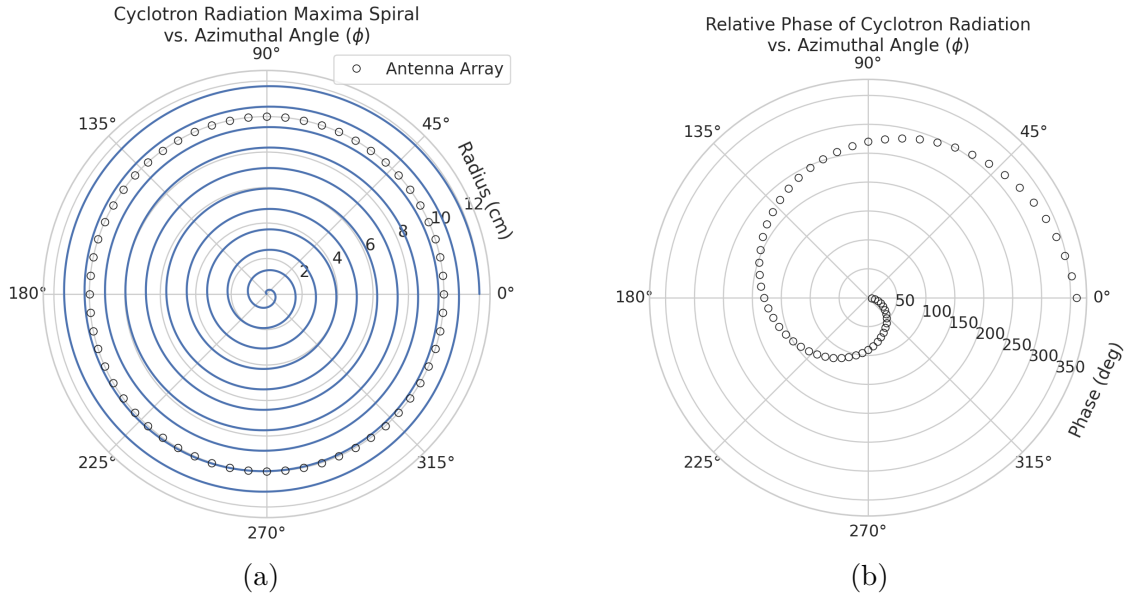


Figure 5.12. The amplitude maxima of the cyclotron radiation form an Archimedean spiral as the radiation propagates outward from the cyclotron orbit center (a). A circular antenna array located at a fixed radius from the orbit center will receive electric fields with equal magnitude in each of its channels, but the phase of the electric field incident on each array channel will be linearly out of phase from its neighbor antennas by an amount equal to the angular separation of the two channels (b).

4197 are the basis of comparison for the radiation produced by the SYNCA and cyclotron
 4198 radiation emitted by electrons and will be used to evaluate the performance of antenna
 4199 designs. The criteria are:

- 4200 1. Electric fields that are ϕ -polarized near $\theta = 90^\circ$
- 4201 2. Uniform time-averaged electric field magnitudes around the circumference of a
 4202 circle centered on the antenna
- 4203 3. Electric fields whose phase is equal to the azimuthal angle at the point of measure-
 4204 ment plus a constant

4205 The Locust simulation package [91] can be used to directly simulate the EM fields
 4206 generated by electrons performing cyclotron motion to validate the analytical calculations.
 4207 Locust simulates the EM fields by first calculating the trajectory of the electrons in
 4208 the magnetic trap using the Kassiopeia software package [92]. The trajectory can then
 4209 be used to solve for the EM fields using the Liénard-Wiechert equations directly with
 4210 no approximations. The resulting electric field solutions drive a receiving antenna by

convolving the time-domain fields with the finite-impulse response filter of the antenna
 or they can be examined directly to study the field characteristics that the SYNCA must
 reproduce. In the next section we compare the radiation field patterns for electrons
 simulated with Locust to patterns from a SYNCA antenna design.

5.3.3 SYNCA Simulations and Design

One potential SYNCA design is the crossed-dipole antenna [93]. A crossed-dipole antenna
 consists of two dipole antennas, one of which is rotated 90° with respect to the other,
 which are fed with signals that are out of phase from the opposite dipole by 90° (see
 Figure 5.13). This arrangement causes the signals fed to each arm of the dipole to be

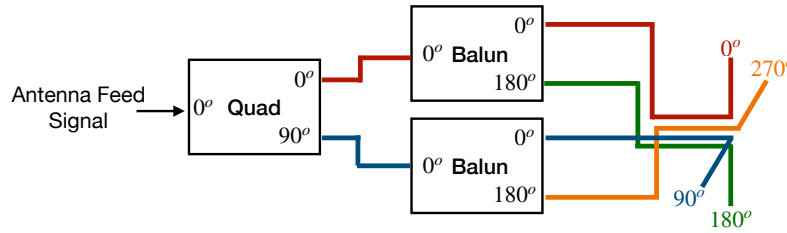


Figure 5.13. An idealized crossed-dipole antenna consists of two electric dipole antennas oriented perpendicular to each other and is fed with four signals with a quadrature phase relationship. An example antenna feed circuit is shown which is composed of a chained combination of a quadrature hybrid-coupler (Quad) and two baluns.

out of phase from each of the neighboring arms by 90°, which mirrors the spatial phase
 relationship of cyclotron radiation fields.

A potential drawback of this design is that standard crossed-dipole antennas do not
 radiate uniform electric fields near the $\theta = \pi/2$ plane. Typical crossed-dipole antennas
 use dipole arm lengths equal to $\lambda/4$ or larger [93], where λ is the wavelength at the
 desired operating frequency. Such large arm lengths cause the electric field magnitude
 to vary significantly around the circumference of the antenna. However, making the
 antenna electrically small by shrinking the arm length can improve the antenna pattern
 uniformity.

In general, the criterion for an electrically small antenna is that the largest dimension
 of the antenna (D) obey $D \lesssim \lambda/10$ [64]. In our application, we are attempting to mimic
 the cyclotron radiation emitted by electrons produced from tritium β -decay with energies
 near the spectrum endpoint. For a background magnetic field of 1 T, the corresponding

4233 cyclotron frequency of tritium endpoint electrons is approximately 26 GHz. Therefore, the
4234 electrically small condition would require that the largest dimension of the crossed-dipole
4235 antenna be smaller than 1.2 mm.

4236 A crossed-dipole antenna with an overall size of 1.2 mm is challenging to fabricate due
4237 to the small dimensions of the dipole arms that, in practice, are fragile and unsuitable
4238 for use as a calibration probe. To mitigate some of the challenges with the fabrication
4239 of such a small antenna, a variant crossed-dipole antenna design using printed circuit
4240 board (PCB) technology (see Figure 5.14) was developed in partnership with an antenna
prototyping company, Field Theory Consulting ¹.

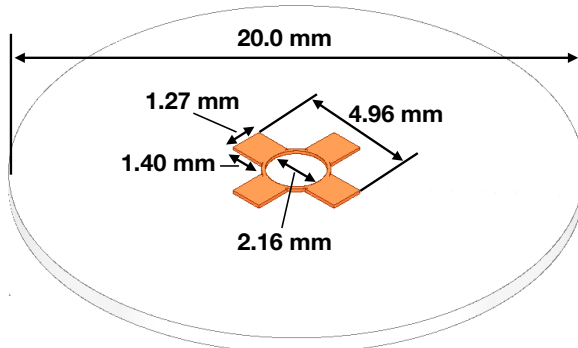


Figure 5.14. A model of the PCB crossed-dipole antenna with dimensions. The design has an inside diameter of 2.16 mm for the central circular trace, which is 0.13 mm wide. The dipole arms each have a width of 1.27 mm and protrude beyond the circular trace by 1.40 mm, which gives an overall width of 4.96 mm for the length of the antenna PCB trace from end-to-end. The overall size of the antenna is 20.0 mm the majority of which is the PCB dielectric material. This design was observed in simulation to maintain the field characteristics of the idealized crossed-dipole while being simpler to fabricate due to the increased size of the antenna.

4241
4242 The PCB crossed-dipole design uses four rectangular pads to represent the dipole arms,
4243 which are connected by a thin circular trace. The circular trace both adds mechanical
4244 stability to the antenna and improves the azimuthal uniformity of the electric fields
4245 compared to a more standard crossed-dipole geometry. Furthermore, the circular trace
4246 allows for a greater separation between dipole arms than standard crossed-dipoles, which
4247 is required to accommodate the coaxial connections to each pad. The pads each contain
4248 a through-hole solder joint to connect coaxial transmission lines using hand soldering.
4249 The antenna PCB has no ground plane on the bottom layer as this was observed in
4250 simulation to significantly distort the radiation pattern in the plane of the PCB. The
4251 only ground planes present in the model are the outer conductors of the four coaxial

¹<https://fieldtheoryinc.com/>

4252 transmission lines which feed the antenna. These are left unterminated on the bottom of
4253 the PCB dielectric material.

4254 The antenna design development utilized a combination of Locust electron simula-
4255 tions and antenna simulations using ANSYS HFSS [65], a commercial finite-element
4256 electromagnetic simulation software. Two antenna designs were simulated: an idealized
4257 electrically small crossed-dipole antenna with an arm length of 0.40 mm and an arm
4258 separation of 0.05 mm, as well as a PCB crossed-dipole antenna with the dimensions
4259 shown in Figure 5.14. Plotting the magnitude of the electric fields generated by the
4260 antennas across a 10 cm square located in the same plane as the respective antennas
4261 reveals the expected cyclotron spiral pattern (see Figure 5.15) which closely matches
4262 the prediction for simulated electrons. The spiral pattern demonstrates that the electric
4263 fields have the appropriate phases to mimic cyclotron radiation, which fulfills SYNCA
criterion 3 identified in Section 5.3.2.

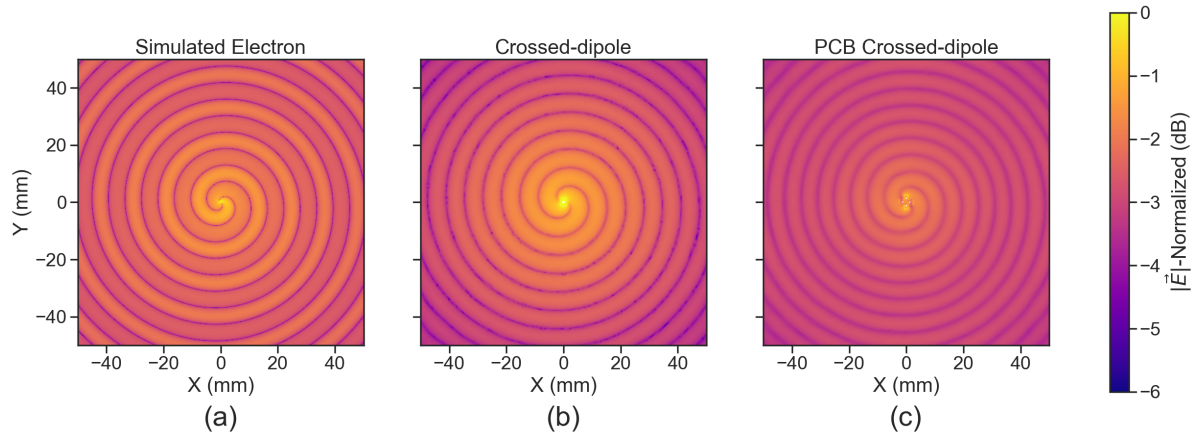


Figure 5.15. A comparison of the electric field magnitudes, normalized by the maximum value of the electric field in each simulation, plotted on a 10 cm square to visualize the Archimedean spirals formed by the electron (a), the crossed-dipole antenna (b), and a PCB crossed-dipole antenna (c). The matching patterns indicate that the electric fields have similar phase characteristics. These images were generated using Locust simulations for the electron and ANSYS HFSS for both antennas.

4264

4265 As we can see from Figure 5.16, the crossed-dipole antenna, which uses an idealized
4266 geometry, exhibits good agreement with simulation. The antenna has a maximum
4267 deviation from a simulated electron of approximately 0.5 dB in the total electric field, 1
4268 dB for the ϕ -polarized electric field and 1 dB for the θ -polarized electric field.

4269 In comparison, the pattern of the PCB crossed-dipole antenna, because the simulation
4270 incorporates the geometry of the coax transmission lines, exhibits some distortion from
4271 the idealized cross-dipole simulations. The vertically oriented ground planes of the coax

4272 lines introduce more θ -polarized electric fields than are observed for simulated electrons
 4273 near $\theta = 90^\circ$. The significant θ -polarized field minimum is still present but shifted
 to approximately $\theta = 65^\circ$. The θ -polarized field deviations of the PCB crossed-dipole

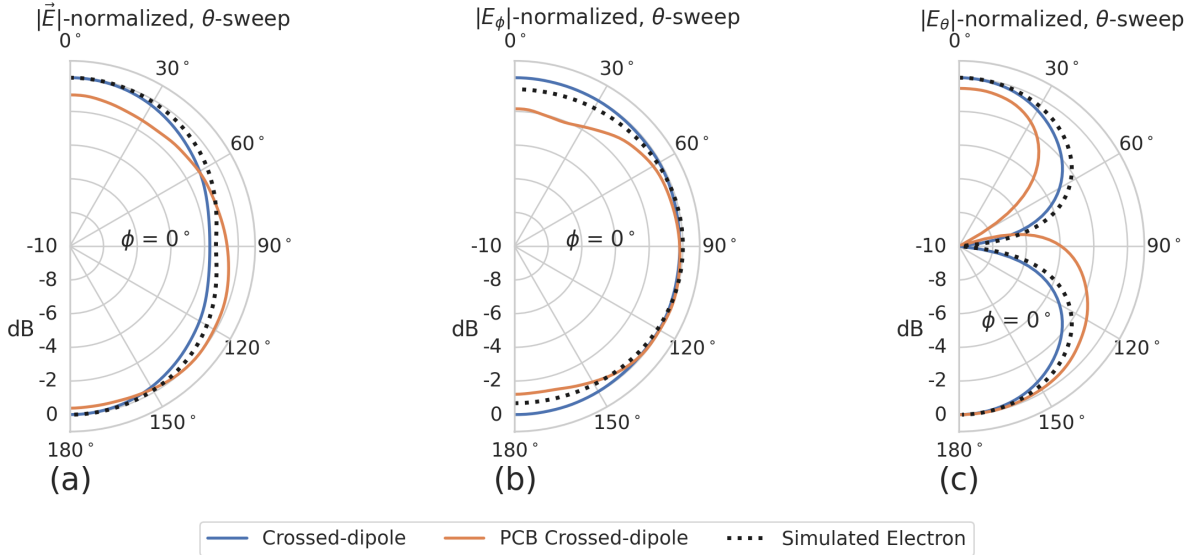


Figure 5.16. A comparison of the normalized electric field magnitudes for the ideal crossed-dipole, PCB crossed-dipole, and a simulated electron as a function of the polar angle (θ). (a) Shows the total electric field, (b) shows the ϕ -polarized electric field component, and (c) shows the θ -polarized electric field component. These images were generated using Locust simulations for the electron and ANSYS HFSS for both antennas.

4274
 4275 antenna should not greatly impact the performance of the antenna because the receiving
 4276 antenna array is primarily ϕ -polarized. Therefore deviations in the θ -polarized fields
 4277 will be suppressed due to the polarization mismatch. More importantly, the ϕ -polarized
 4278 electric field pattern generated by the PCB crossed-dipole closely matches simulated
 4279 electrons across the polar angle range of $50^\circ < \theta < 150^\circ$. In this region the PCB crossed-
 4280 dipole differs by less than 0.5 dB from simulated electrons. This range greatly exceeds
 4281 the beamwidth of the receiving antenna array which is designed to be most sensitive
 4282 to fields produced near $\theta = 90^\circ$. Therefore, we conclude that the PCB crossed-dipole
 4283 antenna generates a ϕ -polarized radiation pattern that fulfills SYNCA criterion 1 from
 4284 Section 5.3.2.

4285 The final SYNCA criterion is related to the uniformity of the electric fields when
 4286 measured azimuthally around the antenna. As we saw for real electrons in Section 5.3.2
 4287 it is expected that the magnitude of the electric field be completely uniform as a function
 4288 of the azimuthal angle due to the symmetry of the cyclotron orbit. In Figure 5.17 we plot
 4289 the total electric field as a function of azimuthal angle for an electron, the crossed-dipole

antenna, and the PCB crossed-dipole antenna. The crossed-dipole antenna exhibits

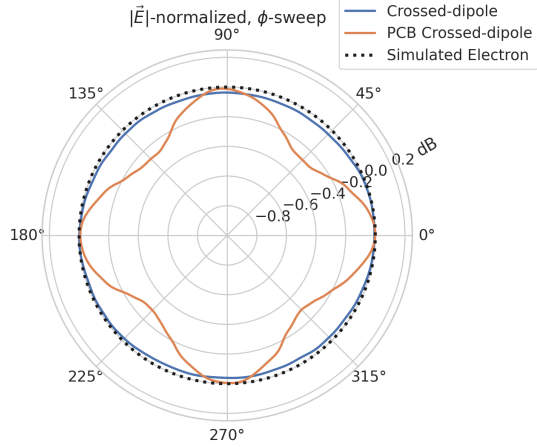


Figure 5.17. A comparison of the normalized electric field magnitudes for the crossed-dipole, PCB crossed-dipole, and a simulated electron as a function of the azimuthal angle (ϕ) evaluated at $\theta = 90^\circ$. This image was generated using Locust simulations for the electron and ANSYS HFSS for both antennas.

4290

4291 perfect uniformity around the azimuthal angle, whereas the PCB crossed-dipole has a
 4292 small periodic deviation with a maximum difference of 0.3 dB caused by the coaxial
 4293 transmission lines below the PCB. Such a small deviation from uniformity is acceptable
 4294 since it is smaller than the expected variation in uniformity caused by imperfections in
 4295 the antenna fabrication process, which modifies the antenna shape in an uncontrolled
 4296 manner by introducing solder blobs with a typical size of a few tenths of a millimeter on
 4297 the dipole arms (see Figure 5.18). Additionally, the SYNCA will be separately calibrated
 4298 to account for azimuthal differences in the electric field magnitude. Therefore we see
 4299 from the simulated performance of the PCB crossed-dipole antenna that this antenna
 4300 design meets all three of the SYNCA criteria.

4301

5.3.4 Characterization of the SYNCA

4302 Two SYNCAs were manufactured using the PCB crossed-dipole design (see Figure 5.18).
 4303 The antenna PCB (Matrix Circuit Board Materials, MEGTRON 6) is connected to
 4304 four 2.92 mm coaxial connectors (Fairview Microwave, SC5843) using semi-rigid coax
 4305 (Fairview Microwave, FMBC002), which also physically support the antenna PCB. The
 4306 antenna PCB consists only of two layers which correspond to the copper antenna trace
 4307 and the PCB dielectric. Each coax line is connected to the associated dipole arm using
 4308 through-hole soldering and phase matched to ensure that the electrical length of each
 4309 of the transmission lines is identical at the operating frequency. The antenna PCB is

4310 further reinforced using custom cut polystyrene foam blocks, which have an electrical
 4311 permittivity nearly identical to air. A custom 3D printed mount is included at the base
 4312 of the antenna to support the coax connectors and to provide a sturdy mounting base.

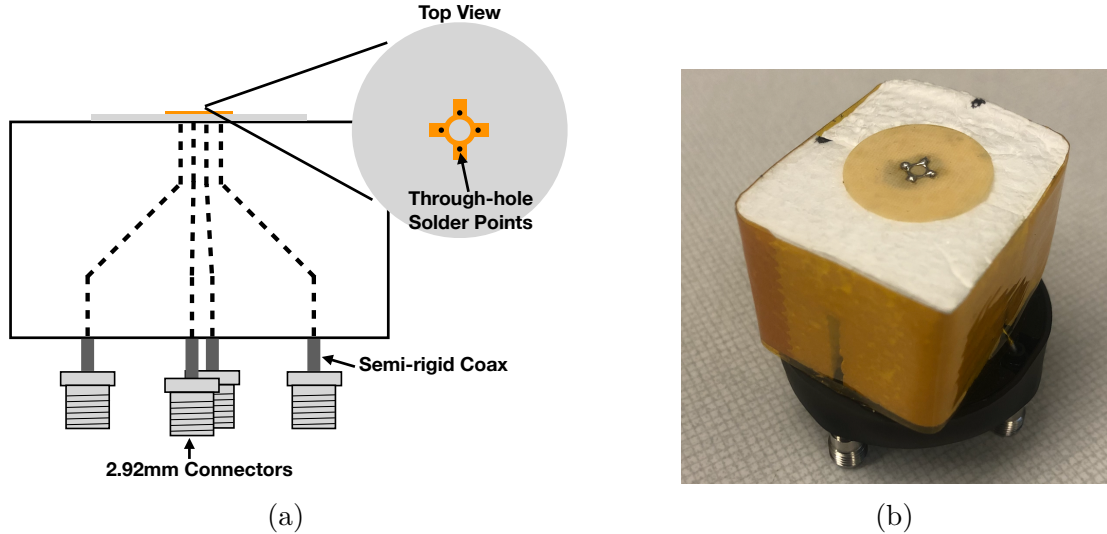


Figure 5.18. (a) A cartoon schematic which highlights the routing of the semi-rigid coax transmission lines. (b) A photograph of a SYNCA constructed using the modified crossed-dipole PCB antenna design. Visible in the photograph of the SYNCA are four blobs of solder which are an artifact of the SYNCA's hand-soldered construction. These solder blobs are the most significant deviation from the SYNCA design shown in Figure 5.14 and are responsible for a significant fraction of the irregularities seen in the antenna pattern.

4313 Characterization measurements were performed using a Vector Network Analyzer
 4314 (VNA) to measure the electric field magnitude and phase radiated by the SYNCA to
 4315 verify the radiation pattern (see Figure 5.19). The VNA is connected to the SYNCA
 4316 at one port through a hybrid-coupler whose outputs are connected to two baluns to
 4317 generate the signals with the appropriate phases to feed the SYNCA (see Figure 5.13).
 4318 The other port of the VNA is connected to a single reference horn antenna that serves
 4319 as a field probe. To position the SYNCA, a combination of translation and rotation
 4320 stages are used to characterize the antenna's fields across the entire radiation pattern
 4321 circumference. This measurement scheme is equivalent to measuring the fields generated
 4322 by the SYNCA using a full circular array of probe antennas.

4323 The antenna measurement space is surrounded by RF anti-reflective foam to isolate
 4324 the measurements from the lab environment (see Figure 5.19b) and remaining reflections
 4325 are removed using the VNA's time-gating feature. The SYNCA is affixed to the stages
 4326 by a custom RF transparent mount made of polystyrene foam. The coaxial cables deliver

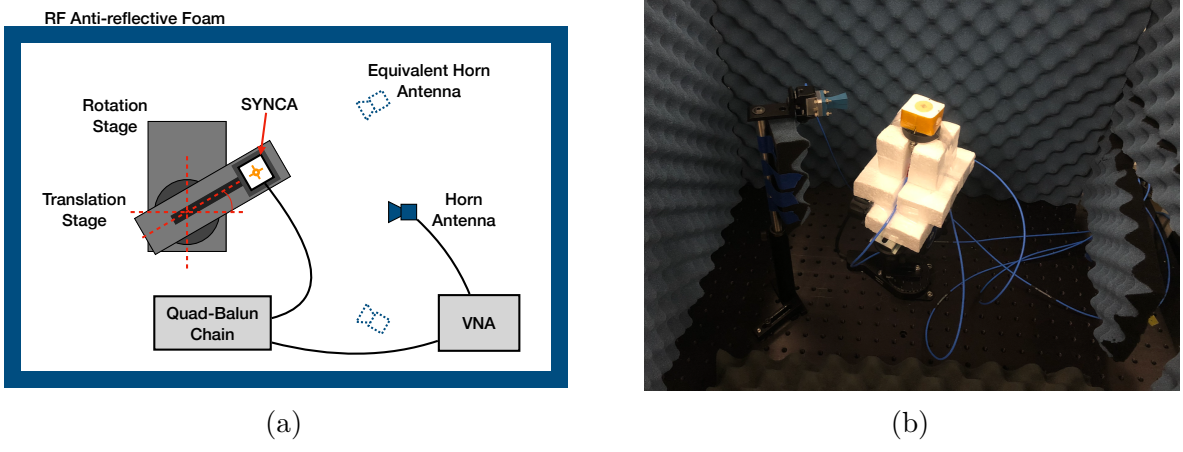


Figure 5.19. A schematic of the VNA characterization measurements (a). This setup allows for antenna gain and phase measurements across a full 360° of azimuthal angles using a motorized rotation stage and control of the radial position of the SYNCA using a translation stage. A photo of the setup in the lab is shown in (b).

4327 the antenna feed signals generated by the VNA to the SYNCA while still allowing
 4328 unrestricted rotation. The horn antenna probe is nominally positioned in the plane
 4329 formed by the antenna PCB ($\theta = 90^\circ$ or $z = 0$ mm) at a distance of 10 cm from the
 4330 SYNCA, to match the expected position of the antenna array relative to the SYNCA in
 4331 the antenna array test stand. The horn antenna can be manually raised or lowered to
 4332 different relative vertical positions to characterize the radiation pattern at different polar
 4333 angles.

4334 Several 360° scans were performed with probe vertical offsets of -10.0 mm, -5.0 mm,
 4335 0.0 mm, 5.0 mm, and 10.0 mm relative to the antenna PCB plane. These probe offsets
 4336 cover a 2 cm wide vertical region centered on the SYNCA PCB, approximately equal to
 4337 ± 6 degrees of polar angle. The measurements show that the SYNCA is generating fields
 4338 with nearly isotropic magnitude across the probed region. The standard deviation of the
 4339 electric field magnitude measured around the antenna circumference is approximately
 4340 2.9 dB for a typical rotational scan. The presence of a significant pattern null is noted
 4341 near 45° (see Figure 5.20), which we attribute to small imperfections in the antenna
 4342 PCB that could be introduced from the hand soldered terminations connecting the coax
 4343 cables to the antenna. There is no significant difference in the radiation pattern when
 4344 measured across the 2 cm vertical range. The measured relative phases closely follow
 4345 the expectation for an electron, being linear with the measurement rotation angle and
 4346 forming the expected spiral pattern. Other than the small phase imperfections there is

4347 a slight sinusoidal bias to the phase data, which we determined is the result of a small
 4348 ($\lesssim 1$ mm) offset of the antenna's phase center from the rotation axis of the automated
 4349 stages.

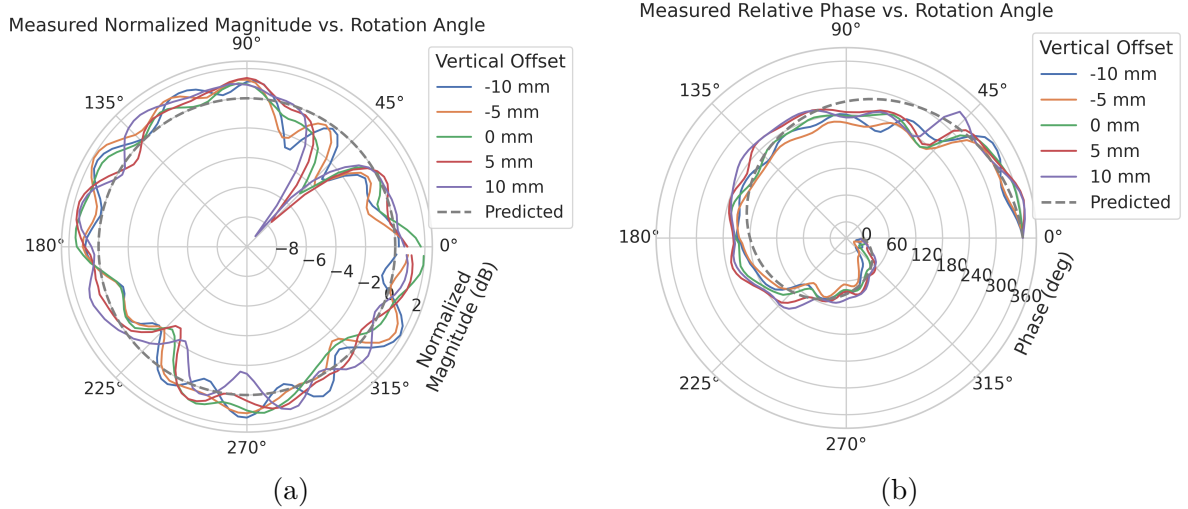


Figure 5.20. Linear interpolations of the measured electric field magnitude (a) and phase (b). The data was acquired using a VNA at 120 points spaced by 3 degrees from 0 to 357 degrees of azimuthal angle. The different color lines indicate the vertical offset of the horn antenna relative to the SYNCA PCB and the dashed line shows the expected shape from electron simulations. No significant difference in the antenna pattern is observed for the measured vertical offsets.

4350 The characterization measurements confirm the simulated performance of the SYNCA.
 4351 As expected the fields generated by the antenna are nearly isotropic in magnitude, ϕ -
 4352 polarized, and are linearly out of phase around the circumference of the antenna as
 4353 predicted for cyclotron radiation in Section 5.3.2. Small imperfections in the magnitude
 4354 and phase of the antenna are expected, particularly at the antenna's high operating
 4355 frequency of 26 GHz where small geometric changes can have significant impacts on
 4356 electrical properties. However, calibration through careful characterization measurements
 4357 can be used to remove the majority of these pattern imperfections, including the relatively
 4358 large pattern null near 45°, which will allow for the usage of the SYNCA as a test source
 4359 for free-space CRES experiments utilizing antenna arrays. In the next section we use the
 4360 VNA measurements obtained here as a calibration for signal reconstruction using digital
 4361 beamforming.

4362 5.3.5 Beamforming Measurements with the SYNCA

4363 Digital beamforming is a standard technique for signal reconstruction using a phased
 4364 array [94]. The SYNCA, since it exhibits the same cyclotron phases as a trapped electron,
 4365 can be used to perform simulated CRES digital beamforming reconstruction experiments
 4366 on the bench-top without the need for the magnet, cryogenics, and vacuum systems
 4367 required by a full CRES experiment. The fields received by the individual elements
 4368 of the antenna array will have phases dependent on the spatial position of the source
 4369 relative to the antennas. Therefore, a simple summation of the received signals will fail
 4370 to reconstruct the signal due to destructive interference between the individual channels
 4371 in the array. However, applying a phase shift associated with the source's spatial position
 4372 removes phase differences and results in a constructive summation of the channel signals
 4373 (see Figure 5.21). We can summarize the digital beamforming operation succinctly using
 4374 the following equation

$$y[t_n] = \sum_{m=0}^{N-1} x_m[t_n] A_m e^{i\phi_m}, \quad (5.35)$$

4375 where $y[t_n]$ represents the summed array signal at time t_n , $x_m[t_n]$ is the signal received
 4376 by channel m at time t_n , ϕ_m is the phase shift applied to the signal received at channel
 4377 m , and A_m is an amplitude weighting factor that accounts for the different signal power
 4378 received by individual channels. By changing the digital beamforming phases, the point
 4379 of constructive interference can be scanned across the sensitive region of the array to

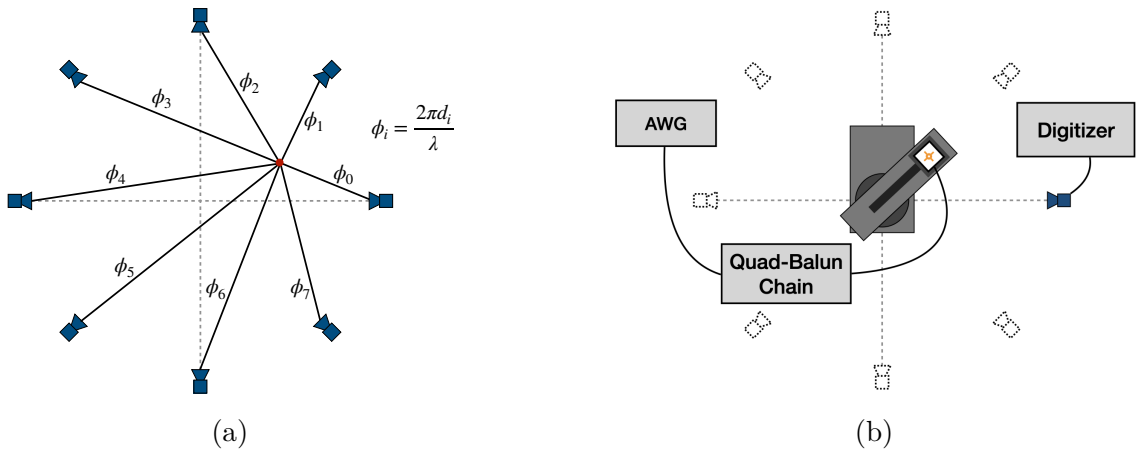


Figure 5.21. (a) A depiction of the relative phase differences for signals received by a circular antenna array from an isotropic source. The phases correspond to a unique spatial position.
 (b) A schematic of the setup used to perform digital beamforming.

4380 search for the location of a radiating source, which is identified as the point of maximum
 4381 summed signal power above a specified threshold. The digital beamforming phases consist
 4382 of two components,

$$\phi_m = 2\pi d_m/\lambda + \theta_m, \quad (5.36)$$

4383 where d_m is the distance from the m -th array element to the source, and θ_m is the
 4384 relative angle between the source position and the m -th antenna. The first component is
 4385 the standard digital beamforming phase that corresponds to the spatial position of the
 4386 source, and the second component is the cyclotron phase that corresponds to the relative
 4387 azimuthal phase offset.

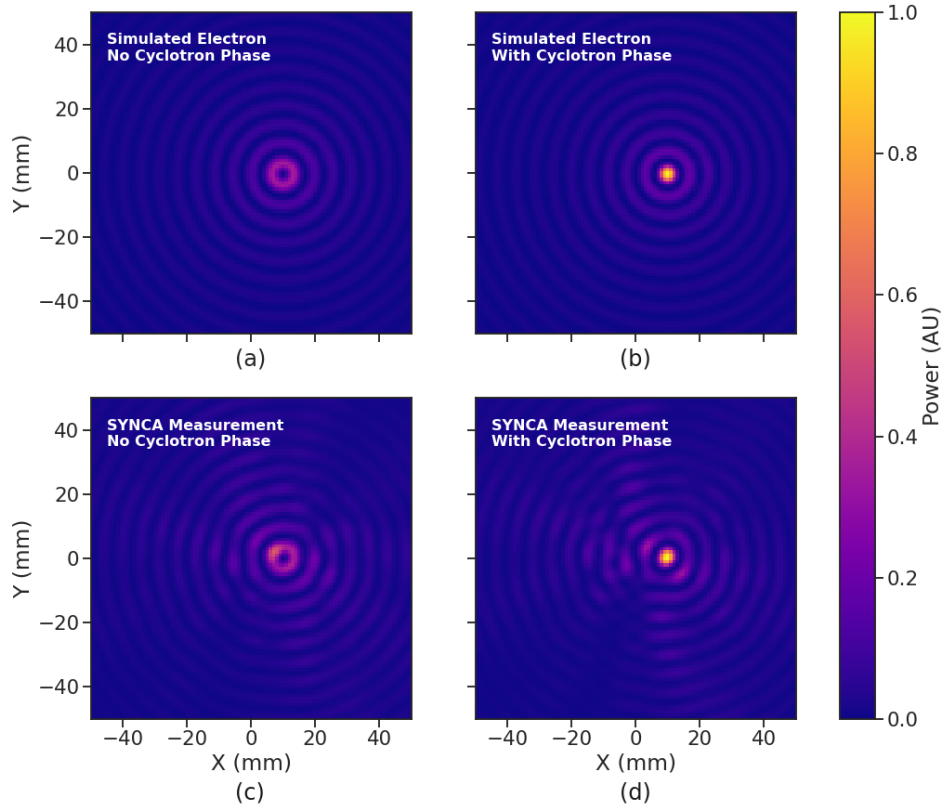


Figure 5.22. Digital beamforming maps generated using a simulated 60 channel array and electron simulated using the Locust package. (a) and (b) show the beamforming maps for simulated electrons without the cyclotron spiral phases and with the cyclotron spiral phases respectively. (c) and (d) show the beamforming maps produced from SYNCA measurements. We observe good agreement between simulated electrons and the SYNCA measurements.

4388 With a small modification to the hardware used to characterize the SYNCA (see
 4389 Figure 5.19), we can perform a digital beamforming reconstruction of a synthetic CRES

4390 event. By replacing the VNA with an arbitrary waveform generator (AWG), the SYNCA
4391 can be used to generate cyclotron radiation with an arbitrary signal structure, which
4392 can then be detected by digitizing the signals received by the horn antenna. Rotational
4393 symmetry allows us to use the rotational stage of the positioning system to rotate the
4394 SYNCA to recreate the signals that would have been received by a complete circular
4395 array of antennas.

4396 Using this setup, signals from a 60 channel circular array of equally spaced horn
4397 antennas were generated with the SYNCA positioned 10 mm off the central array axis,
4398 reconstructed using digital beamforming, and compared to Locust simulation (see Figure
4399 5.22). When the cyclotron spiral phases are not used, which is equivalent to setting θ_m
4400 in Equation 5.36 to zero, the SYNCA's position is reconstructed as a relatively faint ring
4401 as predicted by simulation. However, when the appropriate cyclotron phases are used
4402 during the beamforming procedure, both the simulated electron and the SYNCA appear
4403 as a single peak of high relative power corresponding to the source position. Therefore,
4404 we observe good agreement between the simulated and SYNCA reconstructions. While it
4405 may seem that for the case with no cyclotron phase corrections the ring reconstructs the
4406 position of the electron as effectively as beamforming with the cyclotron phase corrections,
4407 it is important to note that the simulations and measurements were generated without a
4408 realistic level of thermal noise. The larger maxima region and lower signal power, which
4409 occurs without the cyclotron phase corrections, significantly reduce the probability of
4410 detecting an electron in a realistic noise background.

4411 To bound the beamforming capabilities of the synthetic array of horn antennas, we
4412 performed a series of beamforming reconstructions where the SYNCA was progressively
4413 moved off the central axis of the array (see Figure 5.23). To extract an estimate of the
4414 position of the SYNCA using the digital beamforming image we apply a 2-dimensional
4415 (2D) Gaussian fit to the image data and extract the estimated centroid value. We find
4416 that the synthetic horn antenna array reconstructs the position of the SYNCA with a
4417 1σ -error of 0.3 mm with no apparent trend across the 30 mm measurement range. This
4418 reconstruction error is an order of magnitude larger than mean fit position uncertainty
4419 of 0.02 mm indicating that systematic effects related to the SYNCA positioning system
4420 could be contributing additional uncertainty to the measurements. Note that the current
4421 mean reconstruction error of 0.3 mm is a factor of 20 smaller than the full width at half
4422 maximum of the digital beamforming peak (6 mm), which could be interpreted as a naive
4423 estimate of the position reconstruction performance of this technique. Because these
4424 measurements are intended as a proof-of-principle demonstration, we do not investigate

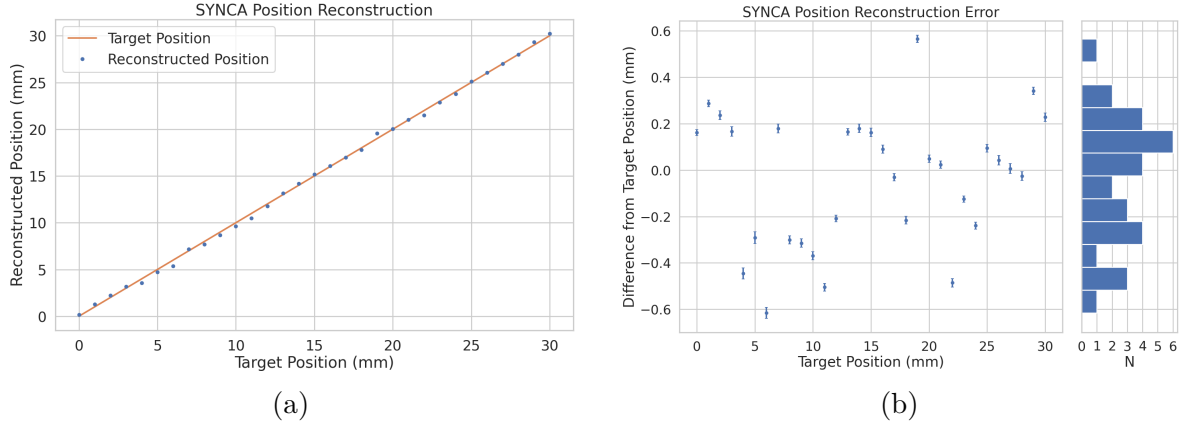


Figure 5.23. A plot of the SYNCA’s reconstructed position using the synthesized horn-antenna array and digital beamforming. (a) Shows the reconstructed position of the SYNCA compared with the target position indicated by the positioning system readout. (b) Shows the reconstruction error, which is the difference between the target and reconstructed positions. The error bars in (b) are the uncertainty in the mean position of the 2D Gaussian used to fit the digital beamforming reconstruction peak obtained from the fit covariance matrix. The mean fit position uncertainty of 0.02 mm is an order of magnitude smaller than the typical reconstruction error of 0.3 mm obtained by calculating the standard deviation of the difference between the reconstructed and target position.

4425 potential sources of systematic errors further; however, we expect that a similar and
 4426 more thorough investigation will be performed using the Project 8 antenna array test
 4427 stand, where typical reconstruction errors can be used to estimate the energy resolution
 4428 limits of antenna array designs.

4429 5.3.6 Conclusions

4430 In this paper we have introduced the SYNCA, which is a novel antenna design that
 4431 emits radiation that mimics the unique properties of the cyclotron radiation generated by
 4432 charged particles moving in a magnetic field. The characterization measurements of the
 4433 SYNCA validated the simulated performance of the PCB crossed-dipole antenna design.
 4434 Additionally, the SYNCA was used to estimate the position reconstruction capabilities
 4435 of a synthesized array of horn antennas and experimentally reproduced the simulated
 4436 digital beamforming reconstruction of electrons.

4437 While the SYNCA performs well, there exist discrepancies in the phase and magnitude
 4438 of the radiation pattern compared to the simulated SYNCA design that are related to
 4439 the small geometric differences in the soldered connections. Future design iterations that
 4440 replace the soldered connections with a fully surface mount design could improve the

4441 radiation pattern at the cost of some complexity and expense. Furthermore, improving
4442 the design of the antenna PCB and mounting system would allow the antenna to be
4443 inserted into a cryogenic and vacuum environment where in-situ antenna measurement
4444 calibrations could be performed.

4445 The discrepancies in the radiation pattern and phases exhibited by the as-built
4446 SYNCA should not greatly impact its performance as a calibration probe. Both magni-
4447 tude and phase variations can be accounted by applying the SYNCA characterization
4448 measurements as a calibration to the data collected by the antenna array test stand. The
4449 separate calibration of the SYNCA radiation does not impact the primary goals for the
4450 antenna array test stand which are array calibration and signal reconstruction algorithm
4451 performance characterization, because it can be performed with standard reference horn
4452 antennas with well understood characteristics.

4453 The SYNCA antenna technology advances the CRES technique by providing a
4454 mechanism to characterize free-space antenna arrays for CRES measurements without
4455 the need for a magnet and cryogenics system, which would be required for calibration
4456 using electron sources. Both the Project 8 collaboration as well as future collaborations
4457 which are developing antenna array based CRES experiments can make use of SYNCA
4458 antennas as an important component of their calibration and commissioning phases.

4459 5.4 SYNCA Development Discussion

4460 A crossed-dipole antenna (see Figure 5.24) was identified early on as a candidate SYNCA
4461 design. The crossed-dipole is a circularly polarized antenna, consequently, the electric
4462 fields measured in the plane of the dipole antenna exhibit the same relative phase offsets
4463 as a 90° electron in a magnetic trap. This is explained in greater detail in Section 5.3.
4464 These phase offsets were measured with the first rudimentary crossed-dipole prototype
4465 manufactured from coaxial cables with the insulation and shield stripped away.

4466 Because the SYNCA is ultimately a calibration tool, it is desireable that the antenna
4467 have a well-characterized and robust antenna pattern. Therefore, manufacturing a
4468 SYNCA using the stripped wire method shown in Figure 5.24 is infeasible. Studies of
4469 crossed-dipole antennas manufactured out of printed circuit boards were performed using
4470 HFSS to identify an antenna design that imitated an electron, while being more robust
4471 and simpler to manufacture (see Figure 5.25).

4472 Identifying a design that was robust, manufacturable, and most importantly matched
4473 the electric fields of a trapped electron proved to be a non-trivial task. The primary

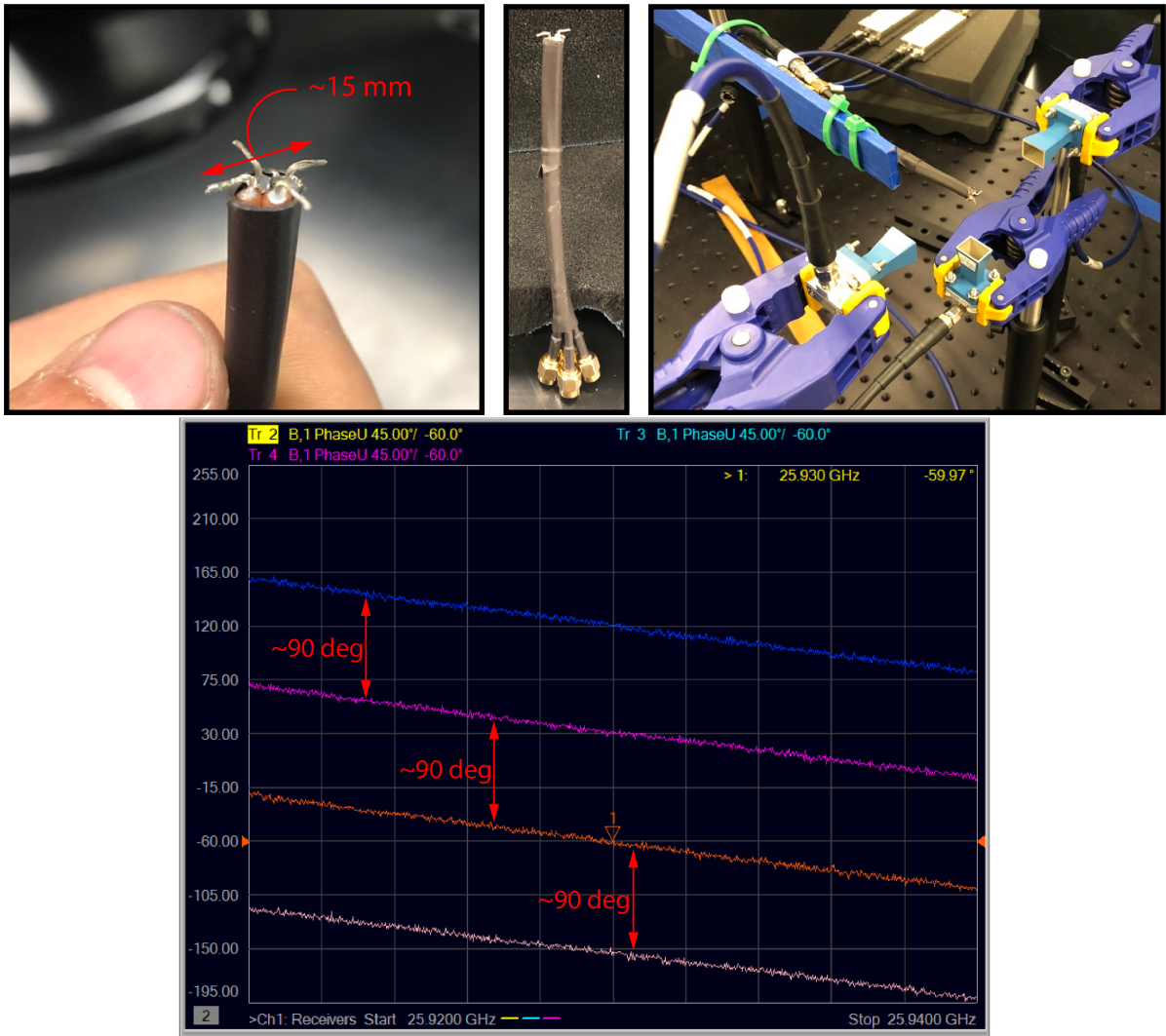


Figure 5.24. Images of an early prototype crossed-dipole antenna manufactured by hand and the first measurement setup. The antenna was constructed by hand using four stripped coaxial cables. The antenna was connected to one port of the VNA, and the remaining three ports on the VNA were connected to horn antenna arranged with 90 deg offsets around the crossed-dipole. The measured unwrapped S-parameter phases exhibit the desired relative phase behavior for a SYNCA. These early measurements were the first laboratory proof-of-principle for the crossed-dipole SYNCA.

factor driving the difficulty was the high operating frequency of the antenna (26 GHz) combined with the requirement that the antenna be electrically-small. An antenna that is electrically-small at 26 GHz has a largest dimension on the order of 1 mm, which poses significant manufacturability challenges given the limited available budget for SYCNA fabrication.

One of the key limitations with the small size requirements is the diameter of the

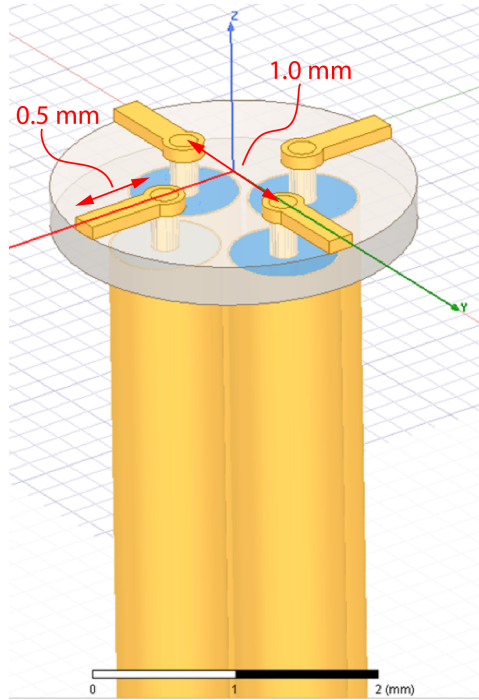


Figure 5.25. An early iteration of a crossed-dipole SYNCA antenna simulated in HFSS. The antenna is electrically small at 26 GHz, which requires dipole arms on the order of 1 mm long. This design is limited by the minimum achievable distance between the dipole arms caused by the available diameters of coaxial cables. The assumed termination scheme for the coaxial cables to the antenna is hand-soldering, which introduces random variation in the antenna pattern from the inevitable blobs of solder left on the surface of the PCB.

4480 coaxial cables needed to feed the crossed-dipole antenna. The smallest commonly available
 4481 rigid coaxial cables available on the market have diameters of approximately 0.5 mm,
 4482 which limited the spacing between dipole arms to a minimum of about 1 mm. The
 4483 crossed-dipole antenna performs better as a SYNCA if the dipole arm separation is
 4484 significantly less than the operating wavelength. Therefore, the high operating frequency
 4485 ultimately limited how well the SYNCA could mimic an electron. If the desired cyclotron
 4486 frequency was lowered by an order of magnitude to approximately 3 GHz a significantly
 4487 higher quality SYNCA could be manufactured at lower cost.

4488 The decision to use coaxial transmission lines terminated on the antenna PCB with a
 4489 hand-soldered connection was driven primarily to limit the costs of SYNCA development
 4490 and contributed to the observable variations in the SYNCA's gain and phase patterns.
 4491 A second iteration of the SYNCA design that minimized hand-soldering by using surface-
 4492 mount components could significantly reduce variations in the antenna pattern. The
 4493 major drawback in the development of a surface-mount SYNCA is the cost, and given the

4494 transition to a cavity based design for Phase IV, such a design was never investigated.

4495 5.5 FSCD Antenna Array Measurements with the SYNCA

4496 5.5.1 Introduction

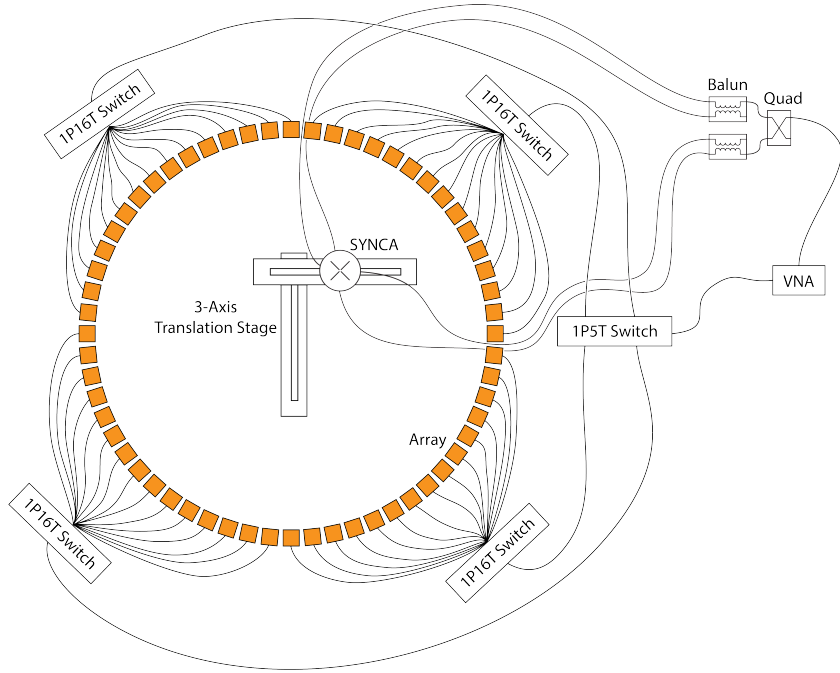


Figure 5.26. A diagram of the array measurement system used to test the prototype FSCD antenna array. A VNA is used as the primary measurement tool, which is connected to the array through a series of switches. The other port of the VNA connects to the SYNCA through the quad-balun chain used to provide the SYNCA feed signals. During measurements the SYNCA is positioned inside the center of the antenna array and translated to different radial and axial positions using a 3-axis manual translation stage setup.

4497 Using the SYNCA we can perform full-array measurements of prototype versions
4498 of the FSCD antenna array to test its performance with a realistic cyclotron radiation
4499 source (see Figure 5.26). The goal is to check how the measured power received by
4500 the array compares to FSCD simulations as a function of the radial and axial position
4501 of the SYNCA. These measurements are intended to validate the antenna research
4502 and development by Project 8, which has been driven primarily by simulations with
4503 Locust [61] and CRESana (see Section 4.2.3), and identify any discrepancies with these
4504 simulations tools. This knowledge will provide confidence in the simulations necessary
4505 for the analysis of the sensitivity of larger antenna array based CRES experiment designs

4506 to the neutrino mass.

4507 As shown in Section 5.3, the SYNCA does have some radiation pattern imperfections
4508 that complicate the comparison between measurement and simulation data. One way to
4509 disentangle some of the effects of these imperfections is to perform an additional set of
4510 measurements using a synthetic antenna array setup along with the SYNCA antenna.
4511 Since the synthetic array setup uses only a single array antenna, the data should be
4512 free of errors associated with individual antenna differences and multi-path interference,
4513 which are two error sources being tested with the full-array setup. By comparing the
4514 synthetic array data to the FSCD array data and to simulation data one can evaluate the
4515 significance of these effects relative to the errors introduced by SYNCA imperfections.

4516 **5.5.2 Measurement Setups**

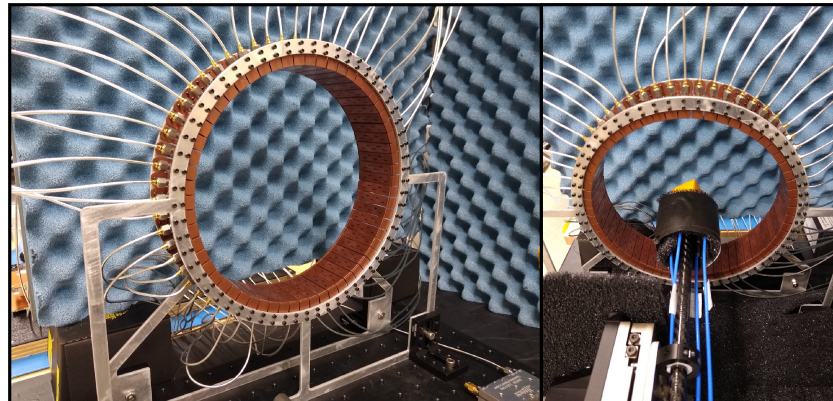
4517 **5.5.2.1 FSCD Array Setup**

4518 The antenna design that composes the array is the 5-slot waveguide antenna developed
4519 for the FSCD experiment (see Figure 5.27a). The antenna is 5 cm long and is constructed
4520 out of WR-34 waveguide with a 2.92 mm coax connector located at the center of the
4521 antenna. Copper flanges located on both ends of the antenna are used to mount the
4522 antenna in the array support structure. The antennas are supported by two circular steel
4523 brackets that can be bolted to both ends of the waveguide to construct the circular array
4524 (see Figure 5.27b). The antenna array consists of sixty identical waveguide antennas
4525 with a radius of 10 cm. The array is mounted perpendicular to an optical breadboard
4526 surface using a pair of the steel brackets, which provide sufficient space for the coaxial
4527 cable connections and allows for easy positioning of the SYNCA antenna. The SYNCA is
4528 mounted on the end of a carbon fiber rod attached to a set of manual translation stages,
4529 which are used to move the SYNCA antenna to different positions inside the array (see
4530 Figure 5.27c). The stages allow for independent motion in three different axes and can
4531 position the SYNCA at radial distances up to 5 cm from the center.

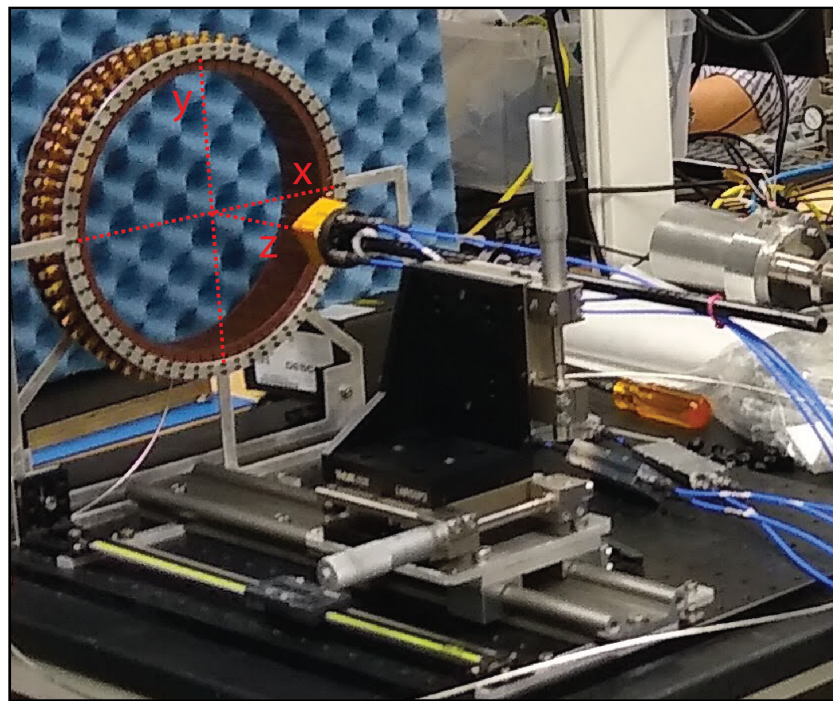
4532 Data acquisition is accomplished using a two-port VNA in combination with a series
4533 of microwave switches that allow the VNA to connect to each channel in the array . The
4534 first port of the VNA is connected to the quad-balun chain used to feed the SYNCA (see
4535 Section 5.3), and the second port of the VNA connects to a 1P5T microwave switch. The
4536 1P5T switch is connected to four separate 1P16T switch boards that connect directly
4537 to the array. The data acquisition is controlled by a python script running on a lab
4538 computer, which is connected to the VNA and an Arduino board programmed to control



(a)



(b)



(c)

Figure 5.27. Photos of the prototype FSCD antenna (a), the FSCD array and SYNCA (b), and the translation stages and coordinate system used to position the SYNCA (c).

4539 the microwave switches. The script uses the switches to iteratively connect each of the
4540 antennas in the array to the VNA. The VNA is configured to load a specific calibration
4541 file for each antenna channel and performs the measurements of all available S-parameters.
4542 The separate calibration files is an attempt to remove phase and magnitude errors caused
4543 by different propagation through the RF switches. Array measurements were performed
4544 for the set of SYNCA positions consisting of radial (x-axis) positions from 0 to 50 mm in
4545 5 mm steps and axial (z-axis) positions from 0 to 50 mm in 5 mm steps resulting in 121
4546 array measurements. At each SYNCA position we measured the two-port S-parameter
4547 matrix using a linear frequency sweep from 25.1 to 26.1 GHz with 101 discrete frequencies.

4548 5.5.2.2 Synthetic Array Setup

4549 A photograph of the setup used to perform the synthetic array measurements is shown
4550 in Figure 5.28. One important difference between this setup and the FSCD array setup
4551 is that the synthetic array measurements were performed with a waveform generator and
4552 digitizer instead of a VNA. The electronics configuration is identical to the diagram in
4553 Figure 5.7b. Despite the differences, one is still able to compare the measured phases of
4554 the synthetic array and the relative magnitude of the power, since the digitized signal
4555 power is directly proportional to S21.

4556 The arbitrary waveform generator in the setup is configured to produce a 64 MHz
4557 sine wave signal that is up-converted to 25.864 GHz using a mixer and the VNA source.
4558 This signal is passed through a bandpass filter and fed to the SYNCA quad-balun chain.
4559 A single FSCD antenna is positioned 10 cm from the SYNCA and aligned vertically so
4560 that the center of the 5-slot waveguide is in the plane of the SYNCA PCB (see Figure
4561 5.28). This position corresponds to $z = 0$ in Figure 5.27c. The SYNCA is rotated
4562 in three degree steps to synthesize an antenna array with 120 channels. This channel
4563 count is more than could physically fit in a 10 cm radius array, but there is no cost to
4564 over-sampling. Additionally, over-sampling allows for a check of the smoothness of the
4565 antenna array radiation pattern. The signals from the FSCD antenna are down-converted
4566 using the second mixer connected to the VNA source before being digitized at 250 MHz
4567 and saved to disk. Several synthetic array measurement scans were performed by using
4568 the linear translation stage to change the radial position of the SYNCA. In total eight
4569 scans were taken from 0 to 35 mm using a radial position step size of 5 mm.

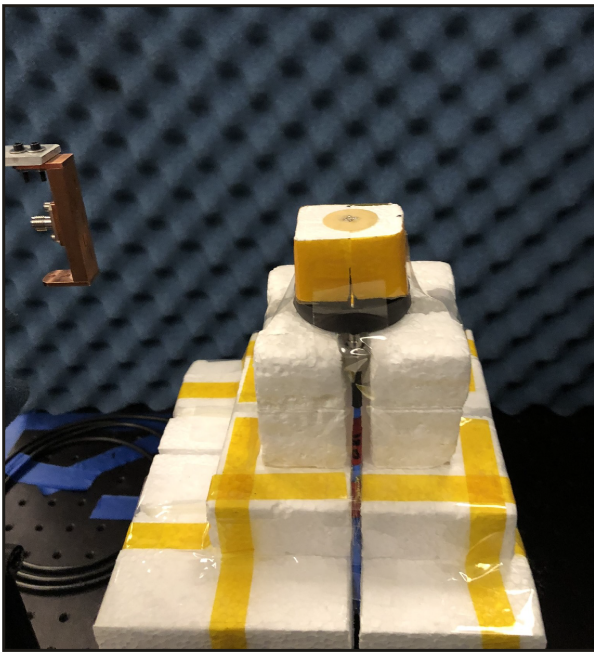


Figure 5.28. A photo of the FSCD antenna and the SYNCA in the synthetic array measurement setup at Penn State.

4570 5.5.3 Simulations, Analysis, and Results

4571 The Locust and CRESana simulation packages utilize the antenna transfer functions
4572 to calculate the power that would be received by each antenna from a CRES electron.
4573 The equivalent quantity in the measurement setup is the S21 matrix element, which
4574 indicates the ratio of the power received by an antenna in the array to the amount of
4575 power delivered to the SYNCA. Therefore, the analysis focuses on comparing the relative
4576 magnitudes and phase of the S21 parameters measured by the VNA as a function of
4577 the array channel and the SYNCA position. Additionally, we apply a beamforming
4578 reconstruction to the S21 data to evaluate how the summed power and beamforming
4579 images change as a function of the position of the SYNCA.

4580 5.5.3.1 Simulations

4581 Simulations for the FSCD array measurements were performed using CRESana, which
4582 performs analytical calculations of the EM-fields produced by an electron at the position
4583 of the antennas. At each sampled time CRESana computes the electric field vector at the
4584 antenna positions, which is projected onto the antenna polarization axis to obtain the
4585 co-polar electric field. The magnitude of the co-polar electric field is then multiplied by
4586 a flat antenna transfer function to calculate the corresponding voltage signal. CRESana

4587 simulations exploit the flat transfer functions of the FSCD antennas, which allows the
 4588 electric field to be multiplied by the antenna transfer function rather than performing
 4589 the full FIR calculation. These calculations produce a voltage time-series for each of the
 4590 antennas in the array that can be compared to the laboratory measurements.

4591 CRESana was configured to simulate a 90° electron in a constant background magnetic
 4592 field of ≈ 0.958 T with a kinetic energy of 18.6 keV. These parameters were chosen
 4593 in order to mimic a CRES event near the tritium beta-decay spectrum endpoint in
 4594 the FSCD experiment. The constant background magnetic field guarantees that the
 4595 guiding center of the electron is stationary across the duration of the simulation which is
 4596 consistent with the SYNCA in the laboratory measurements. Simulations were performed
 4597 with the electron's guiding center at radial positions from 0 to 45 mm in steps of 1 mm
 4598 and axial positions from 0 to 30 mm in steps of 1 mm. The simulations generated time
 4599 series consisting of 8192 samples at 200 MHz for the sixty channel FSCD antenna array
 4600 geometry.

4601 5.5.3.2 Phase Analysis

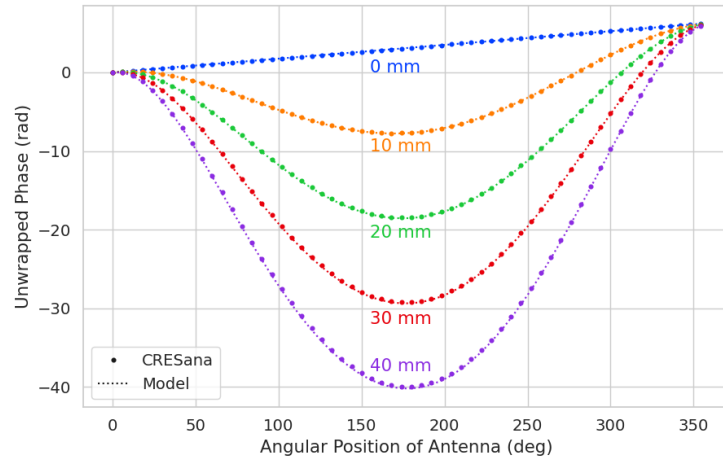


Figure 5.29. The unwrapped phases of signals received by the FSCD antenna array from an electron with a 90° pitch angle located in the plane of the antenna array. The data points indicated the phases extracted from simulation and the dashed lines show the model predictions.

4602 Correct modeling of the signal phases is fundamental to reconstruction for both
 4603 beamforming and matched filter approaches. The beamforming reconstruction relies on
 4604 a signal phase model developed from Locust simulations, which allows one to predict the
 4605 relative signal phases for a specific magnetic trap and electron position. The equation

4606 for the model is

$$\phi_{ij}(t) = \frac{2\pi d_{ij}(t)}{\lambda} + \theta_{ij}(t), \quad (5.37)$$

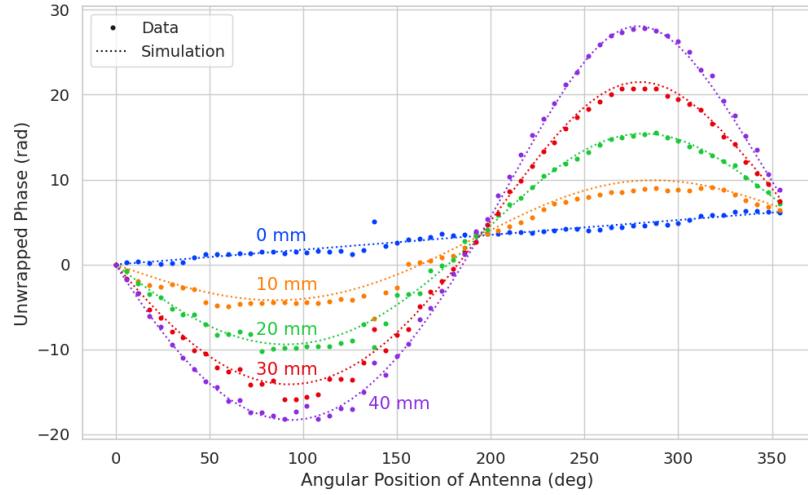
4607 where $d_{ij}(t)$ is distance between the assumed electron position and the antenna position,
4608 and $\theta_{ij}(t)$ is the angular separation between the electron and antenna positions. For
4609 details on the components of the phase model see Section 5.3.2. In Figure 5.29 we
4610 compare the phases predicted by Equation 5.37 to phases extracted from CREESana
4611 simulations of an electron located in the plane of the antenna array at a series of radial
4612 positions. One observes excellent agreement between the model and simulation.

4613 The measured signal phases from the FSCD array and synthetic array are shown
4614 in Figures 5.30a and 5.30b compared to the signal phase model. The axial position of
4615 the SYNCA in both plots is $z = 0$ mm, such that the plane of the PCB is aligned with
4616 the center of the FSCD antenna. The data shown in Figure 5.30a corresponds to the
4617 S-parameters measured at 25.80 GHz which is the frequency closest to the one used in
4618 the synthetic array setup. The different slope and sinusoidal phases exhibited by Figure
4619 5.30a and 5.30b reflects differences in the coordinate system for each setup. In general,
4620 we see that the phase model predicts the large scale features of the phases quite well,
4621 but there are some small scale deviations or errors from the phase model that do not
4622 appear to be present in simulation.

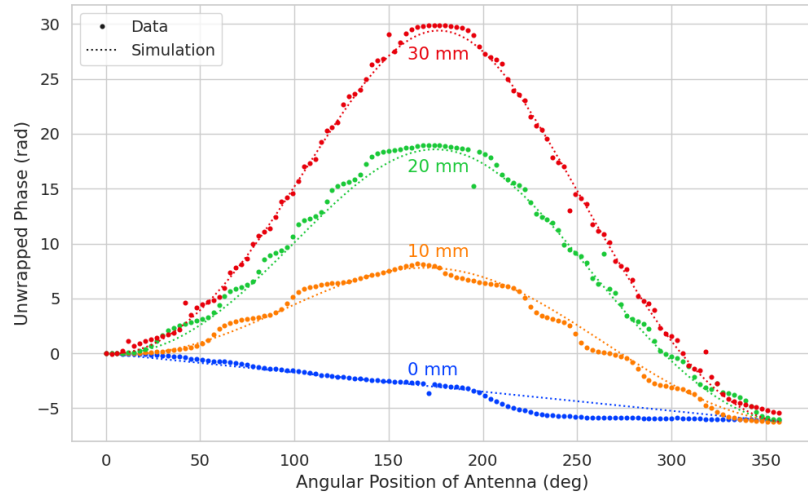
4623 A comparison of the phase errors, which are the difference between measurement and
4624 model is shown in Figure 5.31. The FSCD array data is referred to as the JUGAAD
4625 data in the plot legend, which is an alternative name for the FSCD array setup.

4626 The phase error at $R = 0$ in Figure 5.31 forms a smooth curve, with the exception of
4627 an outlier data point caused by a bug in the data acquisition script. One can attribute
4628 the observed phase error at this position to imperfections in the antenna pattern of the
4629 SYNCA. As the SYNCA is moved away from $R = 0$ mm one observes that the phase
4630 error exhibits oscillations whose frequency increases as a function of the radial position
4631 of the SYNCA. These oscillations have the appearance of a diffraction pattern, which
4632 is particularly clear for the radii ≥ 15 mm, due to the bilateral symmetry of the phase
4633 error peaks around 180° .

4634 One can observe a higher average variance in the phase errors measured for the FSCD
4635 array compared to the synthetic array. This is best seen by comparing the curves at
4636 $R \leq 15$ mm where the smooth synthetic array curves are distinct from the relatively
4637 noisy FSCD array errors. The extra noise in the FSCD array is most likely caused by
4638 differences in the radiation patterns of the antennas that make up the array as well as
4639 differences in the transmission lines through the switch network that introduce additional



(a)



(b)

Figure 5.30. Plots of the measured unwrapped phases from the FSCD array (a) and the synthetic array (b) compared to the model predictions for a series of radial positions. The different phases of the sinusoidal phase oscillations in the two plots reflects differences in the coordinate systems of the measurements.

phase errors into the measurement. Since the synthetic array measurements use only a single antenna, these extra error terms are not present, which explains the relatively smoother phase error curves. Despite the extra phase errors in the FSCD array, it is still possible to observe a similar phase error oscillation effect as the SYNCA is moved away from $R = 0$ mm.

The diffraction pattern exhibited by the phase error oscillations is more easily observed

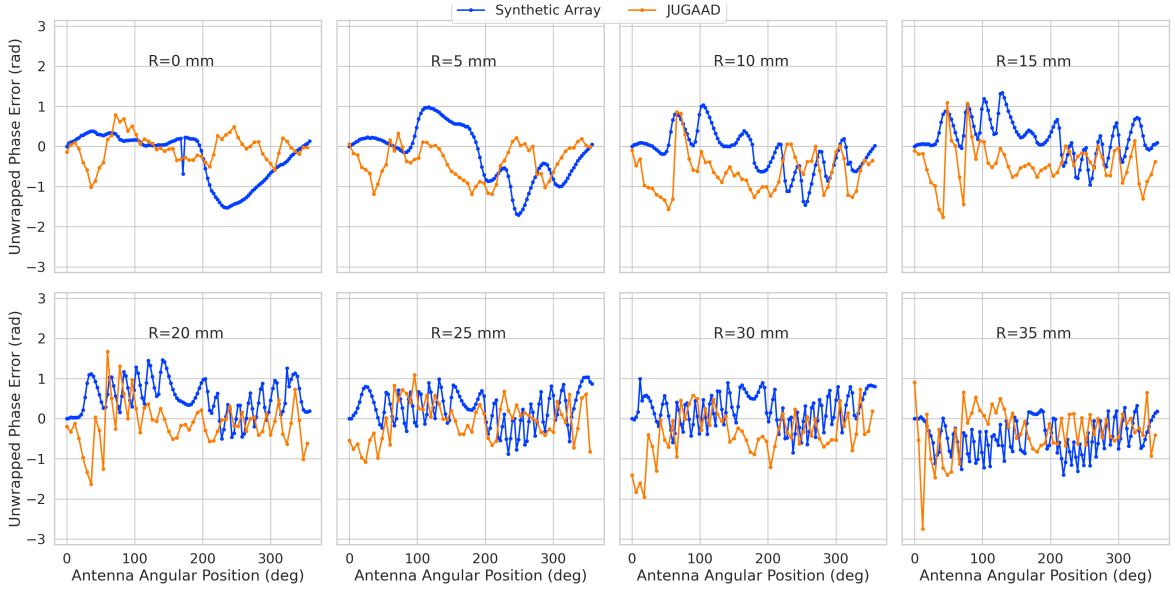


Figure 5.31. The phase errors between the measurement and model for the synthetic array (blue) and the FSCD array (orange) for a series of radial positions. The label JUGAAD refers to an alternative name for the FSCD array setup. As the SYNCA is translated off-axis phase errors with progressively higher oscillation frequency enter into the measurements.

4646 by plotting the phase errors in a two-dimensional map, which is done in Figures 5.32a and
 4647 5.32b. For the synthetic array data ones observes a relatively clear diffraction pattern
 4648 that emerges as the SYNCA is moved radially. The bilateral symmetry of the diffraction
 4649 patterns is due to the bilateral symmetry of the circular synthetic array around the
 4650 translation axis of the SYNCA. A similar pattern is also visible in the FSCD array data,
 4651 although, it is obscured by the additional phase error that results from the multi-channel
 4652 array.

4653 The physical origin of the phase error diffraction pattern is attributed to interference
 4654 effects arising from path-length differences between the individual slots in the FSCD
 4655 antenna and the SYNCA transmitter. Since we are operating in the radiative near-field of
 4656 the FSCD antenna, the path length differences between the slots introduces a significant
 4657 change in the summation of the signals that occurs inside the waveguide, which causes
 4658 the radiation pattern of the antenna to change as a function of distance. Therefore, when
 4659 the SYNCA is positioned off-axis the different path-lengths from the SYNCA to each
 4660 antenna results in different radiation patterns leading to the observed diffraction pattern.

4661 This near-field effect is not present in simulations, because in order to simplify the
 4662 calculations we assume that the far-field approximation can be applied to the FSCD
 4663 antennas. This means that the radiation pattern and antenna transfer functions are

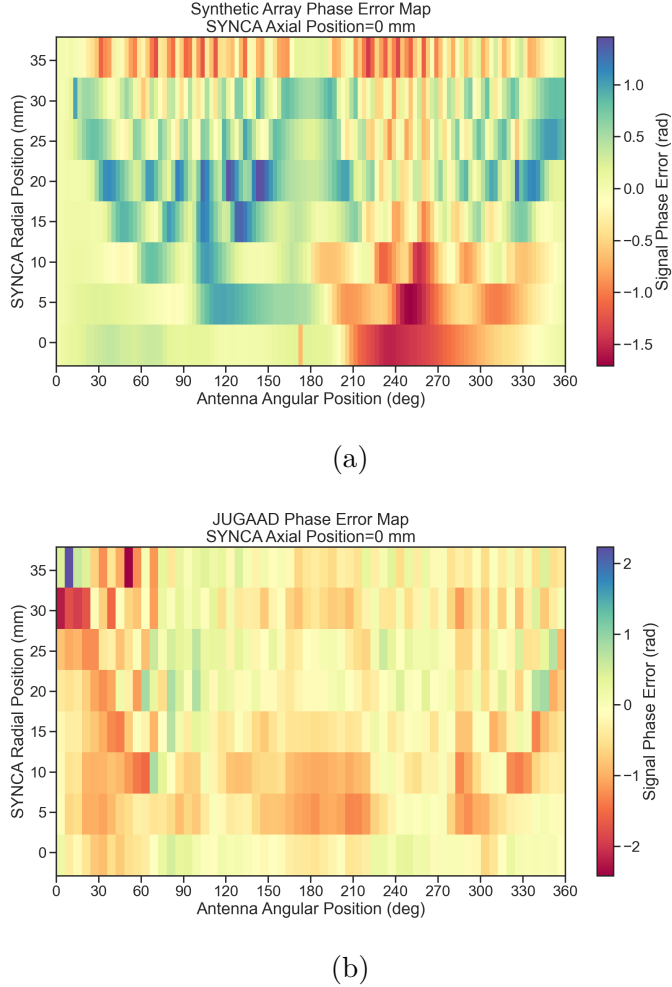


Figure 5.32. Two dimensional plots of the phase errors for the synthetic array (a) and the FSCD (JUGAAD) array (b). In both plots we observe evidence of a similar diffraction pattern with bilateral symmetry, but the FSCD array measurements have an additional phase error contribution from the different antennas and paths through the switch network.

independent of the distance between the transmitter and the receiving antenna. In principle, we can account for these near-field effects with a more detailed simulation of the FSCD antennas either in CRESana or Locust, which would result in an additional term in the beamforming phase model. However, this would increase the computational intensity of the simulation software. In the next section we briefly discuss the impact of these near-field effects on the measured magnitude of the signals.

4670 5.5.3.3 Magnitude Analysis

4671 Exactly as for the signal phase, one can use simulations to construct a model that
4672 describes the magnitude of the signals received by each channel in the antenna array.
4673 By examining the results of simulations or by analyzing the Liénard-Wiechert equation
4674 one can show that radiation pattern from a 90° pitch angle electron in a magnetic field
4675 is omni-directional. Therefore the relative magnitudes of the signals received by each
4676 channel will be determined by the free-space power loss, which is proportional to the
4677 inverse distance between the assumed electron position and the antenna.

4678 A consequence of this is that the signals produced in the array for electrons off the
4679 central axis will have larger amplitudes for the antennas closer to the electron compared
4680 to those which are further away. The amplitudes of the signals received by the array
from an electron located at a series of radial positions are shown in Figure 5.33.

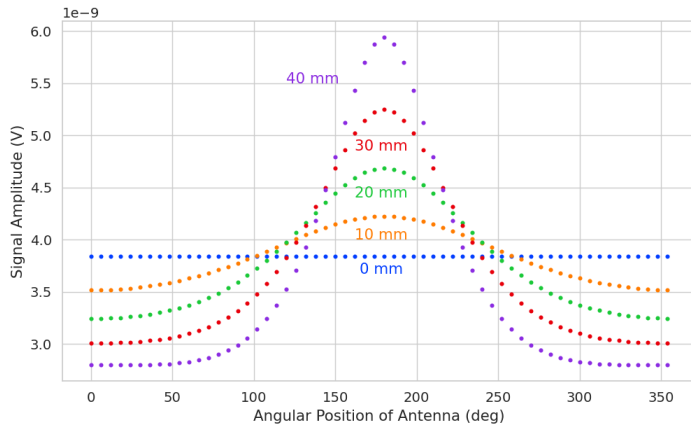


Figure 5.33. The amplitude of the signals from CRESana for the FSCD array from a 90° electron. As the electron is moved from $R = 0$ the signals begin to have unequal amplitudes depending on the distance from the electron to the antenna.

4681
4682 One expects to see a similar trend in the signal magnitudes in both the FSCD and
4683 synthetic arrays. The normalized signal magnitudes extracted from the full and synthetic
4684 array setups for a series of radial SYNCA positions are shown in Figure 5.34. The data
4685 corresponds to a SYNCA axial position of $z = 0$ mm and at a frequency 25.86 GHz. One
4686 complication is that the radiation pattern of the SYNCA is not perfectly omni-directional,
4687 which causes the measured magnitudes at $R = 0$ mm to diverge from the perfectly flat
4688 behavior exhibited by electrons.

4689 As the SYNCA is moved off-axis one observes a similar increase in the number of
4690 magnitude peaks in the synthetic array data that one would expect from a diffraction

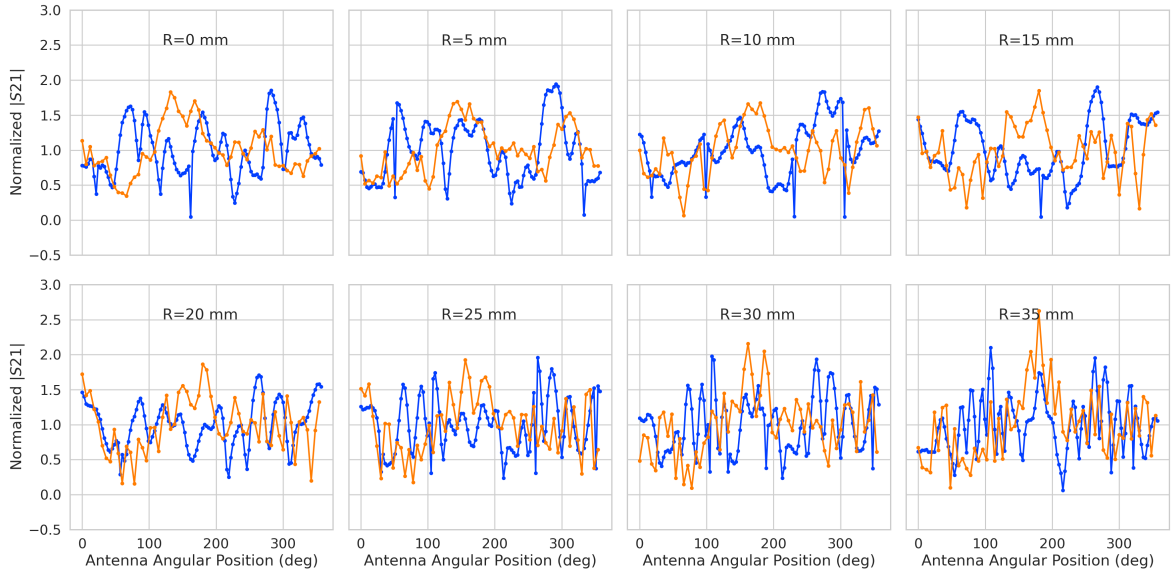
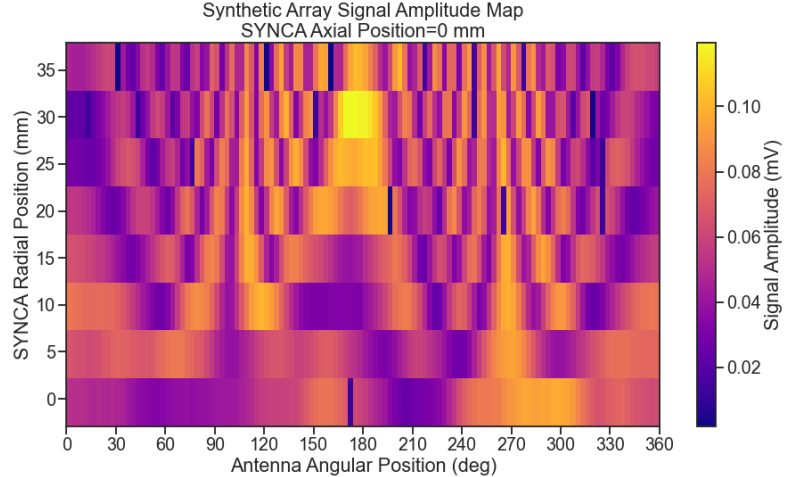


Figure 5.34. The normalized magnitudes of the S21 parameters measured in the FSCD (orange) and synthetic array (blue) setups. The dominant observed behavior as a function of radius is the increase in the number of magnitude peaks, which was noted in the phase error curves. There does not appear to be a strong change in the relative amplitude of a group of antennas as predicted by CRESana.

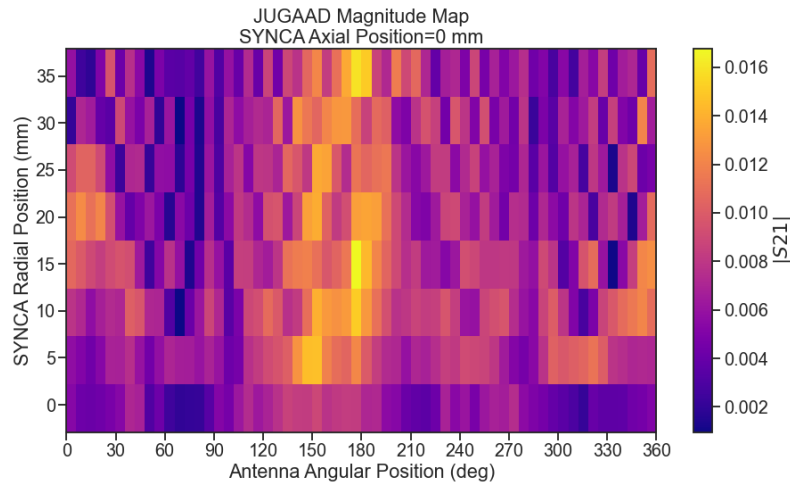
pattern, although this trend is not as stark compared to the phase data. Noticeably, there does not appear to be a set of channels with disproportionately larger amplitude at large R , which would be expected based on the trends from CRESana.

Comparing the magnitudes of the synthetic array to the FSCD array in Figure 5.34 we see that there is a similar amount of variability in the magnitudes at $R = 0$ mm, although there is potentially more small scale error in the magnitude curve caused by channel differences in the FSCD array. We observe a similar trend in the number of magnitude error peaks in the FSCD array data to the synthetic array data, which mirrors the diffraction effect observed in the phase data. The diffraction effect can be visualized more clearly by plotting a similar two-dimensional map of the magnitudes (see Figure 5.35).

The fact that one observes a similar diffraction pattern in the signal magnitudes as a function the SYNCA position reinforces the conclusions from the phase analysis that near-field effects are having a significant impact on the radiation pattern of the FSCD array. These near-field effects lead to changes in the magnitude and phase of the radiation pattern of the FSCD antenna as a function of distance. If left uncorrected these errors reduce detection efficiency by causing power loss in the beamforming or matched



(a)



(b) The two-dimensional maps showing the diffractive pattern exhibited by the FSCD and synthetic array signal magnitudes.

Figure 5.35.

4708 filter reconstruction due to phase mismatch. We explore the impact of these phase and
4709 magnitude errors on beamforming in the next section.

4710 5.5.3.4 Beamforming Characterization

4711 Errors in the signal magnitudes and phases lead to errors in signal reconstruction. For
4712 example, a matched filter reconstruction requires accurate knowledge of the signals in
4713 each channel to achieve optimal performance. Uncorrected errors leads to mismatches
4714 between the template and signal, which reduces detection efficiency and introduces

uncertainty in the parameter estimation. In this section, we analyze the beamformed signal amplitude as a function of the position of the SYNCA to quantify the impact of the phase and magnitude errors on signal reconstruction. Because of the imperfections in the SYNCA source, it is inappropriate to directly compare the beamformed signal amplitude of the FSCD array or synthetic array. Such a comparison would not allow one to disentangle losses that occur because of the antenna array from those that occur because of the source. Therefore, we focus on comparing the beamforming of the FSCD array to the synthetic array.

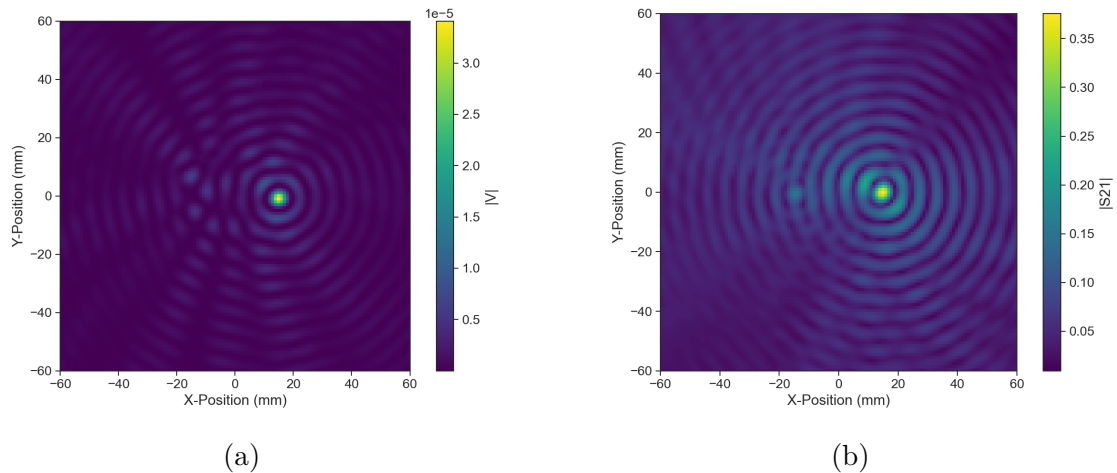


Figure 5.36. Beamforming images from the synthetic array (a) and FSCD array (b) setups with the SYNCA positioned 15 mm off the central axis. In both images we see a clear maxima that corresponds to the true SYNCA position. However, in the FSCD array there is an additional faint peak located at the opposite position of the beamforming maximum. This additional peak is the mirror of the true peak and is the result of reflections between antennas in the FSCD array.

The first method of comparison is to analyze the images generated by applying the beamforming reconstruction specified in Section 4.3.1 to the FSCD and synthetic array data (see Figure 5.36). The beamforming grid consisting of a square 121×121 grid spanning a range of -60-mm to 60 mm in the x and y dimensions. The beamforming images formed from the synthetic array produces a three-dimensional matrix where each grid position contains a summed time series. A single beamforming image is formed from this data matrix by taking the mean over the time dimension. In the case of the FSCD array, the VNA generates frequency domain data such that each grid position contains a summed frequency series produced by the VNA sweep. For this data a single image is formed by averaging in the frequency domain.

There is a clear difference between the synthetic and FSCD array beamforming images,

4734 which is the additional faint beamforming maxima located directly opposite the maxima
 4735 corresponding to the SYNCA position. The images in Figure 5.36 were generated with
 4736 data collected at a SYNCA radial position of 15 mm, which agrees well with the observed
 4737 beamforming maximum in both images. We observe that the faint beamforming peak is
 4738 located directly opposite of the true beamforming maximum similar to a mirror image.
 4739 Therefore, the origin of this additional feature appears to be reflections between the two
 4740 sides of the circular antenna array that are not present for the synthetic array since only
 4741 a single physical antenna is used.

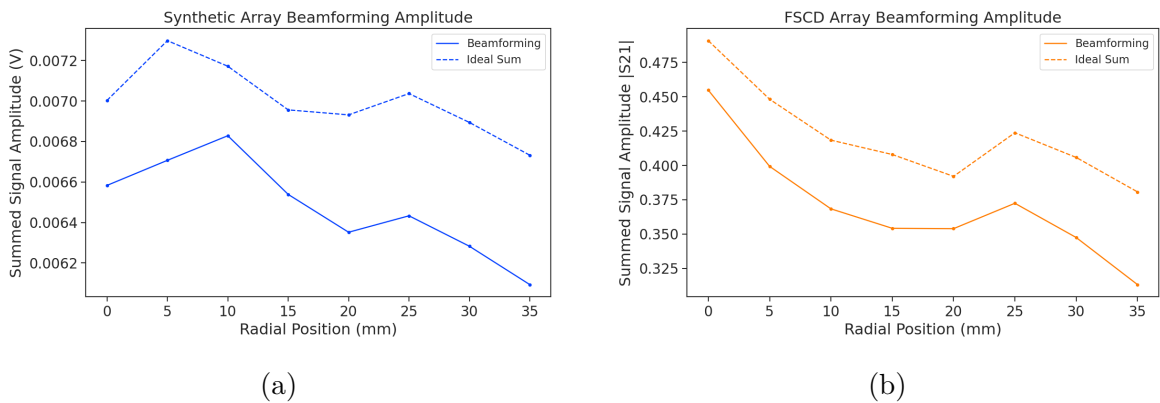


Figure 5.37. A comparison of the maximum signal amplitude obtained by beamforming to the signal amplitude obtained with an ideal summation as a function of the radial position of the SYNCA. The amplitudes for the synthetic array are shown in (a) and the FSCD array are shown in (b). In both setups we observe that the signal amplitudes obtained from beamforming are smaller than the signal amplitude that could be attained with the ideal summation without phase mismatch.

4742 From the beamforming images we extract the maximum amplitude, which we plot
 4743 as a function of the radial position of the SYNCA (see Figure 5.37). The phase errors
 4744 we observed in the FSCD and synthetic arrays leads to power loss at the beamforming
 4745 stage due to phase mismatches between the signals at different channels. This power
 4746 loss can be quantified by comparing the signal amplitude obtained from beamforming to
 4747 the amplitude which would be obtained from an ideal summation. We perform the ideal
 4748 summation by phase shifting each array channel to the same phase and then summing.
 4749 The comparison between the beamforming and ideal sums is shown in Figure 5.37, where
 4750 we observe that both the synthetic and FSCD arrays experience power losses from the
 4751 beamforming summation.

4752 The beamforming power loss can be quantified using the ratio of the beamforming to
 4753 ideal signal amplitudes. Computing this ratio as a function of SYNCA radial position

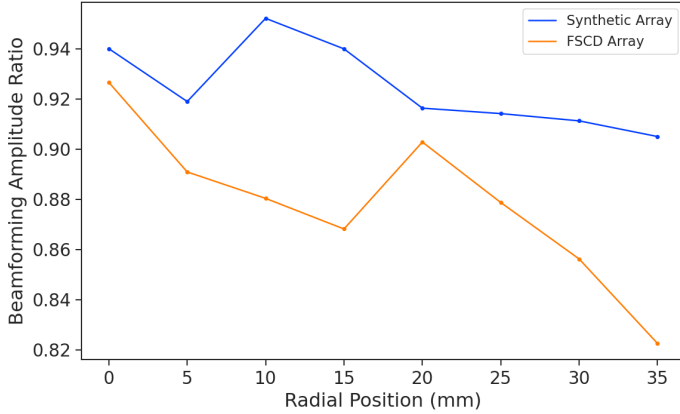


Figure 5.38. The ratio of the beamforming signal amplitude to the ideal signal amplitude for the FSCD and synthetic arrays. We see that the FSCD array has a larger power loss from phase error compare to the synthetic array which indicates that calibration errors associated with the multiple channels as well as reflections are impacting the signal reconstruction.

radius for the FSCD and synthetic arrays we find that the FSCD array has a uniformly smaller beamforming amplitude ratio, which means that the FSCD array has a larger beamforming power loss (see Figure 5.38). The primary contributions to the beamforming power loss in the synthetic array are phase errors from the SYNCA and phase errors from the FSCD antenna near-field. Both of these phase errors contribute to beamforming losses in the FSCD array, but there are clearly additional phase errors in the FSCD array measurements contributing to the smaller ratio. Two potential error sources include phase differences in the different antenna channels that could not be corrected by calibration as well as reflections between antennas in the array. The total effect of these additional phase errors is to reduce the beamforming amplitude ratio by about 5% from the beamforming ratio of the synthetic array. Therefore, we estimate that if no effort is made to correct these phase errors in an FSCD-like experiment, then we expect approximately a 10% total signal amplitude loss from a beamforming signal reconstruction.

5.5.4 Conclusions

The estimated power loss of a beamforming reconstruction obtained from this analysis provides valuable inputs to sensitivity calculations of a FSCD-like antenna array experiment to measure the neutrino mass, since it helps to bound systematic uncertainties from the antenna array and reconstruction pipeline. This power loss lowers the estimated detection efficiency of the experiment since some of the signal power is lost due to improper combining between channels and also increases the uncertainty in the electron's

⁴⁷⁷⁴ kinetic energy by contributing to errors in the estimation of the electron's cyclotron
⁴⁷⁷⁵ frequency.

⁴⁷⁷⁶ If these reconstruction losses prove unacceptable there are steps that can be taken
⁴⁷⁷⁷ to mitigate their effects. Some examples include the development of a more accurate
⁴⁷⁷⁸ antenna simulation approach that can reproduce the observed near-field interference
⁴⁷⁷⁹ patterns of the FSCD antennas and the implementation of a calibration approach that
⁴⁷⁸⁰ allows for the relative phase delays of the array to be measured without changing or
⁴⁷⁸¹ disconnecting the antenna array configuration.

Chapter 6

Development of Resonant Cavities for Large Volume CRES Measurements

6.1 Introduction

The cavity approach was originally an alternative CRES measurement technology under consideration by the Project 8 collaboration for the Phase IV experiment. After pursuing an antenna array based CRES demonstrator design for several years, the increasing costs and complexity of the antenna arrays led to a reconsideration of the baseline technology for the ultimate CRES experiment planned by Project 8. Currently, a cavity based CRES experiment is the preferred technology choice for future experiments by the Project 8 collaboration including the Phase IV experiment.

In this chapter I provide a brief summary of resonant cavities and sketch out the key features of a cavity based CRES experiment. In Section 6.2 I provide a brief introduction to cylindrical resonant cavities and the solutions for the electromagnetic fields in the cavity volume.

In Section 6.3 I describe the main components of a cavity based CRES experiment, including the background and trap magnets, cavity geometry and design, and cavity coupling considerations. I also discuss some relevant trade-offs between an antenna array and cavity CRES experiment, and highlight some reasons for the transition of Project 8 to the development of a cavity based experiment.

Finally, in Sections 6.4 and 6.5, I present the design and development of an open mode-filtered cavity that could be used in a cavity based CRES experiment with atomic tritium. The results of the cavity simulations are confirmed by laboratory measurements of a proof-of-principle prototype that demonstrates key features of the design.

4806 6.2 Cylindrical Resonant Cavities

4807 Resonant cavities are sealed conductive containers, which allows us to describe the
4808 electromagnetic (EM) fields contained in the cavity volume as a superposition of resonant
4809 modes [86]. The field shapes of the resonant modes are determined by Maxwell's equations
4810 and the boundary conditions enforced by the cavity geometry. Of interest to Project 8
4811 for CRES measurements are cylindrical cavities due to their ease of construction and
4812 integration with atom and electron trapping magnets.

4813 6.2.1 General Field Solutions

4814 Consider a long segment of conducting material with a cylindrical cross-section (see
4815 Figure 6.1). A geometry such as this can be used as a waveguide transmission line to
4816 transfer EM energy from point to point, or, if conducting shorts are inserted on both
4817 ends of the cylinder, the waveguide becomes a resonant cavity.

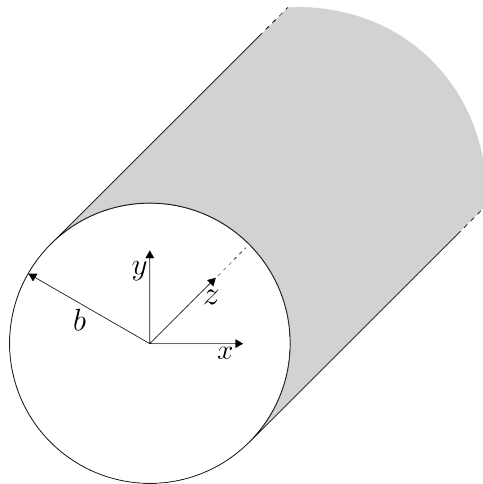


Figure 6.1. Geometry of a cylindrical waveguide with radius b .

4818 The fields allowed inside a cylindrical cavity are determined by the boundary conditions
4819 of the cylindrical geometry. The general approach to solving the fields begins by assuming
4820 solutions to Maxwell's equations of the form

$$\mathbf{E}(x, y, z) = (\mathbf{e}(x, y) + \hat{z}e_z(x, y))e^{-i\beta z}, \quad (6.1)$$

$$\mathbf{H}(x, y, z) = (\mathbf{h}(x, y) + \hat{z}h_z(x, y))e^{-i\beta z}. \quad (6.2)$$

4821 The solutions assume a harmonic time dependence of the form $e^{i\omega t}$ and propagation

4822 along the positive z-axis. The functions $\mathbf{e}(x, y)$ and $\mathbf{h}(x, y)$ represent the transverse
 4823 (\hat{x}, \hat{y}) components of the electric and magnetic fields respectively, and $e_z(x, y)$, $h_z(x, y)$
 4824 represent the longitudinal components. The version of Maxwell's equations in the case
 4825 where there are no source terms can be written as a pair of coupled differential equations,

$$\nabla \times \mathbf{E} = -i\omega\mu\mathbf{H}, \quad (6.3)$$

$$\nabla \times \mathbf{H} = i\omega\epsilon\mathbf{E}, \quad (6.4)$$

4826 where ϵ and μ are the permittivity and permeability of the material inside the waveguide
 4827 or cavity. Using the field solutions from Equations 6.1 and 6.2 one can solve for the
 4828 transverse components of the fields in terms of the longitudinal fields. Because we
 4829 are interested in cylindrical cavities it is advantageous to write the field solutions in
 4830 cylindrical coordinates. After performing this transformation the set of four equations
 4831 for the transverse field components are,

$$H_\rho = \frac{i}{k_c^2} \left(\frac{\omega\epsilon}{\rho} \frac{\partial E_z}{\partial\phi} - \beta \frac{\partial H_z}{\partial\rho} \right), \quad (6.5)$$

$$H_\phi = \frac{-i}{k_c^2} \left(\omega\epsilon \frac{\partial E_z}{\partial\rho} + \frac{\beta}{\rho} \frac{\partial H_z}{\partial\phi} \right), \quad (6.6)$$

$$E_\rho = \frac{-i}{k_c^2} \left(\beta \frac{\partial E_z}{\partial\rho} + \frac{\omega\mu}{\rho} \frac{\partial H_z}{\partial\phi} \right), \quad (6.7)$$

$$E_\phi = \frac{i}{k_c^2} \left(-\beta \frac{\partial E_z}{\partial\phi} + \omega\mu \frac{\partial H_z}{\partial\rho} \right), \quad (6.8)$$

4832 where k_c is the cutoff wavenumber defined by $k_c^2 = k^2 - \beta^2$ with $k = \omega\sqrt{\mu\epsilon}$ being the
 4833 wavenumber of the EM radiation.

4834 This set of equations can be used to solve for a variety of different modes that can be
 4835 obtained by setting conditions on E_z and H_z . For cylindrical cavities two types of modes
 4836 are allowed, which correspond to solutions where $E_z = 0$ and $H_z = 0$ respectively.

4837 6.2.2 TE and TM Modes

4838 The TE family of modes corresponds to the case where $E_z = 0$. This implies that H_z is
 4839 a solution to the Helmholtz wave equation

$$(\nabla^2 + k^2)H_z = 0. \quad (6.9)$$

4840 For solutions of the form $H_z(\rho, \phi, z) = h_z(\rho, \phi)e^{-i\beta z}$, Equation 6.9 can be solved using
 4841 the standard technique of separation of variables. Rather than reproduce the derivation
 4842 here we shall simply quote the solutions for the transverse fields [86], which are

$$H_\rho = \frac{-i\beta}{k_{c_{nm}}} (A \sin n\phi + B \cos n\phi) J'_n(k_{c_{nm}}\rho) e^{-i\beta_{nm}z}, \quad (6.10)$$

$$H_\phi = \frac{-i\beta n}{k_{c_{nm}}^2 \rho} (A \cos n\phi - B \sin n\phi) J_n(k_{c_{nm}}\rho) e^{-i\beta_{nm}z}, \quad (6.11)$$

$$E_\rho = \frac{-i\omega\mu n}{k_{c_{nm}}^2 \rho} (A \cos n\phi - B \sin n\phi) J_n(k_{c_{nm}}\rho) e^{-i\beta_{nm}z}, \quad (6.12)$$

$$E_\phi = \frac{i\omega\mu}{k_{c_{nm}}} (A \sin n\phi + B \cos n\phi) J'_n(k_{c_{nm}}\rho) e^{-i\beta_{nm}z}. \quad (6.13)$$

4843 One can observe that the solutions have a periodic dependence on ϕ , and radial profiles
 4844 given by the Bessel functions of the first kind. The integer indices n and m arise from
 4845 continuity conditions on the EM fields in the azimuthal and radial directions. For the
 4846 TE modes $n \geq 0$ and $m \geq 1$. $k_{c_{nm}}$ is the cutoff wavenumber for the TE_{nm} mode given by

$$k_{c_{nm}} = \frac{p'_{nm}}{b}, \quad (6.14)$$

4847 where b is the radius of the cavity or waveguide and p'_{nm} is the m -th root of the derivative
 4848 of the n -th order Bessel function (see Table 6.1).

Table 6.1. A table of the values of p'_{nm} .

n	p'_{n1}	p'_{n2}	p'_{n3}
0	3.832	7.016	10.174
1	1.841	5.331	8.536
2	3.054	6.706	9.970

4849 The TM mode family corresponds to the case where $H_z = 0$, and $(\nabla^2 + k^2)E_z = 0$.
 4850 Again, we assume solutions of the form $E_z(\rho, \phi, z) = e_z(\rho, \phi)e^{-i\beta z}$, for which the general
 4851 form of the solutions is the same as for the TE modes. However, the different boundary
 4852 conditions for the TM modes results in particular solutions with a different from, which
 4853 we shall quote here without derivation. The transverse fields of the TM modes are given
 4854 by

$$H_\rho = \frac{-i\omega\epsilon n}{k_{c_{nm}}^2 \rho} (A \cos n\phi - B \sin n\phi) J_n(k_{c_{nm}}\rho) e^{-i\beta_{nm}z}, \quad (6.15)$$

$$H_\phi = \frac{-i\omega\epsilon}{k_{c_{nm}}} (A \sin n\phi + B \cos n\phi) J'_n(k_{c_{nm}}\rho) e^{-i\beta_{nm}z} \quad (6.16)$$

$$E_\rho = \frac{-i\beta}{k_{c_{nm}}} (A \sin n\phi + B \cos n\phi) J'_n(k_{c_{nm}}\rho) e^{-i\beta_{nm}z}, \quad (6.17)$$

$$E_\phi = \frac{-i\beta n}{k_{c_{nm}}^2 \rho} (A \cos n\phi - B \sin n\phi) J_n(k_{c_{nm}}\rho) e^{-i\beta_{nm}z}, \quad (6.18)$$

which one may notice are the same solutions as the TE modes with H and E flipped.
 The cutoff wavenumber for the TM modes is given by, $k_{c_{nm}} = p_{nm}/b$, where the values of p_{nm} correspond to the m -th zero of the n -th order Bessel function (see Table 6.2).

Table 6.2. A table of the values of p_{nm} .

n	p_{n1}	p_{n2}	p_{n3}
0	2.405	5.520	8.654
1	3.832	7.016	10.174
2	5.135	8.417	11.620

6.2.3 Resonant Frequencies of a Cylindrical Cavity

A cylindrical cavity is constructed by taking a section of cylindrical waveguide and shorting both ends with conductive material. This means that the electric fields inside a cylindrical cavity are exactly those we derived in Section 6.2.2 with the additional condition that the electric fields must go to zero at $z = 0$ and $z = L$ (see Figure 6.2).

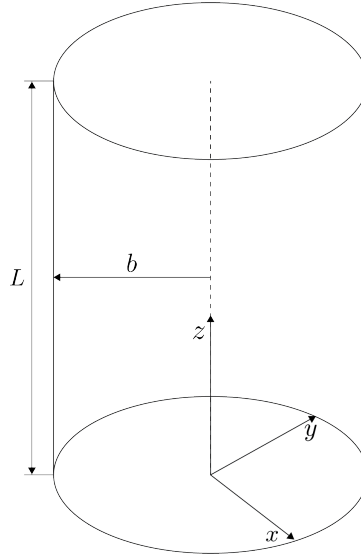


Figure 6.2. The geometry of a cylindrical cavity with length L and radius b .

4863 The transverse electric field solutions for a cylindrical waveguide are of the form

$$\mathbf{E}(\rho, \phi, z) = \mathbf{e}(\rho, \phi) (A_+ e^{-i\beta_{nm}z} + A_- e^{i\beta_{nm}z}), \quad (6.19)$$

4864 where A_+ and A_- are arbitrary amplitudes of forward and backward propagating waves.

4865 In order to enforce that \mathbf{E} is zero at both ends of the cavity we require that

$$\beta_{nm}L = 2\pi\ell, \quad (6.20)$$

4866 where $\ell = 0, 1, 2, 3, \dots$. Using this constraint on the propagation constant we can solve

4867 for the resonant frequencies of the TE_{nml} and the TM_{nml} modes in a cylindrical cavity.

4868 For the TE modes the resonant frequencies are

$$f_{nml} = \frac{c}{2\pi\sqrt{\mu_r\epsilon_r}} \sqrt{\left(\frac{p'_{nm}}{b}\right)^2 + \left(\frac{\ell\pi}{L}\right)^2}, \quad (6.21)$$

4869 and the frequencies of the TM modes are

$$f_{nml} = \frac{c}{2\pi\sqrt{\mu_r\epsilon_r}} \sqrt{\left(\frac{p_{nm}}{b}\right)^2 + \left(\frac{\ell\pi}{L}\right)^2}. \quad (6.22)$$

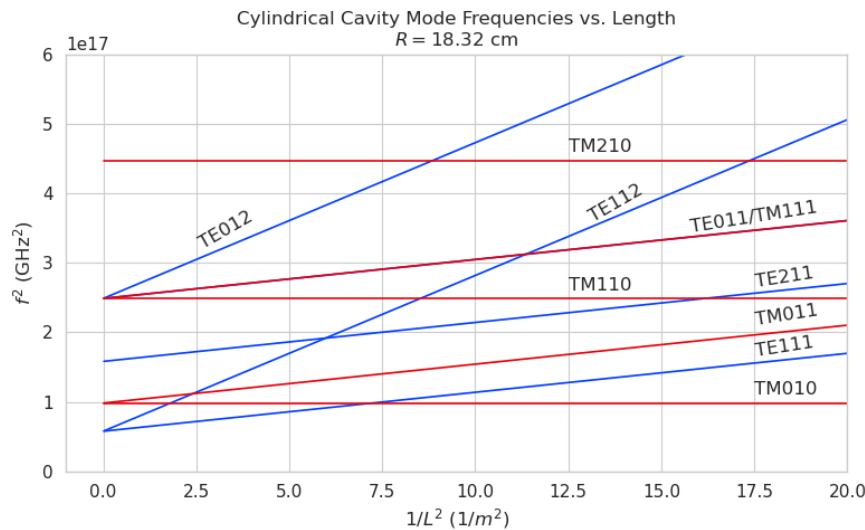


Figure 6.3. Relation of mode frequency to cavity length for a cylindrical cavity with a radius of 18.32 cm.

4870 6.2.4 Cavity Q-factors

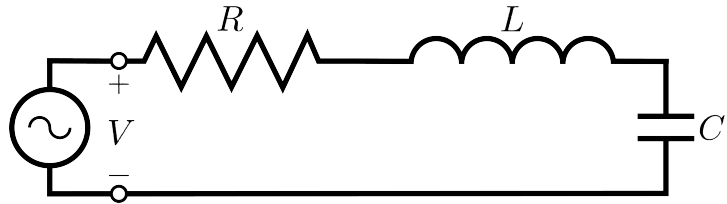


Figure 6.4. A series RLC circuit.

4871 The resonant behavior of cylindrical cavities can be modeled as a series RLC circuit
 4872 (see figure 6.4). The input impedance of the circuit can be obtained by applying
 4873 Kirchhoff's laws to calculate the impedance of the equivalent circuit. For a series RLC
 4874 circuit the input impedance is

$$Z_{\text{in}} = \left(\frac{1}{R} + \frac{1}{i\omega L} + i\omega C \right). \quad (6.23)$$

4875 The resistance in the circuit represents all sources of loss in the cavity, which is primarily
 4876 caused by the finite conductivity of the cavity walls. The inductor and capacitor represent
 4877 the energy stored in the cavity in the form of electric and magnetic fields. If the circuit
 4878 is being driven by an external power source we can write the input power in terms of the
 4879 circuit input impedance and the source voltage

$$P_{\text{in}} = \frac{1}{2} Z_{\text{in}} |I|^2 = \frac{1}{2} |I|^2 \left(\frac{1}{R} + \frac{1}{i\omega L} + i\omega C \right). \quad (6.24)$$

4880 The resistor introduces a loss into the system with a power given by

$$P_{\text{loss}} = \frac{1}{2} |I|^2 R, \quad (6.25)$$

4881 and the capacitor and inductor store energies given by

$$W_e = \frac{1}{4} \frac{|I|^2}{\omega^2 C}, \quad (6.26)$$

$$W_m = \frac{1}{4} |I|^2 L, \quad (6.27)$$

4882 respectively. Using these expressions we can write the input power and input impedance

4883 expressions in terms of the lost power and stored energy

$$P_{\text{in}} = P_{\text{loss}} + 2i\omega(W_m - W_e), \quad (6.28)$$

$$Z_{\text{in}} = \frac{P_{\text{loss}} + 2i\omega(W_m - W_e)}{\frac{1}{2}|I|^2}. \quad (6.29)$$

4884 The condition for resonance in the RLC circuit is that the stored magnetic energy
 4885 is equal to the stored electric energy ($W_e = W_m$). When this occurs $Z_{\text{in}} = R$, which is a
 4886 purely real impedance, and $P_{\text{in}} = P_{\text{loss}}$. The resonant frequency of the circuit can be
 4887 determined from the condition $W_e = W_m$ from which one finds that

$$\omega_0 = \frac{1}{\sqrt{LC}}. \quad (6.30)$$

4888 An important performance parameter for any resonant system is the Q-factor, which
 4889 quantifies the quality of the resonator as the ratio of the stored energy multiplied by the
 4890 resonant frequency to the average energy lost per second. For the series RLC circuit, the
 4891 Q-factor is given by the expression

$$Q_0 = \omega \frac{W_e + W_m}{P_{\text{loss}}} = \frac{1}{\omega_0 RC}, \quad (6.31)$$

4892 from which one observes that as the resistance of the RLC circuit is decreased the quality
 4893 factor of the resonator increases. From the perspective of cylindrical cavities this implies
 4894 that as one decreases the resistance of the cavity walls it is expected that the Q-factor of
 4895 the cavity should increase, which is indeed the case. In certain applications where a high
 4896 Q is desireable it is possible to manufacture a cavity out of superconducting materials in
 4897 order to minimize the power losses of the system.

4898 The Q-factor of the resonator also determines with bandwidth (BW) of the system.
 4899 A cavity with a high Q-factor will resonant with a smaller range of frequencies than a
 4900 cavity with a low Q-factor. To see this we can examine the behavior of the RLC circuit
 4901 when driven by frequencies near the resonance. For a frequency $\omega = \omega_0 + \Delta\omega$, where
 4902 $\Delta\omega = \omega - \omega_0 \ll \omega_0$, we can write the input impedance as

$$Z_{\text{in}} = R + i\omega L \left(\frac{\omega^2 - \omega_0^2}{\omega^2} \right), \quad (6.32)$$

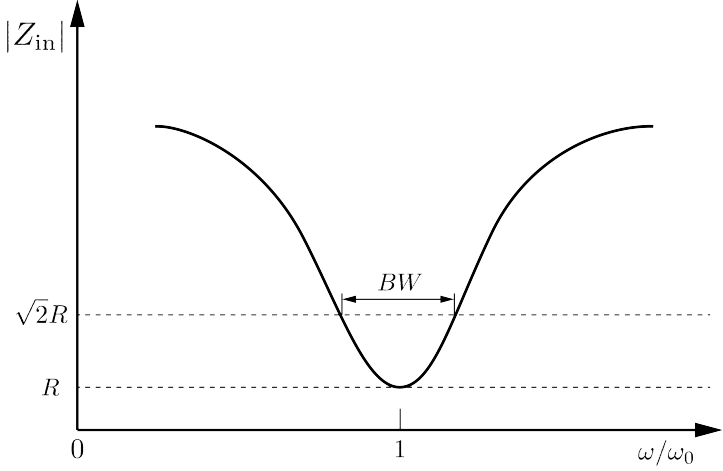


Figure 6.5. Illustration of the behavior of the input impedance of the series RLC circuit as a function of the driving frequency. The BW is proportion to the width of the resonance, which is inversely proportional to Q.

and by expanding $(\omega^2 - \omega_0^2)/\omega^2$ to first order in $\Delta\omega$, we obtain

$$Z_{in} \approx R + i \frac{2RQ_0\Delta\omega}{\omega_0}. \quad (6.33)$$

Therefore, the magnitude of the input impedance near the resonance is given by

$$|Z_{in}| = R \sqrt{1 + 4Q_0^2 \frac{\Delta\omega^2}{\omega^2}}, \quad (6.34)$$

from which we observe that for the series RLC circuit the input impedance is minimized at the resonant frequency, which corresponds to the maximum input power (see Figure 6.5). The half-power BW is the range of frequencies over which the input power drops to half the input power on resonance. This occurs when $|Z_{in}| = \sqrt{2}R$, which corresponds to $\Delta\omega/\omega = BW/2$. Using Equation 6.34 one can find that

$$2R^2 = R^2(1 + Q_0^2 BW^2), \quad (6.35)$$

which implies

$$BW = \frac{1}{Q_0} \quad (6.36)$$

It is important to emphasize that the Q-factor defined here, Q_0 , is technically the unloaded Q. It reflects the quality of the cavity or resonant circuit without the influence of any external circuitry. In practice, however, a cavity is invariably coupled to an

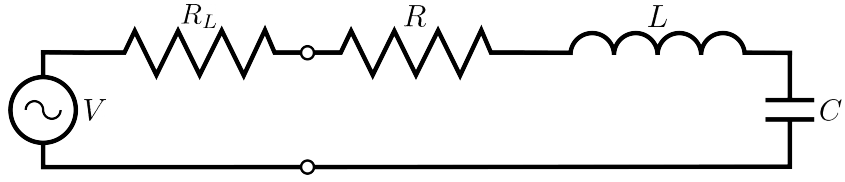


Figure 6.6. A series RLC circuit coupled to an external circuit with input impedance R_L .

4914 external circuit to drive a cavity resonance or to measure the energy of a resonant mode.
 4915 Coupling a cavity to an external circuit changes the Q by loading the equivalent cavity
 4916 RLC circuit (see Figure 6.6). The Q-factor of the cavity when it is loaded by an external
 4917 circuit is called the loaded Q, which is the quantity that one actually measures when
 4918 exciting a resonance in the cavity. Using the series RLC circuit model one can see that
 4919 the load resistor in Figure 6.6 will add in series with the resistor in the circuit for a total
 4920 equivalent resistance of $R + R_L$. Therefore, the loaded Q is given by

$$Q_L = \frac{1}{\omega_0(R + R_L)C}, \quad (6.37)$$

4921 from which one observes that the loaded Q is always less than the intrinsic Q of the
 4922 cavity.

4923 The amount of coupling that is desireable depends on the specific application of
 4924 the resonator. If one wants a resonator that is particular frequency selective than it
 4925 makes sense to limit the amount of coupling to the cavity to maintain a small BW,
 4926 alternatively, if a larger BW is need one can increase the cavity coupling by tuning the
 4927 input impedance of the external circuit. The critical point, where maximum power is
 4928 transferred between the cavity and the external circuit, occurs when the input impedance
 4929 of the cavity matches the input impedance of the external transmission line. For the
 4930 series RLC circuit on resonance, this matching condition corresponds to

$$Z_0 = Z_{in} = R, \quad (6.38)$$

4931 where Z_0 is the impedance of the transmission line. The loaded Q at this critical point
 4932 is, therefore,

$$Q_L = \frac{1}{2\omega_0 Z_0 C} = \frac{Q_0}{2}. \quad (6.39)$$

4933 One can described the degree of coupling between the cavity and an external circuit by

4934 defining a coupling factor, g , such that,

$$g = \frac{Q_0}{Q_L} - 1. \quad (6.40)$$

4935 When $g = 1$ then $Q_L = Q_0/2$, and the cavity is said to be critically coupled as we
4936 described. If $Q_L < Q_0/2$, then the cavity is undercoupled to the transmission line,
4937 corresponding to $g < 1$. Alternatively, if $Q_L > Q_0/2$, then $g > 1$, and the cavity is
4938 overcoupled to the transmission line. Various specialized circuits can be used to tune the
4939 input impedance of the external circuit as seen by the cavity to achieve a wide range of
4940 different coupling factors based on the desired application of the cavity.

4941 6.3 The Cavity Approach to CRES

4942 6.3.1 A Sketch of a Molecular Tritium Cavity CRES Experiment

4943 Resonant cavities can be used to perform CRES measurements, and they represent the
4944 current preferred technology by the Project 8 collaboration. The basic approach to a
4945 neutrino mass measurement using a resonant cavity and molecular tritium beta-decay
source is illustrated by Figure 6.7.

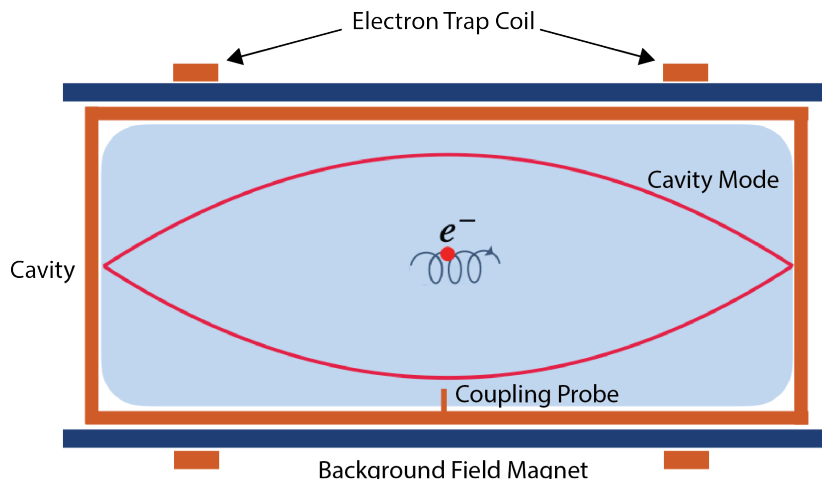


Figure 6.7. A cartoon depiction of a cavity CRES experiment. A metallic cavity filled with tritium gas is inserted into a uniform background magnetic field to perform CRES measurements. Electrons from beta-decays inside the cavity can be trapped and used to excite a resonant mode(s). By coupling to the cavity mode with a suitable probe one can measure the cyclotron frequency of the electron and perform CRES.

4946

4947 At the core of the experiment is a large resonant cavity filled with tritium gas. The
4948 filled cavity is then placed in a uniform magnetic field provided by a primary magnet
4949 that provides the background magnetic field. The value of the background magnetic field
4950 sets the range of cyclotron frequencies for electrons emitted near the tritium spectrum
4951 endpoint. When a beta-decay electron is produced in the cavity it is trapped using a set
4952 of magnetic pinch coils that keep electrons inside the cavity volume.

4953 Electrons trapped inside the cavity do not radiate in the same way as electrons
4954 in free-space. Effectively, the same boundary conditions that were used to derive the
4955 resonant modes of a cylindrical cavity in Section 6.2 apply to the radiation of the electron
4956 as well. The coupling of an electron performing cyclotron motion in a cavity has been
4957 studied in detail for measurements of the electron’s magnetic moment [95–97] If an
4958 electron is emitted with a kinetic energy that corresponds to a cyclotron frequency that
4959 matches a resonant frequency of the cavity, then energy radiated by the electron excites
4960 a corresponding resonance in the cavity. The strength of the electron’s coupling to the
4961 cavity is given to first order by the dot product between the electrons trajectory and
4962 the electric field vector of the resonant mode. Additional effects, such as the Purcell
4963 enhancement [98], alter the emitted power from the free-space Larmor equation [49]. If an
4964 electron is moving with a cyclotron frequency that is far from any resonant modes in the
4965 cavity, then radiation from the electron is suppressed. One can interpret this somewhat
4966 surprising effect as the metallic walls of the cavity reflecting the radiated energy back to
4967 the electron.

4968 Detecting an electron in the cavity is accomplished by coupling the cavity to an
4969 external transmission line that leads to an amplifier and RF receiver chain [99]. The
4970 coupling of the cavity resonance to the amplifier occurs through a coupling probe or
4971 aperture designed to read-out the excitation of the mode(s) excited by the electron. For
4972 CRES measurements, the placement of a wire antenna coupling probe inside the cavity
4973 volume leads to unacceptable losses of tritium atoms due to recombination to molecular
4974 tritium on the antenna surface, therefore, apertures are the preferred coupling method
4975 for cavity CRES experiments.

4976 One of the attractive features of the CRES technique for neutrino mass measurement
4977 is the gain in statistics that comes from the differential nature of the tritium spectrum
4978 measurement. Initially, this seems incompatible with cavities, due to the narrow reso-
4979 nances of cavity modes giving relatively small bandwidth. However, by intentionally
4980 over-coupling to a single cavity mode one can achieve bandwidths of a few 10’s of MHz
4981 (see Section 6.2), which is sufficient for a measurement of the tritium spectrum endpoint

4982 region.

4983 **6.3.2 Magnetic Field, Cavity Geometry, and Resonant Modes**

4984 **Magnetic Field and Volume Scaling**

4985 For a CRES experiment, cylindrical cavities are a natural choice since they match
4986 the geometry of standard solenoid magnets, which are needed in order to produce the
4987 background magnetic field for CRES measurements. Furthermore, the cylindrical shape is
4988 compatible with a Halbach array, which is the leading choice of atom trapping technology
4989 for future atomic tritium experiments by the Project 8 collaboration. Cylindrical
4990 cavities also benefit from well-established machining practices that are able to achieve
4991 high geometric precision at large lengths scales. More exotic cavity designs are under-
4992 consideration and there are on-going efforts to investigate the potential advantages these
4993 may have over the standard cylindrical geometry.

4994 As we saw in Section 6.2, the physical dimensions of the cavity are directly coupled
4995 to the resonant frequencies of the cavity. This dependency links the size of the cavity to
4996 the magnitude of the background magnetic field, because the magnetic field determines
4997 the cyclotron frequencies of trapped electrons. Specifically, as the size of the cavity is
4998 increased to accommodate larger volumes of tritium gas, the frequencies of the resonant
4999 modes decrease proportionally. This requires that the magnetic field also decrease in
5000 order to maintain coupling between electrons and the desired cavity mode.

5001 The required cavity size is ultimately determined by the required statistics in the
5002 tritium spectrum endpoint region. Because the gas density must be kept below a certain
5003 level to ensure that electrons have sufficient time to radiate before scattering, larger
5004 volumes become the only way to achieve higher event statistics. To achieve the sensitivity
5005 goals of Phase III and IV cavity volumes on the order of several cubic-meters are required,
5006 which pushes one towards frequencies in the range of 100's of MHz.

5007 **Single-mode Cavity CRES**

5008 It is tempting to consider maintaining a high magnetic field, while still increasing the size
5009 of the cavity, in order to increase the radiated power from trapped electrons for better
5010 SNR. However, if one were to maintain the same magnetic field while increasing the
5011 size of the cavity, the electrons would begin to couple to higher order modes with more
5012 complicated transverse geometries. The danger with this approach is that a complicated
5013 mode structure could introduce systematic errors into the CRES signals. Example

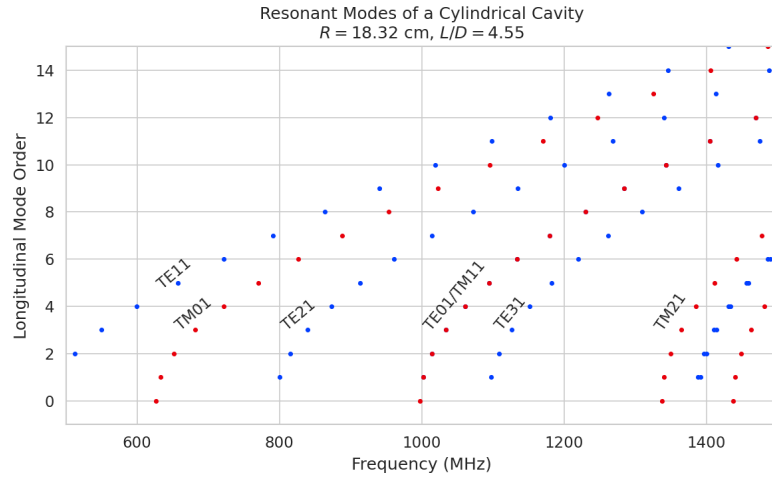
5014 systematics include unpredicted mode hybridization or changes in the mode shapes from
5015 imperfections in the cavity construction, which would prevent reconstruction of the
5016 electron's starting kinetic energies with adequate resolution. For this reason, it is ideal
5017 to operate with magnetic fields that give cyclotron frequencies near the fundamental
5018 frequency of the cavity, where the mode structure is relatively simple (see Figure 6.8).
5019 In this frequency region it is possible to perform CRES by coupling to only a single
5020 resonant mode, however, it is currently an open question if a single mode measurement
5021 will provide enough information about an individual electron's position to reconstruct
5022 the full event. Regardless, developing a solid understanding of the CRES phenomenology
5023 when an electron is coupling to a single mode will be a necessary step towards a future
5024 multi-mode cavity experiment.

5025 Considerations for Resonant Mode Selection

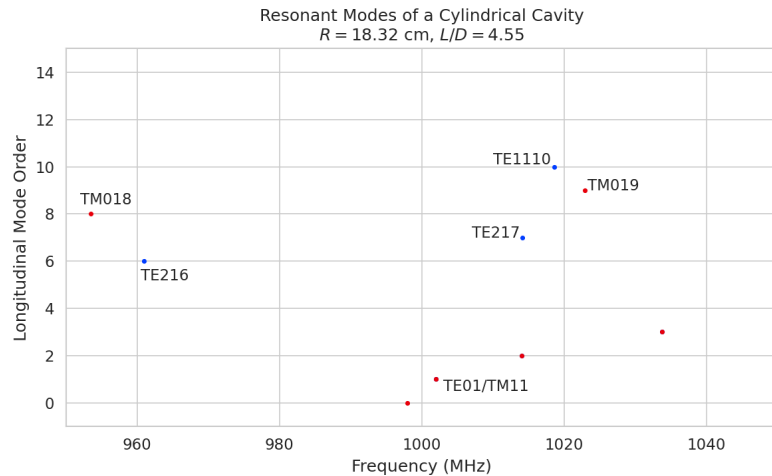
5026 A single-mode cavity experiment begs the question, which resonant mode is best for
5027 CRES measurements? There is an immediate bias towards low order TE_{nm} and TM_{nm}
5028 modes due to the multi-mode considerations discussed above. Additionally, there is a
5029 preference towards modes with longitudinal index $\ell = 1$ with a single antinode along the
5030 vertical axis of the cylindrical cavity. The reason for this is that there is a phase change
5031 in the electric fields between antinodes that leads to modulation effects that destroy the
5032 carrier frequency signal information.

5033 A second consideration for mode selection is the volumetric efficiency of the mode.
5034 Volumetric efficiency can be thought of as an integral over the volume of the cavity
5035 weighted by the relative amplitude of the mode. From the perspective of simply maximiz-
5036 ing the volume useable for CRES measurements this integral would be as close to unity
5037 as possible. However, there is a requirement to reconstruct the position of the electrons
5038 inside the cavity volume so that the local magnetic fields can be used to convert the
5039 measured cyclotron frequency to a kinetic energy. With a single mode this necessarily
5040 requires a variable transverse mode amplitude, which lowers the volumetric efficiency, so
5041 that position of the electron in the cavity can be estimated from the average amplitude
5042 of the CRES signal. Longitudinal indices of $\ell = 1$ have an advantage in volumetric
5043 efficiency over higher order ℓ modes, since there are only two longitudinal nodes, one at
5044 each end of the cavity. Therefore, the average coupling strength of trapped electrons as
5045 they oscillate axially is higher for $\ell = 1$ modes.

5046 The longitudinal variation in the mode strength is ultimately critical for achieving the
5047 energy resolution required for neutrino mass measurements. Correcting for the change in



(a)



(b)

Figure 6.8. Examples of the resonant mode frequencies of a cylindrical cavity. This cavity has a radius of 18.32 cm and a length to diameter ratio of 4.55.

5048 the average magnetic fields experienced by electrons with different pitch angles requires
 5049 that information on the axial motion of the electron be encoded into the CRES signal.
 5050 The longitudinal variation in the mode amplitude leads to amplitude modulation of the
 5051 CRES signal with a frequency proportional to the electron's pitch angle.

5052 An additional factor for mode selection is the intrinsic or unloaded Q of the mode. In
 5053 terms of SNR it is advantageous to use a mode with a very high Q_0 , which is then highly
 5054 overcoupled to achieve the necessary bandwidth to cover the tritium endpoint spectrum.
 5055 This scheme leads to a decoupling of the physical cavity temperature from the effective
 5056 noise temperature after the amplifier, which allows us to achieve adequate SNR without

5057 the requirement of cooling the entire cavity to single Kelvin temperatures.

5058 An example of a resonant mode that exhibits these traits is the TE₀₁₁ mode. At present
5059 the TE₀₁₁ mode is the preferred resonance for a single-mode cavity CRES experiment
5060 by the Project 8 collaboration. TE₀₁₁ is a low order mode located in a region relatively
5061 far from other cavity modes. Furthermore, the separation of the TE₀₁₁ mode can be
5062 improved by various mode-filtering techniques discussed in Section 6.4.2 below. TE₀₁₁
5063 consists of a single longitudinal antinode that can provide pitch angle information in the
5064 form of amplitude modulation, and has an electric field with a radial profile given by the
5065 J'_0 Bessel function allowing for radial position estimation. Lastly, the TE₀₁₁ mode has a
5066 relatively high intrinsic Q compared to nearby modes, which helps with SNR. Unloaded
5067 Q's greater than 80000 are achievable for a 1 GHz TE₀₁₁ resonance using a copper walled
5068 cavity.

5069 **6.3.3 Trade-offs Between the Antenna and Cavity Approaches**

5070 The choice between cavities and antennas for large-scale CRES measurements is not
5071 without trade-offs. Both the antenna array and cavity approaches are relatively immature
5072 techniques, at present there are no known obstacles that would prevent either approach
5073 from being used for a large scale neutrino mass experiment. The preference for cavities
5074 is largely driven by important practical considerations that could make a cavity based
5075 experiment significantly cheaper than an antenna experiment of similar size and scope.
5076 However, the switch to cavities also introduces new challenges less relevant to the
5077 antenna array, which must be solved in order for Project 8 to achieve its neutrino mass
5078 measurement goals.

5079 One of the major relative drawbacks of the antenna array approach is the size and
5080 complexity of the data-acquisition system. A large-scale antenna array experiment
5081 requires $O(100)$ antennas independently digitized at rates of $O(10)$ to $O(100)$ MHz. Since
5082 there is insufficient information in a single antenna channel to detect or reconstruct the
5083 CRES signal, the entire array output must be processed during the signal reconstruction.
5084 Because data storage becomes an issue with these data volumes, there is a real-time
5085 signal reconstruction requirement that allows one to detect CRES signals buried in the
5086 thermal noise. As we discuss in Section 4.4, the computational cost of these real-time
5087 detection algorithms are potentially quite large for even a small scale antenna array
5088 experiment. However, the operating principle of a cavity experiment allows the CRES
5089 signal to be detected using only a single read-out channel digitized at rates of $O(10)$ MHz,
5090 which reduces the cost of the data acquisition system by many orders of magnitude.

5091 From an engineering perspective, the simple geometry and thin-walls of a cylindrical
5092 cavity are simpler to interface with the cryogenic and magnetic subsystems needed for a
5093 CRES experiment. Whereas, the antenna array requires careful design and engineering
5094 to accommodate the antenna array and receiver electronics in proximity to the trapping
5095 magnets. Additionally, due to near-field interference effects, the antenna array is unable
5096 to reconstruct CRES events within the reactive near-field distance of the antennas.
5097 Because atom trapping requirements require magnetic fields which correspond to cyclotron
5098 frequencies for endpoint electrons less than 1 GHz, the required stand-off distance leads to
5099 a significant loss in useable experiment volume, necessitating larger and more expensive
5100 magnets.

5101 Another advantage to the cavity approach is the relatively compact sideband structure,
5102 which is a result of the low modulation index for cavity CRES signals. The axial motion
5103 in an antenna array experiment leads to frequency modulation and sidebands. The shape
5104 of the sideband structure is determined by the modulation index, $h = \frac{\Delta f}{f_a}$, where Δf
5105 is the size of the frequency deviation and f_a is the axial frequency. The large electron
5106 traps required for a cubic-meter-scale experiment leads to high modulation indices, which
5107 causes the signal spectrum to be made up of numerous low power sidebands that make
5108 reconstruction and detection challenging. This behavior was observed in simulations
5109 of the FSCD in which carrier power decreased with pitch angle due to the increase in
5110 modulation index (see Figure 4.31). For cavities, however, the modulation index remains
5111 near $h = 1$ even for very long magnetic traps due to the high phase velocity in cavities
5112 relative to the axial velocity of the electron. This results in an almost ideal spectrum
5113 shape that has a strong carrier frequency with a few sidebands whose relative amplitudes
5114 encode pitch angle information.

5115 A downside of the cavity approach is the apparent difficulty of estimating the position
5116 of the electron using only the coupling of the electron to a single mode. The amplitude of
5117 the TE₀₁₁ mode is completely independent of the azimuthal coordinate, therefore, position
5118 reconstruction using the TE₀₁₁ mode is only able to estimate the radial position of the
5119 electron. This position degeneracy may lead to magnetic field uniformity requirements
5120 that are too challenging to meet due to mechanical uncertainties in cavity and magnet
5121 construction, as well as uncertainties caused by nuisance external magnetic fields such
5122 as the Earth's field and magnetic fields from building materials. A multi-mode cavity
5123 experiment may provide a way to extract more precise information on the position of
5124 the electron by analyzing the coupling of the electron to several modes that overlap in
5125 different ways.

5126 **6.4 Single-mode Resonant Cavity Design and Simulations**

5127 The single-mode cylindrical cavities envisioned for the Phase III and IV experiments must
5128 be carefully engineered in order to measure the neutrino mass with the desired sensitivity.
5129 In this section I summarize some simulation studies performed to analyze early design
5130 concepts for a single-mode cavity. The primary tool for these investigations was Ansys
5131 HFSS, which was also used for the development of the SYNCA antenna described in
5132 Section 5.3.

5133 **6.4.1 Open Cylindrical Cavities with Coaxial Terminations**

5134 **Design Concept**

5135 A basic cavity design question relevant to Project 8's ultimate goal of an atomic tritium
5136 CRES experiment is how to build a cavity that can be efficiently filled with atomic
5137 tritium. To keep the rate of atom loss from recombination on surfaces it is ideal if the
5138 ends of the cylindrical cavity are as open as possible so that tritium atoms can flow
5139 inside unimpeded. Additionally, one of the primary calibration techniques planned for
5140 future CRES experiments involves CRES measurements using electrons injected from
5141 an electron gun source, which also requires an opening at the cavity end. Cylindrical
5142 cavities with open ends can be manufactured, however, the intrinsic Q-factors of these
5143 cavities are orders of magnitude less than their sealed counterparts, which reduces the
5144 signal-to-noise ratio when that cavity is used for CRES measurement.

5145 Cylindrical cavities with mostly open ends that also exhibit Q values for the $TE_{01\ell}$
5146 modes similar to sealed cavities can be built by using coaxial endcaps to terminate the
5147 cavity. Cavities of this type have been manufactured for specialized applications related
5148 to the measurements of the dielectric constants of liquefied gasses (see Figure 6.9) [2, 3].
5149 This cavity design leaves the ends of the cavity wide open, but retains high Q-values for
5150 the $TE_{01\ell}$ modes due to the coaxial endcap, which are designed to perfectly reflect the
5151 electric fields of $TE_{01\ell}$ modes. Coupling to the $TE_{01\ell}$ mode is achieved via an aperture
5152 located at the center of the cavity wall.

5153 A cavity similar to Figure 6.9 is a candidate design for the future CRES experiments
5154 by Project 8, since it appears to elegantly solve many practical issues that arise when
5155 combining cavity CRES and atomic tritium. The coaxial endcaps leave significant regions
5156 of the cavity ends completely open, which allows for the entrance of atomic tritium as
5157 well as the pumping away of molecular tritium that has recombined on the cavity walls.

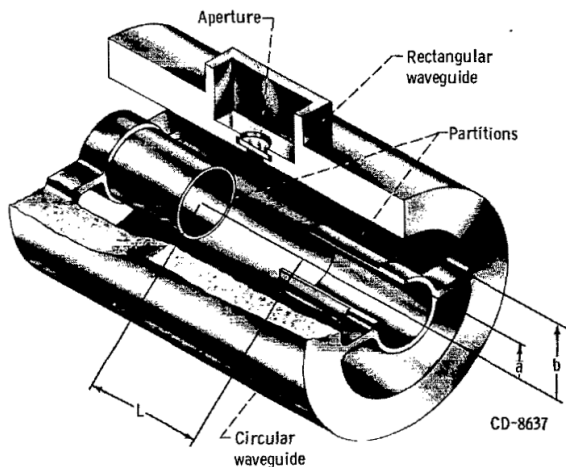


Figure 6.9. An image of an open cavity with coaxial terminations used for dielectric constant measurements. Figure from [2].

These open ends are achieved while preserving the high Q-values of the $\text{TE}_{01\ell}$ modes, which is important for extracting as much signal power from the electron as possible. In subsequent sections we shall analyze this cavity design in more detail, primarily by using HFSS simulations to analyze the resonant mode structure of this cavity geometry.

Coaxial Terminator Constraints

The reason that coaxial endcaps can be used to achieve high Q-values for the $\text{TE}_{01\ell}$ modes is that the electric fields for these modes are purely azimuthally polarized (see Equations 6.12 and 6.13). Therefore, the boundary conditions that require the electric field to go to zero at the cavity ends can be supplied using a coaxial partition of the correct radius (see Figure 6.10). Because the cylindrical shape enforced by the partition does not match the boundary conditions of other cavity modes, these terminations also significantly suppress the Q-factors of non- $\text{TE}_{01\ell}$ modes, which is potentially beneficial for a single-mode cavity CRES experiment.

The correct radius of the cylindrical partition is derived by setting up the boundary value problem in Figure 6.10, and analyzing the reflection and transmission coefficients for waves incident on the coaxial terminators. The basic problem is to identify the radius a where the reflection coefficient for the $\text{TE}_{01\ell}$ modes becomes equal to 1. One can show that if the coaxial partitions are made sufficiently long relative to the wavelength of the TE_{01} modes than perfect reflection can be achieved. This derivation is quite lengthy and complex and is presented in full in [3]. Here, we shall simply explain the resulting

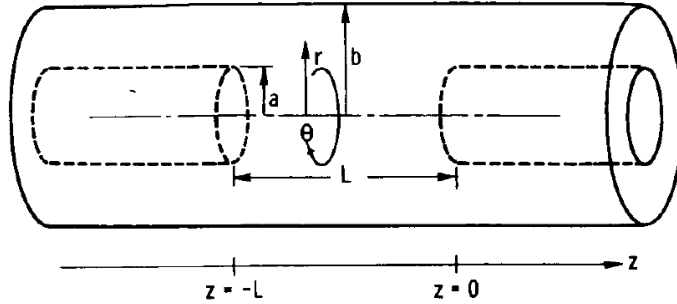


Figure 6.10. The simplified geometry of an open cavity with coaxial terminations. Figure from [3].

5178 conditions on the partition radius for perfect reflection.

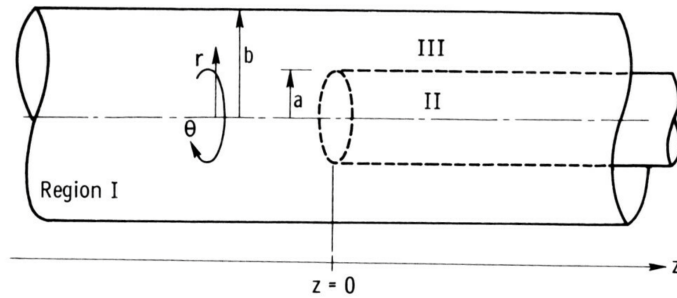


Figure 6.11. Electric field regions for the open cavity boundary value problem. Figure from [3].

5179 The open cavity boundary value problem is solved by expressing the forms of the
 5180 electric fields in the different regions of the cavity and requiring that the electric fields are
 5181 continuous. There are effectively three distinct regions in the open cavity corresponding
 5182 to the central cavity volume, the inner coaxial volume, and the outer coaxial volume (see
 5183 Figure 6.11).

5184 In Region I, the boundary conditions are those of a cylindrical waveguide, and we
 5185 require that E_ϕ for the TE_{0m} modes go to zero at the cavity wall ($r = b$). This requires
 5186 that $J'_{0m}(k_{c0m} b) = 0$. We aim to solve for the radius a in the specific situation where the
 5187 TE_{01} mode can propagate but all other TE_{0m} modes are below the cutoff frequency for
 5188 the circular waveguide. This is equivalent to requiring

$$3.832 < k_{c0m} b < 7.016, \quad (6.41)$$

5189 where the numbers 3.832 and 7.016 correspond to the first and second zeros of the Bessel
 5190 function (see Table 6.1).

5191 In Region II the boundary conditions are those of a cylindrical waveguide, but with
 5192 a smaller radius. The condition that $E_\phi = 0$ at the cylindrical partition radius is that
 5193 $J'_{0m}(k_{c0m}a) = 0$. To ensure perfect reflection, we want all modes in Region 1 of the cavity
 5194 to be below the cutoff frequency of the circular waveguide formed by the inner volume of
 5195 the coaxial terminator. Therefore, we consider the solutions where

$$k_{c0m}a < 3.832. \quad (6.42)$$

5196 Finally, in Region III the boundary condition are those of a coaxial waveguide. We
 5197 need to guarantee that $E_\phi = 0$ at both $r = b$ and $r = a$, which involves finding the
 5198 eigenvalues of the following equation

$$J'_0(k_{c0m}a)Y'_0(k_{c0m}b) - J'_0(k_{c0m}b)Y'_0(k_{c0m}a) = 0, \quad (6.43)$$

5199 where Y'_0 the zeroth-order derivatives of the Bessel function of the second kind. The
 5200 solutions to this equation depend on the value of the ratio b/a . The approximate solution
 5201 is given by

$$\delta_n a \simeq \frac{n\pi}{b/a - 1}, \quad (6.44)$$

5202 where δ_n are eigenvalues of Equation 6.43. Similar to Region II, we are interested in
 5203 solutions for which the TE₀₁ modes of Region I are below the cutoff of Region III.
 5204 Therefore, we require that

$$k_{c0m} < \delta_1. \quad (6.45)$$

5205 In general, one has some freedom in specifying the value of b/a . A value typically used
 5206 in practice is $b/a = 2.082$, which corresponds to positioning the radius of the cylindrical
 5207 partition at the maxima of the TE₀₁ electrical fields.

5208 Using the constraints from the three field regions one can develop a coaxial terminator
 5209 that acts as a virtual perfectly conducting surface for the TE₀₁ modes. The only required
 5210 inputs are the desired frequency of the TE₀₁₁ mode and a choice for the value of b/a .

5211 6.4.2 Mode Filtering

5212 The general case of an electron coupling to a resonant cavity is complicated. This is
 5213 because cavities contain an infinite number of resonant modes, which for higher order
 5214 modes, have couplings to the electron with a complex spatial dependence. The danger is
 5215 that improper modeling of the electron's coupling to the cavity can lead to systematic

5216 errors in the CRES measurements that prevent a high-resolution measurement of the
5217 electron's kinetic energy. This in part drives the preference for a single-mode cavity
5218 experiment that uses only the electron's coupling to the TE_{011} mode to perform CRES,
5219 assuming that sufficient information on the electron's position can be obtained with a
5220 single mode.

5221 The TE_{011} mode is in a region where there are relatively few other modes to which
5222 the electron could couple(see Figure 6.8). However, one can see that the frequency of
5223 the TE_{011} is perfectly degenerate with the TM_{111} mode, which means that electrons will
5224 inevitably couple to both modes if they have the correct cyclotron frequency.

5225 The magnitude of the impact of the electron coupling to both TE_{011} and TM_{111} is
5226 currently unknown. To first order an electron coupling to more both modes will lose more
5227 energy overtime, which can be measured by observing the frequency chirp rate of the
5228 signal. This effect may be small enough to be negligible or simple enough to model that
5229 the cavity can be treated as an effective single-mode cavity. Alternatively, the one could
5230 consider devising a coupling scheme that is sensitive to both the TE_{011} and the TM_{111}
5231 modes. By measuring the coupling of the electron to both modes more information on
5232 the position of the electron could be obtained, which could improve the position and
5233 energy resolution of the CRES measurements.

5234 A different approach is the mode filtering approach, which seeks to obtain a single
5235 TE_{011} mode cavity using perturbations to the cavity walls that selectively impede the
5236 TM modes, while leaving the TE modes mostly unperturbed. The type of perturbations
5237 required can be determined by visualizing the surface currents induced in the cavity
5238 walls by each type of mode (see Figure 6.12). By definition, all TM have electric fields
5239 directed along the vertical axis of the cylindrical cavity, which means that perturbations
5240 that impede currents in this direction will modify TM resonances. On the other hand,
5241 the TE_{01} modes induce azimuthal currents in the cavity walls, therefore, it is possible to
5242 break the degeneracy between TE_{01} and TM_{11} using a cavity perturbation that impedes
5243 axial currents, but does not affect the flow of azimuthal currents.

5244 Figure 6.12 shows two cavity design concepts that achieve this selective current
5245 perturbation. The resistive approach inserts a series of thin dielectric rings into the walls
5246 of the cavity that introduces a resistive and capacitive impedance to the longitudinal
5247 currents, while leaving azimuthal current paths intact. Cavities of this type with high
5248 TE_{01} Q's have also been constructed by tightly wrapping a thin, dielectric coated wire
5249 around a mold to form the cavity wall. An alternative method is to introduce an inductive
5250 impedance by cutting grooves or a thread pattern on the inside wall of the cavity. For

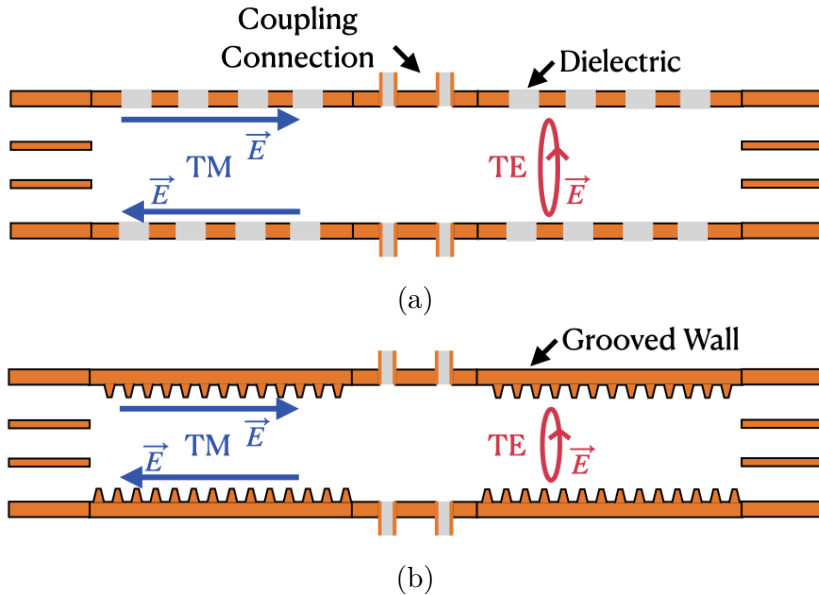


Figure 6.12. Two mode filtering concepts to break the degeneracy of TE_{01} and TM_{11} modes. The resistive approach uses dielectric materials to impede currents that travel vertically along the cavity while leaving azimuthal currents unperturbed. An alternative approach is to impede the currents using grooves cut into the cavity wall, which achieve the same effect with an inductive impedance.

5251 reasons of manufacturability and compatibility with tritium the grooved cavity approach
 5252 is the preferred method for mode-filtered cavity construction by Project 8.

5253 **6.4.3 Simulations of Open, Mode-filtered Cavities**

5254 A candidate design for a single TE_{011} mode CRES experiment is a cavity that utilizes
 5255 the coaxial terminations combined with a mode-filtering wall. The first step towards
 5256 validating that a cavity that combines these two design features will operate as expected
 5257 is a thorough simulation effort for which finite element method (FEM) simulation software
 5258 is invaluable. The primary tool for electromagnetic FEM calculations inside Project 8 is
 5259 Ansys HFSS, which has a robust and well-established eigenmode solver that can identify
 5260 the resonant frequencies and associated Q-factors for given structure.

5261 Four variations of a cavity design with a ~ 1 GHz TE_{011} resonance were implemented
 5262 in HFSS (see Figure 6.13). The four designs include a standard cylindrical cavity, an
 5263 open cavity with smooth walls, an open cavity with resistive walls, and an open cavity
 5264 with grooved walls. The relevant design parameters are summarized in Table 6.3. All
 5265 cavities were simulated using copper walls and filled with a vacuum dielectric. The
 5266 identities of the resonant modes found by HFSS were validated by visual inspection of

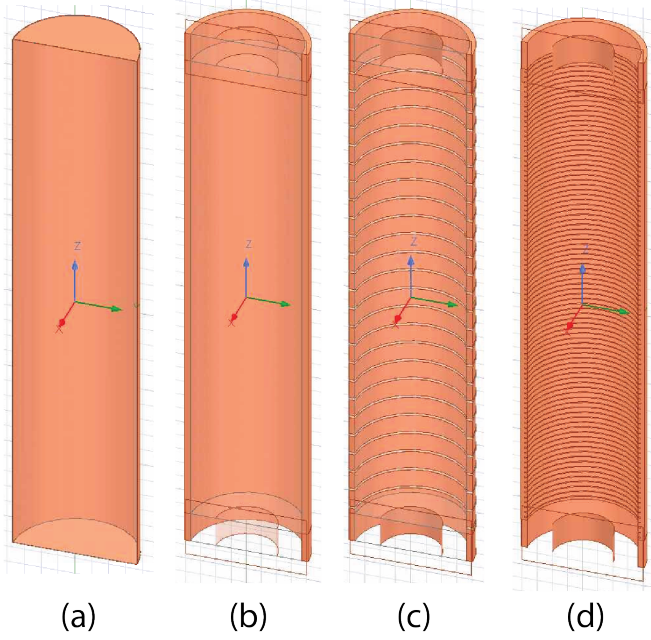


Figure 6.13. Four cavity design variations. (a) is a standard sealed cylindrical cavity, (b) is an open cavity with smooth walls, (c) is an open cavity with resistive walls, and (d) is an open cavity with grooved walls. The main cavity and coaxial terminator parameter are identical for all four cavities.

5267 the electric and magnetic field patterns and by comparison to analytical calculations of
5268 the mode frequencies.

Table 6.3. A table of cavity design parameters used for HFSS simulations.

Name	Qty.	Unit	Description
D_{cav}	326.4	mm	Cavity diameter
L_{cav}	1668.0	mm	Cavity length
D_{term}	200.2	mm	Inner diameter of coaxial terminator
L_{term}	100.0	mm	Terminator length
l_{die}	8.3	mm	Dielectric spacer thickness
Δl_{die}	66.7	mm	Distance between dielectric spacers
l_{groove}	3.0	mm	Groove height
d_{groove}	9.0	mm	Groove depth
Δl_{groove}	18.3	mm	Distance between grooves

5269 The results of the HFSS simulations validate our predictions of the resonant behavior
5270 of an open, mode-filtered cavity developed in the preceding sections (see Figure 6.14) One
5271 can see that for a standard cavity the TE_{01} and the TM_{11} are degenerate in frequency
5272 with relatively high Q-factors. The open-ended cavity preserves the high Q-factors of
5273 the TE_{01} modes, while the other modes, since their boundary conditions do not match

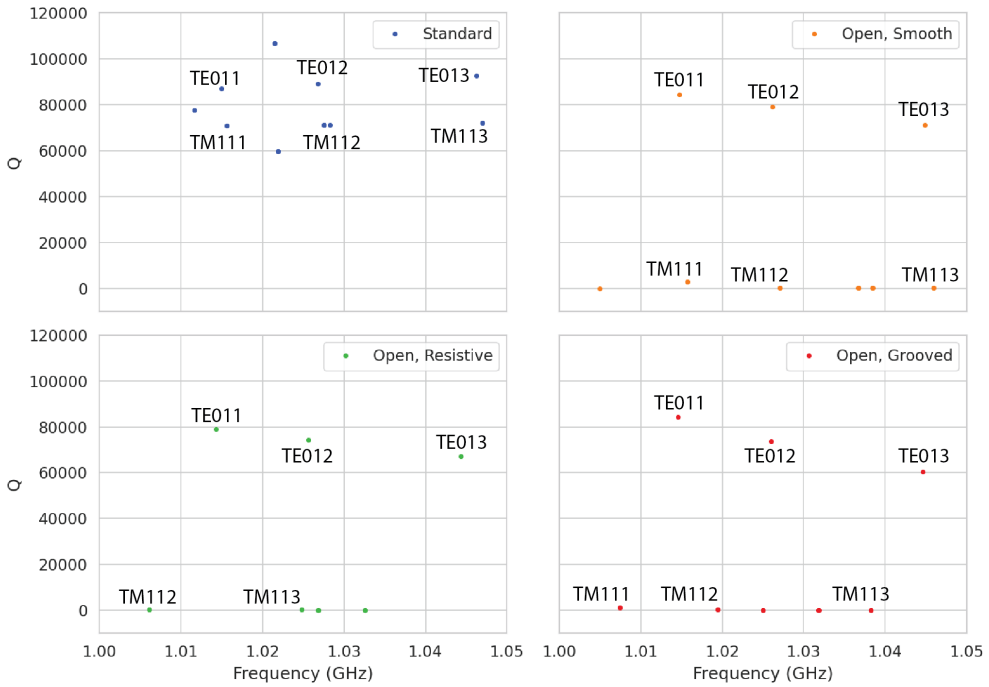


Figure 6.14. The frequencies and Q-factors of the resonant modes identified by HFSS for the cavity variations shown in Figure 6.13. The fully-sealed cavity with smooth walls has several high-Q modes near the TE_{011} resonance. Introducing the open-termination preserves the Q-factors of the $\text{TE}_{01\ell}$ modes and suppresses the Q-factors of the modes whose boundary conditions do not match the cylindrical partition. Both the resistive and grooved wall perturbations shift the resonant frequencies of the TM modes away from the TE_{011} mode. By properly tuning the geometry of the grooves or the resistive spacers several MHz of frequency separation can be achieved.

the coaxial geometry, have their Q-factors suppressed. One can see that the effect of the resistive and inductive mode-filtering schemes is to effectively shift the resonant frequencies of the TM_{11} modes below those of the associated TE_{01} modes, which breaks the degeneracy. Optimization of the dielectric spacer or groove parameters can ensure that the TE_{011} mode is isolated from other modes by $O(10)$ MHz, which provides sufficient bandwidth for a measurement of the tritium spectrum endpoint.

Further optimization of the cavity design requires a more detailed cavity simulation that includes the cavity coupling mechanism as well as other geometry modifications required for integration into the magnetic and tritium gas subsystems. Perhaps more important is the development of the capability to simulate the interaction of electrons with the cavity so that simulated CRES signals can be generated using cavities designed for CRES measurements. Simulated CRES signals can then be used to estimate the neutrino mass sensitivity of the experiment, which allows for the optimization of the cavity

5287 design towards the configuration that provides the best measurement of the neutrino
5288 mass.

5289 **6.5 Single-mode Resonant Cavity Measurements**

5290 Measurement test stands play an important role in the research and development process
5291 that cannot be replaced by simulations. For example, constructing a prototype CRES
5292 cavity forces one to consider important practical issues such as manufacturability and
5293 machine tolerances that may require modifications to the design. Furthermore, by
5294 comparing laboratory measurements of a real cavity to simulations, one can quantify
5295 the impact of imperfections and real-life measurement systematics, which allows for
5296 more accurate sensitivity estimates of the experiment. Lastly, the development of these
5297 prototypes helps to build the necessary experience and expertise within the collaboration
5298 required for more complicated experiments to succeed.

5299 In this spirit a prototype cavity was constructed to demonstrate the open, mode-
5300 filtered cavity concept explored in the previous sections. The primary goal of the
5301 measurements was to validate that an open, mode-filtered cavity suppressed the TM_{11}
5302 modes as predicted by HFSS simulations.

5303 **6.5.1 Cavities and Setup**

5304 Two rudimentary, cavities were constructed using segments of copper pipe available from
5305 McMaster-Carr (see Figure 6.15). The design consists of copper pipes of two diameters.
5306 The larger diameter pipe forms the main cavity wall and the smaller diameter pipe is
5307 used to create a coaxial termination. The diameter of the outer pipe was chosen to
5308 produce a TE_{011} resonance of approximately 6 GHz, while the diameter of the smaller
5309 pipe was selected based on the open termination criteria introduced in Section 6.4.1. The
5310 approximate diameters and lengths of the copper pipe are summarized in Table 6.4.

5311 Coupling to the cavity was achieved using a hand-formable segment of coaxial cable
5312 stripped at one end to form a loop antenna. This was inserted into a small hole located
5313 at the center of the main cavity wall. The coaxial terminators were supported inside the
5314 main cavity by carving a spacer from polystyrene foam (styrofoam) so that they could
5315 be easily inserted into the cavity and repositioned. The dielectric constant of styrofoam
5316 is quite close to air at microwave frequencies so this is expected to have minimal impact
5317 on the resonant properties of the cavity.

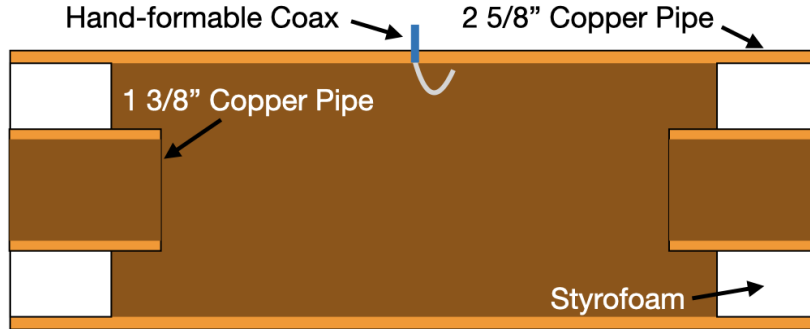


Figure 6.15. A cartoon depicting the design of the open-ended cavity prototype designed to operate at approximately 6 GHz. The main cavity wall was composed of a single copper pipe. A mode-filtered version of this cavity was constructed by

Table 6.4. A table of parameters describing the cavity prototypes. Certain values such as the cavity length and the distance between dielectric spacers are approximate due to variation in the machining of the copper. In particular, the filtered cavity was constructed from conducting copper segments that varied in size from 1.50" to 1.85".

Name	Qty.	Unit	Description
D_{cav}	2.625	in	Cavity diameter
L_{cav}	≈ 13	in	Cavity length
D_{term}	1.375	in	Inner diameter of coaxial terminator
L_{term}	1.575	in	Terminator length
l_{die}	0.75	in	Dielectric spacer thickness
Δl_{die}	≈ 1.50 to 1.85	in	Distance between dielectric spacers

5318 The actual length of the cavity is given by the distance between the inner edges of the
 5319 coaxial terminations. The length of the outer section of pipe that forms the main wall of
 5320 the cavity is approximately 16" in length which leads to a cavity length of $\approx 13"$ when
 5321 both terminators are inserted in the cavity. Because the terminators were not rigidly
 5322 mounted this distance is only approximate, however, the uncertain length of the cavity
 5323 will not prevent us from validating the open cavity design.

5324 Along with the smooth-walled open cavity a resistively mode-filtered cavity was
 5325 constructed by creating dielectric spacers out of segments of clear PVC pipe (see Figure
 5326 6.16). The spacers were machined such that the conductive segments of the cavity would
 5327 be separated by 0.75" when the cavity was fully assembled. Due to variations in the
 5328 lengths of the copper segments that make up the cavity wall the distance between spacers
 5329 has significant variation with average value of about 1.7". Eight total spacers were used
 5330 to build the cavity, which when assembled was approximately 16" in total length similar
 5331 to the non-filtered cavity.

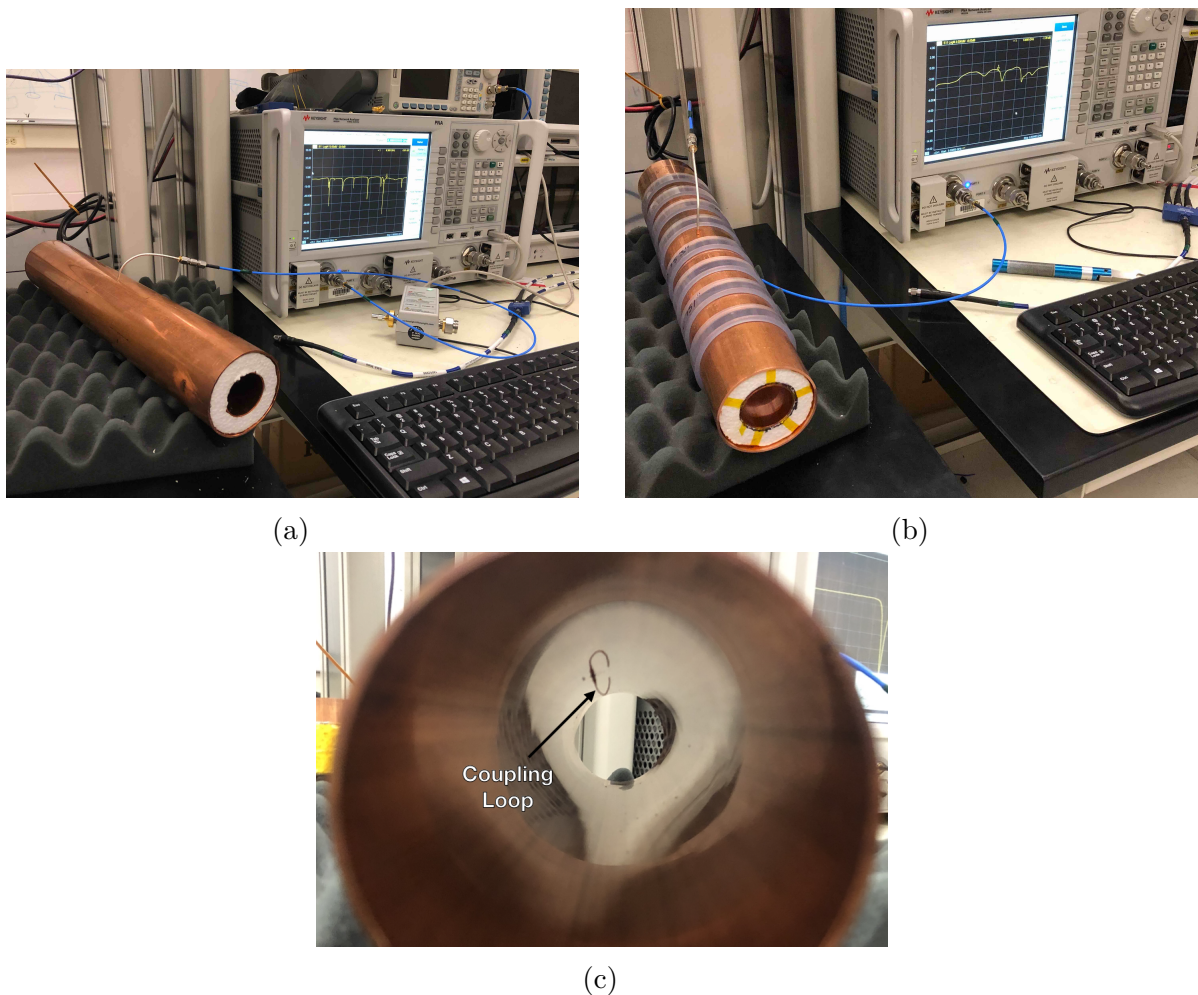


Figure 6.16. Images depicting the measurement of the filtered and non-filtered open cavities using the VNA. The coupling loop in the figure is shown in the TE orientation.

5332 Measurements of both cavities were performed using a VNA connected to the cavity
 5333 coupling probe (see Figure 6.16). By measuring the return loss over a range of frequencies
 5334 one can measure the frequencies and relative Q-factors of the resonant modes in the
 5335 cavity. Due to the opposite polarity of the electric fields for the TE and TM modes,
 5336 the loop coupling probe must be rotated 90° to change the polarity of the loop antenna.
 5337 When the antenna is oriented such that the loop opening faces the ends of the cavity, it
 5338 couples primarily to the TE modes which have magnetic fields directed along the long
 5339 axis of the cavity (see Figure 6.16). If the coupling loop is turned by 90° from where
 5340 it is shown in the image then it will couple to the TM modes which have azimuthally
 5341 directed magnetic fields. In this way both the TE and TM resonances can be measured
 5342 independently.

5343 6.5.2 Results and Discussion

5344 The primary analysis for the prototype cavities involved a simple visualization of the
5345 return loss as measured by the VNA and a comparison between the filtered and non-
5346 filtered variations. Since the resonances measured by the VNA are not labeled, there is
5347 an uncertainty about the true identities of the modes measured by the VNA. To resolve
5348 this I performed a simulation of the simplest possible cavity that could be created from
5349 the prototype components, which is a fully open cavity created by removing the coaxial
5350 inserts. The fully-open cavity with the as-built dimensions was simulated in HFSS to get
5351 estimates on the positions of the TE₀₁₁ and TM₁₁₁ modes (see Figure 6.17).

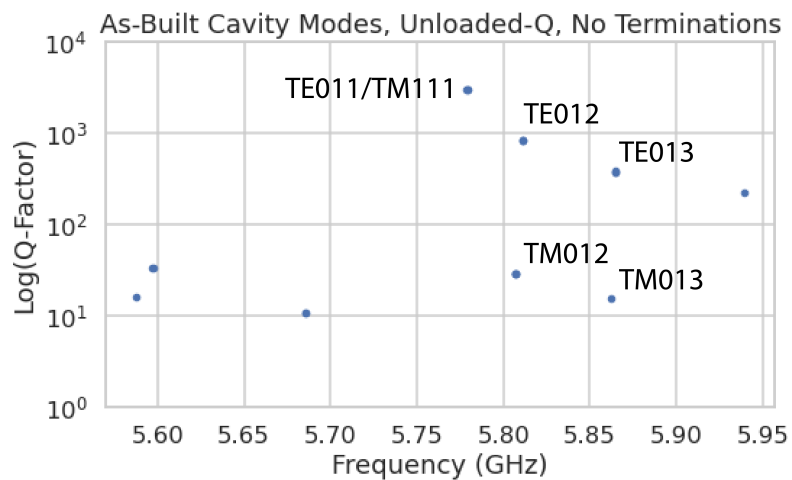


Figure 6.17. HFSS simulation results for a the as-built cavity with the coaxial terminators removed. The TE₀₁₁/TM₁₁₁ frequency is approximately 5.78 GHz.

5352 Simulation of the fully open cavity shows that the TE₀₁₁/TM₁₁₁ modes have a
5353 frequency of approximately 5.78 GHz in the fully open cavity. If the frequency of this
5354 mode is compared to the measurements of the filtered and non-filtered cavities with the
5355 terminators removed one can easily identify the TE₀₁₁ mode at approximately 5.75 GHz
5356 (see Figure 6.18).

5357 Both variations of the non-filtered cavities one sees that the TE₀₁₁ mode is degenerate
5358 in frequency with what appears to be a doublet of TM modes located at the TM₁₁₁
5359 frequency position. This doublet is actually the TM₁₁₁ mode, which has two polarizations
5360 with opposite polarizations. Because the pipe used to construct the cavity is not perfectly
5361 round, the frequency degeneracy between the two polarizations is broken resulting in the
5362 doublet peaks.

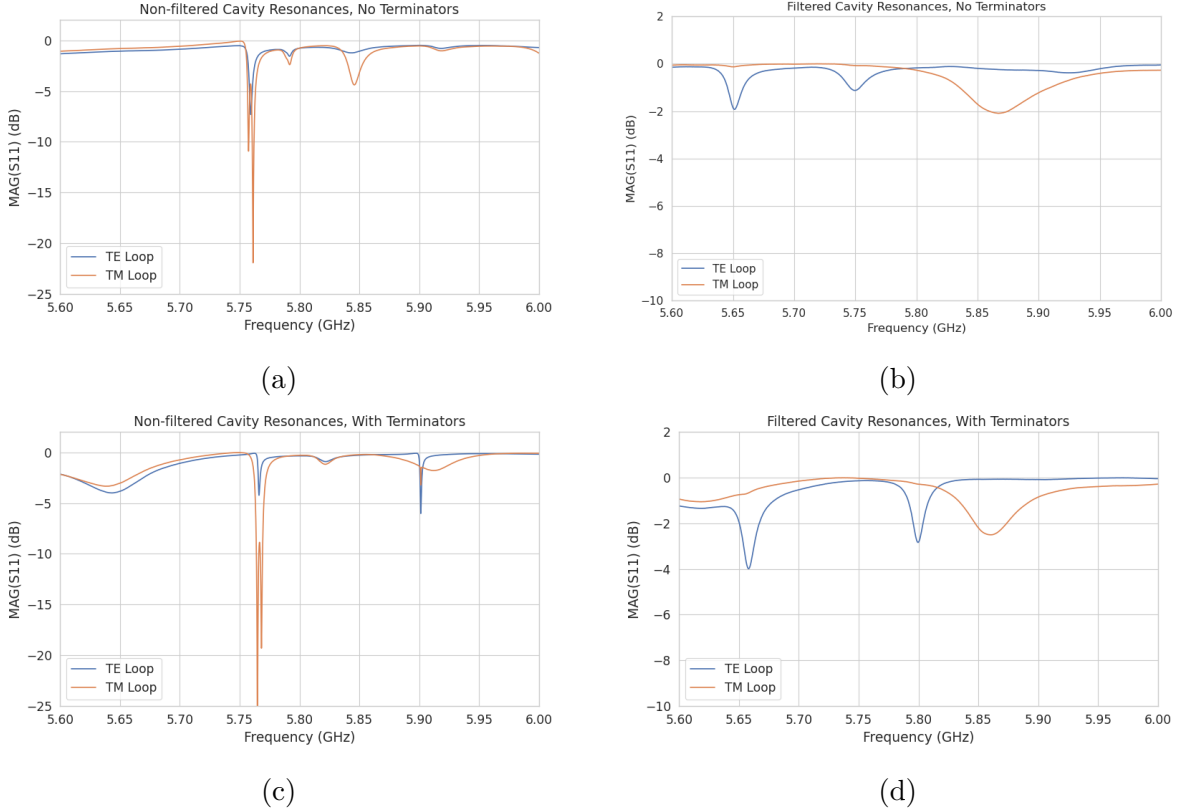


Figure 6.18. Measurements of the filtered and non-filtered prototype cavities acquired with the VNA.

5363 The S-parameter plot for the filtered cavity without terminators has an isolated TE
 5364 resonance at 5.65 GHz, associated with the TE_{011} mode. The frequency of this mode
 5365 is lower than the non-filtered cavity due to a difference in the overall lengths of the
 5366 cavities. An obvious difference between the filtered and non-filtered cavities is that
 5367 there is no TM_{111} doublet at the TE_{011} frequency. This is what one would expect if
 5368 the mode-filtering was suppressing the TM modes. There appears to be a noticeable
 5369 difference in the Q of the TE_{011} resonance between non-filtered and filtered variations as
 5370 indicated by the increased resonance depth for the filtered cavity. Overall, the Q-factors
 5371 of the filtered cavity appear significantly smaller than the non-filtered cavity due to the
 5372 increase in resonance width. This is likely caused by the relatively large widths of the
 5373 dielectric spacers, which are partially impeding the TE modes.

5374 One can see from these cavity measurements that, in principle, resistive mode-filtering
 5375 can be used to separate the TE_{011} resonance from the degenerate TM_{111} modes in
 5376 combination with the open cavity endcaps. This finding agrees with the expectations
 5377 from HFSS, which should provide confidence that the eigenmode solver is correctly

5378 modeling the behavior of the cavity. Although I did not perform a similar study using
5379 a cavity with grooved walls it is expected that the resonant mode structure would be
5380 similar to the cavity studied here.

5381 While this prototype cavity is a good first step, several deficiencies prevent this setup
5382 from providing more than qualitative information to the design of cavities for CRES. This
5383 includes the rudimentary approach to cavity coupling using a stripped coax antenna and
5384 the inability to map the field density in the cavity volume. Improvements in these areas
5385 are required so that measurements from a real cavity can provide useful information to
5386 cavity CRES simulations that will ultimately inform neutrino mass sensitivity estimates.

5387 Future work with prototype cavities must include an improved cavity coupling scheme,
5388 which is robust and compatible with atomic tritium. Since the cavity will ultimately
5389 be filled with atomic tritium, a coupling antenna cannot be used due to the losses of
5390 atomic tritium caused by recombination on the antenna surfaces. Possible non-invasive
5391 coupling schemes include aperture coupling, where the cavity is coupled to an external
5392 waveguide structure through an aperture, or a split-ring coupling approach, where the
5393 center segment of the cylindrical cavity wall is replaced an isolated conductive ring with
5394 a small vertical slit. The aperture coupling approach is a standard coupling scheme [86]
5395 used in a wide range of applications, but at low frequencies the size of the external
5396 waveguide conflicts with design of the atom trapping magnet and cryogenics system.
5397 The split-ring approach could potentially be coupled to a small coaxial transmission line
5398 which is more compatible with the rest of the experiment design. A challenge is achieving
5399 adequate coupling through impedance tuning, which is a focus of current research.

5400 The robustness of the coupling mechanism is relevant due to the difficulty in modeling
5401 its effect on the cavity modes. Small changes in geometry can have a large influence on
5402 the coupling and hence the performance of the cavity, therefore, correctly modeling the
5403 cavity coupling is critical for accurate CRES simulations. Coupling schemes that rely
5404 on connections to coaxial lines are potentially at a disadvantage in this regard due to
5405 the affect of soldering imperfections or unintended bends in the coax on the coupling.
5406 Future work will identify a coupling scheme for the cavity compatible with the neutrino
5407 mass goals of Project 8.

5408 Imperfections in the geometry of a real cavity will necessarily distort the resonant
5409 modes away from simulation predictions. This will change the coupling of an electron
5410 to the cavity and thus change the expected signal structure. Ultimately, this effect will
5411 limit the achievable energy resolution of the experiment unless the differences between
5412 simulation and a real cavity can be sufficiently characterized and calibrated. One possible

5413 approach to this is to utilize a "bead puller" system [100] to strategically perturb the
5414 cavity by moving a conductive bead through the cavity volume. The small perturbation
5415 caused by the bead affects the phase of the cavity resonances proportional to the total
5416 magnitude of the electric field at that position, so by moving the bead through the
5417 cavity volume the total electric field can be mapped and compared to simulation. This
5418 information can provide bounds on the relative perturbations to the cavity mode structure
5419 from real-life imperfections compared to the idealized cavity in HFSS.

5420 **Chapter 7 |**

5421 **Conclusion and Future Prospects**

5422 In this dissertation we have discussed research and development efforts towards the
5423 development of a scalable CRES measurement technology that can be used to build a
5424 CRES experiment at cubic-meter scales with sensitivity to neutrino masses of 40 meV.
5425 The primary contributions of my dissertation are the development and analysis of signal
5426 reconstruction algorithms for an antenna array based CRES experiment [101], which leads
5427 to estimates of the neutrino mass sensitivity; the development of a synthetic cyclotron
5428 radiation antenna (SYNCA) [80], which allowed for laboratory validation of antenna
5429 array CRES simulation models [43]; and the development of an open-ended cavity design
5430 compatible with atomic tritium for a cavity based CRES experiment. A measurable
5431 impact of this work is the transition of the Project 8 collaboration's experimental plan
5432 from an antenna array based approach to a cavity based approach, where my work played
5433 a key role in demonstrating the significantly higher cost and complexity of the antenna
5434 array experiment.

5435 The transition from antenna arrays to cavities requires a new set of demonstrator
5436 experiments to make incremental progress towards a 40 meV measurement of the neutrino
5437 mass. At the time of writing, the near-term plan of Project 8 is to design and construct a
5438 small-scale cavity CRES experiment utilizing the 1 T magnet installed in the UW-Seattle.
5439 This cavity is designed to have a TE011 resonance with a frequency of about 26 GHz with
5440 a length-to-diameter ratio that mimics the larger cavities intended for the pilot-scale and
5441 Phase IV experiments. The goal of this experiment is to demonstrate cavity CRES as
5442 well as validate models of CRES systematics using electrons from ^{83m}Kr and an electron
5443 gun. Though the primary goal is demonstration, near-term physics measurements are
5444 available in the form of high-resolution measurements of the ^{83m}Kr conversion spectrum
5445 of interest to the KATRIN collaboration.

5446 Furthermore, Project 8 is currently constructing a low-frequency CRES setup located
5447 at Yale University to better understand the principles of cavity based CRES at lower

5448 magnetic fields. The Low, UHF Cavity Krypton Experiment at Yale (LUCKEY) is
5449 a 1.5 GHz cavity CRES experiment the will use conversion electrons from ^{83m}Kr to
5450 perform CRES measurements at the lowest frequencies ever attempted with the technique.
5451 LUCKEY will validate frequency scaling models developed by Project 8 and will pave
5452 the way for the future Low-Frequency Apparatus (LFA), which will be a larger, 1 GHz
5453 cavity CRES experiment that includes a molecular tritium source. The target for the
5454 LFA is a measurement of the neutrino mass with a sensitivity of approximately 0.2 eV,
5455 which will build towards the atomic pilot-scale CRES experiment.

5456 In parallel to the development of cavity CRES is the development of the atomic
5457 tritium source. Recent demonstrations of the production of atomic hydrogen are excellent
5458 steps towards the atomic tritium production needed for the pilot-scale experiment. One
5459 area of future study includes the development of a more detailed unstanding of the
5460 efficiency of atomic hydrogen production. Near-term plans include the development of a
5461 magnetic, evaporatively cooled beamline, as well as the prototyping of a Halbach array
5462 atoms trap. Nearly all of the components of the atomic tritium system will require
5463 demonstration before the complete system can be built. The long-term goal of the
5464 atomic tritium work is to construct a full atomic tritium prototype that demonstrates
5465 the production, cooling, trapping, and recycling of tritium at the rates needed for the
5466 pilot-scale experiment.

5467 More broadly, the long-term goal of the Project 8 collaboration is to fully develop
5468 both the atomic tritium and cavity CRES technologies so that both can be combined in
5469 a pilot-scale CRES experiment. It is envisioned that this process will take approximately
5470 10 years for both atomic tritium and cavity CRES. After these developments comes
5471 the pilot-scale experiment which will be the first CRES experiment that simultaneously
5472 demonstrates all the required technologies for Phase IV. Scaling to Phase IV with cavity
5473 CRES will require the construction of multiple copies (approximately 10) of the pilot-scale
5474 experiment to obtain sufficient statistics for 40 meV sensitivity.

5475 Development of the CRES experimental technique by Project 8 has led to new
5476 experiments utilizing the CRES technique for basic physics research, such as the ^6He -
5477 CRES collaboration [102], and has also found applications as a new approach to x-ray
5478 spectroscopy [103]. Recently, a new experimental effort called CRESDA has begun in
5479 the UK to develop new quantum technologies applied to CRES measurements for the
5480 neutrino mass [104]. This flourishing of new experimental efforts based on the CRES
5481 technique is likely to continue as Project 8 continues to develop the technique towards
5482 its neutrino mass measurement goal.

5483

Bibliography

- 5484 [1] AGOSTINI, M., G. BENATO, and J. DETWILER (2017) “Discovery probability of
5485 next-generation neutrinoless double- β decay experiments,” *Phys. Rev. D*, **96**(5), p.
5486 053001, 1705.02996.
- 5487 [2] WENGER, N. C. and J. SMETANA (1972) “Hydrogen Density Measurements Using
5488 an Open-Ended Microwave Cavity,” *IEEE Transactions on Instrumentation and
5489 Measurement*, **21**(2), pp. 105–114.
- 5490 [3] WENGER, N. (1967) “Resonant Frequency of Open-Ended Cylindrical Cavity,”
5491 *IEEE Transactions on Microwave Theory and Techniques*, **15**(6), pp. 334–340.
- 5492 [4] DAS, A. and T. FERBEL (2003) *Introduction to Nuclear and Particle Physics*,
5493 World Scientific.
- 5494 [5] CURIE, P. (1898) “Sur une nouvelle substance fortement radioactive, contenue
5495 dans la pechblende,” *Comptes rendus de l’Academie des Sciences, Paris*, **127**, pp.
5496 1215–1217.
- 5497 [6] RUTHERFORD, E. (1899) “Uranium radiation and the electrical conduction pro-
5498 duced by it,” *Philos. Mag.*, **47**, p. 109.
5499 URL <https://cds.cern.ch/record/261896>
- 5500 [7] GERWARD, L. (1999) “Paul Villard and his Discovery of Gamma Rays,” *Physics
5501 in Perspective*, **1**, pp. 367–383.
- 5502 [8] BECQUEREL, H. (1900) “Deviation du rayonnement du radium dans un champ
5503 électrique,” *C.R.*, **130**, pp. 809–815.
- 5504 [9] D.Sc., E. R. M. and F. S. B.A. (1902) “XLI. The cause and nature of ra-
5505 dioactivity.—Part I,” *The London, Edinburgh, and Dublin Philosophical Mag-
5506 azine and Journal of Science*, **4**(21), pp. 370–396, [https://doi.org/10.1080/
5507 14786440209462856](https://doi.org/10.1080/14786440209462856).
5508 URL <https://doi.org/10.1080/14786440209462856>
- 5509 [10] CHADWICK, J. (1914) *Intensitätsverteilung im magnetischen Spektrum der β -
5510 Strahlen von Radium B+C*, Druck von Friedr. Vieweg und Sohn.
5511 URL <https://books.google.com/books?id=8s8UmQEACAAJ>

- 5512 [11] BROWN, L. M. (1978) “The idea of the neutrino,” *Physics Today*, **31**(9).
- 5513 [12] PAULI, W. (1978) “Dear radioactive ladies and gentlemen,” *Phys. Today*, **31N9**,
5514 p. 27.
- 5515 [13] AMALDI, E. (1984) “From the discovery of the neutron to the discovery of nuclear
5516 fission,” *Physics Reports*, **111**(1), pp. 1–331.
5517 URL <https://www.sciencedirect.com/science/article/pii/037015738490214X>
- 5519 [14] CHADWICK, J. (1932) “The existence of a neutron,” *Proceedings of the Royal
5520 Society of London. Series A, Containing Papers of a Mathematical and Physical
5521 Character*, **136**(830), pp. 692–708, <https://royalsocietypublishing.org/doi/pdf/10.1098/rspa.1932.0112>.
5523 URL <https://royalsocietypublishing.org/doi/abs/10.1098/rspa.1932.0112>
- 5525 [15] WILSON, F. L. (1968) “Fermi’s Theory of Beta Decay,” *American Journal of
5526 Physics*, **36**(12), pp. 1150–1160, https://pubs.aip.org/aapt/ajp/article-pdf/36/12/1150/11891052/1150_1_online.pdf.
5528 URL <https://doi.org/10.1119/1.1974382>
- 5529 [16] CRANE, H. R. and J. HALPERN (1938) “New Experimental Evidence for the
5530 Existence of a Neutrino,” *Phys. Rev.*, **53**, pp. 789–794.
5531 URL <https://link.aps.org/doi/10.1103/PhysRev.53.789>
- 5532 [17] COWAN, C. L., F. REINES, F. B. HARRISON, H. W. KRUSE, and A. D.
5533 MC GUIRE (1956) “Detection of the Free Neutrino: a Confirmation,” *Science*,
5534 **124**(3212), pp. 103–104, <https://www.science.org/doi/pdf/10.1126/science.124.3212.103>.
5536 URL <https://www.science.org/doi/abs/10.1126/science.124.3212.103>
- 5537 [18] ANICIN, I. V. (2005) “The Neutrino - Its Past, Present and Future,” *arXiv e-prints*,
5538 physics/0503172, [physics/0503172](https://arxiv.org/abs/physics/0503172).
- 5539 [19] DAVIS, R. (2003) “Nobel Lecture: A half-century with solar neutrinos,” *Rev. Mod.*
5540 *Phys.*, **75**, pp. 985–994.
- 5541 [20] McDONALD, A. B. ET AL. (2002) “Direct evidence for neutrino flavor transfor-
5542 mation from neutral-current interactions in SNO,” *AIP Conf. Proc.*, **646**(1), pp.
5543 43–58.
- 5544 [21] FUKUDA, Y. ET AL. (1998) “Evidence for oscillation of atmospheric neutrinos,”
5545 *Phys. Rev. Lett.*, **81**, pp. 1562–1567, [hep-ex/9807003](https://arxiv.org/abs/hep-ex/9807003).
- 5546 [22] GIGANTI, C., S. LAVIGNAC, and M. ZITO (2018) “Neutrino oscillations: The rise
5547 of the PMNS paradigm,” *Prog. Part. Nucl. Phys.*, **98**, pp. 1–54, [1710.00715](https://arxiv.org/abs/1710.00715).

- 5548 [23] WORKMAN, R. L. and OTHERS (2022) “Review of Particle Physics,” *PTEP*, **2022**,
 5549 p. 083C01.
- 5550 [24] AN, F. ET AL. (2016) “Neutrino Physics with JUNO,” *J. Phys. G*, **43**(3), p. 030401,
 5551 1507.05613.
- 5552 [25] BIAN, J. ET AL. (2022) “Hyper-Kamiokande Experiment: A Snowmass White
 5553 Paper,” in *Snowmass 2021*, 2203.02029.
- 5554 [26] ABI, B. ET AL. (2020) “Long-baseline neutrino oscillation physics potential of the
 5555 DUNE experiment,” *Eur. Phys. J. C*, **80**(10), p. 978, 2006.16043.
- 5556 [27] ZUBER, K. (2020) *Neutrino Physics*, CRC Press.
- 5557 [28] XING, Z. Z. and S. ZHOU (2011) *Neutrinos in Particle Physics, Astronomy and*
 5558 *Cosmology*, Springer.
- 5559 [29] MOHAPATRA, R. N. ET AL. (2007) “Theory of neutrinos: A White paper,” *Rept.*
 5560 *Prog. Phys.*, **70**, pp. 1757–1867, hep-ph/0510213.
- 5561 [30] DE GOUVÊA, A. (2016) “Neutrino Mass Models,” *Ann. Rev. Nucl. Part. Sci.*, **66**,
 5562 pp. 197–217.
- 5563 [31] WONG, Y. Y. Y. (2011) “Neutrino mass in cosmology: status and prospects,”
 5564 *Ann. Rev. Nucl. Part. Sci.*, **61**, pp. 69–98, 1111.1436.
- 5565 [32] ADE, P. A. R. ET AL. (2016) “Planck 2015 results. XIII. Cosmological parameters,”
 5566 *Astron. Astrophys.*, **594**, p. A13, 1502.01589.
- 5567 [33] CARLSTROM, J. ET AL. (2019) “CMB-S4,” in *Bulletin of the American Astronomical Society*, vol. 51, p. 209, 1908.01062.
- 5569 [34] ELLIOTT, S. R. and P. VOGEL (2002) “Double beta decay,” *Ann. Rev. Nucl. Part.*
 5570 *Sci.*, **52**, pp. 115–151, hep-ph/0202264.
- 5571 [35] DOLINSKI, M. J., A. W. P. POON, and W. RODEJOHANN (2019) “Neutrinoless
 5572 Double-Beta Decay: Status and Prospects,” *Ann. Rev. Nucl. Part. Sci.*, **69**, pp.
 5573 219–251, 1902.04097.
- 5574 [36] FORMAGGIO, J. A., A. L. C. DE GOUVÊA, and R. G. H. ROBERTSON (2021)
 5575 “Direct measurements of neutrino mass,” *Physics Reports*, **914**, pp. 1–54, direct
 5576 measurements of neutrino mass.
 5577 URL <https://www.sciencedirect.com/science/article/pii/S0370157321000636>
- 5579 [37] AKER, M. ET AL. (2022) “New Constraint on the Local Relic Neutrino Background
 5580 Overdensity with the First KATRIN Data Runs,” *Phys. Rev. Lett.*, **129**(1), p.
 5581 011806, 2202.04587.

- 5582 [38] FORMAGGIO, J. A., A. L. C. DE GOUVÊA, and R. G. H. ROBERTSON (2021)
 5583 “Direct Measurements of Neutrino Mass,” *Phys. Rept.*, **914**, pp. 1–54, 2102.00594.
- 5584 [39] MONREAL, B. and J. A. FORMAGGIO (2009) “Relativistic cyclotron radiation
 5585 detection of tritium decay electrons as a new technique for measuring the neutrino
 5586 mass,” *Phys. Rev. D*, **80**, p. 051301.
 5587 URL <https://link.aps.org/doi/10.1103/PhysRevD.80.051301>
- 5588 [40] ESFAHANI, A. A. ET AL. (2022) “The Project 8 Neutrino Mass Experiment,”
 5589 2203.07349.
- 5590 [41] ——— (2023) “Cyclotron Radiation Emission Spectroscopy of Electrons from
 5591 Tritium Beta Decay and ^{83m}Kr Internal Conversion,” 2303.12055.
- 5592 [42] ——— (2023) “Tritium Beta Spectrum and Neutrino Mass Limit from Cyclotron
 5593 Radiation Emission Spectroscopy,” 2212.05048.
- 5594 [43] “Antenna Arrays for Physics Measurements with Large-scale CRES Detectors,” *In
 5595 preparation*.
- 5596 [44] NICHOLSON, T. ET AL. (2015) “Systematic evaluation of an atomic clock at 2 x
 5597 10-18 total uncertainty,” *Nature Communications*, **6**(6896).
- 5598 [45] HÄNSCH, T. W. (2006) “Nobel Lecture: Passion for precision,” *Rev. Mod. Phys.*,
 5599 **78**, pp. 1297–1309.
 5600 URL <https://link.aps.org/doi/10.1103/RevModPhys.78.1297>
- 5601 [46] GABOR, D. (1946) “Theory of communication. Part 1: The analysis of information,”
 5602 *Journal of the Institution of Electrical Engineers-part III: radio and communication
 5603 engineering*, **93**(26), pp. 429–441.
- 5604 [47] ESFAHANI ASHTARI, A. ET AL. (2022) “Viterbi decoding of CRES signals in
 5605 Project 8,” *New J. Phys.*, **24**(5), p. 053013, 2112.05265.
- 5606 [48] JACKSON, J. D. (1999) *Classical electrodynamics*, 3rd ed., Wiley, New York, NY.
 5607 URL <http://cdsweb.cern.ch/record/490457>
- 5608 [49] F.R.S., J. L. D. (1897) “LXIII. On the theory of the magnetic influence on
 5609 spectra; and on the radiation from moving ions,” *The London, Edinburgh, and
 5610 Dublin Philosophical Magazine and Journal of Science*, **44**(271), pp. 503–512,
 5611 <https://doi.org/10.1080/14786449708621095>.
 5612 URL <https://doi.org/10.1080/14786449708621095>
- 5613 [50] ESFAHANI, A. A. ET AL. (2022) “The Project 8 Neutrino Mass Experiment,” in
 5614 *2022 Snowmass Summer Study*, 2203.07349.
- 5615 [51] KRAUS, C. ET AL. (2005) “Final results from phase II of the Mainz neutrino mass
 5616 search in tritium beta decay,” *Eur. Phys. J. C*, **40**, pp. 447–468, [hep-ex/0412056](https://arxiv.org/abs/hep-ex/0412056).

- 5617 [52] ASEEV, V. N. ET AL. (2011) “An upper limit on electron antineutrino mass from
5618 Troitsk experiment,” *Phys. Rev. D*, **84**, p. 112003, 1108.5034.
- 5619 [53] SAENZ, A., S. JONSELL, and P. FROELICH (2000) “Improved Molecular Final-
5620 State Distribution of HeT+ for the β -Decay Process of T2,” *Phys. Rev. Lett.*, **84**(2),
5621 p. 242.
- 5622 [54] BODINE, L. I., D. S. PARNO, and R. G. H. ROBERTSON (2015) “Assessment
5623 of molecular effects on neutrino mass measurements from tritium β decay,” *Phys.
5624 Rev. C*, **91**(3), p. 035505, 1502.03497.
- 5625 [55] ASNER, D. M. ET AL. (2015) “Single electron detection and spectroscopy via
5626 relativistic cyclotron radiation,” *Phys. Rev. Lett.*, **114**(16), p. 162501, 1408.5362.
- 5627 [56] VÉNOS, D., J. SENTKERESTIOVÁ, O. DRAGOUN, M. SLEZÁK, M. RYŠAVÝ, and
5628 A. ŠPALEK (2018) “Properties of 83mKr conversion electrons and their use in the
5629 KATRIN experiment,” *JINST*, **13**(02), p. T02012.
- 5630 [57] LAGENDIJK, A., I. F. SILVERA, and B. J. VERHAAR (1986) “Spin exchange and
5631 dipolar relaxation rates in atomic hydrogen: Lifetimes in magnetic traps,” *Phys.
5632 Rev. B*, **33**, pp. 626–628.
5633 URL <https://link.aps.org/doi/10.1103/PhysRevB.33.626>
- 5634 [58] SILVERA, I. and J. WALRAVEN (1986) “Spin-polarized atomic hydrogen,” *Prog.
5635 Low Temp. Phys.*, **X**, pp. 139–370.
- 5636 [59] FURSE, D. ET AL. (2017) “Kassiopeia: a modern, extensible C++ particle tracking
5637 package,” *New Journal of Physics*, **19**(5), p. 053012.
5638 URL <https://doi.org/10.1088/1367-2630/aa6950>
- 5639 [60] ESFAHANI, A. A. ET AL. (2019) “Electron radiated power in cyclotron radiation
5640 emission spectroscopy experiments,” *Phys. Rev. C*, **99**, p. 055501.
5641 URL <https://link.aps.org/doi/10.1103/PhysRevC.99.055501>
- 5642 [61] ASHTARI ESFAHANI, A. ET AL. (2019) “Locust: C++ software for simulation of
5643 RF detection,” *New J. Phys.*, **21**, p. 113051, 1907.11124.
- 5644 [62] WIECHERT, E. (1901) “Elektrodynamische Elementargesetze,” .
5645 URL <https://doi.org/10.1002/andp.19013090403>
- 5646 [63] LIÉARD, A. (1898) “Champ électrique et Magnétique,” *Léclairage électrique*, **16**(27-
5647 29).
- 5648 [64] BALANIS, C. (2015) *Antenna Theory: Analysis and Design*, Wiley.
5649 URL <https://books.google.com/books?id=PTFcCwAAQBAJ>
- 5650 [65] [https://www.ansys.com/products/electronics/ansys-hfss.](https://www.ansys.com/products/electronics/ansys-hfss)

- 5651 [66] https://en.wikipedia.org/wiki/Linear_time-invariant_system.
- 5652 [67] NYQUIST, H. (1928) “Certain Topics in Telegraph Transmission Theory,” *Transactions of the American Institute of Electrical Engineers*, **47**(2), pp. 617–644.
- 5654 [68] BRUN, R. and F. RADEMAKERS (1997) “ROOT: An object oriented data analysis
5655 framework,” *Nucl. Instrum. Meth. A*, **389**, pp. 81–86.
- 5656 [69] ASHTARI ESFAHANI, A. ET AL. (2021) “Bayesian analysis of a future β decay
5657 experiment’s sensitivity to neutrino mass scale and ordering,” *Phys. Rev. C*, **103**,
5658 p. 065501.
5659 URL <https://link.aps.org/doi/10.1103/PhysRevC.103.065501>
- 5660 [70] KAY, S. (1998) *Fundamentals of Statistical Signal Processing: Detection Theory,*
5661 *Volume II*, Pearson.
- 5662 [71] NEYMAN, J. and E. PEARSON (1933) “On the problem of the the most efficient
5663 tests of statistical hypotheses,” *Phil. Trans. R. Soc. Lond. A*, **231**.
- 5664 [72] STUMPF, M. (2018) *Electromagnetic Reciprocity in Antenna Theory*, Wiley.
- 5665 [73] BISHOP, C. (2016) *Pattern Recognition and Machine Learning*, Springer.
- 5666 [74] PLEHN, T., A. BUTTER, B. DILLON, and C. KRAUSE (2022) “Modern Machine
5667 Learning for LHC Physicists,” [2211.01421](https://arxiv.org/abs/2211.01421).
- 5668 [75] GEORGE, D. and E. A. HUERTA (2018) “Deep Learning for Real-time Gravitational
5669 Wave Detection and Parameter Estimation: Results with Advanced LIGO Data,”
5670 *Phys. Lett. B*, **778**, pp. 64–70, [1711.03121](https://arxiv.org/abs/1711.03121).
- 5671 [76] GABBARD, H., C. MESSENGER, I. S. HENG, F. TONOLINI, and R. MURRAY-
5672 SMITH (2022) “Bayesian parameter estimation using conditional variational au-
5673 toencoders for gravitational-wave astronomy,” *Nature Phys.*, **18**(1), pp. 112–117,
5674 [1909.06296](https://arxiv.org/abs/1909.06296).
- 5675 [77] REIMANN, R. (2022) “Project 8: R&D for a next-generation neutrino mass experi-
5676 ment,” *PoS, PANIC2021*, p. 283.
- 5677 [78] LAROQUE, B. (2020) “Zero-deadtime processing in beta spectroscopy for measure-
5678 ment of the non-zero neutrino mass,” *EPJ Web Conf.*, **245**, p. 01014.
- 5679 [79] BUZINSKY, N. (2021) *Statistical Signal Processing and Detector Optimization in*
5680 *Project 8*, Ph.D. thesis, Massachusetts Institute of Technology.
- 5681 [80] ESFAHANI, A. A. ET AL. (2023) “SYNCA: A Synthetic Cyclotron Antenna for
5682 the Project 8 Collaboration,” *Journal of Instrumentation*, **18**(01), p. P01034.
5683 URL <https://dx.doi.org/10.1088/1748-0221/18/01/P01034>
- 5684 [81] <https://www.nvidia.com/en-us/data-center/v100/>.

- 5685 [82] <https://www.nvidia.com/en-us/data-center/h100/>.
- 5686 [83] HE, K., X. ZHANG, S. REN, and J. SUN (2016) “Deep Residual Learning for
5687 Image Recognition,” in *2016 IEEE Conference on Computer Vision and Pattern
5688 Recognition (CVPR)*, pp. 770–778.
- 5689 [84] SIMONYAN, K. and A. ZISSERMAN (2015) “Very Deep Convolutional Networks
5690 for Large-Scale Image Recognition,” in *3rd International Conference on Learning
5691 Representations, ICLR 2015, San Diego, CA, USA, May 7-9, 2015, Conference
5692 Track Proceedings* (Y. Bengio and Y. LeCun, eds.).
5693 URL <http://arxiv.org/abs/1409.1556>
- 5694 [85] FRIIS, H. (1946) “A Note on a Simple Transmission Formula,” *Proceedings of the
5695 IRE*, **34**(5), pp. 254–256.
- 5696 [86] POZAR, D. M. (2005) *Microwave engineering; 3rd ed.*, Wiley, Hoboken, NJ.
5697 URL <https://cds.cern.ch/record/882338>
- 5698 [87] AKER, M. ET AL. (2022) “Direct neutrino-mass measurement with sub-electronvolt
5699 sensitivity,” *Nature Physics*, **18**(2), pp. 160–166.
5700 URL <https://doi.org/10.1038/s41567-021-01463-1>
- 5701 [88] MONREAL, B. and J. A. FORMAGGIO (2009) “Relativistic Cyclotron Radiation
5702 Detection of Tritium Decay Electrons as a New Technique for Measuring the
5703 Neutrino Mass,” *Phys. Rev. D*, **80**, p. 051301, 0904.2860.
- 5704 [89] ASHTARI ESFAHANI, A. ET AL. (2017) “Determining the neutrino mass with
5705 cyclotron radiation emission spectroscopy—Project 8,” *J. Phys. G*, **44**(5), p. 054004,
5706 1703.02037.
- 5707 [90] ESFAHANI, A. A. ET AL. (2022) “The Project 8 Neutrino Mass Experiment,” in
5708 *2022 Snowmass Summer Study*, 2203.07349.
- 5709 [91] ASHTARI ESFAHANI, A. ET AL. (2019) “Locust: C++ software for simulation of
5710 RF detection,” *New Journal of Physics*, **21**(11), p. 113051.
5711 URL <https://doi.org/10.1088/1367-2630/ab550d>
- 5712 [92] FURSE, D. ET AL. (2017) “Kassiopeia: a modern, extensible C++ particle tracking
5713 package,” *New Journal of Physics*, **19**(5), p. 053012.
5714 URL <https://doi.org/10.1088/1367-2630/aa6950>
- 5715 [93] BALANIS, C. (2011) *Modern Antenna Handbook*, Wiley.
5716 URL <https://books.google.com/books?id=UYpV8L8GNcwc>
- 5717 [94] WIRTH, W. (2001) *Radar Techniques Using Array Antennas*, Institution of Engi-
5718 neering and Technology.
5719 URL <https://books.google.com/books?id=ALht42gkzLsC>

- 5720 [95] BROWN, L. S., G. GABRIELSE, K. HELMERSON, and J. TAN (1985) “Cyclotron
5721 motion in a microwave cavity: Lifetime and frequency shifts,” *Phys. Rev. A*, **32**,
5722 pp. 3204–3218.
5723 URL <https://link.aps.org/doi/10.1103/PhysRevA.32.3204>
- 5724 [96] HANNEKE, D., S. FOGWELL HOOGERHEIDE, and G. GABRIELSE (2011) “Cavity
5725 control of a single-electron quantum cyclotron: Measuring the electron magnetic
5726 moment,” *Phys. Rev. A*, **83**, p. 052122.
5727 URL <https://link.aps.org/doi/10.1103/PhysRevA.83.052122>
- 5728 [97] HANNEKE, D. A. (2007) *Cavity control in a single-electron quantum cyclotron: an
5729 improved measurement of the electron magnetic moment*, Ph.D. thesis, Harvard U.
- 5730 [98] PURCELL, E. (1946) “Spontaneous Emission Probabilities at Radio Frequencies,”
5731 *Phys. Rev.*, **69**, pp. 674–674.
5732 URL <https://link.aps.org/doi/10.1103/PhysRev.69.674>
- 5733 [99] MOSKOWITZ, B. E. and J. ROGERS (1988) “ANALYSIS OF A MICROWAVE
5734 CAVITY DETECTOR COUPLED TO A NOISY AMPLIFIER,” *Nucl. Instrum.
5735 Meth. A*, **264**, pp. 445–452.
- 5736 [100] RAPIDIS, N. M. (2018) “Application of the Bead Perturbation Technique to a
5737 Study of a Tunable 5 GHz Annular Cavity,” *Springer Proc. Phys.*, **211**, pp. 45–51,
5738 1708.04276.
- 5739 [101] “Real-time Signal Detection for Cyclotron Radiation Emission Spectroscopy Mea-
5740 surements using Antenna Arrays,” *In preparation*.
- 5741 [102] BYRON, W. ET AL. (2022) “First observation of cyclotron radiation from MeV-scale
5742 e^{pm} following nuclear beta decay,” 2209.02870.
- 5743 [103] KAZKAZ, K. and N. WOOLLETT (2021) “Using Cyclotron Radiation Emission
5744 for Ultra-high Resolution X-Ray Spectroscopy,” *New J. Phys.*, **23**(3), p. 033043,
5745 1911.05869.
- 5746 [104] CANNING, J. A. L., F. F. DEPPISCH, and W. PEI (2023) “Sensitivity of future
5747 tritium decay experiments to New Physics,” *JHEP*, **03**, p. 144, 2212.06106.

5748

Vita

5749

Andrew Douglas Ziegler

5750

Education

5751

- Doctor of Philosophy, Physics, The Pennsylvania State University, University Park, Pennsylvania, USA, 2023
- Bachelor of Science, Physics, The University of Minnesota, Minneapolis, Minnesota, USA, 2017

5752

5753

Selected Publications

5754

- Astari Esfahani, A. et al. (2023) "Antenna Arrays for CRES-based Neutrino Mass Measurement", *Phys. Rev. C*, In preparation.
- Astari Esfahani, A. et al. (2023) "Real-time Signal Detection for Cyclotron Radiation Emission Spectroscopy Measurements using Antenna Arrays", *Journal of Instrumentation*, In preparation.
- Astari Esfahani, A. et al. (2023) "Tritium Beta Spectrum and Neutrino Mass Limit from cyclotron Radiation Emission Spectroscopy", *Phys. Rev. Lett.*, Accepted.
- Astari Esfahani, A. et al. (2022) "SYNCA: A Synthetic Cyclotron Antenna for the Project 8 Collaboration", *Journal of Instrumentation*, **18**(01).

5755

5756

Selected Presentations

5765

- *New Developments in the CRES Technique for Neutrino Mass Measurement*, Invited Talk, Fall 2022 Meeting of the APS Division of Nuclear Physics, New Orleans, Louisiana, USA, 2022
- *Signal Detection Algorithms for Phase III of the Project 8 Experiment*, Contributed Talk, APS April Meeting 2022, New York, New York, 2022
- *Synthetic Electron Antenna for Calibrating the Project 8 Neutrino Mass Experiment*, Contributed Talk, Fall 2021 Meeting of the APS Division of Nuclear Physics, Virtual, 2021

5766

5767

5768

5769

5770

5771

5772

5773